PHOTOCHEMICAL OZONE FORMATION AND RADICAL CHEMISTRY IN FIVE CHINESE MEGACITIES AND PEARL RIVER ESTUARY: FIELD OBSERVATIONS AND MODEL SIMULATIONS

LIU XUFEI
PhD

The Hong Kong Polytechnic University
2021

The Hong Kong Polytechnic University

Department of Civil and Environmental Engineering

PHOTOCHEMICAL OZONE FORMATION AND RADICAL CHEMISTRY IN FIVE CHINESE MEGACITIES AND PEARL RIVER ESTUARY: FIELD OBSERVATIONS AND MODEL SIMULATIONS

LIU XUFEI

A thesis submitted in partial fulfillment of the requirements for the degree
of Doctor of Philosophy

December 2020

Certificate of originality

I hereby declare that this thesis is my own work and that, to the best of my knowledge and belief, it reproduces no material previously published or written, nor material that has been accepted for the award of any other degree or diploma, except where due acknowledgement has been made in the text.

(Signed)

LIU Xufei (Name of student)

Abstract

As a consequence of the rapid industrialization and urbanization in the past 30 years, ozone (O_3) pollution has become one of the major air pollution problems in China. O_3 is a big concern due to its adverse impact on air quality, human health, ecosystems and climate change. Many studies on O_3 photochemistry have been conducted in one or several megacity clusters in China, such as north China plain (NCP), Yangtze River Delta (YRD), Pearl River Delta (PRD) and Sichuan Basin (SCB) regions, and central and northwestern China. However, there is a dearth of nationwide studies on in-situ O_3 photochemistry in urban areas of major Chinese megacities. In addition, the O_3 photochemistry in small-scale environments such as Pearl River Estuary (PRE) area, including urban Hong Kong, remains unclear. This study aims to comprehensively investigate the O_3 photochemistry in: (1) urban areas of five major megacities in China in the summer of 2018; (2) two sites at the west and east banks of the PRE in the autumn of 2016; and (3) urban Hong Kong in the autumns of 2007, 2013 and 2016.

To investigate the photochemical O_3 pollution in urban areas in China, comprehensive measurements of O_3 and its precursors, including trace gases and volatile organic compounds (VOCs), were simultaneously conducted in urban areas of five major cities in China, *i.e.*, Beijing, Shanghai, Wuhan, Chengdu and Lanzhou, in the summer of 2018. The results showed that Beijing had the highest O_3 mixing ratio (78.6±7.3 ppbv) followed by Lanzhou (67.2±7.8 ppbv) and Wuhan (63.9±6.8 ppbv), while Chengdu and Shanghai had relatively lower O_3 (Chengdu: 52.5±7.5 ppbv; Shanghai: 20.7±1.9 ppbv) ($p < 0.05$), indicating the severe O_3 pollution in northern and central China in summer. Model simulations revealed that the net O_3 production rate in Lanzhou (8.9±1.7 ppbv h^{-1}) was the largest, followed by Beijing (6.4±1.3 ppbv h^{-1}), Wuhan (5.8±1.2 ppbv h^{-1}) and Chengdu (4.0±0.6 ppbv h^{-1}), while it was the lowest in Shanghai (2.8±0. 7 ppbv h^{-1}) ($p < 0.05$). In addition, the simulated RO_x (= $OH+HO_2+RO_2$) concentrations were comparable ($p>0.1$) in Lanzhou ((5.9±1.1) $\times10^8$ molecules cm^{-3}), Beijing ((5.3±1.1) $\times10^8$ molecules cm^{-3}) and Wuhan ((4.3±1.0) $\times10^8$ molecules cm^{-3}), which were significantly higher ($p < 0.05$) than those in Shanghai ((2.7±0.9) $\times10^8$ molecules cm^{-3}) and Chengdu ((1.8±0.7) $\times10^8$ molecules cm^{-3}), indicating the stronger atmospheric oxidative capacity and severer O_3 pollution in northern and central China in

summer. Furthermore, the O_3 formation was mainly controlled by VOCs in most urban areas but co-limited by both VOCs and nitrogen oxide (NO_x) in Lanzhou, indicating that cutting NO_x and VOCs would effectively lead to O_3 alleviation in Lanzhou. Moreover, the dominant VOC groups (species) contributing to O_3 formation were oxygenated VOCs (OVOCs) (*e.g.,* formaldehyde and acetaldehyde) in Beijing and Wuhan, alkenes (*e.g.,* propene) in Lanzhou, and aromatics (*e.g.,* xylenes and trimethylbenzenes) and OVOCs (*e.g.,* formaldehyde and acetaldehyde) in Shanghai and Chengdu. Besides, 1-butene in Shanghai also needed stricter control given its high contribution to O_3 formation. Source apportionment simulations identified six VOC sources in the study cities, including liquefied petroleum gas (LPG) usage, diesel exhaust, gasoline exhaust, industrial emissions, solvent usage and biogenic emissions. VOCs from vehicular emissions including diesel and gasoline exhausts were more abundant in the central and northern cities ($p < 0.05$), while solvent usage contributed the most to ambient VOCs in Shanghai ($p < 0.05$), followed by Chengdu. Industry emission was the top source of VOCs in the northwestern city (*i.e.,* Lanzhou) ($p < 0.05$). For the contributions of these VOC sources to O_3 formation in these cities, diesel exhaust and solvent usage were the largest contributors in Beijing ($p < 0.05$), while diesel exhaust, industrial emissions and solvent usage made comparable contributions in Lanzhou ($p>0.1$). The O_3 formation was solely dominated by solvent usage in the other three cities ($p < 0.05$).

In addition to the five megacities in China, the Pearl River Estuary (PRE) including Hong Kong has also been suffering from severe photochemical O_3 pollution for many years. However, the in-situ O_3 photochemistry in this area is still not fully clear though many studies have been carried out. To explore the photochemical O_3 pollution over the PRE, intensive measurements were simultaneously conducted at a suburban site on the east bank of PRE (Tung Chung, TC) in Hong Kong and a rural site on the west bank (Qi'ao, QA) in Zhuhai, Guangdong in autumn 2016. Throughout the sampling period, three O_3 episode days were captured at both sites (defined as pattern 1) and 13 days with O_3 episodes occurred only at QA (defined as pattern 2). The results indicated that O_3 formation at TC was VOC-limited in both patterns because of the large local NO_x emissions. However, the O_3 formation at QA was co-limited by VOCs and NO_x in pattern 1, but VOC-limited in pattern 2. In both patterns, isoprene, formaldehyde, xylenes and trimethylbenzenes were the top 4 VOCs that modulated local O_3 formation at QA, while they were isoprene, formaldehyde, xylenes and toluene at TC. In pattern 1, the net O_3 production rates were high at both QA and TC sites ($p = 0.40$), so was the hydroxyl radical (*i.e.*, OH), implying high atmospheric oxidative capacity over PRE. In contrast, the net O_3 production rate was significantly higher ($p < 0.05$) at QA than that at TC in pattern 2, and the OH concentration and cycling rate were also higher, indicating considerably stronger photochemical reactions at QA.

Moreover, to discover the temporal variations of photochemical O_3 formation and radical chemistry during last decade in Hong Kong, comprehensive sampling campaigns were conducted in the autumns of 2007, 2013 and 2016. While the simulated locally-produced O_3 remained unchanged ($p = 0.73$) from 2007 to 2013, the observed O_3 increased ($p < 0.05$) at a rate of 1.78 ppbv yr^{-1} driven by the rise in regionally transported O_3 (1.77±0.04 ppbv yr^{-1}). Both the observed and locally produced O_3 decreased ($p < 0.05$) from the VOC sampling days in 2013 to those in 2016 at a rate of −5.31±0.07 ppbv yr^{-1} and −5.52±0.05 ppbv yr^{-1}, respectively. However, a leveling-off ($p = 0.32$) was simulated for the regionally transported O_3 from 2013 to 2016. The mitigation of autumn O_3 pollution in Hong Kong was further confirmed by the continuous monitoring data, which have never been reported. Benefiting from the air pollution control measures taken in Hong Kong, the local O_3 production rate decreased remarkably ($p < 0.05$) from 2007 to 2016, along with the lowering of the recycling rate of the OH. Specifically, VOCs emitted from the source of LPG usage and gasoline evaporation decreased in this decade at a rate of −2.61±0.03 ppbv yr^{-1}, leading to a reduction of the O_3 production rate from 0.51±0.11 ppbv h^{-1} in 2007 to 0.10±0.02 ppbv h^{-1} in 2016. In addition, solvent usage made decreasing contributions to both VOCs (rate=−2.29±0.03 ppbv yr^{-1}) and local O_3 production rate (1.22±0.17 and 0.14±0.05 ppbv h^{-1} in 2007 and 2016, respectively) in the same period. All the rates reported here were for the VOC sampling days in the three sampling campaigns. It is noteworthy that meteorological changes also play important roles in the inter-annual variations in the observed O_3 and the simulated O_3 production rates. Evaluations with more data in longer periods are therefore recommended.

Overall, the findings of photochemical O_3 pollution in China's five megacities and PRE partially addressed the knowledge gaps in O_3 formation mechanism and radical chemistry in China, and provided a scientific basis for dealing with China's national O_3 pollution. In addition, this study analyzed the decadal changes of the local and regional photochemistry in Hong Kong, and the chemical characteristics of O_3 formation in PRE, which will help to understand the O_3 photochemistry in similar microenvironments. These findings are also useful for evaluating the effectiveness of existing and projected O_3 pollution control measures.

The novelty of this study

Owing to the rapid economic development and population growth in the past three decades, severe O_3 pollution often occurs in cities in China during warm seasons. Since each city has its unique industrial structures, energy use pattern and meteorological conditions, the photochemical O_3 formation mechanisms in different cities may be different, which must be considered when formulating O_3 control strategies. Although O_3 photochemistry has been extensively studied in Beijing and Shanghai, a handful of studies have investigated the formation mechanisms and free radical chemistry of photochemical O_3 in central, southwestern and northwestern China in warm season, not to mention simultaneous study in multiple cities in China. This study **for the first time** simultaneously explored in-situ O_3 photochemistry in summer in five major Chinese megacities including those in central, southwestern and northwestern China, partially addressed the knowledge gaps.

Although great efforts have been made by the Guangdong provincial government and the Hong Kong government to alleviate the tropospheric O_3 pollution in the Pearl River Delta (PRD) region including Hong Kong, the O_3 level is still increasing or at least not decreasing at the expected rates. Among the numerous studies of O_3 pollution in urban and industrial areas in inland PRD region, only few focused on comprehensive O_3 photochemistry particularly during high O_3 episodes in the Pearl River Estuary (PRE). The PRE is a critical area in southern China with heavy O_3 pollution despite sparse on-site anthropogenic emissions. Nevertheless, there is a lack of investigations on species-based photochemistry and/or radical chemistry in this area. To my best knowledge, this is **the first attempt** to explore detailed photochemical O_3 formation mechanisms in the PRE, especially on high O_3 episode days. This study deepened the understanding of O_3 photochemistry in the PRD region and guided local governments to develop appropriate O_3 pollution control strategies.

Moreover, though several studies have been conducted on the long-term variations of O_3 precursors and the O_3 formation regimes in Hong Kong during the last decade, the inter-annual variations in O_3 photochemistry and free radical chemistry have not been fully understood. Since 2007, the Hong Kong government has implemented a series of control measures aimed at restricting the emission of O_3 precursors in order to improve the local air quality. The pre-2013 effectiveness of control measures have been evaluated by previous studies. However, the post-2013 variations in the local O_3 production and the regional impacts and the effectiveness of those local and regional control measures were not well documented. This study was **the pioneer** to trace the O_3 evolution underlying mechanisms for the variations in O_3 formation and radical chemistry, with the aid of a photochemical box model and a receptor model. the exploration of O_3 trends and their potential causes in Hong Kong provided a good example for evaluating the evolution of O_3 pollution and the effects of artificial interventions in China. In addition, the changes in the regional contribution to O_3 in Hong Kong identified in this study would shed light upon the variations in O_3 in China, especially in South China.

Publications

Publications as the first author:

1. **Liu, X**., Lyu, X., Wang, Y., Jiang, F. and Guo, H.*, 2019. Intercomparison of O_3 formation and radical chemistry in the past decade at a suburban site in Hong Kong. Atmospheric Chemistry and Physics, 19(7), 5127-5145 (Impact factor: 5.318; Grade A)
2. **Liu, X.**, Wang, N., Lyu, X., Zeren, Y., Jiang, F., Wang, X., Zou, S., Ling, Z. and Guo, H.*, 2020. Photochemistry of ozone pollution in autumn in Pearl River Estuary, South China. Science of The Total Environment. 754, 141812 (Impact factor: 6.551; Grade A).
3. **Liu, X**., Guo, H.*, Zeng, L.W., Lyu, X., Wang, Y., Zeren, Y., Zhang, L. and Yang, J., 2020. Photochemical ozone formation and free radical chemistry in five Chinese megacities in summer (In preparation).

Publications as co-author:

4. Zeren, Y., Guo, H.*, Lyu, X.*, Jiang, F., Wang, Y., **Liu, X.,** Zeng, L., Li, M. and Li, L., 2019. An ozone "pool" in South China: Investigations on atmospheric dynamics and photochemical processes over the Pearl River Estuary. Journal of Geophysical Research: Atmospheres, 10.1029/2019JD030833, (Impact factor: 3.96; Grade A).
5. Zeng, P., Lyu, X., Guo, H., Cheng, H.*, Wang, Z., **Liu, X**. and Zhang, W., 2019. Spatial variation of sources and photochemistry of formaldehyde in Wuhan, Central China. Atmospheric Environment. 214, 116826 (Impact factor: 4.012; Grade A).
6. Meng, Y., Song, J., Zeng, L., Zhang, Y., Zhao, Y., **Liu, X.**, Guo, H., Zhong, L., Ou, Y., Zhou, Y., Zhang, T., Yue, D*. and Lai, S.*, 2022. Ambient volatile organic compounds at a receptor site in the Pearl River Delta region: Variations, source apportionment and effects on ozone formation. Journal of Environmental Sciences, 111, 104-117 (Impact factor: 4.302; Grade A).
7. Lyu, X., Guo, H.*, Zhang, W., Cheng, H., Yao, D., Lu, H., Zhang, L., Zeren, Y., **Liu, X**., Qian, Z. and Wang, S., 2020. Anthropogenic emissions dominate ozone production in a high-elevation and highly forested region in central China: implications on forest

ecosystems and regional air quality. Atmospheric Environment. (Impact factor: 4.039; Grade A) (Under review).

8. Zeren, Y., Guo, H*., Lyu, X., **Liu, X**. and Jiang, F., 2021. Does ozone pollution share the same formation mechanisms in the bay areas of China? (In preparation).
9. Zeren, Y., Guo, H*., Lyu, X., Zhou, B., **Liu, X.**, Yang, L., Yuan, Z., Wang, Y. and Ling, Z., 2021. Driving forces of long-term O_3 trend (2005–2017) in Hong Kong, South China: Meteorology, regional transport, and photochemical precursors. (In preparation).

Acknowledgements

I am truly grateful to spend five years accomplishing my PhD study in the Hong Kong Polytechnic University (PolyU), which would be one of the most memorable experiences in my life. Along the way, I have met many smart and friendly people who provided selfless help, care, inspiration, and support to me. Thus, I would like to express my sincere gratitude to them.

Firstly, my heartfelt gratitude goes to my chief supervisor, Prof. GUO Hai, for providing me all necessary resources of my research work. Meanwhile, I must show my great appreciation to him for his rich knowledge, patience, trust, and strictness in guiding me, especially when I was relatively clumsy when I first started doing research. There is no word that can fully express my gratitude to him.

Secondly, special appreciation and deep thanks are to my former and current teammates and colleagues for their great help in improving my research skills. (1) Thanks to LYU Xiaopu and WANG Yu for their generous help in developing and teaching the PBM-MCM model and establishing my logic thinking; (2) Thanks to WANG Nan for his generous help in running the WRF-CMAQ model; (3) Thanks to CHENG Hairong, LING Zhenhao, WANG Dawei, WANG Hao, ZHANG Fan, LI Kaimin, XU Jingcui for their kind guidance and help during my studies; (4) Thanks to Mr. TAM W.F. and Mr. CHAN Jazz in Air Laboratory for their professional and continuous support on experimental setup and troubleshooting.

Thirdly, I sincerely thank all my teammates who have been colleagues and friends throughout my years at PolyU. They are ZEREN Yangzong, ZENG Lewei, ZENG Pei, LU Haoxian, YAO Dawen, ZHOU Beining, ZHANG Luyao, ZHAN Lingxi, YANG Jin, HUO Yunxi, WANG Jiaying, HUANG Fengwen, NIE Kun, CHEN Genwei, DANG Juan, PAN Wenzhuo, XU Chang, DONG Shuhao, LIANG Zhirong, YUNG Mo Wai, AU Hong Ting, SHEK Kit Ying, CHOW Ting Sing. Without you, my journey would not be so perfect.

Fourthly, this work was supported by the Research Grants Council of the Hong Kong Special Administrative Region via Theme-Based Research Scheme (Project T24-504/l7-N) and General Research Fund (PolyU 152052/14E, PolyU 152052/16E and CRF/C5004-15E), the Strategic Focus Area scheme of the Research Institute for Sustainable Urban Development at

Hong Kong PolyU (1-BBW9), and the FCE Postdoctoral Fellowship Scheme (ZVMN), the National Key R&D Program of China via grant no. 2017YFC0212001, the Public Policy Research Funding Scheme from Policy Innovation and Co-ordination Office of the Hong Kong Special Administrative Region Government (2017.A6.094.17D), and the Hong Kong PolyU PhD scholarships via research project no. RUDC.

Finally, my deepest thank goes to my best parents and grandparents for their endless support and selfless love to me. They may know little about my research, but they know all about me. Their inspiration and encouragement are all I need to overcome difficulties or sadness. It is also their ineffable optimism and fortitude that provided me endless energy to face challenges positively. I am more than lucky to be born in this family and be their beloved little girl forever.

Contents

List of Figures

List of Tables

Chapter 1 Overview

1.1 Introduction

Tropospheric ozone (O_3), as a secondary pollutant and an important component of photochemical smog, not only adversely affects human health, ecosystems, climate change and air quality, but also plays a crucial role in atmospheric chemistry (Chameides et al., 1999; Atkinson, 2000; Bell et al., 2004, 2007; Ashmore, 2005; Thompson et al., 2011). With the rapid industrialization and urbanization in the past three decades, the increasing emissions of O_3 precursors, *i.e.*, nitrogen oxides ($NO_x = NO + NO_2$) and volatile organic compounds (VOCs), have led to more severe O_3 pollution in the near-surface atmosphere and hence aroused increasing attention from international authorities (NRC, 1991; NARSTO, 2000; Oltmans et al., 2004; Monks et al., 2015).

China is the central hub to many megacities, where severe O_3 pollution is common in warm seasons (Wang T. et al., 2017; Wu and Xie, 2017; Li K. et al., 2019). Over the past 20 years, many studies have reported the increasing O_3 trends and strong photochemical reactions in several highly urbanized regions in China, *e.g.*, North China Plain (NCP), Yangtze River Delta (YRD) and Pearl River Delta (PRD) (Wang T. et al., 2017; Wang W. et al., 2017; Lu et al., 2020a). Moreover, cities in central and western China also experience air quality deterioration, especially photochemical pollution, due to their expansion of economy, population and industrialization, such as Wuhan (Lyu et al., 2016a; Hui et al., 2018; Zeng P. et al., 2018), Chengdu (Su et al., 2017; Tan et al., 2018a; Ning et al., 2020) and Lanzhou (Xue et al., 2014a; Jia et al., 2016). Since 2013, the central government has made great effort to combat the air pollution problem in China, including various stringent control strategies on multiple anthropogenic pollutants, *e.g.*, the Air Pollution Prevention and Control Action Plan from 2013-2018 (MEE PRC, 2019), the short-term "blue sky defense battle" between 2018-2020 (MEE PRC, 2018) and the long-term "beautiful China" targets till 2035 (CCIED, 2019) (Liu X. et al., 2019; Lu et al., 2020b). According to Lu et al. (2020a), though many pollutants, including SO_2 and $PM_{2.5}$, have been effectively controlled, increasing O_3 pollution still exists in urban areas in China, indicating that corresponding control actions on O_3 precursors, *i.e.*, VOCs and NO_x, in different regions are supposed to be more strictly enforced as appropriate. Moreover, since each city has its unique industrial structures, energy use pattern and meteorological conditions, the photochemical O_3 formation mechanisms in different cities may be different, which must be considered when formulating O_3 control strategies (Lu H. et al., 2019; Wang M.Y. et al., 2019a). However, there is a dearth of nationwide studies on in-situ O_3 photochemistry in urban areas of major Chinese megacities, especially in central and western China.

The Pearl River Delta (PRD) region including Hong Kong, as one of the most developed regions in China with dense population, transportation and industry, has also been suffering from severe photochemical pollution for many years (Guo et al., 2009; Xue et al., 2014b; Lu et al., 2019). Despite extensive studies of O_3 pollution in urban and industrial areas in inland PRD (*e.g.*, Zhang et al., 2008; Shao et al., 2009a; Lu et al., 2010; Wang X. et al., 2010; Zou et al., 2015; Ou et al., 2016; Wang M.Y. et al., 2019b; Yim et al., 2019) and in Hong Kong (Guo et al., 2009, 2013a; Lam et al., 2013; Ling and Guo, 2014; Xue et al., 2014b, 2016; Wang H. et al., 2018), only a handful of studies focused on comprehensive O_3 photochemistry particularly during high O_3 episodes in the Pearl River Estuary (PRE) (Cheng et al., 2010; Wang Y. et al., 2018, 2019; Zeren et al., 2019). Throughout the thesis, an O_3 episode day is generally defined as the day with maximum hourly O_3 mixing ratio exceeding 100 ppbv (Level II of China National Ambient Air Quality Standard). Note that in autumn (September – November), the PRD region (including Hong Kong) often has fine weather with intense sunlight, high temperatures, and light winds, which facilitates local O_3 formation and thus often leads to high O_3 episodes (Wang T. et al., 2017). Besides, the average temperature during 1991-2020 in Hong Kong indicates that it is usually warmer in autumn (average: 25℃) than in spring (March - May; average: 22℃) (HKO, 2021). Therefore, both summer and autumn were taken as the warm seasons in PRE area in this study. Previous studies of O_3 pollution in PRE conducted by Cheng et al. (2010) and Zeren et al. (2019), however, lacked species-based photochemistry. A more in-depth investigation on the O_3 photochemistry of high O_3 days at the west and east banks of PRE is necessary.

In particular, Hong Kong, a densely populated metropolis in PRE, has been suffering from severe photochemical smog in the past decades, though the locally emitted NO_x and total VOCs (TVOCs) were significantly reduced (Xue et al 2014b; Ou et al., 2015; Lyu et al., 2016b; Wang Y. et al., 2017). Early studies revealed that the local O_3 production is typically limited by VOCs in urban and some suburban areas in Hong Kong (Zhang et al., 2007; Ling et al., 2014; Wang T. et al., 2017). In addition to local O_3 formation, the observed O_3 in Hong Kong is also influenced by the regional transport due to the proximity of the highly industrialized PRD region. For regional transport, studies (Wang T. et al., 2001b, 2017; Ding et al., 2004) indicated that O_3 was generally built up in Hong Kong under the northerly winds, whereas it was often cleaned up by the sea breeze from the South China Sea (SCS) and by the southwest monsoon in warm seasons. Although O_3 pollution has been investigated in many previous studies (Xue et al., 2014b, 2016; Ou et al., 2015; Lyu et al., 2016b; Wang Y. et al., 2017, 2018), the inter-annual variations in the O_3 formation regimes, radical chemistry and regional transport in Hong Kong have yet been fully understood. To improve the air quality in Hong Kong, a series of control measures aiming at restricting VOC emissions have been implemented by the Hong Kong government since 2007. Investigations on the post-2013 variations in the local O_3 production in Hong Kong and the regional impacts are necessary to evaluate the effectiveness of these local and regional measures and provide scientific basis for future O_3 control strategies.

In this study, both field measurements and model simulations were integrated to describe the spatial variations of the chemical characteristics of O_3 and its precursors, O_3 formation mechanisms and radical chemistry, and VOC source contributions to O_3 in five megacities and PRE of China. In addition, detailed analysis was conducted, including the inter-annual variations of local formation and regional transport of O_3, as well as the evaluation of O_3 control measures during the last decade in Hong Kong. Note that to fill the research gaps and build up a coherent study, the spatial variation of O_3 photochemistry in five megacities of China was firstly characterized. Then, both short-term and long-term studies were conducted in the PRE. The short-term study focused on the in-depth O_3 formation mechanisms and radical chemistry, especially during high O_3 events in autumn. Two different patterns of O_3 episodes were identified, and detailed chemical characteristics of each pattern were investigated. Further, based on the new knowledge obtained from the short-term study in the PRE, the long-term temporal variations of local O_3 photochemistry and radical chemistry, and the impact of regional transport on O_3 during the past decade were evaluated. As an extension of the short-term study, the long-term study can get more insightful information on O_3 photochemical pollution in the PRE area and the impact from inland PRD region. These findings provided the latest information on O_3 photochemistry in China and a scientific basis for future control strategies.

1.2 Scope of this study

This doctoral study has the following objectives:

- To investigate the spatial variation of O_3 photochemistry and radical chemistry in urban areas of five megacities in China.
- To explore the detailed photochemical O_3 formation mechanisms in the Pearl River Estuary especially on high O_3 episode days.
- To re-examine the O_3 trend in the pre-2013 emissions and trace the O_3 evolution in the post-2013 emissions in Hong Kong, to investigate the regional contribution to O_3 in Hong Kong, and to explore the underlying mechanisms for the variations in O_3 formation and radical chemistry in Hong Kong.

The broad objectives of this study are to update information on photochemical O_3 pollution and VOC source contributions to O_3 formation in China, fill up the knowledge gaps of O_3 photochemistry in China's urban areas, and in PRE, and advance the knowledge about the O_3-precursor relationship in five megacities and PRE. The findings are expected to be applicable to similar urban areas in metropolitan environments and estuaries worldwide.

1.3 Outline of this thesis

This thesis is divided into 7 chapters:

1) Chapter 1 provides the research background and the main research objectives of this thesis.
2) Chapter 2 briefly presents the literature review on O_3 photochemistry in major metropolis in China and in PRE, including ground-level O_3 pollution, O_3-precursor relationship, O_3 photochemistry and contribution of VOCs to O_3 formation.
3) Chapter 3 introduces the methodology used in this study, including sampling sites, measurement techniques and model description and configurations.
4) Chapter 4 investigates the photochemical O_3 formation and radical chemistry in the urban areas of five megacities in China.

5) Chapter 5 explores the photochemical O_3 pollution in PRE of South China, particularly during high O_3 events.
6) Chapter 6 examines the inter-comparison of O_3 formation and radical chemistry in the past decade at a suburban site in Hong Kong.
7) Chapter 7 summarizes the main findings and the significant contributions of this thesis. In addition, suggestions for future studies in this research area were proposed.

Here I clarify that I participated the entire field measurements in 2016 and 2018, and the analysis of VOC and OVOC samples collected in these two sampling campaigns. All model-related analysis in Chapter 3 and the data analysis in Chapters 4-6, except for model simulations using WRF-CMAQ model in Chapter 5, were carried out by myself.

Chapter 2 Literature review

2.1 Ground-level O_3 pollution

O_3 is one of the most representative air pollutants in photochemical smog, which is produced through photochemical reactions between volatile organic compounds (VOCs) and nitrogen oxides (NO_x) in the presence of sunlight (NRC; 1992; Jacob et al., 1999; Guo et al., 2017). In recent decades, O_3 pollution has attracted growing attention of the public and authorities globally (Monks, et al., 2015; Turner et al., 2016; Lu H. et al., 2019; Xue et al., 2020). It is well documented that O_3 is harmful to human health (Bell et al., 2004), crops (Wang et al., 2005) and natural ecosystems (Ashmore, 2005). Notable increases in atmospheric O_3 has been widely reported, which were mainly ascribed to the fast-increasing O_3 precursor emissions, *i.e.*, VOCs and NO_x (Cooper et al., 2010; Ding et al., 2013), and the global climate change (Lelieveld et al., 2004; Zhao et al., 2013; Duncan et al., 2016). Besides, the O_3 hot spots were also more frequently found in populous urban regions in the world (Zhang et al., 2016).

2.1.1 Historical review of global O_3 pollution

Photochemical O_3 pollution, first reported as a component of Los Angeles smog in 1950s (Haagen-Smit et al., 1952), has been widely discovered in major urban and polluted rural areas throughout the world since 1970s (Levy, 1971; Chameides and Walker, 1973; Crutzen, 1974; Liu et al., 1987). Many studies have reported that O_3 increased significantly in the second half of the 20th century in the world. For example, studies indicated that the annual average O_3 level at a remote site in Antarctica increased around 30% from 14 ppbv in 1957 to 18 ppbv in mid-1960s (Wexler, 1960; Oltmans and Komhyr, 1976). Later, Oltmans and Komhyr (1986) reported the positive O_3 trends in Alaska, USA, in the North Hemisphere (NH) and America Samoa in the South Hemisphere (SH) from 1976 to 1983. According to Feister and Warmbt (1987) and Parrish et al. (2012), the yearly average O_3 concentrations doubled from 1950s to 1990s in northern German coast, which was consistent with the O_3 trend measured at a high elevation site in Europe (Marenco et al., 1994; Staehelin et al., 1994).

Since 1990s, many studies found that severe O_3 pollution in many urban areas in North America and Europe has been extensively alleviated because of the stringent emission control measures. Lefohn et al. (2008) revealed that O_3 decreased or showed no change in most of the sites across US from 1990 to 2005. Later, Simon et al. (2015) claimed that the significant reduction of O_3 in US from 1998 to 2003 was mainly attributable to the declined VOCs and NO_x levels, indicating the large success of US control measures targeting at decreasing peak O_3 concentrations during this period. Further, Oltmans et al. (2013) reported the unchanged O_3 trend in central and western Canada and decreasing O_3 at a remote marine boundary layer site of Japan from 1994 to 2010. Additionally, IPCC (2013) indicated that the increasing trend of O_3 in Europe almost ended in late 1990s and O_3 showed decreasing or unchanged trend at multiple sites in Europe in 2000s. By processing the surface O_3 database collected from monitoring sites around the world in 2000-2014, Chang et al. (2017) summarized that O_3 levels continued to decrease significantly over eastern North America and Europe during this period.

However, O_3 pollution is still a serious problem in many other regions in the world. Mills et al. (2018) provided a global distribution of 6-month average O_3 mixing ratio in the daytime during April-September from 2010 to 2014. They found that in the NH, high O_3 levels (> 40 ppbv) mainly distributed in western US, western Europe, northern Africa and the East Asia. Abnormally high O_3 values were also observed at some monitoring sites in western Canada, the Mediterranean Sea, the Middle East and the East China Sea. Despite the limited O_3 measurements conducted in the SH, high O_3 mixing ratios (> 40 ppbv) were also frequently reported in the Highveld in South Africa (Gaudel et al., 2018). Recent studies also indicate that the global O_3 pollution problem is still severe, particularly in the developing countries in Asia, such as India (Lu et al., 2018; Gao et al., 2020) and China (Guo et al., 2017; Wang T. 2017; Zheng et al., 2018), where the rapid urbanization and industrialization caused significant increases in anthropogenic O_3 precursor emissions in recent years (Zhao et al., 2013; Duncan et al., 2016; Tarasick et al., 2019). Through the simulations over 1990-2010 using GEOS-Chem model, Lu et al. (2018) implied a significant increasing trend of O_3 (rate: 0.19 ± 0.07 ppbv yr^{-1}, $p < 0.01$) in India. It was also reported by Lu et al. (2018) that the highest monthly average O_3 mixing ratio happened in May (54.1 ppbv) and the lowest in August (40.5 ppbv) based on the analysis of Ozone Monitoring Instrument (OMI) satellite data collected in the lower troposphere over India from 2006 to 2010. In China, the O_3 pollution was even worse. By analyzing the surface O_3 measurement data in 2013-2017, Li K. et al. (2019) indicated an increasing O_3 trend of 1-3 ppbv yr^{-1} in megacity clusters of eastern China and found that the summer mean maximum daily 8-hour average (MD8A) ozone reached up to 60-80 ppbv in North China Plain (NCP) over 2013-2017. Thus, China is in urgent need to deal with the O_3 pollution problem, which initiated this study to explore the photochemical mechanisms in megacity clusters in China and to provide scientific basis for formulating and implementing corresponding control strategies. In Section 2.1.2, the O_3 pollution in China was investigated in detail.

2.1.2 O_3 pollution in China

The increasing O_3 concentration has been widely reported in China since 1990s as a consequence of the fast-growing urbanization and economy. For instance, Xu X. et al (2008) reported the positive trend of maximum O_3 mixing ratios from 1991 to 2006 at Lin'an, a rural site near Shanghai. Ding et al. (2008) and Cheng et al. (2016) found increasing O_3 concentrations in Beijing during the 1995-2005 and 2004-2015 periods, respectively, where the increasing trend in the latter period was probably due to the decrease of NO_x concentrations and the increase of background O_3 in NCP during these years. Gao et al. (2017) reported that O_3 had increased by 67% and NO_x had decreased by 38% from 2006 to 2015 at an urban site near Shanghai, while very small variations of O_3 and NO_x were observed at the background site, suggesting that regional transport of O_3, solar radiation or variations of VOCs were not the major reasons for the local O_3 production. However, the decrease of NO titration caused the significant increase of local O_3 formation during this period. Li K. et al. (2019) mentioned that the higher O_3 concentrations in megacity clusters of eastern China were attributable to the decreasing anthropogenic NO_x mixing ratios under slightly varied VOC levels from 2013 to 2017. Fu et al. (2019) also reported that the mean value of the 90th percentile of MD8A of O_3 in warm seasons (April - September) in China increased from 65 ppbv in 2013 to 78 ppbv in 2017 while particulate matter (PM) and NO_2 significantly decreased. Besides, the reduction of $PM_{2.5}$ over the 2013-2017 period could be one of the factors facilitating the local O_3 production since there was less aerosol sink of hydroperoxyl radicals (HO_2) in the atmosphere. Further, Liu and Wang (2020a, 2020b) indicated that the emission-control measures by the government from 2013 to 2017 led to effective O_3 mitigation in rural areas in China but O_3 was elevated in urban areas due to the non-linear relationship between O_3 and precursors and the aerosol effects, while the impacts from meteorological variations should also be considered. Overall, the previous studies have greatly deepened the understanding of O_3 pollution in China.

It was reported that China was still experiencing deterioration in air quality related to O_3 pollution in the late 2010s. Figure 2.1 presents the distribution of 90th percentile of the MD8A O_3 concentrations in urban areas of 338 cities in China in 2018 (Yang et al., 2020), with the top 10 cities with heavy O_3 pollution mainly located in the NCP, Central China and Yangtze River Delta (YRD) regions. Besides, the O_3 pollution in megacities of northwestern China (Lanzhou), Sichuan Basin (SCB), and Pearl River Delta (PRD) was more severe than their surrounding regions. This situation has aroused more attention in these regions when implementing tighter O_3 control strategies in the future.

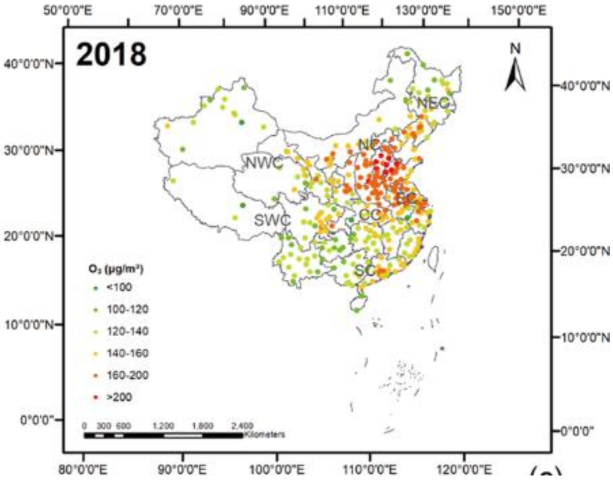

Figure 2.1 The spatial distribution of the 90th percentile of MD8A O_3 values in China in 2018. The maps were generated in ArcGIS10.2 (Yang et al., 2020).

The PRD region including Hong Kong, with dense population, transportation and industry, has been suffering from severe photochemical pollution for more than 20 years (Chan et al., 1998a, 1998b; Ding et al., 2004; Zhang et al., 2007; Guo et al., 2009; Wang et al., 2009; Xue et al., 2014b; Lu H. et al., 2019; Liu X. et al., 2019). Studies on O_3 pollution began in 1990s. Wang et al. (1998) found that the transport of “aged” air masses from the inland urban area resulted in high O_3 levels at a monitoring coastal site in Hong Kong. Later, Wang et al. (2001a, 2001b) revealed that O_3 episode events in PRD region were usually captured when northwestern winds prevailed, which carried polluted urban plumes from the inland continent to the coastal areas. The O_3-precursor relationship in a typhoon-related O_3 episode event was investigated by Huang et al. (2005) through a three-dimensional air quality model and it was found that O_3 production was VOC-limited in Hong Kong. After that, Zhang et al. (2007) confirmed the O_3 formation was basically controlled by VOCs in Hong Kong and explored the sensitivity of O_3 to the variations of its precursors with the aid of an observation-based model (OBM). Moreover, Zhang et al. (2008) found that the O_3 formation in both urban and rural areas in Guangzhou was generally limited by VOCs, while Zheng et al (2010a) reported a negative response of O_3 formation to NO_x levels at a rural site in PRD region. Ling et al. (2013) investigated the observation data in Hong Kong from 2005 to 2010 and summarized that the O_3 episode events in Hong Kong were highly influenced by the air masses from regional (*i.e.*, PRD region) or super-regional (*i.e.*, NCP and YRD regions) areas. In addition, Wang H. et al. (2018) made the first attempt to explore O_3 photochemistry under the interactions between marine and continental air and revealed that O_3 pollution could be magnified over the South China Sea when continental air intruded into marine atmosphere. In summary, O_3 pollution in PRD region is a complex issue in connection with the emissions of precursors, local O_3 photochemistry and meteorological conditions (Wang T. et al., 2017; Lu H. et al., 2019).

2.2 O_3 precursors and their sources in China

2.2.1 NO_x studies in China

As a key primary pollutant in China, NO_x is released to the atmosphere from both anthropogenic combustion of fossil fuels and/or biofuels and natural phenomena (wildfires, lightnings, or soil emissions), which are closely related to the fast development of economy and urbanization (Wang et al., 2012). As one of the pivotal precursors of ground level O_3, NO_x regulates O_3 formation by NO titration and participating NO-NO_2-O_3 cycle. Theoretically, the NO-NO_2-O_3 null cycle (R16-R18 in Section 2.5.1) provides rapid conversions between NO and NO_2. However, the NO titration effect greatly consumes photochemical O_3 in urban area under high NO_x conditions which has also been extensively reported in cities in China, such as Beijing (Chou et al., 2009; Shao et al., 2009b; Zhang Q. et al., 2014), Shanghai (Tang et al., 2008; Ran et al., 2009; Li et al., 2012), Guangzhou (Shao et al., 2009a; Ou et al., 2016) and Hong Kong (Ling and Guo, 2014).

Over the past few decades, source apportionment of NO_x in China has been well documented (*e.g.*, Hao et al., 2001, Lu Q. et al., 2013; Lyu et al., 2016a; Liu et al., 2017; Liu X. et al., 2019; Liu H. et al., 2020). Overall, vehicle emissions contributed the most to NO_x among different sources, counting from 22% in central China (Lyu et al., 2016a), 40% in NCP (Hao et al., 2001) to 50% in PRD region (Lu Q. et al., 2013) and 70% in Hong Kong (Liu X. et al., 2019), followed by coal burning or power plants as the second contributor. Because of the great effects in controlling industrial and vehicle emissions in 2010s, the NO_x emissions over 48 Chinese cities significantly reduced by 21 % from 2011 to 2015 (Liu et al., 2017). However, the reduction of NO_x led to the large elevation of O_3 concentration in China due to the lowered NO titration effect, particularly in urban areas (Gao et al., 2017; Li K. et al., 2019; Fu et al., 2019). Note that it is the combination of both VOCs and NO_x that determines the local O_3 formation mechanism, which will be further described in Section 2.4.

2.2.2 VOC studies in China

Over the past decades, the rapid urbanization and industrialization of China have accelerated the consumption of energy, enlarged the emissions of VOCs and led to more O_3 production (Li M. et al., 2019; Tan et al., 2018a; Xu et al., 2019). Many studies have examined the VOC abundance and distributions in China. For example, Liu Y.F. et al. (2020) detected 99 VOC species in urban Beijing in 2016, finding that acetaldehyde (6.28±5.08 ppbv) ranked the first among all VOCs, followed by ethane (5.31±3.20 ppbv) and propane (4.18±3.18 ppbv). Cai et al. (2010) reported propane (4.84±2.14 ppbv) and toluene (4.70±4.21 ppbv) were the top two VOC species among the 32 measured VOCs in urban Shanghai during 2007-2010. Lyu et al. (2020) reviewed the toxicity and distribution of 17 hazardous VOCs in China, among which formaldehyde, toluene, benzene, trichloroethylene and chloroform were more detrimental to human health. In addition, it is well documented that alkanes and aromatics usually had the largest abundance among all VOC groups in NCP, YRD and PRD regions (*e.g.*, Guo et al., 2006; Shao et al., 2009a; Cai et al., 2010; Louie et al., 2013; Huang et al., 2015; Li M. et al., 2019), while oxygenated VOCs (OVOCs) or alkenes were occasionally dominant in some cases, such as sampling in industry or rural areas (Ho et al., 2004; Guo et al., 2004; Shi et al., 2015).

In addition to VOC distributions, a variety of natural and anthropogenic sources, which directly emit hundreds of VOC species into the atmosphere and contribute differently to local O_3 formation, have been extensively studied to examine the air quality in China (*e.g.*, Guo et al., 2017; Wang T. et al., 2017; Jia et al., 2016; Lyu et al., 2016a; Song et al., 2018; Liu Y.H. et al., 2019). For example, Wang B. et al. (2010) identified six VOC sources in summer Beijing, including vehicle exhaust, LPG usage, gasoline evaporation, biogenic emission, paint and solvents and chemical industry, among which vehicle exhaust contributed the most to VOCs (57-60%), followed by LPG usage (10-19%) and gasoline evaporation (7-17%). The largest contribution of vehicular emissions was also found in both Wuhan (27.8%; Lyu et al., 2016a) and Chengdu (45.0%; Song et al., 2018). Five out of six sources identified in Wuhan and Chengdu respectively were the same as those in Beijing (Wang B. et al., 2010), except for gasoline evaporation replaced by coal burning in Wuhan (Lyu et al., 2016a) and LPG usage replaced by a second industrial source in Chengdu (Song et al., 2018). The differences of VOC sources among cities may be partially affected by the different sampling seasons and industrial structures of the cities. According to the study by Liu Y. et al. (2019), petrochemical industry was the largest contributor to VOCs in Shanghai (35.6%). Given that Lanzhou is a highly industrialized city, Jia et al. (2016) reported that the mixed industrial processes in Lanzhou contributed the most to VOCs (26.8%). Moreover, a great number of studies on VOCs sources have been carried out in inland PRD region (*e.g.*, Liu et al., 2008a, 2008b; Zheng et al., 2009a; Ling et al., 2011; Guo et al., 2011, 2017) and Hong Kong (Guo et al., 2004, 2007). Ling et al. (2011) identified 10 sources in PRD, among which three solvent usage sources dominated VOC concentrations (39%) in urban site, followed by biomass/biofuel burning (12%), diesel emissions (11%) and LPG usage (10%). However, it was different in Hong Kong. According to Guo et al. (2011), by applying PMF model, it was found that paint/varnish/solvents (43%) took the first place among the 4 sources, including paint/varnish/solvent, gasoline exhaust, diesel exhaust, and biomass burning, while diesel (21%) and gasoline (27%) exhausts ranked the second and the third accordingly. Despite these studies investigating VOC sources in different megacity clusters of China, there is a lack of studies that examine the spatial variations of VOC sources through concurrent sampling campaigns in multiple megacities across China.

2.3 Contributions of VOCs and their sources to O_3 formation

2.3.1 Contribution of VOCs to O_3 formation

The contribution of VOCs to O_3 formation was initially evaluated by estimating the O_3 formation potential (OFP) of individual VOCs, which depends on the photochemical reactivity with OH radical and the concentration of each VOC species (Carter, 1994). This approach was used in many studies in cities (*e.g.*, Beijing, Shanghai, Wuhan, Chengdu, Lanzhou) of China (*e.g.*, Duan et al., 2008; Xie et al., 2008; Cai, et al., 2010; Jia et al., 2016; Hui et al., 2018; Mo et al., 2018; Deng et al., 2019; Li M. et al., 2019), and in the PRD region (*e.g.*, Tang et al., 2007; Barletta et al., 2008; Lai et al., 2009; Zheng et al. 2009b; Tan et al., 2012), especially in earlier years. However, this approach has obvious drawbacks due to the fact that it considers individual VOCs in isolation, while the actual photochemical O_3 formation is the results of complex photochemical relations in the atmosphere involving many VOC species and NO_x. In 1980s, Liu et al. (1983) applied a one-dimensional model with the measurement data as input to simulate the O_3 budget in the atmosphere above equatorial pacific. Later, Cardelino and Chameides (1995) developed an observation-based model (OBM) incorporating carbon-IV mechanism to estimate the contributions of VOC species to local O_3 formation according to the model-derived relative incremental reactivity (RIR) value of VOC species. A number of studies have applied RIR values to investigate the sensitivity of O_3 formation to different VOC groups in cities of China. For example, with the aid of a near explicit Master Chemical Mechanism (MCM) model, Xue et al. (2014a) reported that the O_3 formation was most sensitive to both aromatics and alkenes in suburban Shanghai in spring 2005 and rural Beijing in summer 2005. However, alkenes played a predominant role in an industrial area in Lanzhou in the summer of 2006. According to Xu et al. (2017), OVOC was the least important group contributed to O_3 formation during the National Day holiday in 2014, while alkanes, alkenes and aromatics competed to be the dominant precursor of O_3 production when different weather conditions occurred. In addition, Tan et al. (2018a) summarized that alkenes dominated over

50% of the O_3 production in the autumn of 2016, based on the simulations by Regional Atmospheric Chemical Mechanisms version 2 (RACM2) model. However, only a few studies further explored the RIR values to individual VOC species. For instance, Lyu et al. (2016a) reported that ethene and toluene were the primary species contributing to O_3 formation in Wuhan during 2013-2014, and C_4 alkenes and alkenes from the LPG usage source contributed significantly. Wang M. et al. (2020) indicated that xylenes and light alkenes were the key species in O_3 formation in urban Nanjing through the one-year online measurements in 2016. Moreover, Zhao et al. (2020) revealed that O_3 formation in Hangzhou in the summer of 2018 was most sensitive to ethene, *m*-xylene and toluene.

In addition, RIR values of VOCs were extensively studied in the PRD region. Using the OBM model, Zhang et al. (2007) reported that aromatics dominated the O_3 formation among the anthropogenic VOC groups, of which xylenes and toluene were the most important, in the autumn of 2002 in Hong Kong. Zhang et al. (2008) found that propene, toluene and *m/p/o*-xylenes contributed the most to O_3 formation at an urban site in Guangzhou in the autumn of 2004, while Cheng et al. (2010) revealed that the summed RIR values of top 12 VOC species (*i.e.*, formaldehyde, acetaldehyde, *m/p/o*-xylenes, 1,2,3/1,2,4/1,3,5-trimethylbenzenes, isoprene, etc.) contributed to more than 85% of the total RIRs at a downwind rural site in the PRD region and a suburban site in Hong Kong in the autumn of 2010, implying that local O_3 formation was attributed to a small number of VOCs. Furthermore, Ling and Guo (2014) investigated the contributions of VOCs in each source and found that *m/o/p*-xylene and ethylbenzene in paint and sealant solvents, toluene in gasoline exhaust, *n/i*-butane, ethene, propene and propane in LPG usage and *n*-butane and ethene in diesel exhaust were the significant contributors to O_3 formation at an urban site in Hong Kong in the autumn of 2013. In recent years, Lam et al. (2013) developed a photochemical box model coupled with the near-explicit Master Chemical Mechanism (PBM-MCM) to investigate the contribution of VOCs to O_3 formation. Using the PBM-MCM, Lyu et al. (2016c) reported that O_3 production had the highest sensitivity to propene among the VOCs related to LPG usage emission in Hong Kong in 2012-2014. Further, alkenes and aromatics were found to be the most predominant VOCs for O_3 formation at the roadside sites in Hong Kong in 2013-2014, while aromatics dominated at the urban and suburban sites (Lyu et al., 2016b). Through the investigations at a marine site in South China Sea (SCS), Wang Y. et al. (2018) summarized that the top 10 AVOC species (*i.e.*, formaldehyde, toluene, *m/p/o*-xylenes, 1,2,3/1,2,4/1,3,5-trimethylbenzenes, acetaldehyde, ethene, *etc.*) accounted for 77% of the total RIRs of all AVOCs, indicating O_3 formation over SCS was mainly dominated by a few VOC species. Besides, OVOCs, especially formaldehyde, made important contribution to O_3 formation on episode days in the marine atmosphere. Despite these studies in China, the contributions of VOCs to O_3 formation in major Chinese megacities and PRE area remain unclear.

2.3.2 Contribution of VOC sources to O_3 formation

Due to the complexity and nonlinearity of O_3 formation, it is important to quantify the contributions of major sources of O_3 precursors to O_3 formation in order to formulate cost-effective pollution control strategies. The contributions of anthropogenic and biogenic VOC sources to O_3 formation have been widely investigated in megacities of China, most of which applied OFPs of VOCs emitted from different sources. For example, Xie et al. (2008) reported that biogenetic VOC (*i.e.*, isoprene) accounted for 11% (urban) and 22% (suburban) of total OFPs of all measured VOCs in Beijing in the summer of 2006. Later, Lai et al. (2009) reported that the alkanes related to LPG usage accounted for only 7% of total OFP although they accounted for 24% of TVOC concentrations in the autumn of 2004. Cai et al. (2010) investigated the OFP of measured VOCs from 2007 to 2010 in urban Shanghai and found that solvent based industrial sources (27%) and paint solvent usage (24%) contributed the most to local O_3 formation, followed by vehicle related emissions (17%), steel related industrial productions (14%), fuel evaporations (9%), coal burning (6%) and biomass burning (3%). In the PRD region, Ling et al. (2011) was the first to combine a receptor model (PMF) and an OBM at a suburban site in the autumn of 2007 and reported that solvent usage, diesel vehicular exhaust and biomass/biofuel burning were the largest contributors to local O_3 formation. Using the same models, Ling and Guo (2014) found that paint and sealant solvents, diesel exhaust and LPG usage made the largest contributions to O_3 production at an urban site in Hong Kong in the autumn of 2010. Moreover, Lyu et al. (2016b) reported the success of the LPG exhaust control program during 2013-2014 period in Hong Kong. Later, through the investigation of the measurement data at a roadside site in Hong Kong from 2012 to 2017, Yao et al. (2019) indicated that VOCs emitted from LPG exhaust still decreased significantly in the third year (*i.e.*, 2017) after the completion of the control program in 2014. In addition, the net negative contributions of both VOCs and NO_x related to LGP exhaust to O_3 formation were strengthened from 2012 to 2017. Based on the long-term variations of VOC sources in Hong Kong from 2005-2013, Lyu et al. (2017a) further confirmed the effectiveness of O_3 control measures on solvent usage and diesel commercial vehicle (DCV) implemented by the Hong Kong Government during this period. In addition, Wang Y. et al. (2019) adopted a photochemical trajectory model (PTM) coupled with MCM and assessed the contribution of continental VOC sources to the maritime O_3 formation for the first time. It was reported that gasoline vehicle exhaust and solvent usage were the largest contributors to O_3 formation over the South China Sea (SCS), which contributed 5.2 ppbv and 3.8 ppbv, respectively.

Overall, the VOC source contributions to O_3 formation were extensively investigated in China. However, there is a lack of studies that investigate the spatial variations of source contributions to O_3 production in major Chinese megacities. Besides, the long-term O_3 formation mechanism and radical chemistry related to VOC sources in PRE remain unclear. Therefore, understanding the O_3 photochemistry in terms of VOC source contributions in megacities in China and PRE will help local governments formulate control strategies for VOCs and O_3 control.

2.4 O_3-precursor relationship

Although many national control measures on O_3 precursors were carried out over the past decades, it is still difficult for policy makers to formulate regulations suitable for local conditions due to the nonlinear relationship between O_3 and its precursors (Chameides, et al., 1992; Chin et al., 1994; Sillman, 1995, 1999). Therefore, studying the temporal and spatial variations of O_3 formation regimes is necessary to develop O_3 control strategies in China.

2.4.1 Spatial variation of O_3 formation regimes in China

The nonlinear relationship between O_3 and its precursors is the main puzzle for formulating local O_3 control strategies. In China, O_3 formation in urban areas is usually VOC-limited, which means cutting the NO_x could result in O_3 elevation, while reducing VOCs is effective to reduce

O_3 formation. However, in rural areas, O_3 formation tends to be co-limited by both VOCs and NO_x or even solely limited by NO_x, indicating reduction on either NO_x or VOCs would inhibit local O_3 formation while cutting NO_x would be more effective than VOCs in NO_x-limited regime. The sensitivity of local O_3 formation to precursors is usually tested by applying chemical box models or transport models.

Recently, a great number of studies have investigated the O_3 formation regimes in megacities in China (Geng et al., 2008; Ran et al., 2009; Tang et a., 2010; Xue et al., 2014a; Zhang Q. et al., 2014; Wang Z. et al., 2015; Jia et al., 2016). For instance, in Beijing, either NO_x or VOC-sensitive photochemistry frequently existed (Wang Z. et al, 2015). VOC-limited regime usually dominated the O_3 formation in urban areas, where severe air pollution problems have been widely reported with the rapid development of urbanization and industrialization in recent decades (Xu J. et al., 2008; Chou et al., 2009; Tang et al., 2010; Zhang Q. et al., 2014). However, the way O_3 is formed has gradually changed to be controlled by both VOCs and NO_x, or mainly by NO_x in downwind or rural areas (Shao et al., 2009a; Zong et al.,2018a). In Shanghai, both chemical transport models and box models have been extensively applied to analyze the sensitivity of local O_3 formation to precursors. Similar to the situation in Beijing, previous studies reported that the O_3 formation in urban area was VOC-sensitive with high NO_x emissions, while it usually turned to NO_x-sensitive chemistry in rural and industrial areas (Geng et al., 2008; Ran et al., 2009; Tie et al., 2009; Li et al., 2012). The limited studies of O_3 photochemistry in Wuhan (Lyu et al., 2016a; Zeng P. et al., 2018), Chengdu (Tan et al., 2018a) and Lanzhou (Xue et al., 2014a; Jia et al., 2016) also revealed that the relatively low NO_x in the atmosphere (with high VOCs/NO_x ratio) led to NO_x-limited regime in rural, suburban or background areas. In contrast, VOC-limited chemistry was common at downtown sites in central or western China. Although many efforts were made to investigate the O_3-precursor relationship in China, the variations of O_3 sensitivity to different precursors have not been comprehensively studied in many megacities in China, which is related to the key mechanisms that control local O_3 production.

In the PRD region, extensive studies reported that O_3 formation in urban/suburban areas was generally limited by VOCs (*e.g.*, Zhang et al., 2007; Shao et al., 2009a; Cheng et al., 2010; Lu et al., 2010; Wang X. et al., 2010; Guo et al., 2013a; Ling et al., 2013; Xue et al., 2014b; Lyu et al., 2016b). For instance, Wang X. et al. (2010) analyzed the spatial variations of O_3 formation regimes in the PRD region in the autumn of 2004 using the Community Multiscale Air Quality (CMAQ) model and found that O_3 formation was VOC-limited in main urban areas of PRD, such as Guangzhou and Shenzhen, but NO_x-limited in rural areas in the southwestern PRD. By using an OBM, Shao et al. (2009a) revealed that the O_3 formation in urban areas of Guangzhou in the autumn of 2000 was dominated by VOCs, and there were also some positive contributions from NO_x. Later, Lu et al. (2010) reported that O_3 formation was controlled by VOCs in the urban area in PRD while it was mainly limited by NO_x in the downwind suburban area in the summer of 2006. In Hong Kong, it was first reported by Zhang et al. (2007) that O_3 formation was mainly dominated by VOCs, and O_3 was titrated by NO in high NO environment in autumn 2002 with the aid of an OBM model. Cheng et al. (2010) later applied the same model and confirmed the VOC-limited regime of O_3 formation, and further pointed out the great contribution of OVOCs to O_3 formation at a suburban site in Hong Kong in the autumn of 2007. Afterwards, PBM-MCM was more widely used to explore the O_3-precursor relationship in Hong Kong. For example, using this model, Guo et al. (2013a) found that O_3 formation was limited by VOCs at an urban site but sensitive to both VOCs and NO_x at a mountainous site in the autumn of 2010. Lyu et al. (2016b) investigated 13 sites in Hong Kong in 2013-2014 and confirmed that the O_3 formation was all VOC-limited in urban/roadside/suburban areas, but co-limited by both NO_x and VOCs at rural sites, which was also in line with the findings conducted at a suburban site in Hong Kong by Xue et al. (2014b) and Wang Y. et al. (2017). Although there are extensive studies that investigated the O_3 photochemistry in inland PRD and Hong Kong, a handful of studies focused on photochemical O_3 formation mechanisms during high O_3 episodes especially in the PRE, where sparse anthropogenic emissions exist.

2.4.2 Temporal variation of O_3 formation regimes in China

2.4.2.1 Long-term variation of O_3 formation regimes

Although the sensitivity of O_3 to VOCs and NO_x has been extensively investigated in the past 20 years, only a few studies explored long-term variations of O_3 formation regimes in China. For example, Jin and Holloway (2015) analyzed the satellite data of HCHO and NO_2 collected over China from 2005 to 2013 and indicated that O_3 formation was more sensitive to VOCs with the increasing NO_2 level in major city clusters (*i.e.*, NCP, YRD and PRD regions). However, NO_x level was successfully lowered by 10% from 2013 to 2016 in China after the implementation of a series of control measures in the 12th Five-Year-Plan (Zhu et al., 2017) although VOC reductions were not very effective during this period. Therefore, the shift to VOC-limited regimes was slowed down and some VOC-limited regions changed to transition or NO_x-limited regimes (Wang T. et al., 2017). Wu et al. (2018) further confirmed this assumption by using OMI satellite data collected by NASA from 2005 to 2016. It was found that the NO_x-limited regime in Beijing-Tianjin-Hebei (BTH) region expanded during this period, which was mainly attributable to the effective NO_x control during 12th Five-Year-Plan.

In PRD region, Wang Y. et al. (2017) evaluated the long-term O_3-precursor relationships, who applied an OBM to investigate the real-time measurement data from 2005 to 2014 in Hong Kong and revealed that O_3 formation was much more sensitive to VOCs than to CO and NO_x. Besides, Wang Y. et al. (2017) reported a significant increase ($p < 0.05$) of in-situ local O_3 formation in spring and an obvious reduction in autumn, which were closely related to the variations of NO titration and VOC concentrations in each season. However, the real-time measurement data used in the previous long-term O_3 studies may hinder a comprehensive understanding of the local O_3 formation mechanisms, due to the unavailability of many reactive VOCs such as formaldehyde. Moreover, the trends of the local O_3 formation mechanism were only updated to 2013 (Xue et al., 2014b; Wang Y. et al., 2017). Therefore, the post-2013 variations in the O_3 formation mechanisms remain unclear in Hong Kong.

2.4.2.2 Seasonal variation of O_3 formation regimes

The seasonality of O_3 level has been well documented in major city clusters in China. Wang T. et al. (2017) summarized that higher O_3 levels generally happened in the summertime in both NCP and YRD regions, while O_3 level usually reached a maximum value in autumn in the PRD region although high O_3 levels were observed in both summer and autumn. However, only a handful of studies investigated the seasonal variation of O_3 formation regimes. Previous studies showed that the O_3 formation regime in urban and rural/remote areas did not change through the year, while it varied with seasons in suburban areas (Geng et al., 2008; Zheng et al., 2010b; Zou et al., 2015). For instance, Geng et al. (2008) applied a chemical mechanism model (NCAR-MM) to find that O_3 formation was mainly limited by VOC in the urban areas of Shanghai in all seasons in 2006-2007. By analyzing the diurnal variations of O_3 and NO_x levels in PRD region from 2006 to 2007, Zheng et al. (2010b) later indicated that O_3 production was mostly limited by VOCs in urban areas but possibly controlled by NO_x in rural areas throughout the entire year. In contrast, through investigating the VOCs/NO_x ratios at a suburban site in Guangzhou from 2011 to 2012, Zou et al. (2015) found that the O_3 formation was more likely to be sensitive to VOCs in spring and winter, while it shifted between VOCs-limited and NO_x-limited in summer and autumn. Moreover, using the CMAQ model, Liu et al. (2010) indicated that megacities in NCP, YRD and PRD regions, such as Beijing, Tianjin, Shanghai and Guangzhou, were under VOC-limited regime throughout 2008 since NO_x was largely emitted from vehicles or industries. However, O_3 formation in other areas in China was likely to shift from transition or NO_x-limited regimes in summer to VOC-limited regime in winter. In addition, Jin and Holloway (2015) analyzed the HCHO/NO_2 ratios collected from 2005 to 2013 using satellite by NASA and confirmed that in warm seasons the O_3 production in urban areas of megacities (*i.e.*, Beijing, Shanghai and Guangzhou) and industrial cities (*i.e.*, Tangshan, Shijiazhuang and Zibo) was mainly controlled by VOCs, while transition regime was widely observed in other cities in NCP, YRD and PRD regions.

2.4.2.3 Diurnal variation of O_3 formation regimes

Although a number of studies were conducted to explore the long-term or seasonal variations of O_3 formation regime, only a few studies investigated the diurnal variations. Instead, the diurnal variation of O_3 levels affected by precursors was often taken into consideration when characterizing the O_3 pollution in targeted areas. O_3 pollution usually happens during the daytime since sunlight is necessary to drive the photochemical reactions. Generally, O_3 level increases in the morning, peaks in the afternoon and gradually drops till the nighttime. During the night, O_3 concentration is mainly determined by the NO_x level (Brown et al., 2012). In the absence of sunlight, a net conversion of O_3 to NO_2 happens without the photolysis of NO_2 forming O_3 afterwards. Further, NO_2 consumes O_3 to form nitrate radicals and thus O_3 is reduced. Therefore, the different diurnal variations of O_3 formation in urban and rural areas can be highly influenced by the different patterns of anthropogenic NO_x emissions (Lu H. et al., 2019). For example, based on the O_3 measurements in Beijing in 2005-2006, Ma et al. (2011) indicated that 90% of the O_3 episode events occurred before 16:00 in the urban areas, while the O_3 peaks appeared after the sunset at more than 80% of the rural sites, which could be attributable to the much higher NO_x levels in urban areas than rural areas. Later, Xu et al. (2011) confirmed this assumption by finding that O_3 peaks appeared 2-3 hours later at a rural site compared to an urban site in Beijing during 2005-2008 period. In addition to field observations, Li et al. (2012) applied the CMAQ model to simulate the O_3 episode days in YRD region during the summer of 2010. A fast decrease of O_3 caused by strong NO titration after sunset was found in urban areas, while O_3 still maintained high levels during the night in rural areas. In PRD region, Zou et al. (2015) found that the O_3 formation shifted from VOCs-limited (07:00-12:00) to NO_x-limited during 12:00-16:00 LT in summer and autumn by investigating the VOCs/NO_x ratios at a suburban site in Guangzhou in 2011-2012. Besides, Wang N. et al. (2016) adopted the Weather Research and Forecasting (WRF) - CMAQ model to investigate the diurnal variations of O_3 formation regimes in PRD region during 2006-2014 period. It was reported that the regime changed from VOC-limited in the morning (7:00 - 12:00 LT) to the NO_x-limited in the afternoon (13:00 – 17:00 LT) in some cities (*i.e.*, Guangzhou, Dongguan and Shenzhen), indicating that O_3 peaks in these areas could be lowered if NO_x emissions were further controlled in the afternoon.

2.5 O_3 photochemistry

2.5.1 Photochemical mechanisms

In 1970s, studies revealed that photochemical formation is the major source of tropospheric O_3 (Levy et al., 1971; Crutzen et al., 1973, 1974; Chameides, et al., 1976; Fishman et al., 1978). Since then, many researchers started to explore the photochemical mechanisms. Their findings are mainly embodied in the building-up of a series of chemical mechanisms through these years. For example, the condensed chemical kinetic mechanism Carbon Bond 4 (CB4) was developed in 1988 (Gery et al., 1988) based on the previous Carbon Bond-I/II/III versions (Whitten et al., 1980a, 1980b; Killus and Whittern, 1982). In 2005, a most updated version Carbon Bond 05 (CB05) was developed, with updates in kinetics, photolysis rates, extended organic/inorganic reactions and better representation of more VOC species (Yarwood and Raw, 2005). Throughout 1990s-2010s, many other chemical mechanisms for atmospheric chemistry models, such as RADM2 (Stockwell et al., 1990), RACM1 (Stockwell et al., 1997), SAPRC-99 (Carter, 2000a, 2000b), SAPRC-07 (Carter, 2010) and RACM2 (Goliff et al., 2013), were developed and put into use one after another.

All the abovementioned gas-phase chemical mechanisms could be applied in chemical transport models (CTMs) when simulating the complex chemical processes in the atmosphere based on the emission inventory (*e.g.*, Dodge, 2000; Tessum et al., 2015; Woody et al., 2015; Lv et al., 2018; Moradzadeh, et al., 2019; Kryza et al., 2020). Besides, CB4/05 and RACM1/2 have also been extensively adopted to simulate photochemical reactions based on observations. For instance, Cheng et al. (2010) investigated the O_3 photochemistry in PRD region in autumn 2007 using an OBM with CB4 mechanism. Wang Y. et al. (2017) also reported the long-term O_3-precursor relationship in Hong Kong from 2005 to 2013 by applying the CB05 mechanism in an OBM. In summer 2014, the radical chemistry at a rural site in NCP region was revealed by using the chemical box model RACM2 (Tan et al., 2017). In addition, RACM2 was also applied to investigate the radical chemistry to O_3-VOC-NO_x sensitivity in September 2016 in Chengdu (Tan et al. 2018a).

However, these highly lumped chemical mechanisms could not fully explain the photochemical mechanisms of VOC species. For example, Zong et al. (2018b) reported that the oversimplification of the lumped peroxy acyl radicals (RCO_3) and $\geqslant C_3$ aldehydes chemistry of RACM2 might lead to the overestimation of $C_2H_5O_2$ and CH_3CHO in a polluted scenario. Therefore, a speciated master chemical model was in demand. The near-explicit MCM was first introduced by Jenkin et al. (1997) and Saunders et al. (2003) with mainly non-aromatic schemes built up. Later, the interior photochemical mechanisms have been keeping updated and revised until the recent years. Jenkin et al. (2003) and Bloss et al. (2005) investigated the aromatic schemes, while Jenkin et al. (2012) figured out the β-caryophyllene scheme and Jenkin et al. (2015) added the detailed isoprene scheme into the photochemical mechanisms of MCM. Besides, Xue et al. (2015) developed a more comprehensive chlorine chemistry module to better present the atmospheric oxidative capacity. Lately, Lyu et al. (2015, 2017b) and Ling et al., (2016a) updated the C_1-C_5 alkyl nitrates ($RONO_2$) schemes, which have been adopted to simulate the impacts of $RONO_2$ on O_3 photochemistry in Hong Kong (Zeng L. et al., 2018).

In recent years, MCM has been extensively applied to simulate the in-situ photochemical mechanisms in different cities over the world (*e.g.*, Osthoff et al., 2008; Elshorbany et al., 2009a; Riedel et al., 2014; Bannan et al., 2015). Meanwhile, many studies using MCM to explore O_3 formation mechanisms and radical chemistry bursted in China (Xue et al., 2014a; Xu et al., 2017; Zeng P. et al., 2018), particularly in the PRD region (*e.g.*, Ling et al., 2014; Lyu et al., 2016b, 2016c; Wang T. et al., 2016; Wang H. et al., 2018; Wang Y. et al., 2018). However, there is a lack of studies that investigate spatial variations of in-situ O_3 photochemistry in urban areas of multiple megacities and PRE area of China.

Based on the previous studies, the present photochemical mechanisms of O_3 formation can be briefly described as follows. Tropospheric O_3 is formed through complex photochemical reactions of VOCs and NO_x under the sunlight, during which the photochemical cycling of radicals plays a crucial role in regulating the O_3 budget (Crutze, 1995). Generally, the O_3 formation process is regarded as the composition of "RO_x cycle" (RO_x = hydroxyl radical (OH) + hydroperoxyl radical (HO_2) + organic peroxyl radical (RO_2); photochemical radicals cycling) and "NO_x cycle" (O_3 formation cycling), which are shown in green and red, respectively, in

Figure 2.2. The O_3 precursors, *i.e.*, VOCs, CO and NO_x, are initiated by OH radical in the atmosphere and then produce O_3 through the photochemical cycling, in which VOCs and CO are oxidized and consumed and NO_x are cycled (Seinfeld and Pandis, 2016; Wang T. et al., 2017; Lu H. et al., 2019).

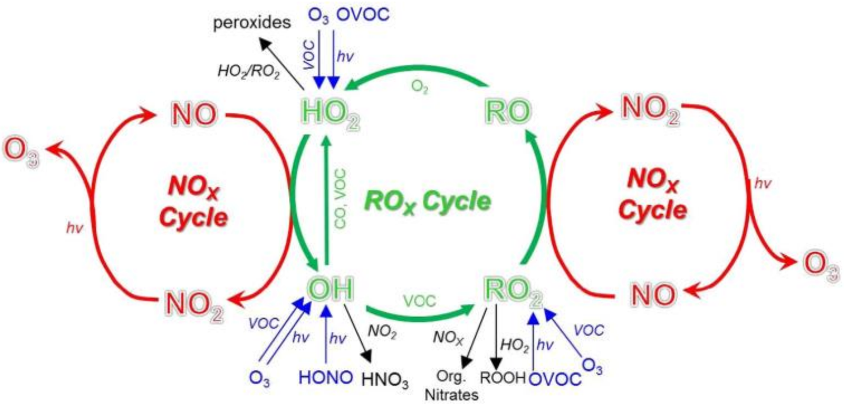

Figure 2.2 Sketch of “RO_x cycle” (in green) and “NO_x cycle” (in red) and reaction pathways of initiation (in blue) and termination (in black) processes (Wang T. et al., 2017).

The HO_x budget ($HO_x = OH + HO_2$) refers to the cycling between OH and HO_2 radicals, which can facilitate the chain propagation reactions (Wang T. et al., 2017). Wang Y. et al. (2018) summarizes the principal reactions in photochemical O_3 formation in the following equations (R1-R18), where, R7 + R1 + R16 + R17 and R6 + R10 + R16 + R17 are predominant chain reactions in which RO_x and NO_x accelerate the O_2 oxidation process of VOCs and CO (Jacob, 1999), *hv* represents the sunlight, M is an energy-absorbing molecule, *e.g.* N_2 or O_2. During one chain propagation cycle, two O_3 molecules are generated according to the radical cycling (*i.e.*, R6 + R10 + R1). The following formation and loss pathways of OH radical (formation: R1-R4; loss: R5- R9) and HO_2 radical (formation: R7, R10-R12; loss: R1, R13-R15) are generally taken into consideration. The NO_x cycle includes NO_2 photolysis to produce O_3 (R16-R17) and the reaction between O_3 and NO which regenerates NO_2 (R18), leading to a null cycle (R16-R18) without any other chemical species involved. However, the participation of peroxy radicals (*i.e.*, HO_2 and RO_2) in the atmosphere accelerates the conversion from NO to NO_2 (R1 and R10), resulting in more O_3 reservation. Therefore, HO_x budget plays a key role in O_3 photochemistry (Wang Y. et al., 2018).

$HO_2\cdot + NO \rightarrow OH\cdot + NO_2$ (R1)

$O_3 + h\nu\ (\lambda < 320\ \mathrm{nm}) \rightarrow O_2 + O(^1D)$ (R2)

$HONO + h\nu\ (\lambda < 320\ \mathrm{nm}) \rightarrow NO + OH\cdot$ (R3)

O_3+ unsaturated VOCs $\rightarrow$ carbonyls + Criegee biradicals (R4)

$OH\cdot + O_3 \rightarrow HO_2\cdot + O_2$ (R5)

$OH + VOCs + O_2 \rightarrow RO_2\cdot + H_2O$ (R6)

$OH + CO + O_2 + M \rightarrow HO_2\cdot + CO_2 + M$ (R7)

$OH + NO_2 + M \rightarrow HNO_3 + M$ (R8)

$OH + NO \rightarrow HONO$ (R9)

$RO_2\cdot + NO + H_2O \rightarrow HO_2\cdot + R\text{-}CHO + NO_2$ (R10)

$HCHO + 2\ O_2 + h\nu\ (\lambda < 320\ \mathrm{nm}) \rightarrow 2\ HO_2 + CO$ (R11)

$OH\cdot + HCHO + O_2 \rightarrow HO_2\cdot + H_2O + CO$ (R12)

$HO_2\cdot + O_3 \rightarrow OH\cdot + 2\ O_2$ (R13)

$HO_2\cdot + HO_2\cdot \rightarrow HOOH + O_2$ (R14)

$RO_2\cdot + HO_2\cdot \rightarrow ROOH + O$ (R15)

$NO_2 + h\nu \rightarrow NO + O\ (^3P)$ (R16)

$O\ (^3P) + O_2 + M \rightarrow O_3 + M$ (R17)

$O_3 + NO \rightarrow NO_2 + O_2$ (R18)

To sum up, OH radical, as the most reactive species in the atmosphere, reacts with primary pollutants, *i.e.*, VOCs and CO, and initiates a sequence (*i.e.*, RO_2-RO-HO_2) under the presence of NO_x. At the same time, HO_2 can react with NO or O_3 and reproduce OH to form a loop, and the entire recycling of RO_x radicals (*e.g.*, OH → RO_2 → RO → HO_2 → OH) produces O_3 and OVOCs (Sheehy, et al., 2010; Zhu J. et al., 2020). The HO_x cycling reactions can be greatly elevated by increasing temperature, solar radiation and/or the abundance of other precursors in the air (Coates et al., 2016; Xing et al., 2017), but can only be terminated by the cross-reactions with NO_x under high NO_x conditions and radicals themselves (*i.e.*, $HO_2 + HO_2$, $RO_2 + RO_2$ and $RO_2 + HO_2$) at low NO_x levels to form organic nitrates, nitric acid or peroxides (Wood et al., 2009; Liu et al., 2012; Xue et al., 2016). The combination of both "NO_x cycle" and "RO_x cycle" leads to O_3 formation in the atmosphere.

2.5.2 In-situ net O_3 production

Generally, the difference between the O_3 gross production rate and the destruction rate represents the net O_3 production rate (Equation 2.1) (Xu et al., 2017; Tan et al., 2018b; Wang Y et al., 2018). The O_3 gross production rate is calculated by the oxidation of NO by HO_2 and RO_2 (Equation 2.2), while the O_3 destruction rate is calculated by O_3 photolysis and reactions of O_3 with OH and HO_2 (Equation 2.3). The equations are listed below:

$$P_{O_3-NO} = G_{O_3-NO} - D_{O_3-NO} \qquad \text{(Equation 2.1)}$$

$$G_{O_3-NO} = k_{HO_2+NO}[HO_2][NO] + \sum k_{RO_2+NO}[RO_2][NO] \qquad \text{(Equation 2.2)}$$

$$D_{O_3-NO} = k_{HO_2+O_3}[HO_2][O_3] + k_{OH+O_3}[OH][O_3] + k_{O(^1D)+H_2O}[O(^1D)][O_3] +$$

$$k_{OH+NO_2}[OH][NO_2] + k_{alkenes+O_3}[alkenes][O_3] \qquad \text{(Equation 2.3)}$$

where, P_{O_3-NO} is the net O_3 production rate, G_{O_3-NO} and D_{O_3-NO} represent O_3 gross production rate and O_3 destruction rate, respectively. O^3P, $O(^1D)$, NO and NO_2 are put into instantaneous steady state. The constants (k) are the rate coefficients of each reaction.

Over the past decade, the net O_3 production rate has been widely investigated in megacities in China. For example, the average daytime net O_3 production rate was 25.8 ppbv h^{-1} at an urban site in Beijing in the summer of 2007 (Liu et al., 2012). Based on the field measurement data at an urban site in Wuhan in the autumn of 2013, Lu et al. (2017) reported the average daytime net O_3 production rate was 8.8 ppbv h^{-1}. Recently, Zhu J.X. et al. (2020) revealed that the net O_3 production rate increased from non-O_3 episode days (urban: 2.1 ppbv h^{-1}; suburban: 1.7 ppbv h^{-1}) to O_3 episode days (urban: 5.6 ppbv h^{-1}; suburban: 3.5 ppbv h^{-1}) in August 2018 in Wuhan. Su et al. (2017) found that the daily average net O_3 production rates were between 30 and 35 ppbv h^{-1} at three suburban and urban sites in Chongqing in the summer of 2015, which were relatively higher than other studies reported. Many studies also reported the daily peak net O_3 production rate in different cities of China. The simulated daily peak net O_3 production rate was 50ppbv h^{-1} at a suburban site in Shanghai in May 2005 and 40 ppbv h^{-1} in an industrial area in Lanzhou in summer 2006 (Xue et al., 2014a). Zeng et al (2019) investigated the net O_3 production rates at three sites in Wuhan during the summer of 2016 and found that the average daily peak net O_3 production rate was 4 ppbv h^{-1}, 10 ppbv h^{-1} and 12 ppbv h^{-1} at a roadside site, an urban site and a rural site, respectively. Besides, Tan et al. (2018a) reported that the peak net O_3 production rate was within 20-28 ppbv h^{-1} in Chengdu based on the data collected at four urban/suburban sites in September 2016 (Tan et al., 2018a). Even so, there is a dearth of nationwide studies on in-situ O_3 production in urban areas of major Chinese megacities.

In the PRD region, Zhang et al. (2007) was the first to apply an OBM to investigate the net O_3 production rates in Hong Kong from October to December in 2002. It was found that the daily average net O_3 production rate at a remote coastal site with frequent high O_3 events in autumn was more than twice that at an urban area in central-western Hong Kong. Lu et al. (2012) applied an OBM coupled with RACM to simulate the net O_3 production rate and reported 10.7 ppbv h^{-1} during afternoon period (12:00 – 16:00 LT) in rural Guangzhou in summer 2006. Tan et al. (2019) found the daily maximum gross O_3 production rate (*i.e.*, sum of reaction rate of HO_2 + NO and RO_2 + NO) of 22 ppbv h^{-1} in Heshan in autumn 2014. More studies using PBM-MCM explored the photochemical mechanisms in Hong Kong. For example, based on the sampling campaign conducted at an urban site (TW) and a mountainous site (TMS) in Hong Kong in autumn 2010, Ling et al. (2014) revealed that the daytime average net O_3 production rate at TW (8.1 ppbv h^{-1}) was significantly greater than that at TMS (2.9 ppbv h^{-1}). Xue et al. (2016) found the gross O_3 production rate at TC was 21.5-22.9 ppbv h^{-1} in August 2011. Moreover, the net O_3 production rate in marine atmosphere was found to be much higher than in the coastal area due to the weaker NO titration and stronger oxidative capacity of the marine atmosphere (Wang H. et al., 2018). These studies indicated strong O_3 formation in inland PRD and Hong Kong; however, the O_3 photochemistry remains unclear in PRE area.

2.5.3 Radical chemistry

RO_x radicals play key roles in the O_3 photochemistry. The concentration and cycling rate of RO_x in the atmosphere somewhat reflect the atmospheric oxidative capacity (AOC) (Stone et al., 2012; Xue et al., 2016; Li Z. et al., 2018; Wang H. et al., 2018; Lyu et al., 2019). Previous studies show that the radical chemistry in each metropolitan area is unique (Lyu et al., 2016a, 2019; Xue et al., 2016; Wang H.et al., 2018; Wang Y. et al., 2018, 2019; Zhu J. et al., 2020). For instance, the main source of OH radicals was photolysis of OVOCs in Milan (Alicke et al., 2002), Mexico City (Sheehy et al., 2010) and London (Emmerson et al., 2007); HONO photolysis in Paris (Michoud et al., 2012) and Santiago (Elshorbany et al., 2009b); O_3 photolysis in California and Nashville (Martinez et al., 2003; Volkamer et al., 2010). The source of HO_x radicals also have temporal-spatial variations. For example, the principle HO_x source was HONO photolysis during the daytime but oxidation of VOCs at night in winter in New York City (Ren et al., 2003), oxidation of VOCs during the day in winter in Tokyo but HONO photolysis in the morning in summer and photolysis of OVOCs at noon in summer in the same city (Kanaya et al., 2007). However, the contribution of HONO photolysis in identifying radical sources may be underestimated when the simulated HONO concentrations by box models were applied instead of direct field measurements (Emmerson et al., 2005, 2007). In sum, identifying the major sources of radicals is essential for understanding the local formation mechanism of air pollution.

However, a handful of studies probed into radical chemistry in China. For example, Liu et al. (2012) investigated the radical budget at an urban site in Beijing in August 2007 and revealed that the photolysis of OVOCs was the main source of OH radical. Lu et al. (2017) studied the air pollution in urban Wuhan in autumn and highlighted the significant contribution of HONO to AOC and suggested that VOC control, especially the prohibition of agricultural biomass burning, was necessary to improve the air quality in Central China. Tan et al. (2018a) analyzed the RO_x budget with simulated radical concentrations at four sites of Chengdu in autumn, and first revealed the severe O_3 pollution in view of comprehensive radical chemistry in southwestern China. In addition, Zhu J. et al. (2020) recently performed a study to explore the AOC, OH reactivity, OH chain length and HO_x budget with an observationally constrained box model in polluted urban environments in Shanghai in May – September, 2018, and provided the detailed local radical chemistry which implied control of key VOC species for O_3 mitigation in YRD region. In the PRD region, Ling et al. (2014) revealed that the radical cycling processes at an urban site were much faster than those at a mountainous site in Hong Kong in the autumn of 2010. Later, Xue et al. (2016) provided new insights into the radical chemistry which caused photochemical pollution in high-NO_x conditions in both PRD region and Hong Kong in August 2011. Moreover, the radical chemistry in marine atmosphere over a coastal region of the SCS in autumn 2013 was explored by Wang H. et al. (2018) and Wang Y. et al. (2018, 2019), who reported that both the concentrations and the cycling rates of radicals were greatly magnified over SCS when continental air intruded into marine atmosphere.

In addition, only few studies investigated the OH concentrations in urban areas in China. For example, the measured diurnal maximum OH concentration was found to be 1 - 8 × 10^6 molecules cm^{-3} in urban areas in Beijing in the winters of 2016 (Ma et al., 2019) and 2017 (Slater et al., 2020). A measured daytime average OH concentration of 3.1 × 10^6 molecules cm^{-3} was reported in an industrial area in Lanzhou in 2018 (Wang G. et al., 2020). Moreover, the simulated daytime average OH concentration by an OBM was 3.5 × 10^6 molecules cm^{-3} at an urban site in Hong Kong in the autumn of 2010 (Ling et al., 2014). Zhu J.X. et al. (2020) also applied an OBM to simulate the diurnal variations of OH in urban/suburban sites in Wuhan in August 2018 and reported that the maximum OH concentration was between 3.2 and 6.4 × 10^6 molecules cm^{-3} during this period. Further, the simulated maximum OH concentration was found to be 4 - 8 × 10^6 molecules cm^{-3} in urban/suburban sites in Chengdu in the autumn of 2016 (Tan et al., 2018a).

In summary, despite the above-mentioned studies, the photochemical mechanisms and radical chemistry in urban areas of many megacities and PRE in China in warm seasons are far from understanding. For example, the spatial variations of net O_3 production rate and radical cycling rate in major city clusters in China, the in-depth O_3 photochemistry during high O_3 events in PRE area and long-term trend of local O_3 formation mechanisms and regional transport in Hong Kong, deserve further exploration.

Chapter 3 Methodology

3.1 Sampling sites

In this study, field measurements were conducted at different sites in major city clusters of China in autumn of 2007, 2013 and 2016, and summer of 2018. The sites included two sites in Pearl River Estuary (PRE), *i.e.*, a rural site in inland Pearl River Delta (PRD) region (Qi'ao, referred to as QA hereafter) and a suburban site in southwestern Hong Kong (Tung Chung, referred to as TC hereafter), and five urban sites in North China Plain (NCP), Yangtze River Delta (YRD), central China, Sichuan Basin (SCB) and northwestern China (*i.e.*, Beijing, Shanghai, Wuhan, Chengdu and Lanzhou, respectively). Figure 3.1 shows the geographical location of the sampling sites.

On September 25 – November 28, 2016, a concurrent sampling campaign was conducted on two banks of the PRE (Figure 3.1(a)), which is located at the center of the PRD region, and surrounded by five inland cities (*i.e.*, Zhuhai, Shenzhen, Zhongshan, Dongguan and Guangzhou) and two Special Administrative Regions of China (*i.e.*, Hong Kong and Macau). On the west bank, the sampling site QA was set on the top of a small mountain with a height of 167 meters at an island in Zhuhai, where sparse anthropogenic sources except for local ship exhausts and vehicular emissions were observed, while on the east bank the site TC was set up on the rooftop of 6-storey building in a residential and commercial area of the southwestern Hong Kong, where the air masses originated from the city center of Hong Kong and the inland PRD region in autumn. In addition, sampling campaigns at the same site in TC were conducted in September – November of 2007 and 2013, respectively. Furthermore, during August 1 – 31, 2018, a comprehensive concurrent sampling campaign was carried out in five megacities in China (Figure 3.1(b)). Each sampling site was in a mixed residential and commercial area in each megacity. Table 3.1 gives the detailed information and descriptions of the areas around the two sites in PRE area and five urban sites in the megacities.

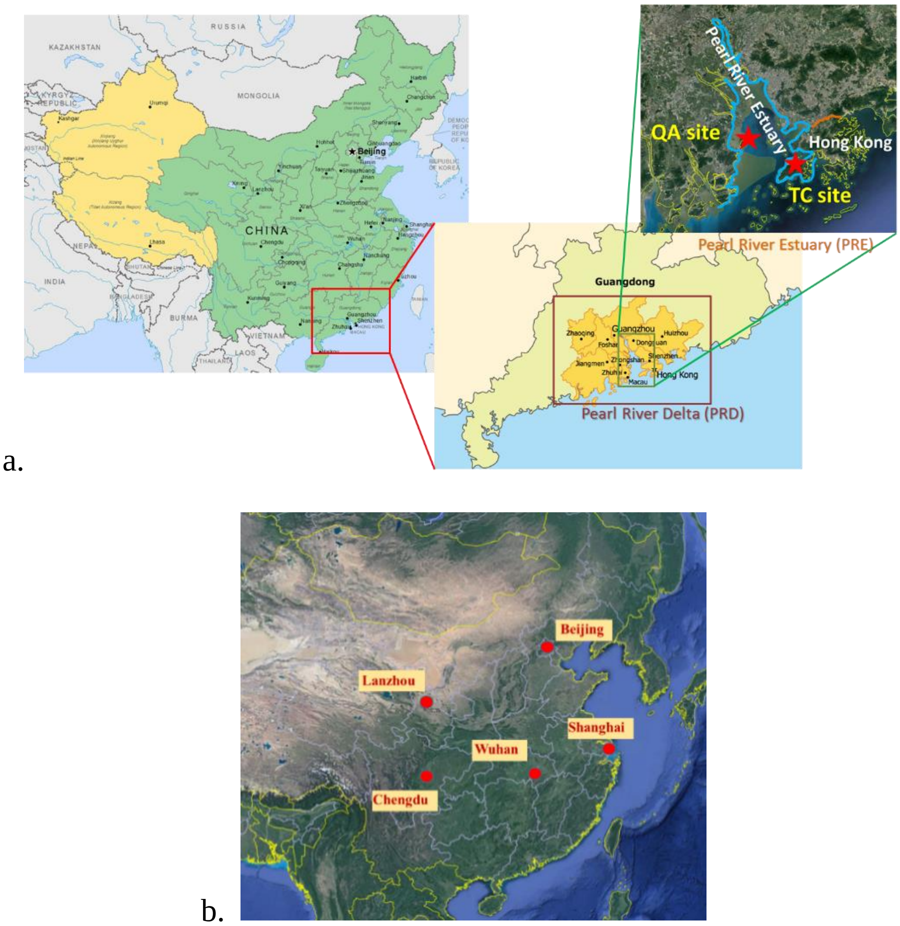

Figure 3.1 Maps showing the locations of (a) the two sampling sites in PRE, *i.e.*, QA and TC (marked with red stars), where the coastal line of PRE and borderline between mainland China and Hong Kong are marked with blue and orange lines, respectively; (b) the five megacities in China, *i.e.*, Beijing, Shanghai, Wuhan, Chengdu, and Lanzhou.

Table 3.1 Description of the seven sampling sites including two in PRE and five in megacities.

City (site)	Coordinate	Nature of land use	Location	Sampling period	Number of VOC/OVOC samples	Number of VOC sampling days (O3 episodes)
Zhuhai (Qi’ao)	22°22'12” N, 113°39'01” E	Rural	Top of the mountain in Qi’ao Island, Zhuhai	Sep. – Nov. 2016	118/119	17 (8)
Hong Kong (Tung Chung)	22°17'24” N, 113°56'24” E	Suburban	Southwestern Hong Kong	Sep. – Nov. 2007, 2013, 2016	414/275	45 (7)
Beijing	39°58'28” N, 116°22'13” E	Urban	Tower Branch, Institute of Atmospheric Physics, Chinese Academy of Sciences	Aug. 2018	42/42	8 (5)
Shanghai	31°11'27” N, 121°26'04” E	Urban	Xujiahui Observatory	Aug. 2018	30/30	7 (0)
Wuhan	30°31'50” N, 114°18'28” E	Urban	Wuchang Culture and Sports Bureau	Aug. 2018	30/30	6 (2)
Chengdu	30°37'45” N, 104°03'50” E	Urban	Sichuan Academy of Environmental Science	Aug. 2018	42/42	8 (3)
Lanzhou	36°06'11” N, 103°37'48” E	Urban	Lanyuan Hotel, Xi Gu	Aug. 2018	48/48	7 (4)

3.2 Measurement techniques

3.2.1 Continuous measurements of trace gases and collection of VOC/OVOC samples

3.2.1.1 Simultaneous sampling campaign in Pearl River Estuary in autumn 2016

Trace gases (*i.e.*, O_3, CO, NO-NO_2-NO_x and SO_2) and meteorological parameters (*i.e.* temperature, relative humidity, wind speed and direction and solar radiation) were continuously measured at QA and TC sites simultaneously during the sampling periods. The sampling days with maximum hourly average O_3 exceeding 100 ppbv (Level II of China National Ambient Air Quality Standard) were defined as O_3 episode days. At QA, ambient air was drawn to a manifold through a ~5 m Teflon tube at a flow rate of 5 L/min. The sampling tube inlet was located 3 m above the rooftop of a 2-storey building. O_3 was monitored with a commercial UV photometric analyzer (TH, model 2003i). SO_2 was measured by a pulsed UV fluorescence (TH, model 2002i). A nondispersive infrared analyzer (TH, model 2004i) with a gas filter correlation was used to measure CO. NO and NO_x were detected by a chemiluminescence analyzer (TH, model 2001i). At TC, trace gases were continuously measured at the TC air quality monitoring station operated by the Hong Kong Environmental Protection Department (HKEPD), ~50 m to the sampling site. The instruments were the same as those used in the US air quality monitoring program (HKEPD, 2017a). Table 3.2 summarizes the instruments, analysis techniques, detection limits and the time resolutions for measurements of the trace gases. The high-resolution data were collected and averaged into the hourly averages. All the analyzers except O_3 analyzer were zeroed daily by analyzing scrubbed ambient air and calibrated every two weeks by a span gas mixture with a NIST (National Institute of Standards and Technology) traceable standard, while the O_3 analyzer was calibrated using a transfer standard (Thermo Environmental Instruments (TEI) 49PS) every two weeks. At both sites, the meteorological parameters, including temperature, relative humidity, pressure, wind speed, wind direction, precipitation, and solar radiation, were also continuously monitored by a mini weather station (Vantage Pro TM & Vantage Pro 2 Plus TM Weather Stations, Davis Instruments) during the sampling periods. Data were integrated into 30-minute averages by a built-in program in the weather station.

During the sampling period, the hourly whole air samples of VOCs were collected using pre-cleaned and evacuated 2 L electropolished stainless-steel canisters every hour or every other hour from 07:00 to 19:00 LT at TC and QA sites. At TC, one-hour sample was collected in each hour during the daytime (07:00-19:00 LT) on O_3 episode days, but every other hour on non-O_3 episode days. However, VOC samples were collected every 2 hours from 07:00 to 19:00 at QA regardless of O_3 episode or non-episode days. The O_3 episode days were predicted prior to sampling based on weather forecast and numerical simulation of O_3. Overall, the O_3 episodes were usually associated with high temperature, strong solar radiation, low humidity, and weak or northerly winds. In total, 118 and 172 VOC samples were collected at QA and TC, respectively. The sampling dates were identical at the two sites, except for Sept. 26 when samples were not collected at QA (Table 3.3). In addition to VOC samples, OVOC samples were also collected on the same days as those for the collection of VOCs. Dinitrophenylhydrazine (DNPH)-silica cartridges (Waters Sep-Pak DNPH-Silica, Milford, MA) were used to collect the OVOC samples. An ozone scrubber (Sep-Pak; Waters Corporation, Milford, MA) was connected in front of the DNPH cartridge to prevent interference of ozone. The ozone scrubber was replaced every two OVOC samples. For each OVOC sample, air was drawn to pass the O_3 scrubber and the cartridge for 2 hours at a flow rate of 0.5 L min^{-1}, which was controlled by a rotameter. A total of 119 and 123 OVOCs samples were collected on the VOC sampling days at QA and TC, respectively.

Table 3.2 Instruments, analysis techniques, detection limits and time resolutions for the real-time measurements of trace gases at the QA and TC sites.

Species	Instrument	Analysis technique	Detection limit	Time resolution
QA				
SO_2	TH, model 2002i	UV fluorescence	1 ppb	1 sec
CO	TH, model 2004i	Infra-red absorption with gas filter correlation	0.04 ppm	1 sec
NO-NO_2-NO_x	TH, model 2001i	Chemiluminescence	0.4 ppb	1 sec
O_3	TH, model 2003i	UV spectrophotometry	0.5 ppb	1 sec
TC				
SO_2	API 100E	UV fluorescence	0.4 ppb	1 sec
CO	API 300	Non-dispersive infra-red absorption with gas filter correlation	<0.050 ppm	1 sec
NO-NO_2-NO_x	API 200A	Chemiluminescence	0.4 ppb	1 sec
O_3	API 400	UV absorption	0.6 ppb	1 sec

Table 3.3 Sixteen and three O_3 episode days, and nine and seventeen O_3 non-episode days with VOC/OVOC observation data collected at QA and TC, respectively, during the whole sampling period in autumn 2016. The dates, *i.e.*, pattern 1, with high O_3 episodes at both sites are bolded, while the other episode days are in pattern 2.

Date	Episode days		Non-episode days	
	QA	TC	QA	TC
September, 2016	26, 27	26*, 27		
October, 2016	5, 6, 7, 10, 14*, 15*, 16*, **20**, 31*	20	17*, 23*	14*, 15*, 16*, 17*, 23*, 31*
November, 2016	4*, 8, 14*, 15*, 17*		1*, 3*, 5*, 6*, 7*, 16*, 18*	1*, 3*, 4*, 5*, 6*, 7*, 14*, 15*, 16*, 17*, 18*
Total number of days	16 days	3 days	9 days	17 days

* Days with VOC and OVOC observation data.

3.2.1.2 Sampling campaigns at TC in autumns of 2007, 2013 and 2016

Same settings for the measurements of trace gases and meteorological parameters were applied in the sampling campaigns in autumns of 2007 and 2013 as those in 2016 at the TC site, so were the collection of VOCs and OVOCs. Briefly, pre-cleaned and evacuated 2 L electropolished stainless-steel canisters were used to collect VOC samples. On O_3 episode days, one-hour sample was collected in each hour during the daytime (07:00-19:00 LT), generating 13 samples per day, while 5-7 one-hour samples were collected every other hour on non-O_3 episode days from 07:00 to 19:00 LT in the 2013 and 2016 sampling campaigns. However, 12 one-hour samples were collected on each VOC sampling day between 07:00 and 18:00 in 2007, regardless of O_3 episode or non-episode days. A total of 414 canister samples, including 96 samples in 2007, 146 in 2013 and 172 in 2016, were collected and analyzed during the three sampling periods (Table 3.1). During the sampling periods in 2013 and 2016, 5-7 OVOC samples were collected every two hours from 06:00-20:00 LT on both O_3 episode and non-episode days. In 2007, only 2 samples (2.5 hours each) were collected on non-O_3 episode days at 10:30-13:00 and 13:00-15:30, and 4 samples between 08:00 and 18:00 on O_3 episode days. In total, 275 OVOC samples (28 in 2007, 124 in 2013 and 123 in 2016) were collected and analyzed in the three sampling campaigns (Table 3.1).

3.2.1.3 Concurrent sampling campaigns in five Chinese megacities in summer 2018

Trace gases and meteorological parameters were continuously measured at an urban site in Beijing, Shanghai, Wuhan, Chengdu and Lanzhou, respectively, in August 2018 (Table 3.1). Different instruments for trace gases measurements at each sampling site were applied during this comprehensive sampling campaign (Table 3.4). In addition, the meteorological variables were synchronously monitored by weather stations of model QS/T 1-2000 at Beijing and Shanghai sites (QX/T 1-2000) and mini weather stations (model HX-2000) in Wuhan, Chengdu and Lanzhou, respectively.

During the sampling period, the hourly canister samples of VOCs were collected every other hour from 07:00 to 18:00 LT at each site, while OVOC samples were collected every two hours during the daytime hours (07:00 – 18:00 LT). In total, 192 VOCs and 192 OVOC samples were obtained at the five sites (Table 3.1).

Table 3.4 Details of instruments used for trace gas observation at the five sampling sites (Unit for limit of detection (LOD) and precision: ppbv).

	O_3 analyzer			CO analyzer			NO-NO_2-NO_x analyzer			SO_2 analyzer		
	Model	LOD	Precision	Model	LOD	Precision	Model	LOD	Precision	Model	LOD	Precision
Beijing, Shanghai, Wuhan, Lanzhou	TEI Model TE49i	0.5	±1.0	TEI Model 48iTL	40	±0.1	TEI Model 42iTL	0.05	±0.4	TEI Model 43iTL	0.05	±0.2
Chengdu	ECOTECH EC9810	0.4	±1.0	ECOTECH EC9830	50	±0.1	TEI Model T200U	0.05	±5.0	ECOTECH EC9850	0.5	±0.5

3.2.2 Chemical analysis of VOCs/OVOCs

The concentrations of 44 speciated VOCs in the canisters were determined with a gas chromatography-mass selective detection, flame ionization detection, and electron capture detection (GC-MSD/FID/ECD) system. In brief, two GC units were assembled separately. In GC-1 unit, 250 ml of canister samples were injected into a pre-concentrator to be pre-concentrated and then separated into two pathways. One pathway went to MSD and the other one was connected to ECD. In GC-2 unit, the air samples were pre-concentrated in a cryogenic pre-concentrator and then injected into FID. EPA TO-15 method (William and Michael, 1999) reported that the precision and accuracy for VOCs was below 4.3% and 10%, respectively. Table 3.5 summarizes the limit of detection (LoD), precision and accuracy of the 44 VOCs including 18 alkanes, 16 alkenes and 10 aromatics, with the precision below 9.76% and accuracy below 10.42%.

It is noteworthy that the VOCs were analyzed in Guangzhou Institute of Geochemistry (GIG), Chinese Academy of Sciences for the samples collected in both 2007 and 2013, and in The Hong Kong Polytechnic University (HKPolyU) for the samples collected in 2016 and 2018. The GC-MSD/FID/ECD systems in these two laboratories was the same as that in Rowland/Blake laboratory at the University of California at Irvine (UCI), which has conducted VOC analysis of whole air samples since 1970s (Colman et al., 2001; Simpson et al., 2010). Inter-comparisons were performed regularly among the three laboratories, which showed reasonably good agreements (Ling et al., 2014; Wang H. et al., 2018; Zeng L. et al., 2018). Figure 3.2 (a) – (h) shows the inter-comparison of typical VOC species between the HKPolyU laboratory and the UCI laboratory, including ethane, propane, *n*-butane, *n*-pentane, ethyne, isoprene, benzene, and toluene. Good correlations with high R^2 values from 0.85 to 0.97 and slopes close to 1 (*i.e.*, 0.85 – 1.24) indicated the reliability of the system in HKPolyU and ensured the data quality of this study.

Table 3.5 The limit of detection (LoD), precision and accuracy of 44 VOC species analyzed by GC-MSD/ECD/FID system.

VOCs	LoD (pptv)	Precision	Accuracy
Alkane			
Ethane	31.11	2.74%	0.71%
Propane	23.18	2.32%	3.26%
i-Butane	28.46	7.16%	2.69%
n-Butane	55.77	4.57%	5.85%
2,2-Dimethylbutane	18.88	6.32%	2.34%
2,3-Dimethylbutane	15.69	6.33%	8.29%
i-Pentane	18.02	2.81%	2.68%
n-Pentane	10.54	5.58%	4.62%
2-Methylpentane	16.04	2.08%	1.64%
3-Methylpentane	16.84	3.02%	2.28%
n-Hexane	8.52	4.40%	5.79%
Cyclohexane	8.31	5.30%	4.10%
2-Methylhexane	9.46	5.78%	3.03%
3-Methylhexane	16.21	5.49%	5.79%
n-Heptane	10.71	5.99%	5.58%
n-Octane	10.81	8.55%	2.72%
n-Nonane	10.19	5.45%	0.74%
n-Decane	18.33	4.43%	7.12%
Alkene			
Ethene	30.02	0.86%	3.11%
Ethyne	34.12	2.41%	3.11%
Propene	53.78	7.93%	2.70%
1-/*i*-Butene	36.39	5.71%	4.53%
1,3-Butadiene	18.97	6.41%	7.47%
trans-2-Butene	9.40	5.48%	7.59%
cis-2-Butene	15.59	8.78%	3.99%
2-methyl-*1*-Butene	22.91	9.76%	1.45%
3-methyl-*1*-Butene	21.21	8.13%	1.93%
2-methyl-2-Butene	8.89	6.87%	1.96%
1-Pentene	35.49	7.75%	8.04%
trans-2-Pentene	9.40	5.48%	7.59%
cis-2-Pentene	15.59	8.78%	3.99%
Isoprene	21.00	3.23%	10.42%
α-Pinene	13.16	6.17%	3.47%
β-Pinene	13.07	7.11%	5.13%
Aromatics			
Benzene	18.14	9.24%	8.46%
Toluene	10.53	9.16%	6.58%
Ethylbenzene	12.66	5.86%	3.85%
*m/p/*o-Xylene	15.22	6.20%	5.08%
1,3,5/1,2,4/1,2,3-Trimethylbenzene	16.51	4.41%	9.41%
i-Propylbenzene	12.20	7.66%	1.87%
n-Propylbenzene	16.96	6.02%	5.86%
2-Ethyltoluene	15.19	8.64%	7.21%
3-Ethyltoluene	12.76	6.66%	8.91%
4-Ethyltoluene	8.95	6.92%	7.98%

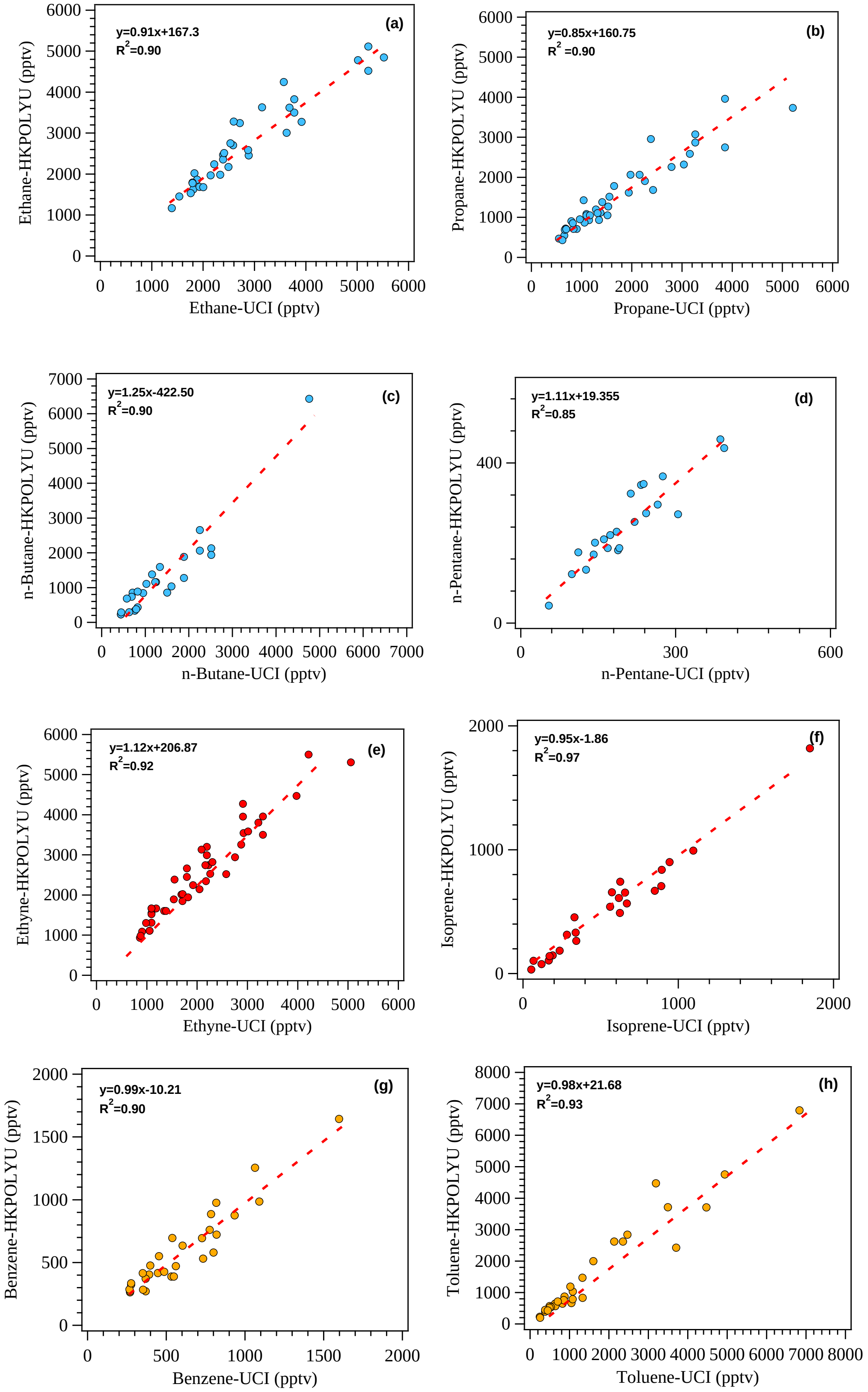

Figure 3.2 Inter-comparison of 8 typical VOCs between UCI and HKPolyU analytical systems.

The OVOC samples were stored in a refrigerator at 4°C after sampling. For analysis of OVOCs, the cartridges were eluted slowly with 2 ml of acetonitrile into a 2-ml volumetric flask. A high-performance liquid chromatography (HPLC) system (Perkin Elmer Series 2000, MA, USA) coupled with an ultraviolet (UV) detector operating at 360 nm was used for analysis. The instrument was calibrated using standards of different gradient concentrations covering the concentrations of interest for different OVOCs in ambient air. Good linear relationships ($R^2 > 0.999$) between the standard concentrations and responses of the instrument were obtained for the 16 analyzed OVOC species. The built-in computerized programs of quality control systems such as auto-linearization and auto-calibration were used to guarantee the data quality. Table 3.6 provides the detailed procedures and related parameters of HPLC analytical system. For all targeted OVOC species in this system, the detection limits were lower than 0.2 ppbv, precision was smaller than 10% and accuracy was below 15%. Due to the low detection rate of many OVOCs, this study only focused on formaldehyde, acetaldehyde, acetone and propionaldehyde, which had relatively high concentrations.

Table 3.6 The operation parameters of the HPLC system.

Parameter	Description
Column	A Brownlee Spheri-5 C18 ODS column (5 μm, 25 cm × 4.6 mm I.D.)
Mobile phase	(A) 6:3:1 (v/v/v) water-acetonitrile-tetrahydrofuran (B) 4:6 (v/v) water-acetonitrile
Gradient program	(1) 80% A/20% B for 2 min; (2) a linear gradient to 60% A/40% B for 5 min; (3) a linear gradient to 0% A/100% B for 20 min; (4) a linear gradient to 80% A/20% B for 8 min.
Flow rate	2 ml/min
Injection volume	20 μl
Detection wavelength	360 nm

3.3 Model descriptions and configurations

3.3.1 Chemical transport model

To obtain the VOCs concentrations on some specific days when canister samples were not collected at QA and TC sites in autumn 2016, a chemical transport model, *i.e.*, the Weather Research and Forecasting-Community Multiscale Air Quality (WRF-CMAQ) model, was utilized to simulate VOCs on these days. The VOCs values were extracted from the WRF-CMAQ modeling and calibrated using observed data available on other days. The offline meteorological field (CMAQ v5.0.2) was supported by WRF v3.6.1. Two-nested domain was applied with the same resolution of 36 km (outer domain) and 12 km (inner domain). The 2016-based Multi-resolution Emission Inventory for China (MEIC), developed by Tsinghua University, was used to provide anthropogenic emissions of air pollutants (grid resolution: 0.25°× 0.25°). Five emission sectors were included in MEIC, which were agriculture, industry, power plant, residence and transportation. Considering the curvature effect of the earth, linear interpolation to the domains was applied in the emission inventory. The biogenic emissions were calculated using the Model of Emissions of Gases and Aerosols from Nature (MEGAN, version 2.04) (Guenther et al., 2006), with its good performance validated by previous studies (Wang N. et al., 2015, 2016, 2019).

3.3.1.1 Model performance

The index of agreement (IOA) with values between 0 and 1, defined in Equation 3.1, was applied to evaluate the model performance (Huang et al., 2005; Wang N. et al., 2015; Lyu et al., 2015, 2016a). The better agreement between simulated results and observed data is, the closer the IOA value to 1 is (Huang et al., 2005).

$$\text{IOA} = 1 - \frac{\sum_{i=1}^{n}(O_i - S_i)^2}{\sum_{i=1}^{n}(|O_i - \tilde{O}| + |S_i - \tilde{O}|)^2} \qquad \text{(Equation 3.1)}$$

where Si and Oi represent simulated and observed values, respectively; $\tilde{O}$ represents the mean of observed values, and n is the number of samples.

Figure 3.3 (a) presents the comparison between the WRF-CMAQ simulated O_3 (marked as “before correction”) and the observed O_3 on all VOC sampling days (17 days at QA and 18 days at TC), with IOA values of 0.74 and 0.76 for QA and TC, respectively, indicating a reasonable simulation of photochemical O_3 formation by the chemical transport model. The model performance was further evaluated by introducing more site-to-site comparisons in nine cities of the PRD region., *i.e.*, Guangzhou, Shenzhen, Foshan, Dongguan, Huizhou, Zhuhai, Zhongshan, Zhaoqing and Jiangmen. Statistical metrics, including mean bias (MB; MB = $\mathrm{Obs}_{\mathrm{mean}} - \mathrm{Sim}_{\mathrm{mean}}$), normalized mean bias (NMB; NMB $= \sum_{i=1}^{n} \left[\frac{Sim_i - Obs_i}{Obs_i}\right]$), root-mean-square error (RMSE; RMSE $= \sqrt{\frac{1}{n}\sum_{i=1}^{n}(Sim_i - Obs_i)^2}$), and the IOA, were used to assess the simulated results. The performance vas validated by comparing both meteorological parameters (temperature and relative humidity, data were obtained from China Meteorology Administration (CMA)) and air quality data (NO_2 and O_3, data were obtained from Ministry of Ecology and Environment). Generally, the statistical result showed that the simulated values agreed well with those observed values (*i.e.* temperature, relative humidity, NO_2 and O_3) (Table 3.7), indicating that the model performance was acceptable in this study. However, large differences were found between the simulated levels of most lumped VOCs groups and the measured VOCs mixing ratios, mainly due to highly biased emission inventories (*e.g.*, Grell et al., 2005; Zheng et al., 2009a, 2009b; Jiang et al., 2010; Wang N. et al., 2015; Wang H. et al., 2020). Therefore, corrections of CMAQ-simulated concentrations of lumped VOC groups using the observed VOCs were conducted in Section 3.3.1.2.

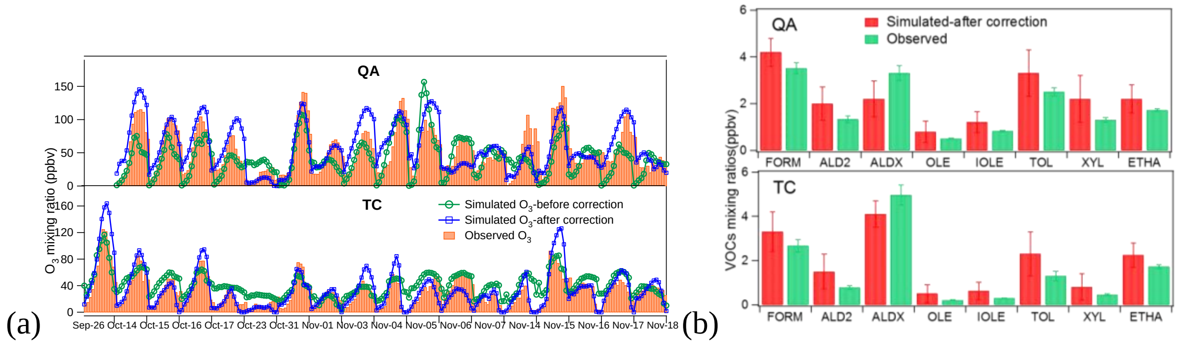

Figure 3.3 Comparison between (a) the WRF-CMAQ simulated O_3 (before and after corrections) and observed O_3; and (b) the WRF-CMAQ simulated (after correction) and observed VOCs (groups) on all VOC sampling days in autumn 2016, *i.e.*, 17 days at QA and 18 days at TC.

Table 3.7 Statistical metrics of the model performance in the nine cities in PRD (*i.e.*, Guangzhou, Shenzhen, Foshan, Dongguan, Huizhou, Zhuhai, Zhongshan, Zhaoqing and Jiangmen), where MB, NMB, RMSE and IOA stand for mean bias, normalized mean bias, root mean square error and the index of agreement, respectively.

Simulated variable	MB	NMB	RMSE	IOA
T (°C)	1.3	−0.01	2.2	0.92
RH (%)	8.1	−0.1	10.6	0.82
NO_2 (ppbv)	−14.5	1.3	20.5	0.68
O_3 (ppbv)	−12.8	0.5	28.1	0.80

3.3.1.2 Correction of the simulated VOCs using observation data

Using the method developed by Wang H. et al. (2020), the biased emissions of the VOCs in the emission inventory were corrected using the in-situ observations with the WRF-CMAQ simulations. Specifically, the emissions of the target VOC species were adjusted using the observed mixing ratios. The adjusted emissions of the speciated VOCs were lumped into groups for inputs of the WRF-CMAQ. The WRF-CMAQ generated outputs of the lumped VOCs groups were regarded as corrected lumped groups. The lumped VOC groups were speciated for the inputs of PBM-MCM model based on the average measured VOC composition in the atmosphere during the sampling period, *i.e.* 17 VOC sampling days at QA and 18 days at TC (Table 3.3), as described in Section 3.3.2.2. Figure 3.3 (a) and (b) shows the WRF-CMAQ simulated O_3 using corrected emission inventory (marked as "after correction") and the observed O_3, and the corrected simulated lumped VOCs groups and the observed VOCs on all VOC sampling days, respectively. The IOA values between simulated and observed O_3 were enhanced (0.83 at QA and 0.86 at TC), while the differences between simulated lumped VOCs and observed VOCs were reduced, revealing the acceptable performance of the WRF-CMAQ model. Since there were no observed VOC data on three days, the corrected WRF-CMAQ simulated VOCs on these three days at QA and TC were extracted for further investigation of O_3 photochemistry.

It is noteworthy that though the WRF-CMAQ model considers both physical and chemical atmospheric processes in simulating photochemical O_3 formation, its performance depends directly on the comprehensiveness and accuracy of the input emission data, the meteorological fields, and the description of the transport, dispersion, chemical transformations and deposition processes. Most importantly, the VOC chemistry module in this kind of model is approximated with two simplified approaches, *i.e.*, VOCs are grouped by classes (*e.g.*, short-chain alkenes) and represented by one chemical species of each class, and/or VOC molecules are decomposed into their functional groups (*e.g.*, double bond, carbonyl group) and the reactivity of the functional groups is simulated (Seigneur and Moran, 2004). Therefore, this model is unable to provide detailed understanding of O_3 photochemistry, such as the main reactions for O_3 formation and destruction, the formation and loss pathways of OH and HO_2 radicals, and the impact of speciated VOCs on in-situ O_3 formation pathways. In contrast, the PBM-MCM is a near-explicit chemical mechanism model involving 6700 chemical species and around 17000 elementary reactions, which fully describes the homogeneous gas-phase reactions in the atmosphere though it cannot perfectly reproduce the atmospheric processes (Saunders et al., 2003; Lam et al., 2013). Therefore, in this study the PBM-MCM model was mainly utilized to simulate the detailed O_3 photochemistry. The model performed well in deciphering the in-situ photochemistry in the previous studies (Lam et al., 2013; Ling et al., 2014; Lyu et al., 2017b; Wang Y et al., 2018; Liu X. et al., 2019).

3.3.2 Photochemical box model

3.3.2.1 Model description

PBM-MCM was used to simulate the photochemical O_3 formation in this study. MCM v3.2, a near explicit chemical mechanism consisting of 6700 species and around 17000 reactions which fully describes the homogeneous gas phase reactions in the atmosphere, was used (Jenkin et al., 1997, 2003; Saunders et al., 2003). In the O_3 study in 2016 at PRE area, the observation data of temperature, relative humidity, O_3, SO_2, CO, NO, NO_2 and 48 C_2-C_{10} VOCs/OVOCs were input into the model. Though previous studies (Guo et al., 2013b; Ling et al., 2016b) indicated that secondary formation dominated the sources of OVOCs in Hong Kong, the primary emissions cannot be neglected. Therefore, formaldehyde, acetaldehyde, acetone and propionaldehyde with relatively high abundances were constrained to the observed concentrations in the model, while the other OVOCs with low detection rates were simulated by the model. The same settings were applied in both five-megacity study in 2018 and inter-annual O_3 study in Hong Kong, except for that ambient O_3 was not used to constrain the model in the latter study so that the contributions of regional transport to O_3 in Hong Kong could be evaluated by calculating the difference between the observed and simulated O_3.

Note that nitrous acid (HONO) was not monitored in this study. In the O_3 study in 2016 at PRE area, the average diurnal cycles of HONO mixing ratios measured at a coastal background site in southeast Hong Kong in autumn 2012 (Zha et al., 2015) and TC in autumn 2011 (Xu et al., 2015) were used as inputs to represent its values at QA and TC, respectively, despite uncertainties (Wang H et al., 2018; Liu X. et al., 2019). To assess the uncertainties in 2016 sampling campaign, the HONO concentrations were calculated according to the measured diurnal variations of HONO/NO_x ratios in autumn 2011 (Xu et al., 2015) and the NO_x concentrations measured at TC and QA, respectively. The daytime HONO concentration was underestimated by 16.2% at QA, while it was overestimated at TC by 3.9%. Subsequently, the simulated O_3 was underestimated by 4.4% at QA, while it was overestimated by 1.5% at TC. For the inter-annual O_3 study in Hong Kong, the average diurnal cycle of HONO mixing ratios measured at TC in autumn in 2011 (Xu et al., 2015) was also input into the model to roughly represent its role in O_3 formation and atmospheric radical chemistry in 2007, 2013 and 2016. Due to the data limitation, the trends of HONO at TC in the three sampling campaigns were not traceable. However, the measurements at a background site in Hong Kong indicated comparable levels of HONO ($p > 0.1$) between the autumn in 2012 and in 2018 (unpublished data). Therefore, adopting the HONO measured in 2011 as the inputs of the simulations in the three sampling campaigns was likely a plausible assumption, despite some uncertainties. In the five-megacity study in summer 2018, PBM-MCM was not constrained by the observed HONO due to lack of HONO data in these five megacities.

The model was also tailored to the real situations in the PRE area and five megacities, respectively. Specifically, the coordinates of each sampling site were applied in the model. The height of the planetary boundary layer could vary from 300 m at night to 1400 m at noon. The photolysis rates were calculated according to the measured solar radiations by the Tropospheric Ultraviolet and Visible Radiation model (Madronich and Flocke, 1999; Wang Y. et al., 2017), which considers actual location and modeling time periods of each sampling campaign. In addition to the chemical processes, the exchange between the lower troposphere and free troposphere, and dry deposition were also considered in the model. The concentrations of air pollutants in the free troposphere were set according to the observations at a mountainous site in the PRD region (Lam et al., 2013), which were also applied in the five megacities study due to limited data access in mountainous areas in the five megacities. The dry deposition rates were adopted from the previous studies (Saunders et al., 2003; Lam et al., 2013). The other physical processes were not included in the model, which might lead to insufficient description of the transport. However, since the model was constrained to the observations which included the transported air pollutants, the regional transport was partially considered. Besides, the observations at 07:00 on each day were used to initiate each day's modelling, through which the effect of regional transport before the daytime modelling was also considered. It is noted that the PBM-MCM cannot perfectly reproduce the real atmospheric processes. However, it performed well in describing the in-situ photochemistry in previous studies (Lam et al., 2013; Ling et al., 2014; Lyu et al., 2017b; Wang Y. et al., 2017). The deficiency of PBM-MCM in consideration of the atmospheric dynamics enabled us to assess the contributions of regional transport to O_3 in Hong Kong, based on the differences between the observed and simulated O_3 (Wang Y. et al., 2017).

It should be noted that PBM-MCM model is usually applied to simulate locally produced O_3 and the in-situ O_3 formation mechanisms. Since the regional processes were not well considered in the PBM-MCM, the difference between simulated (*i.e.*, locally produced) and observed O_3 indicated the contribution of regional transport in the long-term study in Hong Kong. In this case, the model was not constrained by O_3 observations. However, as an important source of free radicals in photochemical reactions, O_3 plays an important role in simulating the production and destruction pathways of O_3 and radical chemistry in the atmosphere. Thus, O_3 observations were applied to constrain the PBM-MCM model for an explicit simulation of in-situ photochemistry in the five-megacity study and the PRE study. In such circumstance, the regional transport was partially considered. In sum, the model configurations varied with different research objectives of each study.

3.3.2.2 Model validation of PBM-MCM with VOCs derived from WRF-CMAQ

The PBM-MCM model with corrected VOCs derived from WRF-CMAQ in Section 3.3.1.2 as inputs was applied to simulate the photochemical O_3 at QA and TC when both sites had high O_3 levels in 2016 sampling campaign, which was compared with the observed O_3 for validation. Figure 3.4 shows the PBM-MCM-simulated and observed O_3 levels at QA and TC. The simulated O_3 generally followed the patterns of observed O_3. Good agreements were found between the simulated and observed O_3 with IOA values of 0.81 and 0.79 at QA and TC, respectively, much better than the simulations using uncorrected VOCs as inputs (IOA was 0.53 at QA and 0.68 at TC), indicating that it is reasonable to use the corrected WRF-CMAQ simulated VOC values for further analysis of the photochemistry. Moreover, the simulated average O_3 in the daytime hours (07:00-19:00 LT) at QA (83.2±5.2 ppbv) and TC (83.8±7.9 ppbv) were comparable ($p = 0.70$), and consistent with the observed values (QA: 66.6±11.4 ppbv; TC: 59.2±13.8 ppbv).

Since the accuracy of the in-situ photochemistry simulated by the PBM-MCM is highly sensitive to the simulated isoprene by the WRF-CMAQ, the WRF-CMAQ derived isoprene can be evaluated by comparing the simulated O_3 values with the input of the WRF-CMAQ derived isoprene and the observed isoprene on all VOC/OVOC sampling days for the 2016 sampling campaign in PRE. It was found the WRF-CMAQ derived isoprene caused underestimation of the simulated O_3 by 2.2% at QA and overestimation by 2.7% TC, indicating the reasonable photochemical simulation by adopting WRF-CMAQ derived isoprene at both sites.

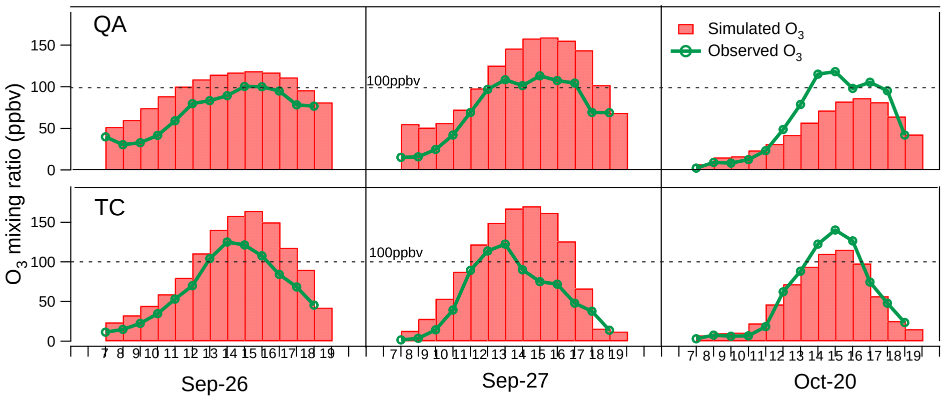

Figure 3.4 Comparison between observed O_3 and PBM-MCM-simulated O_3 with corrected VOCs derived from WRF-CMAQ in pattern 1 in autumn 2016 at both sites.

3.3.2.3 Estimate of relative incremental reactivity (RIR)

Relative incremental reactivity (RIR), reflecting the relative variation in O_3 production rate for a change of mixing ratios in precursors, is used to evaluate the sensitivity of O_3 formation to precursors (Cardelino and Chameides, 1995), which can be derived from the outputs of the PBM-MCM. The O_3 production is more effectively reduced by cutting down the concentrations of the precursors with larger positive RIRs. Considering the weighted contributions to O_3 production, the integrated RIR values will be used in this study. The equations (Equation 3.2 and Equation 3.3) are defined as follows:

$$RIR(X) = \frac{\left[P^{S}_{O_3-NO}(X) - P^{S}_{O_3-NO}(X-\Delta X)\right]/P^{S}_{O_3-NO}(X)}{\frac{\Delta S(X)}{S(X)}} \qquad \text{(Equation 3.2)}$$

$$Integrated\ RIR(X) = \frac{\sum_{i=1}^{n}\left(RIR(X)_i \times O_{3_I}\right)}{\sum_{i=1}^{n} O_{S_i}} \qquad \text{(Equation 3.3)}$$

S(X) is the simulated mixing ratio of a specific precursor X (*i.e.*, VOC species, CO or NO_x (ppbv)); $\frac{\Delta S(X)}{S(X)}$ is the hypothetical change of mixing ratio of X, *i.e.*, 10% in this study; $P^{S}_{O_3-NO}(X)$ is the net O_3 production in a base run with original mixing ratios, while $P^{S}_{O_3-NO}(X-\Delta X)$ represents the constrained run with 10% reduction of species X but other species remain unchanged. $RIR(X)_i$ and O_{3_i} stand for the hourly RIR value and simulated O_3

level, respectively, and *i* means the *i*th hour during a day. The equations of O_3 production $P^S_{O_3-NO}$ were illustrated in Equations 3.4 - 3.6 in Section 3.3.2.4.

3.3.2.4 Simulation of photochemical pathways of O_3 and radicals

In this study, the photochemical O_3 production and destruction pathways were simulated using the PBM-MCM model, and the simulated O_3 production and destruction rates were output every hour. The O_3 gross production was calculated by the oxidation of NO by HO_2 and RO_2 (Equation 3.4), while the O_3 destruction was calculated by O_3 photolysis and reactions of O_3 with OH and HO_2 (Equation 3.5), and the difference between them was the net O_3 production (Equation 3.6). The equations are listed below:

$$G_{O_3-NO} = k_{HO_2+NO}[HO_2][NO] + \sum k_{RO_2+NO}[RO_2][NO]$$

(Equation 3.4)

$$D_{O_3-NO} = k_{HO_2+O_3}[HO_2][O_3] + k_{OH+O_3}[OH][O_3] + k_{O(^1D)+H_2O}[O(^1D))][O_3] + k_{OH+NO_2}[OH][NO_2] + k_{alkenes+O_3}[alkenes][O_3]$$

(Equation 3.5)

$$P_{O_3-NO} = G_{O_3-NO} - D_{O_3-NO}$$

(Equation 3.6)

Where, P_{O_3-NO} is the net O_3 production, G_{O_3-NO} and D_{O_3-NO} represent O_3 gross production and O_3 destruction, respectively. O^3P, $O(^1D)$, NO and NO_2 are put into instantaneous steady state. The constants (k) are the rate coefficients of each reaction. The radicals and intermediates, as well as the formation and loss pathways of each radical, can be derived from the PBM-MCM model.

3.3.3 Positive matrix factorization

Positive matrix factorization (PMF) is a receptor model that has been extensively used for source apportionment of airborne particulate matters and VOCs (Lee et al., 1999; Brown et al., 2007). In the inter-annual study in Hong Kong and the five-megacity study in 2018, US EPA PMF 5.0 model (USEPA, 2017) was applied to identify the sources of O_3 precursors, according to Equation 3.7 (Paatero, 1997; Ling et al., 2014). To identify the sources of VOCs in the five cities, selected VOC species in all VOC samples were input into PMF model for source apportionment. The selection of the VOC species was based on the criteria: 1) their abundances and 2) tracers of VOC sources.

$$x_{ij} = \sum_{k=1}^{p} g_{ik} h_{kj} + e_{ij} \qquad \text{(Equation 3.7)}$$

where x_{ij} is the measured concentration of *j*th species in *i*th sample, g_{ik} represents the contribution of *k*th source to *i*th sample, f_{kj} denotes the fraction of *j*th species in *k*th source, and e_{ij} is the residual for *j*th species in *i*th sample. *p* stands for the total number of independent sources (Paatero, 2000a, b).

The PMF provides solutions with minimum *Q* values (see Equation 3.8), which converges based on the uncertainties (*u*) of input data.

$$Q = \sum_{i=1}^{n} \sum_{j=1}^{m} \left[\frac{x_{ij} - \sum_{k=1}^{p} g_{ik} f_{kj}}{u_{ij}} \right]^2 \qquad \text{(Equation 3.8)}$$

where u_{ij} stands for the uncertainty of the *j*th species in the *i*th sample; *n* and m are the total numbers of samples and species, respectively.

The uncertainties of the concentrations applied to PMF were set in the same way as Polissar et al. (1998) and Reff et al. (2007). Values below or equal to the LoD were replaced by half of the LoDs and the uncertainties for these values were set as 5/6 of the corresponding LoDs. For the values greater than LoDs, the uncertainties were calculated as [(Error Fraction × concentration)^2 + (LoD)^2]$^{1/2}$ where 10% was assigned as the error fraction. Missing values (mainly due to maintenance or malfunction of the instruments) were replaced by the geometric mean of the measured values and their accompanying uncertainties were set as four times the geometric mean value. More details about the settings of the uncertainty were provided in Norris et al. (2008) and Zhang et al. (2012).

The model was run for 20 times with a random seed, and tests with different number of factors were conducted. Several criteria were considered before finally determining the optimum solution of the model. (1) A lower Q value (Equation 3.8) was suggested. (2) A $\frac{Q_{rubust}}{Q_{ture}}$ lower than 1.5 was preferred. (3) The correlation coefficients (R^2) between the observed and predicted values for most of the species were good and both R^2 and the slope were closed to 1. (4) Data points with residuals below -3 or above 3 were excluded in the data analysis. The percentage of data utilization should be close to 100%.

3.3.3.1 Simulation scenarios

The PBM-MCM simulates the in-situ O_3 photochemistry based on the observed O_3 precursors. Figure 3.5 shows the average mixing ratios of some O_3 precursors in different wind sectors in the 2007, 2013 and 2016 sampling campaigns at TC. The higher levels of CO, ethyne, ethane, propane and toluene under northwest winds indicated the transport of these species from PRD to Hong Kong. Meanwhile, O_3 might also be transported to Hong Kong. The determinations of the locally-produced and regionally-transported O_3, as well as the uncertainties, were taken into consideration. As an observation based model, PBM-MCM has been widely used to simulate the in-situ O_3 production (Lam et al., 2013; Ling et al., 2014; Lyu et al., 2017b; Wang Y. et al., 2017). The O_3 simulated by PBM-MCM can be regarded as the locally-produced O_3, and the differences between the observed and simulated O_3 were taken as the regionally-transported O_3. However, it should be noted that the observed concentrations of O_3 precursors could be partially built up by regional transport. For example, under the northwest winds, the average mixing ratios of CO (693.9±25.5 ppbv), ethyne (2.15±0.22 ppbv), ethane (2.31±0.25 ppbv), propane (2.97±0.51 ppbv) and toluene (2.42±0.52 ppbv) were the highest among all the wind sectors. Since the PBM-MCM was constrained by the observed concentrations of O_3 precursors, the share of regionally-transported O_3 precursors in the observations made contributions to the simulated O_3, which in fact represented a kind of regional transport. Therefore, the locally produced O_3 were to some extent overestimated in this way. Conversely, the regionally-transported O_3 were underestimated. However, it is difficult to accurately quantify the contributions of regional transport to O_3 precursors at the site, and also due to the non-linear relationships between O_3 and its precursors, the overestimation of the locally-produced O_3 and the underestimation of the regionally-transported O_3 were not quantitatively evaluated.

Further, to evaluate the contributions of VOC sources to the local O_3 production in the inter-annual sampling campaign in Hong Kong and the 2018 sampling campaign in five megacities, two scenarios of model simulation were performed, *i.e.,* Scenario A and Scenario B. The scenario A simulated the O_3 photochemistry in the whole air, which was constrained by the observed concentrations of all the O_3 precursors. The model simulations in scenario B (including six assumed sub-scenarios) were constrained by the concentrations of O_3 precursors with those contributed by individual sources being subtracted from the observed concentrations. The base scenario (scenario A) was established to simulate the local production of O_3, with the observed concentrations of air pollutants (excluding O_3) as model inputs. The simulated O_3 in scenario A was regarded as the locally produced O_3, as the observed O_3 concentrations were not input to constrain the model. Bearing in mind that the regional effects cannot be fully eliminated in this approach, due to the impacts of regional air on the observed concentrations of O_3 precursors. The scenario B was established to simulate O_3 under the assumption that a source of VOCs was totally removed. Namely, the VOCs emitted from a specific source were subtracted from the observed VOCs when allocating the model inputs. In this study, six sources of VOCs were identified in sampling campaigns conducted in Hong Kong in 2016 and in five megacities in 2018, respectively. Therefore, 6 sub-scenarios were included in scenario B, because the VOCs emitted from the individual sources were subtracted one by one. In this approach, the differences in simulated O_3 between scenario A and scenario B were the contributions of individual VOC sources to the local O_3 production. It should be noted that due to the nonlinear relationships between O_3 and its precursors, the subtraction approach only qualitatively but not quantitatively evaluate the contributions of VOC sources to O_3 production.

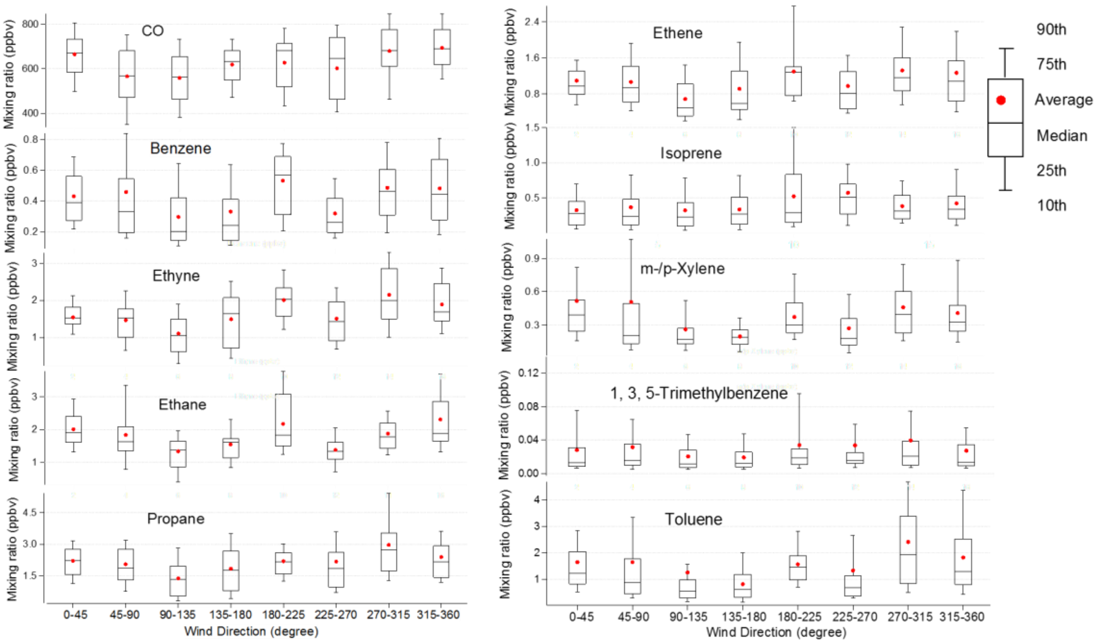

Figure 3.5 Average mixing ratios of some O_3 precursors in different wind sectors at TC in the 2007, 2013 and 2016 sampling campaigns in Hong Kong.

Chapter 4 Photochemical ozone formation and free radical chemistry in five Chinese megacities in summer 2018

4.1 Introduction

Ozone (O_3) pollution has attracted increasing attention in China due to its adverse impact on human health (Bell et al., 2004), crops (Wang et al., 2005) and vegetation (Ashmore, et al., 2005). Tropospheric O_3 is produced through complex chemical reactions between its precursors, *i.e.*, VOCs and NO_x, in the presence of sunlight. However, the nonlinear relationship between O_3 and its precursors makes it difficult to control O_3 formation (NRC, 1992; Carter, 1994).

Recently, high O_3 levels have been frequently reported in warm seasons in many megacities of China (Wang T. et al., 2017; Wu and Xie, 2017; Li et al., 2019). Over the past 20 years, many studies have reported the increasing O_3 trends and strong photochemical reactions in several highly urbanized regions (Wang T. et al., 2017; Wang W. et al., 2017; Lu et al., 2020a), such as North China Plain (NCP) (Zhang et al., 2014; Tan et al., 2017, 2018b; Yang et al., 2018), Yangtze River Delta (YRD) (Tang et al., 2008; Ran et al., 2009, 2012; Zhu J. et al., 2020), and Pearl River Delta (PRD) (Wang Y et al., 2017; Lu X. et al., 2019; Liu and Wang, 2020a, 2020b; Yang et al., 2020). Moreover, cities in central and western China also experience air quality deterioration, especially photochemical pollution, due to their expansion of economy, population and industrialization, such as Wuhan (Lyu et al., 2016b; Hui et al., 2018; Zeng P. et al., 2018), Chengdu (Su et al., 2017; Tan et al., 2018a) and Lanzhou (Xue et al., 2014a; Jia et al., 2016). Since 2013, the central government has made great effort to fight against the air pollution problem in China, including various stringent control strategies on multiple anthropogenic pollutants, *e.g.*, the Air Pollution Prevention and Control Action Plan from 2013-2018 (MEE PRC, 2019), the short-term “blue sky defense battle” between 2018-2020 (MEE PRC, 2018) and the long-term “beautiful China” targets till 2035 (CCIED, 2019) (Liu X. et al., 2019; Lu et al., 2020b). According to Lu et al. (2020b), though many pollutants such as SO_2 and $PM_{2.5}$ have been effectively controlled, increasing O_3 pollution still exists in urban areas in China, indicating that corresponding control actions on O_3 precursors, *i.e.*, VOCs and NO_x, in different regions are supposed to be more strictly enforced as appropriate.

Moreover, since each city has its unique industrial structures, energy use pattern and meteorological conditions, the photochemical O_3 formation mechanisms in different cities may be different, which must be considered when formulating O_3 control strategies (Lu et al., 2019). In the past decade, a large number of studies have investigated the net O_3 production rate and/or radical chemistry in the urban areas of Chinese megacities. For example, Liu et al. (2012) reported that the average daytime net O_3 production rate was 25.8 ppbv h^{-1}, and the photolysis of VOCs was the main source of OH radical at an urban site in Beijing in the summer of 2007. Base on the field measurement data at an urban site in Wuhan in the autumn of 2013, Lu et al. (2017) found that the average daytime net O_3 production rate was 8.8 ppbv h^{-1}, and highlighted the significant contribution of HONO to the atmospheric oxidative capacity in central China. Most recently, Zeng et al. (2019) explored the net O_3 production rates at an urban site in Wuhan in summer 2016 using an observation-based model and indicated that the average daily peak net O_3 production rate was 10 ppbv h^{-1}. However, the radical chemistry was not investigated. Tan et al.(2018a) first revealed the peak net O_3 production rate of 20-28 ppbv h^{-1} at four urban/suburban sites of Chengdu in autumn 2016. Moreover, they analyzed the RO_x budget using simulated radical concentrations and proved severe O_3 pollution based on comprehensive radical chemistry in southwestern China. However, there is a dearth of nationwide studies on in-situ O_3 photochemistry in urban areas of major Chinese megacities, especially in central and western China, not to mention simultaneous study in multiple cities in China.

In the past decades, the rapid urbanization and industrialization in China has accelerated the consumption of energy, enlarged the emissions of VOCs and led to more O_3 production (Li M. et al., 2019; Tan et al., 2018a; Xu et al., 2019). A variety of natural and anthropogenic sources, which directly emit hundreds of VOC species into the atmosphere and contribute differently to local O_3 formation, have been extensively studied to examine their impact on air quality in China (Guo et al., 2017; Wang T. et al., 2017; Jia et al., 2016; Lyu et al., 2016a; Song et al., 2018; Liu Y.H. et al., 2019). For example, Wang B. et al. (2010) identified six VOC sources in summer Beijing, including vehicle exhaust, LPG usage, gasoline evaporation, biogenic emission, paint and solvents, and chemical industry, among which vehicle exhaust contributed the most to VOCs (57-60%), followed by LPG usage (10-19%) and gasoline evaporation (7-17%). The largest contribution of vehicular emissions was also found in Wuhan (27.8%; Lyu et al., 2016a) and Chengdu (45.0%; Song et al., 2018). Five out of six sources identified in Wuhan and Chengdu, respectively, were the same as those in Beijing (Wang B. et al., 2010), except for gasoline evaporation replaced by coal burning in Wuhan (Lyu et al., 2016a) and LPG usage replaced by a second industrial source in Chengdu (Song et al., 2018). According to the study conducted by Liu Y. et al. (2019), petrochemical industry was the largest contributor to VOCs in Shanghai (35.6%). Given that Lanzhou is a highly industrialized city, Jia et al. (2016) reported that the mixed industrial processes in Lanzhou contributed the most to VOCs (26.8%). The different VOC sources among cities may be partially affected by the different sampling seasons and industrial structures of the cities. However, there is a lack of studies that simultaneously investigate the spatial variations of VOC sources and their contributions to O_3 formation in urban areas of multiple megacities in China, particularly in warm seasons.

In this study, intensive measurements of O_3 and its precursors were simultaneously conducted in urban areas in five megacities, including Beijing, Shanghai, Wuhan, Chengdu and Lanzhou, in summer 2018. Through comprehensive data analysis, I investigated the chemical characteristics of O_3 and its precursors, evaluated the sensitivity of O_3 production to precursors and the production and destruction pathways of O_3 and radicals using an observation-based photochemical box model, and quantified the spatial variations of VOC sources and the contributions of each source to local O_3 formation in each megacity. These findings are expected to help solve O_3 pollution across the country.

4.2 General features

During the sampling period, VOC samples were collected on 6 – 8 selective days in each city, among which 0 – 5 O_3 episode days (maximum hourly O_3 > 100 ppbv) were captured. Figure 4.1 presents the time series of O_3, CO, SO_2, NO_x, VOC groups and meteorological parameters during the daytime hours (08:00-18:00LT) on the VOC sampling days in the five cities in August 2018. Table 4.1 summarizes the daytime average values of air pollutants and meteorological parameters in the five cities. Here the TVOCs and VOC groups refer to the 44 VOCs and 4 OVOCs listed in Table 4.2. It was found that Beijing had the highest O_3 mixing ratios (78.6±7.3 ppbv) ($p < 0.05$), followed by Lanzhou (67.2±7.8 ppbv) and Wuhan (63.9±6.8 ppbv), indicating the severe O_3 pollution in northern and central China in summer. The lower O_3 in Chengdu (52.5±7.5 ppbv) ($p < 0.05$) can be partly attributed to the stronger NO titration effect (NO_x: 23.8±2.8 ppbv) and lower TVOCs levels (23.7±2.5 ppbv). During the sampling period, Shanghai had the lowest levels of air pollutants with O_3 mixing ratio of 20.7±1.9 ppbv, which was mainly due to the unstable weather conditions with continuous precipitation caused by a few tropical storms over the East China Sea (CMA, 2019). In addition, moderate wind speeds (lower than 2.0 m s^{-1}), strong solar radiation (359.4 – 385.5 W m^{-3}) and high ambient temperature (27.5 – 34.7 °C) in all the five cities indicated favorable meteorological conditions for local O_3 production in summer 2018.

During the sampling period, the cities in northern China, *i.e.*, Beijing and Lanzhou, had the largest TVOC concentrations (44.2±4.3 ppbv and 45.3±5.9 ppbv, respectively), followed by Wuhan in central China (30.2±3.1 ppbv) and Chengdu in southwestern China (23.7±2.5 ppbv), and Shanghai (19.1±1.9 ppbv) in eastern China had the lowest TVOCs. Among the four VOC groups, alkanes accounted for the highest proportions of TVOCs in Chengdu and Lanzhou (31.9-44.6%), while OVOCs ranked the first in Beijing (55.0%). Alkanes and OVOCs had equal contributions in Shanghai (alkanes: 31.9%; OVOCs:35.6%) and Wuhan (alkanes: 36.1%; OVOCs: 35.8%). Furthermore, alkenes made the second contribution in Beijing (21.7%) and Lanzhou (27.8%), implying different chemical compositions in different cities though all the cities had severe O_3 pollution problem. Moreover, aromatics had the lowest proportions in all the five cities with percentages of 8.2-11.8%, in line with the range of 7-35% reported by previous studies in China (*e.g.* Liu et al., 2008c; Geng et al., 2009; Jia et al., 2016; Zhu et al., 2016).

In comparison, the levels of NO and NO_2 measured in the five cities were consistent with those reported at urban sites in China in summer. For VOCs/OVOCs, the mixing ratios of the observed TVOCs at multiple sites were between the values found in the previous studies in urban areas (*e.g.*, Duan et al., 2008; Cai et al., 2010; Han et al., 2015; Zou et al., 2015; Yang et al., 2018).

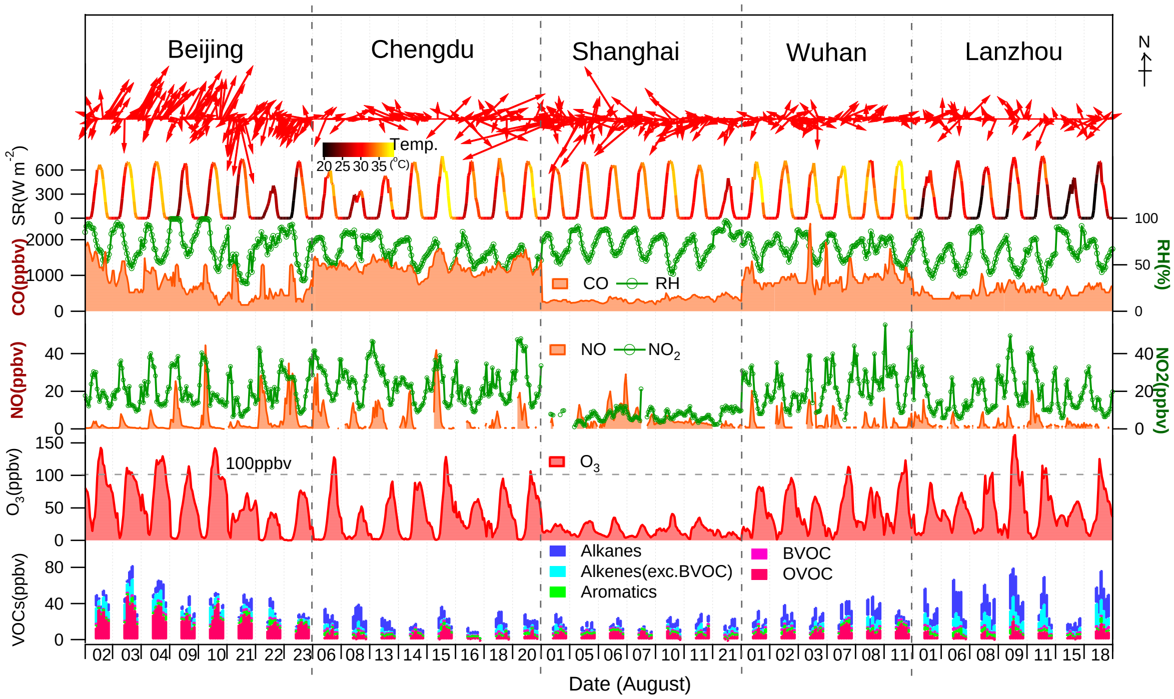

Figure 4.1 Time series of trace gases, VOCs and meteorological parameters in the five sampling cities. RH, Temp., and SR refer to relative humidity, temperature, and solar radiation, respectively.

Table 4.1 Descriptive statistics of air pollutants and meteorological parameters during daytime hours (08:00-18:00 LT) in the sampling periods in the five cities. The value represents mean± 95% confidence interval (C.I.).

City	Beijing	Shanghai	Wuhan	Chengdu	Lanzhou
Trace gases (ppbv)					
O_3	78.6±7.3	20.7±1.9	63.9±6.8	52.5±7.5	67.2±7.8
CO	657.5±83.7	352.4±15	934.8±78.2	1244.2±44.8	573.8±35
NO	2.1±0.5	5.0±1.0	3.2±1.1	4.9±1.5	2.9±0.7
NO_2	16.8±1.2	7.7±0.8	17.5±2.2	20±1.7	15.8±2
NO_x	18.8±1.5	12.5±1.3	20.4±3	23.8±2.8	18.2±2.4
VOCs (ppbv)					
TVOCs	44.2±4.3	19.1±1.9	30.2±3.1	23.7±2.5	45.3±5.9
Alkanes	7.0±1.2	6.1±0.9	10.9±1.8	10.0±1.5	20.2±3.1
Alkenes*	9.6±1.6	4.3±0.6	5.3±0.9	4.8±0.7	12.6±2.0
Aromatics	3.3±0.7	1.9±0.3	3.1±0.6	2.8±0.6	4.9±1.0
OVOCs	24.3±2.7	6.8±1.0	10.8±1.5	6.1±1.0	7.6±1.3
Meteorological parameters					
Wind speed (m s^{-1})	1.4±0.1	1.4±0.2	0.8±0.1	1.0±0.2	0.7±0.1
Solar radiation (W m^{-2})	432.4±44.6	421.4±49.5	437.5±51	415.5±39.6	431.8±42.3
Relative humidity (%)	59±3.3	63.9±2.9	59.5±2.1	55.3±2.7	52.5±2.8
Temperature (°C)	31.8±0.8	32.5±0.5	35.2±0.5	32.7±0.7	28.1±0.8

*Alkynes (*e.g.*, ethyne) were grouped into alkenes in this study.

Table 4.2 Descriptive statistics of VOC and OVOC mixing ratios measured at the five sites on VOC sampling days. The 95% C.I. and Max. denote the 95% confidence interval and maximum of the mixing ratios of VOC and OVOC species, respectively (Unit: pptv).

VOC species	Beijing			Shanghai			Wuhan			Chengdu			Lanzhou		
	Mean	95%C.I.	Max	Mean	95%C.I.	Max	Mean	95%C.I.	Max	Mean	95%C.I.	Max	Mean	95%C.I.	Max
Ethane	2450.8	81.9	9389.7	1499.8	48.7	4798.7	2172.5	98.4	4798.7	2249.9	58.2	6734.3	4060.3	70.2	10084.5
Ethene	2620.0	88.2	8555.3	1155.2	72.0	6035.9	1723.8	90.3	6035.9	2114.9	57.6	6794.0	3942.2	80.2	9898.5
Ethyne	3215.4	68.7	8986.1	2159.9	47.7	6041.7	1963.4	74.7	6041.7	1155.4	39.3	3016.0	1629.4	29.8	2961.9
Propane	502.3	32.6	1935.8	1170.8	37.9	4045.0	2851.6	89.6	4045.0	1800.4	62.0	6235.3	4316.5	72.8	11780.4
Propene	2606.3	63.4	6498.4	369.3	28.9	1596.0	468.8	32.9	1596.0	381.7	32.1	1538.6	3134.5	88.3	10055.4
i-Butane	193.2	41.7	1164.6	189.5	45.0	1490.6	605.0	69.6	1490.6	875.6	46.7	3983.6	1766.8	105.0	8244.8
n-Butane	970.3	64.9	4118.2	851.5	35.4	2302.0	1159.5	53.3	2302.0	1449.2	53.2	5281.6	1278.6	82.2	5723.4
1-/i-Butene	396.4	43.1	1923.4	166.6	17.9	656.2	260.1	25.4	656.2	427.6	44.9	2256.7	1558.8	64.2	5069.5
trans-2-Butene	61.9	12.7	262.5	25.5	4.4	48.7	36.5	7.2	48.7	31.5	13.6	160.0	130.9	36.3	1003.7
cis-2-Butene	49.5	12.0	215.7	21.5	4.4	46.6	33.9	7.9	46.6	24.3	11.9	117.0	70.5	21.0	347.5
3-methyl-1-Butene	44.1	19.4	410.7	4.4	2.4	11.3	24.0	7.5	11.3	40.2	68.2	1515.6	14.2	17.2	129.0
2-methyl-1-Butene	67.5	28.9	830.5	32.1	6.3	89.6	40.5	8.0	89.6	21.2	9.9	85.0	44.9	25.3	475.1
cis-2-Pentene	34.2	8.3	127.2	15.8	2.9	29.6	6.2	2.3	29.6	17.0	10.2	68.2	75.2	12.5	344.5
2-methyl-2-Butene	106.2	19.5	449.5	9.4	3.8	32.8	59.6	9.7	32.8	45.2	9.7	123.8	84.9	30.8	881.8
Butyne	30.7	9.4	106.2	20.1	5.2	58.9	17.3	8.2	58.9	101.0	24.0	421.4	685.4	50.0	2505.9
i-Pentane	604.6	45.2	2077.5	758.3	48.4	3452.5	2444.8	84.1	3452.5	1455.6	53.9	4237.2	640.7	73.6	4087.6
n-Pentane	137.9	28.8	1049.6	378.2	33.0	1652.9	607.3	42.2	1652.9	485.0	33.1	1708.3	918.6	67.1	4473.9
1-Pentene	79.0	30.4	888.3	28.8	10.7	139.4	20.5	12.6	139.4	148.5	37.9	849.3	676.7	39.9	2011.0
trans-2-Pentene	8.9	6.0	38.8	28.8	6.7	78.0	30.4	8.9	78.0	27.7	11.8	124.0	52.4	34.4	816.2
2-Methylpentane	275.8	43.9	2088.4	65.2	12.0	221.2	141.8	19.0	221.2	350.0	27.1	1477.0	1230.8	78.3	6516.4
n-Hexane	292.7	31.5	1007.2	628.8	44.3	2124.8	225.3	33.4	2124.8	322.4	25.2	1008.0	1368.5	72.0	6545.0
n-Heptane	206.7	25.5	720.3	62.5	11.3	173.4	58.2	16.8	173.4	140.0	22.4	536.2	121.4	15.3	397.0

n-Octane	176.3	24.9	669.4	37.7	8.8	114.5	44.5	13.7	114.5	141.6	22.4	551.6	577.4	33.8	2082.8
2,2-Dimethylbutane	35.9	18.4	320.2	9.7	3.1	23.9	17.6	6.8	23.9	51.5	10.7	168.0	137.8	31.3	973.7
2,3-Dimethylbutane	119.0	16.7	370.6	56.0	14.9	206.4	10.6	5.9	206.4	88.0	17.2	423.0	888.2	95.0	7012.3
3-Methylpentane	375.6	40.5	1586.5	136.7	15.0	337.3	177.9	17.1	337.3	192.9	21.2	762.0	801.7	58.2	3788.6
Cyclohexane	121.7	41.5	1091.7	56.4	25.8	455.1	75.0	25.5	455.1	89.0	32.1	1019.8	281.0	28.6	1080.7
2-Methylhexane	79.4	19.3	368.8	98.1	17.6	326.7	116.9	22.8	326.7	96.7	42.5	1058.8	1147.8	94.3	7476.4
3-Methylhexane	154.0	21.9	558.8	42.0	11.4	161.0	80.0	13.7	161.0	20.8	22.9	222.0	178.4	23.9	741.8
n-Nonane	236.7	29.4	980.0	27.0	7.4	81.0	34.3	13.0	81.0	65.1	13.5	248.7	389.4	78.1	4590.0
n-Decane	95.2	13.2	356.3	36.6	10.5	130.0	44.8	8.9	130.0	100.0	33.2	1036.3	118.7	26.5	650.3
Isoprene	183.8	25.7	901.3	165.3	10.6	383.0	403.1	24.9	383.0	281.7	31.3	1053.9	135.4	15.9	380.4
α-Pinene	54.8	15.5	217.5	14.3	5.2	43.4	140.4	20.5	43.4	56.6	31.3	786.3	543.4	81.1	4001.2
β-Pinene	65.3	19.0	329.4	59.6	18.1	211.7	159.4	25.0	211.7	34.1	47.3	972.5	90.9	40.1	803.0
Benzene	151.3	16.9	409.9	87.4	10.1	227.2	214.0	16.3	227.2	114.1	12.5	319.6	248.0	33.4	1131.9
Toluene	561.2	63.1	3049.9	584.5	42.8	2085.4	690.3	53.1	2085.4	348.8	31.8	1342.5	279.0	39.2	1522.4
Ethylbenzene	185.4	27.6	796.2	258.0	16.8	609.9	521.8	41.5	609.9	260.6	22.6	698.0	468.2	40.3	1901.3
m/*p*/*o*-Xylenes	921.7	43.5	3051.3	357.4	14.2	624.6	652.9	34.5	624.6	884.1	49.8	3364.0	1504.3	56.0	4656.7
1,3,5/1,2,4/1,2,3-Trimethylbenzenes	82.0	8.9	182.4	83.4	5.7	180.0	103.3	7.6	180.0	103.1	14.4	331.0	202.7	14.3	455.9
i-Propylbenzene	58.0	26.6	596.6	24.8	5.0	50.3	45.1	10.8	50.3	12.9	6.6	77.6	95.8	17.1	425.0
n-Propylbenzene	193.4	28.0	840.2	26.8	7.0	77.8	28.4	12.2	77.8	23.5	10.8	148.4	154.3	18.9	650.4
3-Ethyltoluene	20.9	6.5	55.2	7.8	4.7	22.6	15.7	6.8	22.6	21.9	7.3	83.0	56.0	11.0	140.3
4-Ethyltoluene	67.3	9.9	169.4	32.2	5.4	71.2	51.5	9.2	71.2	45.7	11.1	161.0	116.8	14.9	344.6
2-Ethyltoluene	43.5	5.3	88.9	29.0	2.4	50.2	35.3	3.8	50.2	29.7	6.7	82.8	84.1	13.8	379.1
Formaldehyde	9572.9	94.4	20621.4	2267.8	46.6	5291.0	5167.9	59.4	5291.0	2294.3	55.3	6053.1	1840.0	81.0	10841.5
Acetaldehyde	7210.1	75.6	17651.6	1405.2	41.4	4333.7	1660.0	24.1	4333.7	1261.2	47.6	4231.0	1700.1	79.9	9472.1
Acetone	6602.9	74.5	12902.6	2447.4	70.4	7064.9	3456.5	83.7	7064.9	1750.8	82.4	7586.4	3251.9	77.8	8771.5
Propionaldehyde	1017.4	17.5	1829.1	762.1	29.8	2090.2	1025.5	26.6	2090.2	818.8	28.3	1671.7	771.3	27.4	2147.9

4.3 O_3 photochemistry

4.3.1 Model verification

Prior to investigating the local O_3 photochemistry, the performance of PBM-MCM was evaluated. Figure 4.2 displays the daytime variations of simulated and observed O_3 mixing ratios on the VOC sampling days in summer 2018 in the five cities. The simulated O_3 agreed well with the observed O_3 variations with peaks at noon and lower values in the morning and evening. The IOA values in Beijing, Wuhan, Chengdu and Lanzhou were between 0.74-0.87 (Table 4.3), within the ranges of 0.67-0.89 reported in previous studies (Lyu et al., 2015, 2016a, 2016b; Wang N. et al., 2015; Wang Y. 2018; Liu X. et al., 2019). However, the IOA in Shanghai was a bit lower (0.61), probably due to the fact that PBM-MCM usually performs better on high O_3 days with intense in-situ photochemical reactions (*e.g.*, Lam et al., 2013; Lyu et al., 2017b; Wang H. et al., 2018; Liu X. et al., 2020). The discrepancies between the observations and simulation results at all sites might be attributable to the physical processes, *e.g.*, horizontal and vertical transport, which were not well considered in PBM-MCM (Wang Y. et al., 2017; Liu X. et al., 2019; Lyu et al., 2019). Note that PBM-MCM simulations were only constrained by O_3 precursors when simulating O_3 to evaluate the model performance (Section 4.3.1). However, PBM-MCM was constrained by both observed O_3 and its precursors when the photochemical oxidative processes were investigated in this study, in which both regional transported and locally produced O_3 were taken into consideration by the model (Section 4.3.2 – Section 4.5).

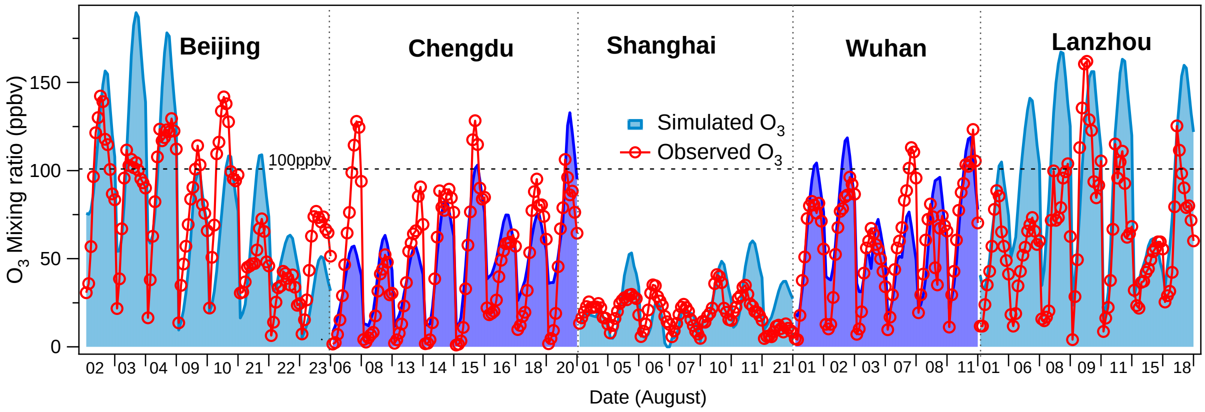

Figure 4.2 Hourly mixing ratios of simulated and observed O_3 in the five cities during the VOC sampling periods in August 2018.

Table 4.3 IOA value of model performance in the five cities during the VOC sampling periods in August 2018.

City	Beijing	Chengdu	Shanghai	Wuhan	Lanzhou	Overall
IOA	0.80	0.87	0.61	0.87	0.74	0.78

4.3.2 In-situ net O_3 production

Figure 4.3 displays the average diurnal variations of the simulated O_3 production and destruction rates in each city. The daytime average reaction rates and the contribution of each pathway are further illustrated in Table 4.4. Among the five cities, Lanzhou had the highest net O_3 production rate (8.9±1.7 ppbv h^{-1}) while Shanghai had the lowest value (2.8±0.7 ppbv h^{-1}) ($p < 0.05$). The net O_3 production rate in Beijing (6.4±1.3 ppbv h^{-1}), Wuhan (5.8±1.2 ppbv h^{-1}), and Chengdu (4.0±0.6 ppbv h^{-1}) was at a moderate level ($p = 0.08$ and $p = 0.11$ related to Beijing and Wuhan, respectively). HO_2+NO (51.9 - 65.2%) and RO_2+NO (34.6 - 47.3%) were the dominant pathways of O_3 production, consistent with previous studies in China (Wang H. et al., 2018; Wang Y. et al., 2018; Lyu et al., 2016a, 2019). The higher contributions of RO_2+NO in Beijing (41.5±8.3%) and Lanzhou (47.3±8.5%) than other cities (34.6 - 39.9%) might be attributable to the higher RO_2 concentrations enhanced by the higher local VOCs. In contrast, the prominent destruction pathway of O_3 was OH+NO_2 (45.0 - 69.6%) in all the five cities. However, the second important destruction pathway of O_3 was different in the cities. It was the O_3 reaction with alkenes in Beijing (16.1%) and Lanzhou (29.5%), but photolysis of O_3 in Chengdu (14.1%), Shanghai (18.6%) and Wuhan (19.2%). Overall, the simulated net O_3 production rates among the five cities were consistent with those in previous studies conducted in warm seasons in China. For example, Han et al. (2020) found that the average daytime net O_3 production rate was 11 ppbv h^{-1} during an O_3 episode event in the NCP region in August 2018. Zeng et al (2019) investigated the net O_3 production rates at three sites in Wuhan during the summer of 2016 and indicated that the average daily peak net O_3 production rate was 4 ppbv h^{-1} and 10 ppbv h^{-1} at a roadside site and an urban site, respectively. Recently, Zhu J.X. et al. (2020) revealed that the net O_3 production rate at an urban site increased from 2.1 ppbv h^{-1} on non-O_3 episode days to 5.6 ppbv h^{-1} on O_3 episode days in August 2018 in Wuhan.

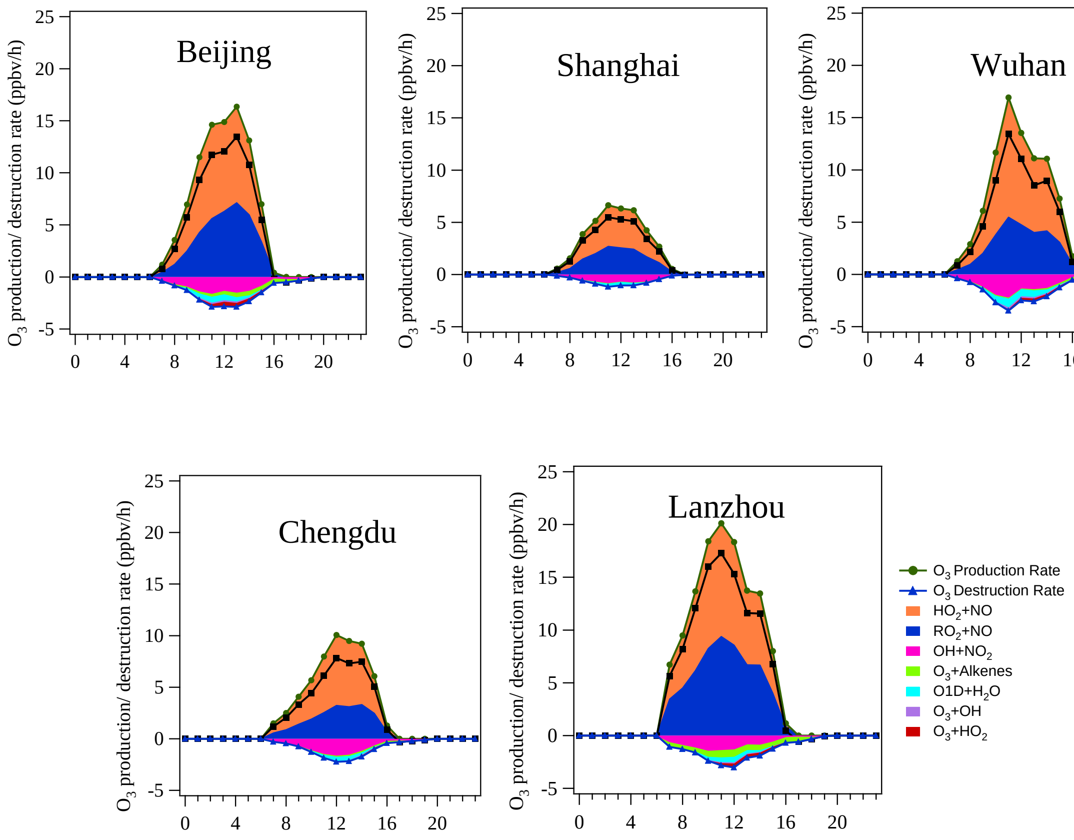

Figure 4.3 Average diurnal profiles of the local O_3 production and destruction rates in the five cities.

Table 4.4 Production and destruction rates of main pathways to O_3 formation during daytime in the five cities.

Site	Net O_3 production rate (ppbv/h)	Production pathways (ppbv h^{-1} (%))			Destruction pathways (ppbv h^{-1} (%))					
		HO_2+NO	RO_2+NO	Total O_3 production	OH+NO_2	O_3+VOCs	O^1D+H_2O	O_3+OH	O_3+HO_2	Total O_3 destruction
Beijing	6.4±1.3	4.7±0.9 (58.1±11.2%)	3.3±0.7 (41.5±8.3%)	8.0±1.5	-0.9±-0.1 (52.6±8.5%)	-0.3±-0.1 (16.1±3.5%)	-0.2±-0.1 (13.4±3.5%)	-0.1±-0.01 (4.1±0.9%)	-0.2±-0.1 (13.3±3.2%)	-1.7±0.3
Shanghai	2.8±0.7	2.0±0.5 (59.9±14.7%)	1.3±0.3 (39.9±10.0%)	3.4±0.8	-0.4±-0.1 (69.6±15.8%)	0.0±0.00 (4.3±0.6%)	-0.1±0.0 (18.6±4.3%)	0.0±-0.01 (3.5±1.1%)	0.0±-0.01 (3.8±1.3%)	-0.6±0.1
Wuhan	5.8±1.2	4.8±1.0 (64.1±13.4%)	2.7±0.5 (35.5±6.8%)	7.5±1.5	-1.0±-0.2 (60.5±11.3%)	-0.1±-0.02 (6.2±1.1%)	-0.3±-0.1 (19.2±5.0%)	-0.1±-0.02 (4.4±1.2%)	-0.2±0.0 (9.1±2.2%)	-1.6±0.3
Chengdu	4.0±0.6	3.3±0.6 (65.2±12.6%)	1.8±0.4 (34.6±7.3%)	5.1±1.0	-0.8±-0.1 (68.7±12.0%)	-0.1±-0.02 (7.9±1.6%)	-0.2±0.0 (14.1±3.3%)	0.0±-0.01 (2.7±0.7%)	-0.1±0.0 (6.4±2.4%)	-1.1±0.2
Lanzhou	8.9±1.7	5.5±1.1 (51.9±10.1%)	5.0±0.9 (47.3±8.5%)	10.6±2.0	-0.7±-0.2 (45.0±9.2%)	-0.5±-0.1 (29.5±4.6%)	-0.2±0.0 (10.9±3.0%)	0.0±-0.01 (2.9±0.7%)	-0.2±0.0 (11.0±2.6%)	-1.6±0.3

4.3.3 Cycling of OH radical

Hydroxyl radical (OH) initiates the oxidation of VOCs, leading to atmospheric O_3 formation. Figure 4.4 illustrates each formation and loss pathway of OH radical in the five cities. The formation and loss rates of OH in all cities were basically balanced. The simulated OH concentration was $(3.3\pm0.7) \times 10^6$ molecules cm^{-3} in Wuhan, $(2.4\pm0.4) \times 10^6$ molecules cm^{-3} in Beijing, $(2.3\pm0.6) \times 10^6$ molecules cm^{-3} in Shanghai, $(2.0\pm0.3) \times 10^6$ molecules cm^{-3} in Lanzhou, and $(1.7\pm0.3) \times 10^6$ molecules cm^{-3} in Chengdu (Table 4.5). The levels of the simulated OH radicals in the five cities were consistent with previous studies in urban areas of China. For example, the measured peak OH concentration was $(1\text{-}8) \times 10^6$ molecules cm^{-3} in Beijing (Ma X. et al., 2019; Slater et al., 2020), and the daytime average OH concentration was 3.1×10^6 molecules cm^{-3} in urban Lanzhou (Wang G. et al., 2020). In addition, the simulated maximum OH concentration was $(3.2 - 6.4) \times 10^6$ molecules cm^{-3} in Wuhan (Zhu J.X. et al., 2020) and $(4 – 8) \times 10^6$ molecules cm^{-3} in Chengdu (Tan et al., 2018a). Among the formation pathways of OH in all the five cities, HO_2+NO was dominant (83.0 - 84.8%), followed by photolysis of HONO, photolysis of O_3, O_3+VOCs and photolysis of H_2O_2. In contrast, OH was mainly consumed through OH+VOCs (38.8 - 64.5%), followed by OH+CO (13.1 - 38.7%) and OH+NO_2 (11.3 - 19.6%) in the five cities.

RO_x radicals (= hydroxyl radical (OH) + hydroperoxyl radical (HO_2) + organic peroxyl radical (RO_2)) play key roles in O_3 photochemistry, and its concentrations in the atmosphere reflect the atmospheric oxidative capacity (AOC). Table 4.5 displays the concentration of RO_x in the five cities during the sampling period. It was found that RO_x had comparable concentrations (p>0.1) in Lanzhou ($(5.9\pm1.1) \times10^8$ molecules cm^{-3}), Beijing ($(5.3\pm1.1) \times10^8$ molecules cm^{-3}) and Wuhan ($(4.3\pm1.0) \times10^8$ molecules cm^{-3}), while it was much lower ($p < 0.05$) in Shanghai ($(2.7\pm0.9) \times10^8$ molecules cm^{-3}) and Chengdu ($(1.8\pm0.7) \times10^8$ molecules cm^{-3}), indicating that the AOC was stronger and O_3 pollution was more serious in northern and central China in summer.

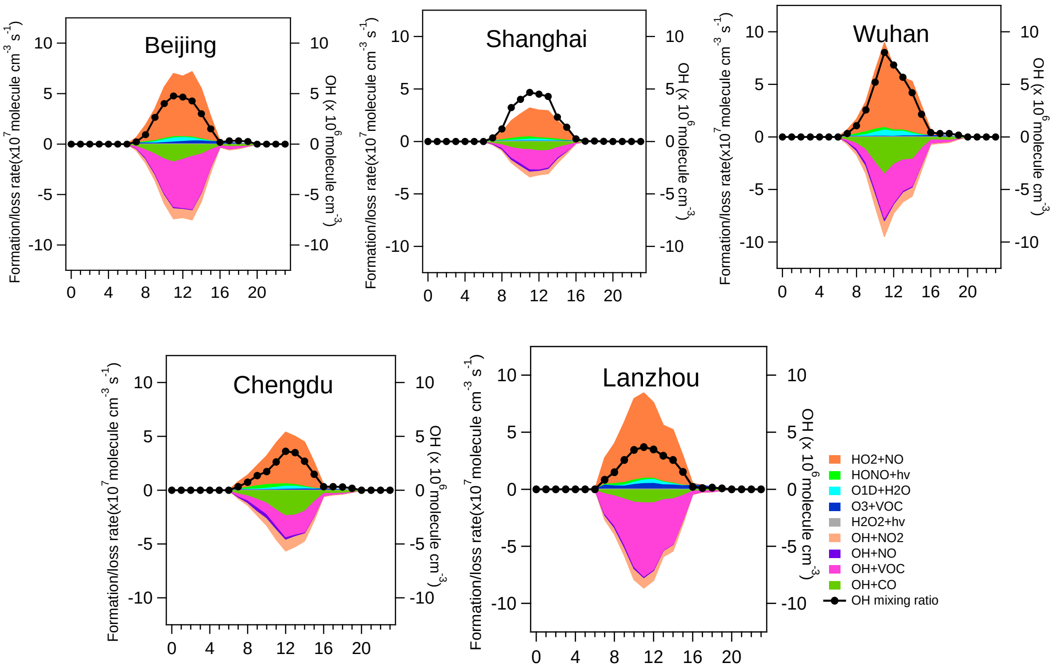

Figure 4.4 Average diurnal cycles of the OH formation and loss rates in the five cities.

Table 4.5 Simulated average daytime concentrations of OH and RO_x and the formation and loss pathways of OH in the five cities.

Site	OH concentration ($\times 10^6$ molecules cm^{-3})	OH cycling rate ($\times 10^7$ molecules cm^{-3} s^{-1})	Formation pathways ($\times 10^7$ molecules cm^{-3} s^{-1} (%))					Loss pathways (($\times 10^7$ molecules cm^{-3} s^{-1} (%))				RO_x concentration ($\times 10^8$ molecules cm^{-3})
			HO_2+NO	HONO+$h\nu$	O^1D+H_2O	O_3+ VOCs	$H_2O_2+h\nu$	OH+CO	OH+VOCs	OH+NO	$OH+NO_2$	
Beijing	2.4±0.4	3.9±0.7	3.3±0.6	0.1±0.01	0.2±0.04	0.2±0.04	0.004±0.001	-0.8±-0.2	-2.5±-0.5	-0.1±-0.01	-0.6±-0.1	5.3±1.1
			(84.8±85.8%)	(1.7±1.4%)	(4.0±5.5%)	(4.8±5.5%)	(0.1±0.1%)	(20.1±23.8%)	(64.5±68.6%)	(1.6±1.5%)	(15.8±13.4%)	
Shanghai	2.3±0.6	1.7±0.4	1.4±0.3	0.1±0.02	0.1±0.02	0.0±0.00	0.004±0.001	-0.4±-0.1	-0.9±-0.2	-0.1±-0.03	-0.3±-0.1	2.7±0.9
			(83.0±87.9%)	(6.5±6.2%)	(4.5±4.5%)	(1.0±0.6%)	(0.2±0.2%)	(23.1±23.5%)	(52.9±58.5%)	(6.6±6.5%)	(16.8±16.4%)	
Wuhan	3.3±0.7	4.0±0.8	3.4±0.7	0.1±0.03	0.2±0.06	0.1±0.01	0.005±0.001	-1.4±-0.3	-1.9±-0.4	-0.1±-0.03	-0.7±-0.1	4.3±1.0
			(83.4±85.0%)	(3.1±3.4%)	(5.5±6.9%)	(1.8±1.5%)	(0.1±0.1%)	(34.8±37.1%)	(46.9±45.7%)	(3.2±3.7%)	(17.4±15.7%)	
Chengdu	1.7±0.3	2.8±0.5	2.3±0.5	0.1±0.03	0.1±0.03	0.1±0.01	0.004±0.001	-1.1±-0.2	-1.1±-0.2	-0.2±-0.04	-0.5±-0.1	1.8±0.7
			(84.2±87.9%)	(5.2±6.2%)	(4.0±5.1%)	(2.3±2.4%)	(0.1±0.1%)	(38.7±38.6%)	(38.8±47.7%)	(5.5±6.9%)	(19.6±18.7%)	
Lanzhou	2.0±0.3	4.6±0.9	3.9±0.8	0.1±0.02	0.1±0.03	0.3±0.05	0.005±0.001	-0.6±-0.1	-3.3±-0.6	-0.1±-0.02	-0.5±-0.1	5.9±1.1
			(84.2±87.6%)	(1.9±2.4%)	(2.7±4.0%)	(7.4±6.2%)	(0.1±0.1%)	(13.1±12.7%)	(72.2±75.5%)	(1.8±2.4%)	(11.0±12.3%)	

4.4 VOC sources and their contributions to O_3 formation

4.4.1 Source apportionment

To identify the sources of VOCs in the five cities, 22 species including 11 alkanes, 5 alkenes/alkynes and 6 aromatics in 192 VOC samples were input into PMF model for source apportionment. The selection of the 22 species was based on the criteria: 1) their abundances and 2) tracers of VOC sources. To reduce the uncertainty of the source apportionment results, compared to separate source apportionments for each city, the samples collected in all the five cities as a whole were used for model input. Figure 4.5 shows the six sources resolved based on the distributions of the VOC tracers. The first source, having moderate to high levels of propane and *i-/n*-butanes, represented LPG usage (Jorquera, et al., 2004; Guo et al., 2013a; Wu F. et al., 2016; Wu R. et al., 2016; Lyu et al., 2017a, Song et al., 2017; Lyu et al., 2019). The considerable loadings of *i/-n*-pentanes and n-hexane and moderate amount of C_2 hydrocarbons suggested the second source as gasoline exhaust (Liu et al., 2008c; Ho et al., 2009; Ling and Guo et al., 2014; Lyu et al., 2019). The third source containing moderate levels of heavy hydrocarbons (C_6-C_{10}), benzene and high percentages of C_2-C_3 hydrocarbons especially alkenes, which was defined as diesel exhaust (Schauer et al., 1999; Liu et al., 2008b, 2008c; Sahoo et al., 2011; Lyu et al., 2019). Considering the great amount of 1,3-butadiene and styrene, and moderate loadings of aromatics, the fourth source was assigned to industrial emissions (Liu et al., 2008b, 2008c; Knighton et al., 2012; Jones, 2014). The fifth source was more related to solvent usage because of the high levels of C_7-C_9 aromatics (Yuan et al., 2010; Ling and Guo, 2014; Shao et al., 2016). Lastly, the source of biogenic emission was identified due to the dominance of isoprene in factor 6 (Guenther, 2006).

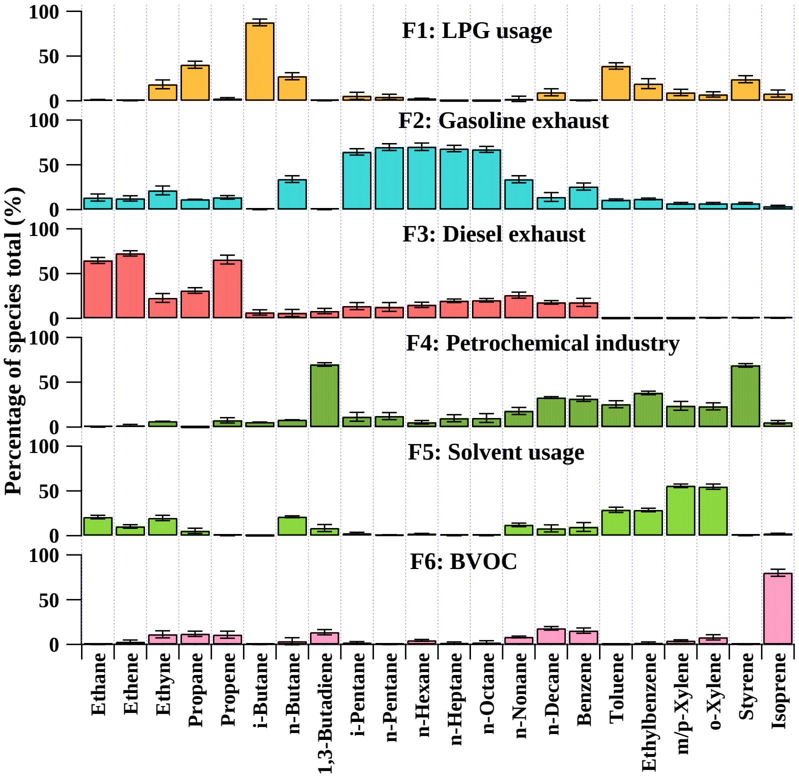

Figure 4.5 Average profile of the six sources in the five cities extracted from PMF.

4.4.2 Source contribution to VOCs and O_3 production

Table 4.6 presents the contribution of each source to ambient VOC mixing ratios and to the O_3 mixing ratios in the five cities. Note that the uncertainty of each value was at a considerable level (*i.e.*, at an average of 35.2% of their mean values), which may be due to the limited number of VOC samples collected in each city. Among the six VOC sources, vehicular exhausts, including gasoline exhaust and diesel exhaust, contributed the most to VOC mixing ratios in all the five cities (34.7-51.0%), followed by solvent usage (12.1-24.0%), industrial processes (10.8-22.8%) and LPG usage (10.7-20.2%). Elevated contribution of vehicle exhausts to ambient VOCs (27-62%) has been widely reported in NCP (Yuan et al., 2009; Han et al., 2015; Wang G. et al., 2016; Song et al., 2019), YRD (Wang et al., 2013; An et al., 2017; Liu Y. et al., 2019) and Sichuan Basin (SCB) regions (Zhang J. et al., 2014; Li J. et al., 2018). Apart from traffic related sources, solvent usage was the second VOC source in Shanghai and Chengdu, which was consistent with the previous studies, in which solvent usage contributed 19-32% in Shanghai (Cai et al., 2010; Wang H. et al., 2013; Liu Y. et al., 2019) and 13-23.7%

in SCB region (Zhang J. et al., 2014; Li J. et al., 2018). In comparison, Lanzhou had the largest industrial emissions (22.8±10.8%) among the five cities, consistent with the contribution of 23.2% reported by Jia et al. (2016). Compared to anthropogenic sources, the contribution of biogenic emissions (5.8-15.3%) was least except for Beijing (15.3%).

In terms of the contributions of the six sources to the O_3 production in each city, it was found that solvent usage was the largest contributor to O_3 production in Shanghai, Chengdu and Wuhan, while diesel exhaust and solvent usage made similar contributions in Beijing, and diesel exhaust, industrial emissions and solvent usage equally contributed to O_3 production in Lanzhou. In addition, the contribution of biogenic emission to O_3 production in Beijing, Wuhan and Chengdu was more obvious than that of other sources.

Table 4.6 Source contributions to VOC mixing ratios and O_3 production in the five cities.

Sources	LGP usage	Gasoline exhaust	Diesel exhaust	Industrial emissions	Solvent usage	BVOC
Contribution to VOCs mixing ratio (%)						
Beijing	10.7±5.4	17.4±5.1	33.6±12.0	10.8±3.9	12.2±4.5	15.3±3.1
Shanghai	13.0±6.3	16.4±4.3	26.1±5.6	15.8±5.0	24.0±3.2	4.7±1.5
Wuhan	20.2±10.2	21.6±10.1	24.2±12.2	14.5±5.9	12.3±3.6	7.3±1.4
Chengdu	16.2±12.5	11.6±4.7	23.1±21.1	18.5±11.6	20.4±4.6	10.3±6.3
Lanzhou	15.2±9.1	24.0±9.4	20.1±7.5	22.8±10.8	12.1±5.7	5.8±1.7
Contribution to O_3 production (%)						
Beijing	5.8±1.0	3.2±3.0	33.4±2.6	11.1±4.4	28.7±2.6	17.8±3.3
Shanghai	11.2±3.1	13.4±5.2	16.3±3.7	13.9±10.3	37.1±3.7	8.1±2.3
Wuhan	17.1±3.1	6.0±3.6	13.2±1.2	15.5±6.2	28.9±2.7	19.3±3.9
Chengdu	9.0±1.4	2.6±2.7	15.0±0.4	21.1±6.1	36.4±3.3	15.9±2.6
Lanzhou	6.8±1.0	5.5±5.3	29.2±2.7	30.2±3.3	22.2±4.6	6.1±1.1

4.5 Potential control measures for O_3 pollution

4.5.1 O_3-precursor relationship

Figure 4.6 shows the average integrated RIR values of O_3 precursors on all the VOC sampling days in the five cities. The local O_3 formation in Shanghai, Wuhan and Chengdu was limited by VOCs (in particular AVOCs), whereas the negative RIRs of NO_x indicated that cutting NO_x

would cause the increase of O_3. In Lanzhou, the local O_3 formation was co-limited by VOCs and NO_x, but more sensitive to the variations of VOCs. In Beijing, the NO_x reduction led to either increase or decrease of O_3 formation on different sampling days given the RIR values ranged from positive to negative values, implying the complexity of local O_3 formation in these five cities. Among different anthropogenic VOC (AVOC) groups, it was found that O_3 formation was more sensitive to OVOCs in Beijing and Wuhan, accounting for 46.7% and 35.6% of the total RIRs of AVOCs, respectively, while aromatics and OVOCs made comparable contributions in Shanghai (aromatics: 28.4%; OVOCs: 29.5%) and Chengdu (aromatics: 33.2%; OVOCs: 30.9%). In Lanzhou, alkenes made the largest contribution (43.1%) to the total RIR value of AVOCs, followed by aromatics (29.6%). In comparison, cities in south part of China (southwestern China, eastern China and central China), *i.e.*, Chengdu, Shanghai and Wuhan, had relatively larger RIR values of biogenic VOCs (BVOCs), indicating the higher vegetation emissions of BVOCs in the summer in the lower mid-latitude areas of China.

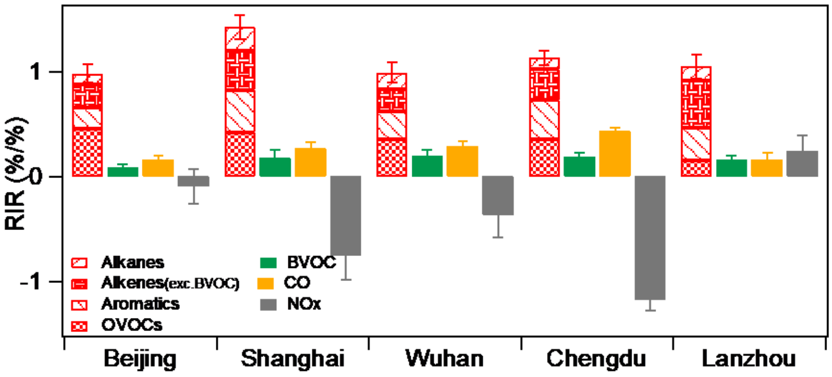

Figure 4.6 Average integrated RIR values of O_3 precursors, *i.e.*, AVOCs, BVOCs, CO and NO_x on all VOC sampling days in the five cities. AVOCs are further categorized into alkanes, alkenes (excluding BVOCs), aromatics and OVOCs, which refer to the 18 C_2-C_{10} alkanes, 13 C_2-C_7 alkenes and alkynes, 10 C_6-C_9 aromatics and 4 C_1-C_3 OVOCs, respectively. BVOCs include isoprene and α-/β-pinenes.

Since O_3 formation was more sensitive to VOCs in all cities, the relative importance of VOC species in O_3 formation was further examined. Figure 4.7 shows the average RIR values of top 13 VOCs in each city, including 12 AVOCs and isoprene. The summed RIR values of the 13 VOCs occupied 75.7 - 96.8% of the overall RIR values in the five cities, highlighting the dominant role of a small number of VOC species in local O_3 formation. It was found that among the AVOC species, formaldehyde, acetaldehyde and xylenes had high RIR values in all the five cities, except for acetaldehyde in Lanzhou. In addition, propene had the third largest RIR values among all VOC species in Beijing and Lanzhou. Moreover, trimethylbenzenes and 1-butene were also the key VOC species contributing to O_3 formation in Shanghai.

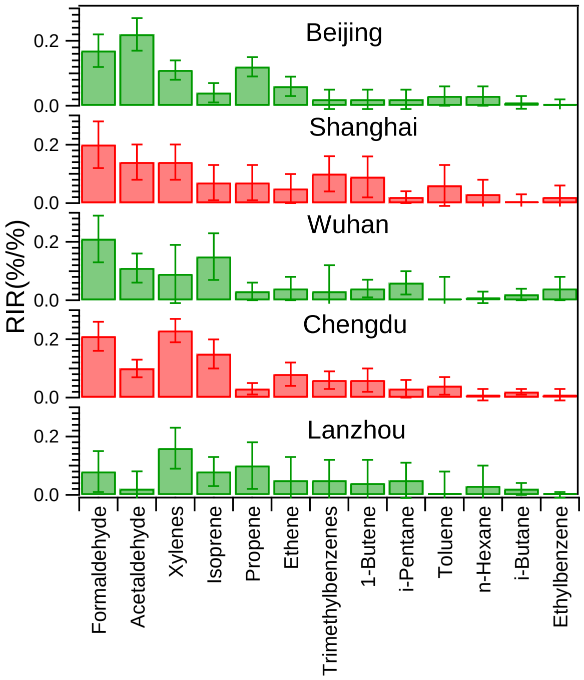

Figure 4.7 Average RIR values for individual VOC species in the five cities.

4.5.2 O_3 control measures

Figure 4.8 shows the average isopleth of daily maximum O_3 mixing ratios within the cutting range of 0-100% of VOCs and NO_x on O_3 episode days in the five cities. Specifically, during the sampling period, there were 5, 0, 2, 3 and 4 O_3 episode days captured in Beijing, Shanghai, Wuhan, Chengdu and Lanzhou, respectively. In each city, the diurnal profiles of O_3 precursors on all O_3 episode days were input into the PBM-MCM to simulate the O_3 formation as the base case. Then, the O_3 formation in different scenarios was simulated by cutting the mixing ratios of VOCs and NO_x at different ratios between 0 and 100%. Finally, the average isopleth of each city was produced based on the daily maximum O_3 values in base case and different scenarios. Since no O_3 episode day was observed in Shanghai during this sampling period, the average profile of all VOC sampling days in Shanghai was applied instead. It was found that on high

O_3 days, O_3 formation in Chengdu and Shanghai was VOCs-limited, while O_3 was co-limited by both VOCs and NO_x in Beijing, Wuhan and Lanzhou. Cutting VOCs would be more effective than cutting NO_x in Beijing and Wuhan, while reducing either VOCs or NO_x would effectively lower O_3 formation in Lanzhou. In Chengdu and Shanghai, the results suggested controlling VOCs be effective to mitigate O_3 formation, whereas reducing NO_x too fast would result in more locally produced O_3. Therefore, cutting VOCs and NO_x with a ratio of larger than 1:1 and 1:1.5 were suggested for O_3 alleviation in Shanghai and Chengdu, respectively.

(a) VOC-limited:

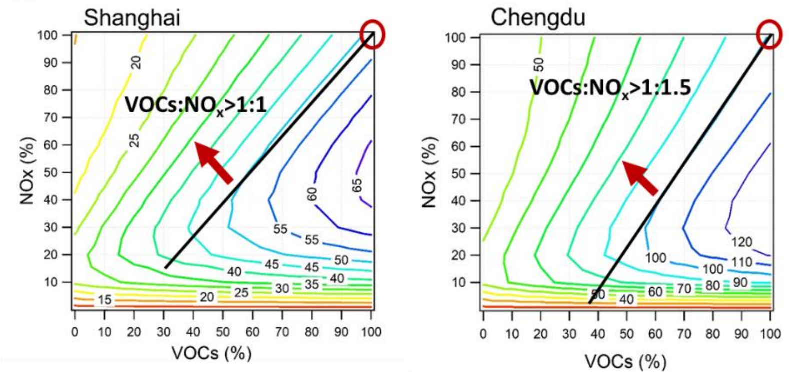

(b) Co-limited by both VOCs and NO$_x$:

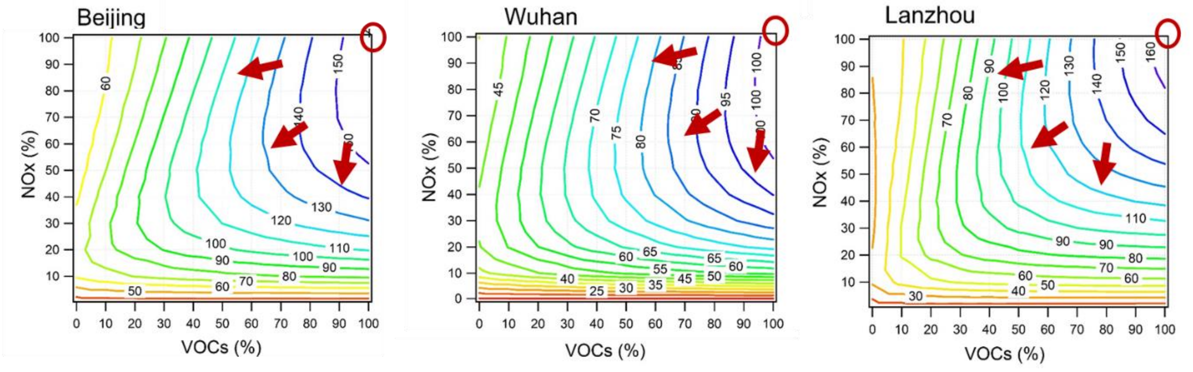

Figure 4.8 Average isopleths of the daily maximum O_3 mixing ratios within the cutting range of 0-100% of VOCs and NO_x on episode days in the five cities. The black lines represent the lowest suggested cutting ratios of VOCs/NO_x in Shanghai and Chengdu, respectively. The red circles show the present O_3 formation regime before implementing control strategies. The red arrows indicate the suggested scenarios to cut O_3 precursors for O_3 alleviation in each city.

4.6 Summary

Through concurrent sampling campaigns in the five Chinese megacities in summer 2018, it was found that O_3 pollution was more severe in northern and central China, *i.e.*, Beijing, Lanzhou and Wuhan. Most pollutants were at the lowest level in Shanghai due to the abnormally frequent tropical cyclones in the East China Sea. In northern China, *i.e.*, Beijing and Lanzhou higher VOC concentrations were found as well. Among these five cities, alkanes and/or OVOCs were the main contributors to TVOCs.

Among the VOC groups, aromatics and OVOCs were the largest contributors and made comparable contributions to O_3 formation in Chengdu and Shanghai, mainly dominated by xylenes, formaldehyde and acetaldehyde, while OVOCs contributed the most in Beijing and Wuhan. Alkenes, *i.e.*, isoprene and propene, caused more O_3 formation in Lanzhou. Model simulations revealed that the net O_3 production rate in Lanzhou (8.9±1.7 ppbv h^{-1}) was the largest, followed by Beijing (6.4±1.3 ppbv h^{-1}) and Wuhan (5.8±1.2 ppbv h^{-1}), while it was the lowest in Shanghai (2.8±0. 7 ppbv h^{-1}) ($p < 0.05$). In addition, the simulated RO_x (= $OH+HO_2+RO_2$) concentrations were comparable ($p>0.1$) in Lanzhou ((5.9±1.1) $\times10^8$ molecules cm^{-3}), Beijing ((5.3±1.1) $\times10^8$ molecules cm^{-3}) and Wuhan ((4.3±1.0) $\times10^8$ molecules cm^{-3}), which were significantly higher ($p < 0.05$) than those in Shanghai ((2.7±0.9) $\times10^8$ molecules cm^{-3}) and Chengdu ((1.8±0.7) $\times10^8$ molecules cm^{-3}), implying stronger atmospheric oxidative capacity and severer O_3 pollution in northern and central China in summer.

In this study, six VOC sources were identified in the five cities, among which vehicular emissions, consisting of gasoline and diesel exhausts, contributed the most to ambient VOCs. VOCs from vehicular emissions were more abundant in central and northern/northwestern China, *i.e.*, Beijing, Wuhan and Lanzhou, while VOCs from solvent usage were relatively higher in Shanghai and Chengdu. Instead, solvent usage made the largest contributions to O_3 formation in all the five cities, except for diesel exhaust in Beijing that was equally the largest contributor to solvent usage. Moreover, diesel exhaust, industrial emissions and solvent usage made similar contributions in Lanzhou.

Ozone (O_3) formation in Shanghai and Chengdu was typically limited by VOCs with the suggested VOC to NO_x cutting ratios over 1:1 and 1:1.5, respectively, while it was co-limited by both VOCs and NO_x in Beijing, Wuhan and Lanzhou on O_3 episode days. Specifically, cutting VOCs would be more effective than cutting NO_x in Beijing and Wuhan, while reducing either VOCs or NO_x would effectively mitigate O_3 production formation in Lanzhou. The findings are valuable for the cities to formulate and implement appropriate control measures on O_3 precursors.

Chapter 5 Photochemistry of ozone pollution in autumn in Pearl River Estuary of South China

5.1 Introduction

Tropospheric ozone (O_3), as a secondary pollutant and an important component of photochemical smog, not only adversely affects human health, ecosystems, climate change and air quality, but also plays a crucial role in atmospheric chemistry (Chameides et al., 1999; Atkinson et al., 2000; Bell et al., 2004, 2007; Ashmore, 2005; Thompson et al., 2011). With rapid industrialization and urbanization in the past three decades, the increasing emissions of O_3 precursors, *i.e.*, nitrogen oxides ($NO_x = NO + NO_2$) and volatile organic compounds (VOCs), have led to more severe O_3 pollution in the near-surface atmosphere and hence aroused increasing attention from international authorities (NRC, 1992; NARSTO, 2000; Oltmans et al., 2004; Monks et al., 2015). Subsequently, O_3 pollution has been widely studied in North America (Chin et al., 1994; Cooper et al., 2010), Europe (Solomon et al., 2000; Guerreiro et al., 2014) and Asia (mainly in China) (Guo et al., 2017; Wang T et al., 2017; Lu X. et al., 2019). Although O_3 pollution has been mitigated in some cities of North America and Europe (*e.g.*, Derwent et al., 2013; Simon et al., 2015; Lin et al., 2017), due to the non-linear relationship between O_3 and its precursors, the O_3 pollution problem is still severe, particularly in developing countries such as China (Guo et al., 2017; Wang T et al., 2017; Zheng et al., 2018) and India (Lu et al., 2018; Gao et al., 2020).

The Pearl River Delta (PRD) region including Hong Kong, one of the most developed regions in China with dense population, transportation and industry, has been suffering from severe photochemical pollution for many years (Guo et al., 2009; Xue et al., 2014b; Lu et al., 2019; Liu X. et al., 2019). Despite extensive studies of O_3 pollution in urban and industrial areas in inland PRD (*e.g.*, Zhang et al., 2008; Shao et al., 2009a; Lu et al., 2010; Wang X. et al., 2010; Zou et al., 2015; Ou et al., 2016) and in Hong Kong (Guo et al., 2009, 2013a; Lam et al., 2013; Ling and Guo, 2014; Xue et al., 2014b, 2016; Wang H et al., 2018; Liu X. et al., 2019), a handful of studies focused on comprehensive O_3 photochemistry particularly during high O_3 episodes in the Pearl River Estuary (PRE) (Cheng et al., 2010; Wang Y et al., 2018, 2019;

Zeren et al., 2019). The PRE is a key area in southern China with heavy O_3 pollution despite sparse on-site anthropogenic emissions. Cheng et al. (2010) investigated the contemporary photochemistry on inner bank and east bank of the PRE using an observation-based model. The dynamics and brief photochemistry in the PRE were outlined by Zeren et al. (2019) who proved that O_3 and its precursors were easily transported to and accumulated in this area, especially when the region suffered from typhoons or continental anticyclones. Both previous studies, however, are lack of species-based photochemistry.

In this study, comprehensive measurement data were simultaneously collected on the west and east banks of PRE in autumn 2016. Through detailed data analysis with the application of numerical models, the sensitivity of O_3 formation to its precursors, and the dominant formation and loss pathways of O_3 and radicals were investigated. The impacts of major VOC species on O_3 formation pathways were also quantified. To my best knowledge, this is the first attempt to explore detailed photochemical mechanisms in the PRE, especially on high O_3 episode days. The findings will help improve the understanding of O_3 photochemistry in the PRD region and guide local governments to develop appropriate O_3 pollution control strategies.

5.2 General features

Table 5.1 presents the descriptive statistics of O_3, CO, SO_2, NO, NO_2, TVOCs and meteorological parameters during daytime hours (07:00-19:00 LT) in patterns 1 and 2 at QA and TC sites. Here, patterns 1 and 2 mean the situations that both sites had high O_3 levels, and only QA presented high O_3 values, respectively. TVOC refers to the 48 measured/corrected simulated VOC and OVOC species (Table 5.2). In pattern 1, though the average O_3 mixing ratio at TC was comparable to that at QA ($p = 0.21$), the maximum hourly O_3 level was higher at TC. For the precursors, the mixing ratios of CO and TVOCs were similar ($p = 0.12$ and 0.17, respectively) at both sites while NO_x value at QA was much lower than that at TC ($p < 0.05$), mainly due to more vehicular emissions at TC. In addition, lower wind speed, lower relative humidity, and stronger solar radiation were found at TC ($p < 0.05$), facilitating more intense local photochemistry there. In pattern 2, both the daytime average and maximum hourly O_3 mixing ratios were much higher at QA than at TC ($p < 0.05$), while the TVOCs were higher at

QA than at TC, and NO_x was opposite ($p < 0.05$). Furthermore, more frequent northeasterly winds were observed at QA, while more clean coastal air arrived at TC (Zeren et al., 2019).

In comparison, the daytime average O_3 levels in pattern 1 and pattern 2 at QA were similar ($p = 0.35$), whereas the maximum hourly O_3 value was higher in pattern 2; however, TC had higher average O_3 level ($p < 0.05$) in pattern 1 than in pattern 2, so was the maximum hourly O_3. Besides, in both patterns at QA, high O_3 episode days were captured while at TC nonattainment days were only observed in pattern 1 and no O_3 episode days were identified in pattern 2, reflecting potentially different mechanisms of O_3 formation in different patterns at different sites. Moreover, higher temperature in pattern 1 ($p < 0.05$) was found, implying a more favourable meteorological condition for local photochemical O_3 formation than in pattern 2.

Compared to previous studies, the levels of NO and NO_2 measured at QA and TC were consistent with those reported at non-urban sites in inland PRD region (Cheng et al., 2010; Zou et al., 2015; Wang Y. et al., 2018) and TC (Wang H. et al., 2018; Lyu et al., 2018; Liu X. et al., 2019), respectively. For VOCs/OVOCs, the mixing ratios of the observed TVOCs at both sites were between the values found in the previous studies. At TC, Wang H et al. (2018) indicated TVOC level of 32.2 ± 1.7 ppbv (48 VOCs: 20.2±2.2 ppbv, 4 OVOCs: 12.0±1.3 ppbv) on O_3 episode days in 2013, and Liu X. et al. (2019) found the TVOC levels (44 VOCs and 4 OVOCs) ranged from 21.1 – 49.7 ppbv in autumn 2007-2016, while Zou et al. (2015) reported the TVOC (55 VOCs) values of 37.6 - 63.6 ppbv in autumn 2011 in suburban PRD.

Table 5.1 Descriptive statistics of air pollutants and meteorological parameters during daytime hours (07:00-19:00 LT) in pattern 1 and pattern 2 at QA and TC (unit of air pollutants: ppbv; 95% C.I.: 95% confidential interval).

Pattern 1	QA		TC	
	Average±95% C.I.	Maximum	Average±95% C.I.	Maximum
O_3	66.6±11.4	118.2	58.4±13.8	140.2
CO	882.6±44.4	1240.2	848.7±39.3	1127.1
NO	3.4±1.9	24.1	12.4±5.2	75.0
NO_2	9.8±2.8	28.4	42.4±5.3	75.0
SO_2	3.9±0.8	10.9	6.5±1.1	18.3
TVOCs	48.9±12.5	99.7	40.5±11.6	82.5
Wind speed (m s^{-1})	4.5±0.9	9.7	1.4±0.4	3.8
Temperature (℃)	30.0±1.1	35.7	30.4±0.8	35.0
Solar radiation (W m^{-2})	219.0±32.3	525.0	284.9±33.5	738.0
Relative humidity (%)	88.7±3.6	98.0	72.6±3.8	91.5
Pattern2	QA		TC	
	Average±95% C.I.	Maximum	Average±95% C.I.	Maximum
O_3	61.9±5.8	150.2	30.0±3.5	92.2
CO	749.9±19.3	1310.6	755.9±17.2	1127.1
NO	4.0±1.2	34.2	16.8±3.0	94.6
NO_2	11.3±1.3	52.3	28.9±2.3	103.2
SO_2	5.5±0.7	39.0	3.5±0.2	10.7
TVOCs	24.2±1.2	50.1	16.3±1.9	55.8
Wind speed (m s^{-1})	3.8±0.3	7.9	0.9±0.1	4.3
Temperature (℃)	25.7±0.4	31.9	27.0±0.4	32.0
Solar radiation (W m^{-2})	253.4±35.7	727.0	263.1±36.6	829.0
Relative humidity (%)	78.5±1.2	97.0	72.7±1.2	94.5

Table 5.2 Descriptive statistics of VOC and OVOC mixing ratios measured at QA and TC on 8-episode days in pattern 2. The 95% C.I. and Max. denote the 95% confidence interval and maximum of the mixing ratios of VOC and OVOC species, respectively (Unit: pptv).

VOC species	QA			TC		
	Mean	95%C.I.	Max.	Mean	95%C.I.	Max.
Ethane	1649.2	105.1	3979.6	1998.1	143.3	3951.1
Ethene	1146.3	81.4	2293.1	1140.8	158.2	4335.5
Ethyne	749.8	54.7	1733.7	1702.5	151.8	4254.6
Propane	2805.3	242.4	7030.5	3165.7	438.6	13269.8
Propene	145.5	13.8	351.6	220.7	26	773.6
i-Butane	2057.1	209.4	7263.8	1048.3	124	3229.9
n-Butane	3751.3	360.7	9575.1	1723	214.5	5001.2
1-/i-Butene	480.1	29.5	1110.6	98.7	9.7	292
trans-2-Butene	212	3.4	317.1	11.4	1.9	52.7
cis-2-Butene	88.9	3.2	149.8	7.8	1.5	48
3-methyl-1-Butene	4.9	1.4	28.7	6.2	3.1	56.5
2-methyl-1-Butene	15.5	3.2	60.6	9.3	2.1	58
cis-2-Pentene	52.5	5.4	261.4	3.5	1.2	20
2-methyl-2-Butene	24.1	3.6	109.3	9	2.2	27.5
Butyne	84.3	16.6	534.5	21.5	4	76.2
i-Pentane	693.7	59.1	1694.9	548.5	58.5	1681.3
n-Pentane	456.8	54.6	1572.9	317.8	41.5	1076.9
1-Pentene	36.9	8.9	210.6	17.2	4.7	174
trans-2-Pentene	20.9	5.2	51.1	7.8	2.6	40.8
2-Methylpentane	385.5	39.5	1060.6	269.1	55.5	1171.7
n-Hexane	528.7	46	1092.5	224.4	52.3	1426.7
n-Heptane	413	10.3	610.1	77.7	10.5	290.8
n-Octane	260.1	6.6	424	35.3	5.2	153.2
2,2-Dimethylbutane	37.9	3.1	96.3	24.5	4.6	91.9
2,3-Dimethylbutane	86.9	7.4	226.7	57.5	12.7	262.2
3-Methylpentane	260.8	27.6	753.6	184.9	40.6	1025.8
Cyclohexane	60.2	4.3	159.4	76.8	13.8	281.4
2-Methylhexane	808	117.9	3497.4	183.1	22.9	318.8
3-Methylhexane	404.5	12	695.6	54.9	12.3	271.4
n-Nonane	238.6	8.6	490.6	41.3	9.8	443.7
n-Decane	217.2	12.2	544.3	35.3	5.2	153.2
Isoprene	710.9	75.5	1595	446.2	82.5	3122
α-Pinene	124.8	5.3	284.7	19.9	5.3	218

β-Pinene	109.5	9.4	352.2	9.4	1.2	32
Benzene	537.7	34.6	1057.7	296.7	23.8	568
Toluene	2119.5	264.4	6496.3	1493.7	425.2	13376.1
Ethylbenzene	481.5	62.5	2032.7	247.1	42.6	1350.3
m/p/o-Xylenes	1354.5	157	5629.9	532.7	79.4	2492.1
1,3,5/1,2,4/1,2,3-Trimethylbenzenes	494.1	61.8	2844.5	74.6	15.4	556.6
i-Propylbenzene	78.2	14.9	538.4	8.9	1.6	63.1
n-Propylbenzene	158.5	24	1007.9	15.9	4.3	188.6
3-Ethyltoluene	148	21.6	833.1	28.5	5.3	171.5
4-Ethyltoluene	214.6	20.8	922.5	20.4	5	220.2
2-Ethyltoluene	157.3	14.5	575.3	17.5	4.5	186.2
Formaldehyde	4491.8	349.6	8318.7	3121.1	359.6	8743.3
Acetaldehyde	1681.5	270.7	6995.2	827.8	136.6	3126
Acetone	3543.7	316.6	8278.9	6007.8	744.4	12907.7
Propionaldehyde	532	753.9	2402	22.1	21.7	591.3

5.3 Relationships between O_3 and its precursors

5.3.1 Average RIRs of O_3 precursors in the two patterns

Figure 5.1 shows the average integrated RIR values of O_3 precursors in pattern 1 ((a)-(b)) and pattern 2 ((c)-(d)) at both sites. In pattern 1, the RIR values of anthropogenic VOC (AVOC), biogenic VOC (BVOC, including isoprene and α-/ β-pinenes) and CO were positive while it was negative for NO_x at TC, indicating that the O_3 formation was VOC-limited. This is in line with previous studies (Cheng et al., 2010; Wang Y et al., 2017). In contrast, the RIRs of all pollutants including NO_x were positive at QA, suggesting that both VOCs and NO_x constrained O_3 formation. Similar to pattern 1, the O_3 formation was VOC-controlled in pattern 2 at TC, while it was in the VOC-limited regime with tiny RIR of NO_x (*i.e.* cutting NO_x would not affect O_3 mixing ratio significantly) at QA. The different control regimes found in different patterns at different sites revealed the sophisticated mechanisms of O_3 formation in the PRE.

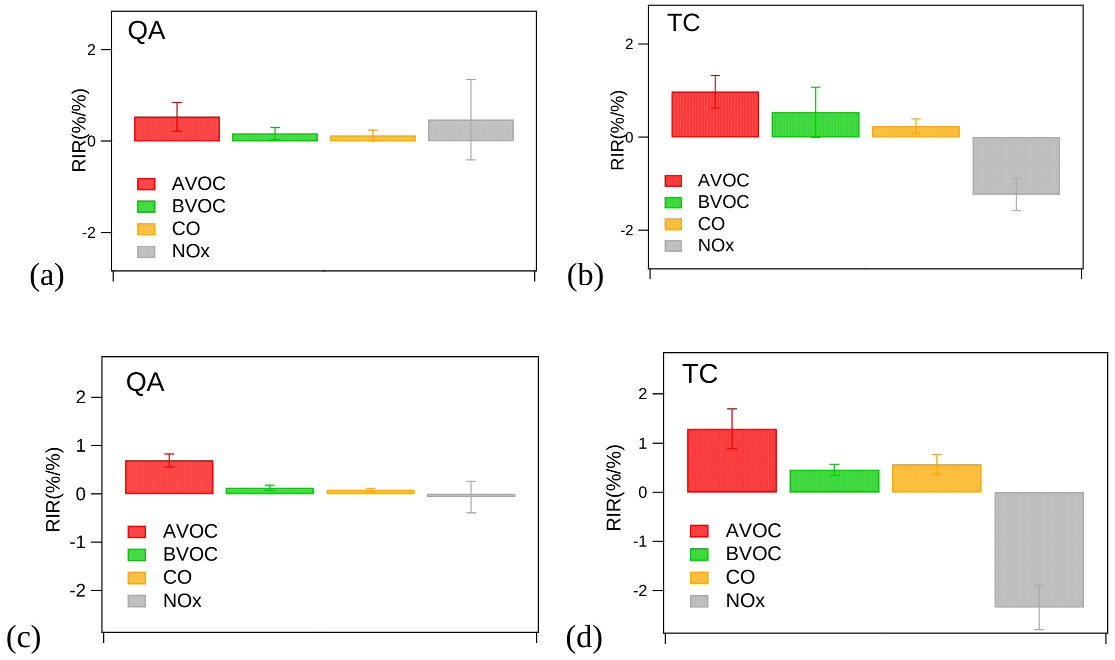

Figure 5.1 Average integrated RIRs of AVOC, BVOC, CO and NO_x at (a) QA and (b) TC in pattern 1, and (c) QA and (d) TC in pattern 2. Error bars represent the 95% C.I. of each value, which are relatively large due to limited number of days in each pattern.

To further understand the relationships of O_3 with its precursors, the integrated RIRs of precursors on each VOC sampling day in the two patterns at both sites are given in Figure 5.2. In pattern 1, the RIR patterns on each day were similar to the average RIR mode at TC, except for the high RIR of BVOCs on Oct. 20, implying the important role of BVOCs in producing local O_3 on that day. However, the different RIR values of NO_x on different days at QA indicated that the O_3 formation mechanism varied even at the same site. The positive RIR of NO_x on Sep. 26 was much higher than that of AVOCs/BVOCs at QA, implying that cutting NO_x would be more effective than reducing VOCs to mitigate O_3 formation even though it was co-limited by VOCs and NO_x. In contrast, cutting VOCs was more efficient on Sep. 27 and Oct. 20 at QA given higher RIR values of AVOCs/BVOCs. Moreover, the negative RIR of NO_x on Oct. 20 at QA implied that cutting NO_x did not mitigate O_3 but increased O_3.

In pattern 2, the RIRs of VOCs and NO_x were positive on October 14-16 while RIRs of NO_x were negative on the other days at QA. It is noteworthy that the PRE experienced a tropical cyclone on October 14-16, which led to the northeasterly winds. Thus, both sites received the air masses parallel to each other from the northeast (Zeren et al., 2019). The air arrived at TC was mostly from the coastal regions which mixed the local fresh emissions of precursors (average NO_x: 26.79 ppb; TVOC/NO_x: 0.51), causing lower O_3 with VOC-limited regime (Guo et al., 2009; Wang H et al., 2018), while the air reached the QA was mainly from polluted inland areas with aged continental air with low NO_x values (average NO_x: 10.0 ppb; TVOC/NO_x: 3.04) due to its short lifetime, shifting to transitional regime. In comparison, on the other O_3 episode days, the PRE was under control of continental anticyclones, leading to the VOC-limited regime at both sites but the O_3 formation was more sensitive to VOCs and NO_x on the five episode days with continental anticyclones at TC.

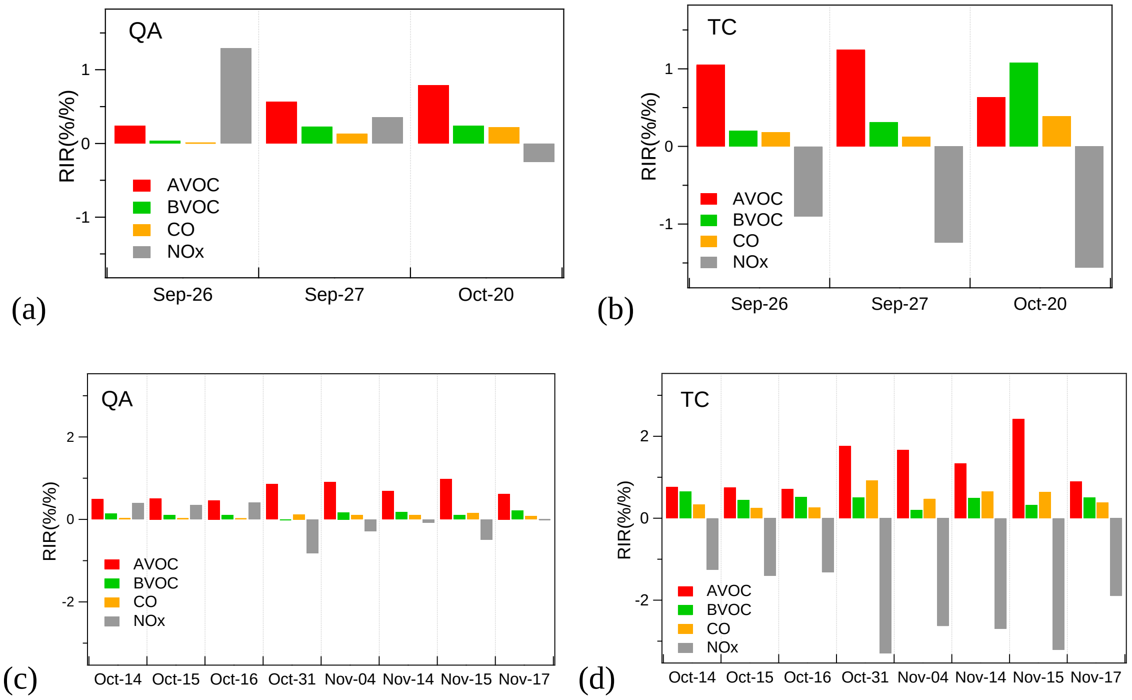

Figure 5.2 Simulated average integrated RIRs on each VOC sampling day at (a) QA and (b) TC in pattern 1, and (c) QA and (d) TC in pattern 2. Since there is only one integrated RIR value for each sampling day, no error bar is shown for each RIR.

5.3.2 Diurnal variations of RIR values of O_3 precursors

Due to the potential changes of O_3 formation mechanisms in a diurnal cycle driven by the changes in the profile of O_3 precursors, analysis was given to the diurnal patterns of the RIRs of O_3 precursors on the VOC sampling days in patterns 1 and 2 at both sites (Figure 5.3). Positive RIRs of VOCs and CO and negative RIRs of NO_x were determined in the daytime (07:00-16:00 LT) in both patterns at TC, indicating consistent VOC-limited regime in O_3 formation. However, the diurnal patterns were different at QA. In pattern 1, most of the RIRs of O_3 precursors were positive except the morning negative values of NO_x, implying the transition from VOC-limited regime in the morning to co-limited regime in the afternoon. Interestingly, the RIRs of VOCs were much higher than those of NO_x in the morning, and the RIRs of VOCs gradually decreased while they increased for NO_x from morning to afternoon, suggesting that cutting VOCs would be more efficient to O_3 reduction in the morning whereas it was opposite in the afternoon (Figure 5.3 (a)). Similarly, in pattern 2, O_3 formation was limited by VOCs in the morning, and switched to the co-limited (transitional) regime in the afternoon, revealing that O_3 formation mechanisms could be diverse within a day (Figure 5.3

(b)). The reasons could be owing to the fresh emissions of NO_x from nearby ships and local scattered vehicular emissions/household combustion activities in the morning, which were reduced through photochemical consumption, atmospheric dispersion and dry deposition in the afternoon. Similar phenomena were found in other regions (Zou et al., 2015; Jia et al., 2016; Yang et al., 2019). In summary, in both patterns at QA and TC sites, cutting VOCs always helped mitigate O_3 formation, while reducing NO_x would increase the O_3 at TC but decreased O_3 in the afternoon at QA.

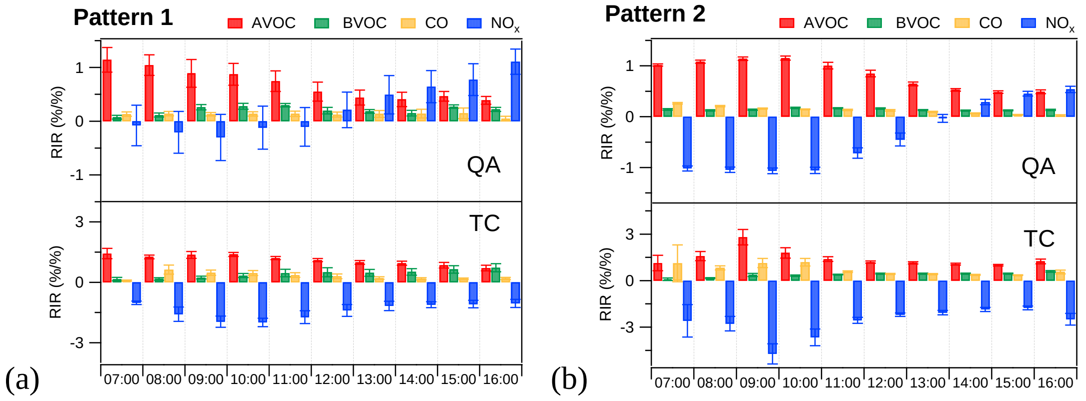

Figure 5.3 Average diurnal variations of RIR values of O_3 precursors at QA and TC in (a) pattern 1 and (b) pattern 2.

5.3.3 Relative importance of VOCs in O_3 formation

Figure 5.4 shows the top 10 RIRs of VOCs, including 9 AVOCs and isoprene, in patterns 1 and 2 at both sites. The summed RIR values of the top 10 VOCs occupied 74% and 83% of the overall RIR values at QA and TC, respectively, in pattern 1, and 82% at QA and 81% at TC in pattern 2, implying that the O_3 formation in PRE was dominated by a small number of VOCs, similar to previous studies in the region (Cheng et al., 2010; Ling and Guo, 2014; Wang Y et al., 2018). It was found that the top ten VOCs were the same in both patterns at the two sites including one alkane, two OVOCs, four aromatics and three alkenes. In both patterns, isoprene, formaldehyde, xylenes and trimethylbenzenes were the top four species at QA while they were isoprene, formaldehyde, xylenes and toluene at TC. Furthermore, the RIR values of all VOCs except trimethylbenzenes and 1-butene at TC were higher than those at QA for both patterns. The results implied that controlling these VOCs would be most effective to alleviate O_3 pollution at both sites regardless of patterns. In addition, the RIRs of OVOCs at TC were higher than those at QA in both patterns ($p < 0.05$), indicating the importance of OVOCs in O_3 formation at this suburban site.

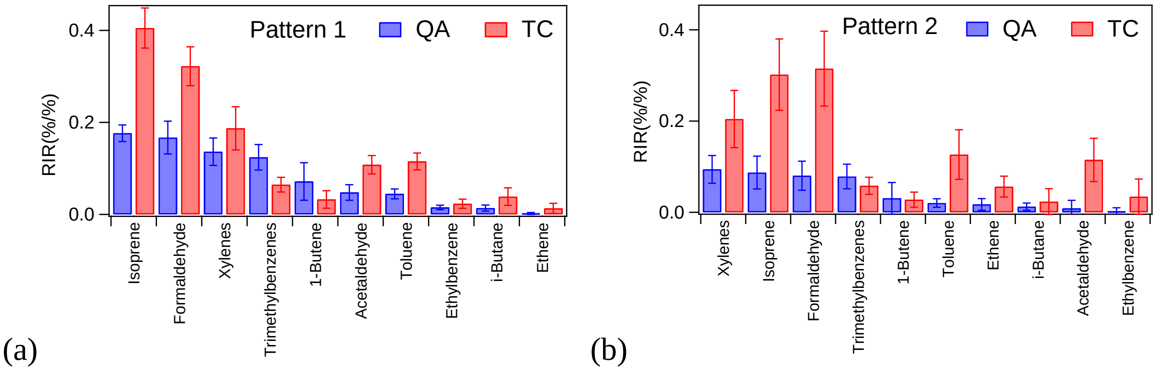

Figure 5.4 RIR values of Top 10 VOCs at both sites in (a) pattern 1 and (b) pattern 2. Error bars indicate the 95% C.I. of the average.

5.4 O_3 photochemistry

5.4.1 In-situ net O_3 production

Figure 5.5 displays the simulated O_3 production and destruction rates of main pathways at QA and TC in pattern 1 and pattern 2. In pattern 1, the net O_3 production rate at QA (13.1±1.6 ppbv h^{-1}) was comparable to that at TC (12.1±1.5 ppbv h^{-1}) ($p = 0.40$), suggesting similar oxidative capacity at both sites. The high values of net production rates indicated strong photochemical processes on both banks of the PRE in pattern 1. The leading production pathways were HO_2+NO and RO_2+NO at both sites, with similar percentage contributions of 49.9±6.0% at QA and 54.7±6.1% at TC for the former ($p = 0.31$) and 50.1±5.6% at QA and 45.3±5.3% at TC for the latter ($p = 0.45$) (Table 5.3). In contrast, the ruling O_3 destruction pathways at QA were OH+NO_2 (44.8±7.3%), followed by O_3 photolysis (22.0±3.4%) and O_3+VOCs (17.6±2.1%), while at TC OH+NO_2 (82.1±7.9%) dominated the O_3 destruction.

In pattern 2, however, the net O_3 production rate at QA (16.3±0.4 ppbv h^{-1}) was much higher than that at TC (4.7±0.2 ppbv h^{-1}) ($p < 0.05$), implying much stronger oxidative capacity on west bank of the PRE. The O_3 production pathways were dominated by HO_2+NO (QA: 51.6±1.3%; TC: 62.1±1.9%) and RO_2+NO (QA: 48.4±1.2%; TC: 37.9±1.2%), while the O_3 destruction was mainly due to the reaction between OH and NO_2 (QA: 56.0±1.5%; TC: 89.1±2.1%) (Table 5.3). In comparison, the average net O_3 production rates in both patterns were analogous to the levels reported in previous investigations in inland PRD region (1.8 – 39.0 ppbv h^{-1}) (Xue et al., 2014b; Wang Y. et al., 2018; Zeren et al., 2019) and in Hong Kong (1.6 – 16.9 ppbv h^{-1}) (Xue et al., 2016; Liu X. et al., 2019). However, only a handful of studies investigated the in-situ O_3 photochemistry at sites in inland PRE area. For example, Lu et al. (2012) applied an OBM coupled with RACM to simulate the net O_3 production rate and reported 10.7 ppbv h^{-1} during afternoon period (12:00 – 16:00 LT) in rural Guangzhou in summer 2006. Tan et al. (2019) found the daily maximum gross O_3 production rate of 22 ppbv h^{-1} in Heshan, Jiangmen in autumn 2014. Very limited studies probed into radical chemistry in inland cities of PRE, *e.g.*, Guangzhou, Dongguan, Zhongshan or Jiangmen. Most of the sites with in-depth photochemical O_3 studies were either coastal or remote island sites, such as Wan Qing Sha (WQS) in Guangzhou on north coast of PRE (Cheng et al., 2010), Wan Shan Island (WSI) in the South China Sea (Wang Y. et al., 2018) and QA and TC, at west and east banks of PRE (this study). It is suggested that more inland studies in PRE should be conducted in the future to gain complete knowledge in O_3 photochemical mechanisms in this region.

As the main O_3 production pathway, the RO_2+NO pathway contains more than 1000 different RO_2 radicals. To further understand the O_3 formation in the PRE, the top 10 pathways of RO_2+NO towards O_3 formation at both sites in pattern 1 and pattern 2 are listed in Table 5.4. In pattern 1, CH_3O_2+NO was the main pathway at both sites, followed by CH_3CO_3+NO, accounting for 23.4% and 18.1%, respectively (production rate: 1.5±0.1 ppbv h^{-1} and 1.2±0.2 ppbv h^{-1}, not shown in Table 5.4) of the total pathways of RO_2+NO at QA, and 22.2% (1.6±0.2 ppbv h^{-1}) and 16.6% (1.2±0.3 ppbv h^{-1}) at TC. The contributions of other pathways were all below or equal to 5.5% at both sites. In total, the top 10 production pathways of RO_2+NO accounted for 55.2% (3.6±0.4 ppbv h^{-1}) at QA and 56.3% (4.0±0.3 ppbv h^{-1}) TC, among which the reactions of C_1-C_2 radicals with NO dominated (45.4% and 44.3%, respectively), followed by the reactions between NO and C_3-C_5 radicals (8.7-10.6%) and the radicals generated from aromatic compounds (≤1.4%).

Similarly, in pattern 2, CH_3O_2 (23.1%) and CH_3CO_3 (18.1%) dominated the reactions between RO_2 and NO at QA, and at TC (29.5% and 20.7%, respectively). It is noteworthy that though the top 10 production pathways of RO_2+NO at TC accounted for a larger percentage (65.4%) than QA (55.9%) ($p < 0.05$), their overall reaction rates at TC (1.9±0.3 ppbv h^{-1}) were much lower than at QA (4.0±0.4 ppbv h^{-1}), indicating a much weaker local photochemical O_3 production through RO_2+NO pathways at TC in pattern 2, in line with the findings abovementioned in this study.

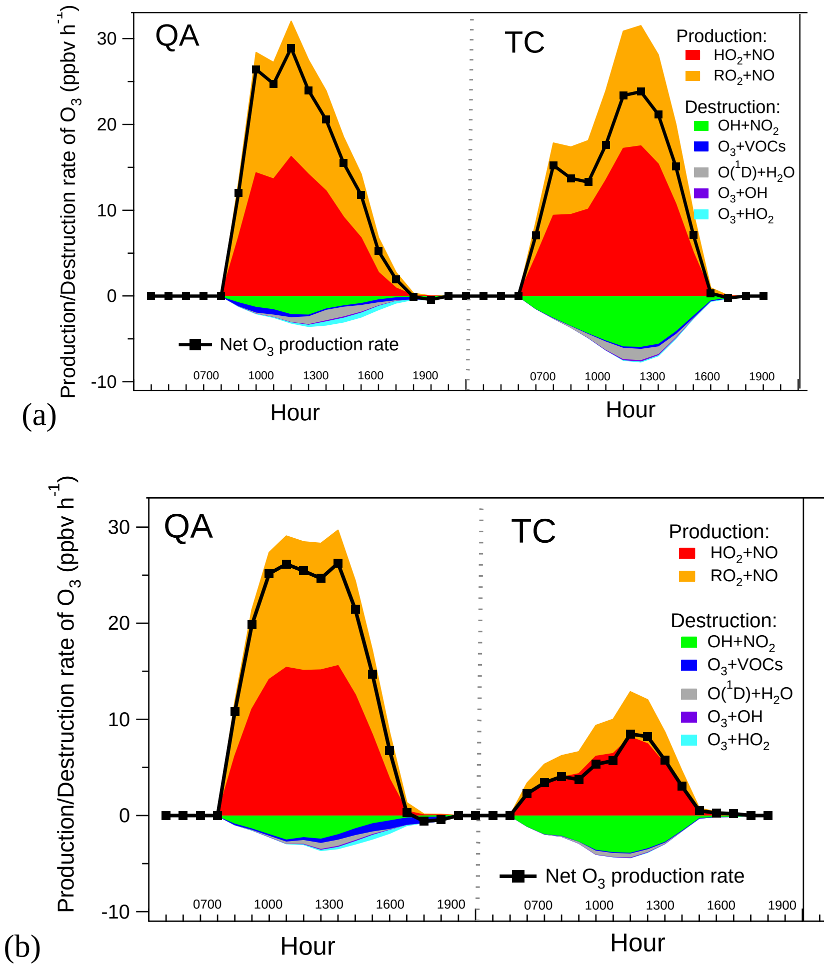

Figure 5.5 Simulated O_3 production and destruction rates of main pathways at QA and TC in (a) pattern 1 and (b) pattern 2.

Table 5.3 Production and destruction rates of main pathways to O_3 formation in pattern 1 and pattern 2 at both sites.

Site	Net O_3 production rate (ppbv/h)	Production pathways (ppbv h^{-1} (%))			Destruction pathways (ppbv h^{-1} (%))					
		HO_2+NO	RO_2+NO	Total O_3 production	OH+NO_2	O_3+VOCs	O^1D+H_2O	O_3+OH	O_3+HO_2	Total O_3 destruction
Pattern 1										
QA	13.1±1.6	7.5±0.9 (49.9±6.0%)	7.5±0.8 (50.1±5.6%)	15±1.7	-0.9±-0.1 (44.8±7.3%)	-0.3±-0.04 (17.6±2.1%)	-0.4±-0.1 (22.0±3.4%)	-0.05±-0.01 (2.4±0.4%)	-0.3±0.0 (13.28±1.9%)	-1.9±-0.2
TC	12.1±1.5	8.7±1.0 (54.7±6.1%)	7.2±0.8 (45.3±5.3%)	16±1.8	-3.1±-0.3 (82.1±7.9%)	-0.1±0.0 (3.5±0.4%)	-0.4±-0.1 (11.5±1.9%)	-0.05±-0.01 (1.3±0.2%)	-0.1±-0.01 (1.5±0.2%)	-3.8±-0.4
Pattern 2										
QA	16.3±0.4	9.5±0.2 (51.6±1.3%)	8.9±0.2 (48.4±1.2%)	18.4±0.5	-1.2±0.03 (56.0±1.5%)	-0.5±0.01 (23.0±0.5%)	-0.2±0.01 (11.0±0.4%)	-.05±0.001 (2.2±0.1%)	-0.2±0.01 (7.8±0.3%)	-2.1±0.04
TC	4.7±0.2	4.4±0.1 (62.1±1.9%)	2.7±0.08 (37.9±1.2%)	7.0±0.2	-2.1±0.05 (89.1±2.1%)	-0.06±0.002 (2.5±0.1%)	-0.2±0.01 (6.8±0.3%)	-0.02±0.001 (1.0±0.0%)	-0.01±0.001 (0.6±0.0%)	-2.3±0.06

Table 5.4 Top 10 pathways of RO_2+NO to O_3 production in pattern 1 and pattern 2 at QA and TC sites.

Pattern 1						
	QA site			TC site		
No.	Radical name in MCM	Structure	Classification (Proportion)	Radical name in MCM	Structure	Classification (Proportion)
1	CH_3O_2	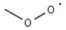	C_1 (23.4%)	CH_3O_2	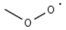	C_1 (22.2%)
2	CH_3CO_3	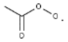	C_2 (18.1%)	CH_3CO_3	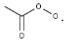	C_2 (16.6%)
3	$C_2H_5O_2$	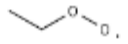	C_2 (3.9%)	$C_2H_5O_2$	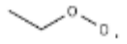	C_2 (5.5%)
4	$SC_4H_9O_2$	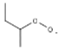	C_4 (2.1%)	$SC_4H_9O_2$	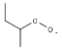	C_4 (3.3%)
5	$C_2H_5CO_3$	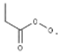	C_3 (1.8%)	$TC_4H_9O_2$	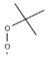	C_4 (1.9%)
6	NBUTOLAO$_2$	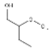	C_4 (1.5%)	IPECO$_2$	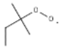	C_5 (1.5%)
7	BUT$_2$OLO$_2$	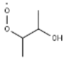	C_4 (1.2%)	$IC_3H_7O_2$	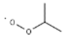	C_3 (1.5%)
8	ISOPBO$_2$	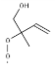	C_5 (1.1%)	TLBIPERO$_2$	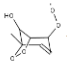	TOL (1.4%)
9	TLBIPERO$_2$	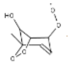	TOL (1.1%)	HYPROPO$_2$	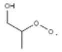	C_3 (1.3%)
10	TC4H9O$_2$		C_4 (1.0%)	$C_2H_5CO_3$	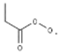	C_3 (1.1%)
	Total		55.2%	Total		56.3%
	C_1-C_2 radicals		45.4%	C_1-C_2 radicals		44.3%
	C_3-C_5 radicals		8.7%	C_3-C_5 radicals		10.6%
	Aromatic radicals		1.1%	Aromatic radicals		1.4%

Pattern 2						
	QA site			TC site		
No.	Radical name in MCM	Structure	Classification (Proportion)	Radical name in MCM	Structure	Classification (Proportion)
1	CH_3O_2	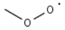	C_1 (23.1%)	CH_3O_2	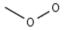	C_1 (29.5%)
2	CH_3CO_3	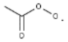	C_2 (18.1%)	CH_3CO_3	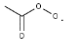	C_2 (20.7%)
3	$C_2H_5O_2$	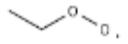	C_2 (3.1%)	$HOCH_2CH_2O_2$		C_2 (3.3%)
4	$HOCH_2CH_2O_2$		C_2 (2.2%)	$C_2H_5O_2$	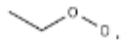	C_2 (2.9%)
5	TLBIPERO$_2$	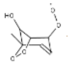	TOL (2.1%)	HMVKBO$_2$	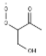	C_4 (2.3%)
6	$SC_4H_9O_2$	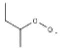	C_4 (1.7%)	ISOPBO$_2$	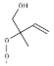	C_5 (1.7%)
7	$C_2H_5CO_3$	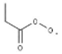	C_3 (1.7%)	TLBIPERO$_2$	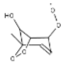	TOL (1.4%)
8	$HCOCH_2O_2$		C_2 (1.4%)	$SC_4H_9O_2$	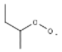	C_4 (1.3%)
9	TLFUO$_2$	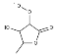	TOL (1.2%)	HYPROPO$_2$	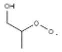	C_3 (1.2%)
10	MCATEC$_1$O$_2$	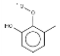	TOL (1.1%)	$HCOCH_2O_2$		C_2 (1.1%)
	Total		55.9%	Total		65.4%
	C_1-C_2 radicals		47.9%	C_1-C_2 radicals		57.5%
	C_3-C_5 radicals		3.4%	C_3-C_5 radicals		6.5%
	Aromatic radicals		4.5%	Aromatic radicals		1.4%

5.4.2 Cycling of OH radical

The OH radical is the initiator of photochemical O_3 formation. Figure 5.6 plots the simulated average daytime OH concentrations and its formation and loss pathways dominating the cycling of OH in the two patterns at both sites, which roughly followed the typical pattern of the intensities of photochemical reactions, *i.e.*, higher at noon/early afternoon and lower at the beginning and end of the day. The simulated average OH concentration was comparable (p = 0.47) between QA ($(2.4\pm0.3) \times 10^6$ molecules cm^{-3}) and TC ($(2.3\pm0.2) \times 10^6$ molecules cm^{-3}) in pattern 1, while the value at QA ($(2.7\pm0.1) \times 10^6$ molecules cm^{-3}) was much higher ($p < 0.05$) than that at TC ($(2.0\pm0.1) \times 10^6$ molecules cm^{-3}) in pattern 2 (Table 5.5), among which the OH level at TC in pattern 2 was the lowest. These OH levels were higher than previous findings at TC (Liu X. et al., 2019) because this study only focused high O_3 episode days while Liu X. et al. (2019) averaged OH concentrations on both episode and non-episode days.

As expected, the formation and loss rates of OH were basically balanced at both sites in both patterns. The reaction of HO_2 + NO, the secondary source of OH, dominated OH formation in both patterns at the two sites, accounting for 65.1-87.2% of the total OH formation rate (Table 5.5). The dominant role of HO_2+NO in OH formation on both banks of the PRE in the two patterns is consistent with the results in Xue et al. (2016) and Liu X. et al. (2019) simulated in the same area. Specifically, the OH formation rate of HO_2 + NO at QA ($(5.3\pm0.6) \times 10^7$ molecules cm^{-3} s^{-1}) was comparable (p = 0.31) to that at TC ($(6.1\pm0.7) \times 10^7$ molecules cm^{-3} s^{-1}) in pattern 1, while it was much higher ($p < 0.05$) at QA ($(6.7\pm0.2) \times 10^7$ molecules cm^{-3} s^{-1}) than that at TC ($(3.1\pm0.1) \times 10^7$ molecules cm^{-3} s^{-1}) in pattern 2, confirming similar oxidative capacity at both sites in pattern 1 and much higher oxidative capacity at QA in pattern 2. Interestingly, the second contributor of OH in both patterns at TC was photolysis of HONO (14.2±1.2% in pattern 1 and 29.3±0.6% in pattern 2), whereas it was O_3 photolysis (4.9±0.8%) in pattern 1 and the photolysis of OVOCs (6.5±0.1%) in pattern 2 at QA. Clearly, the total contribution of primary sources of OH (*i.e.*, O_3+VOCs, photolysis of HONO, O_3 and H_2O_2) was much lower than that of secondary source (*i.e.* HO_2+NO), implying that OH cycling was dominantly aggregated by the secondary source.

However, the primary sources of OH were the key initiators of the photochemical oxidative processes (Li Z. et al., 2018).

OH was mainly consumed by the reaction with VOCs at both sites in both patterns (pattern 1: 69.5 ± 7.8% at QA and 50.6 ± 6.4% at TC; pattern 2: 68.6±1.7% and 34.1±1.3%, respectively) (Table 5.5). The second loss pathway was OH+CO at QA (18.7 ± 2.5% in pattern 1; 16.7±0.4% in pattern 2), but OH+NO_2 at TC (27.7 ± 2.7% in pattern 1 and 30.9±0.7% in pattern 2). In pattern 1, the loss rate of OH by VOCs was comparable (p = 0.33) at QA ($(4.6\pm0.5)\times10^7$ molecules cm^{-3} s^{-1}) and TC ($(4.0\pm0.5)\times10^7$ molecules $cm^{-3}s^{-1}$), while the values of OH+NO_2 ($(0.6\pm0.1) \times 10^7$ molecules cm^{-3} s^{-1}) and OH+NO ($(0.2\pm0.03) \times 10^7$ molecules cm^{-3} s^{-1}) at QA were much lower than those at TC ($(2.2\pm0.2) \times 10^7$ molecules cm^{-3} s^{-1} and $(0.6\pm0.1)\times10^7$ molecules cm^{-3} s^{-1}, respectively) ($p < 0.05$), due to much higher levels of NO and NO_2 at TC (Table 5.1). In pattern 2, the loss rate of OH by VOCs at QA ($(5.3\pm0.1) \times 10^7$ molecules cm^{-3} s^{-1}) was much greater ($p < 0.05$) than that at TC ($(1.6\pm0.1)\times10^7$ molecules cm^{-3} s^{-1}), likely related to lower VOC levels and hence lower HO_2 and RO_2 concentrations at TC. However, the loss rates of OH by NO and NO_2 at TC were higher than those at QA ($p < 0.05$), owing to larger emissions of NO_x at TC (Table 5.1).

To further understand the reactivity of VOCs with OH, VOCs were classified into sub-groups (*i.e.* alkanes, alkenes, aromatics and OVOCs) for their OH reactivity calculation. Similar to PBM-MCM simulated average OH concentrations, the calculated total OH reactivity of VOCs was comparable ($p>0.1$) between QA (13.6±3.5 s^{-1}) and TC (8.6±2.3 s^{-1}) in pattern 1, so was the OH reactivity of each VOC group except the higher OH reactivity of alkenes and aromatics at QA than that at TC ($p < 0.05$) (Table 5.6). In pattern 2, however, the OH reactivity of all VOC sub-groups at QA was higher than at TC ($p < 0.05$). Furthermore, the OH reactivity of alkenes ranked the first in both patterns at both sites, while the OH reactivity of alkanes was the second highest at both sites in pattern 1, and the OH reactivity of aromatics and OVOCs ranked the second at QA and TC, respectively, in pattern 2. The results of OH reactivity are consistent with the high RIR values and main contribution to RO_2 + NO pathway of top ten VOCs/OVOCs simulated by the PBM-MCM (Section 5.3.3 and Section 5.5.1).

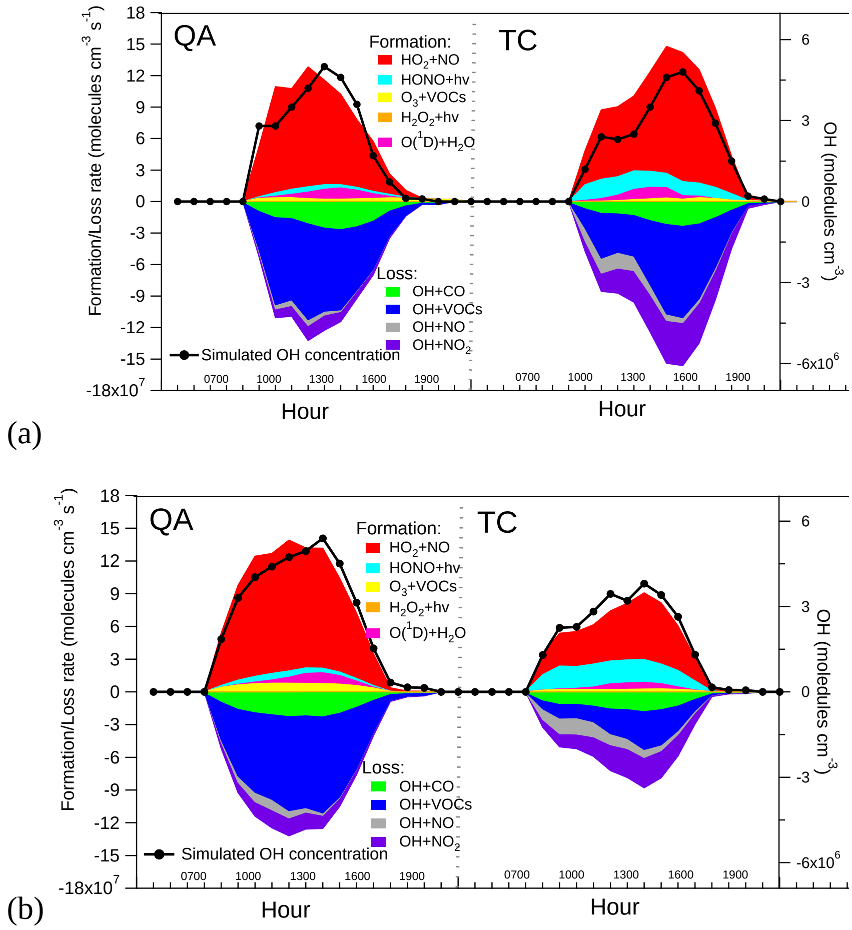

Figure 5.6 Average diurnal cycles of the OH formation and loss rates at both sites in (a) pattern 1 and (b) pattern 2.

Table 5.5 Simulated average daytime (07:00-19:00 LT) OH concentration and its formation and loss pathways in the two patterns at both sites. The OH cycling rate, *i.e.*, the overall formation or loss rate of OH, is the sum of the average daytime OH cycling rate of each individual pathway.

Site	OH concentration ($\times10^6$ molecules cm^{-3})	OH cycling rate ($\times10^7$ molecules cm^{-3} s^{-1})	Formation pathways ($\times10^7$ molecules cm^{-3} s^{-1} (%))					Loss pathways (($\times10^7$ molecules cm^{-3} s^{-1} (%))			
			Secondary source	Primary source							
			HO_2+NO	HONO+*hv*	O^1D+H_2O	O_3+VOCs	H_2O_2+*hv*	OH+CO	OH+VOCs	OH+NO	OH+NO_2
QA*	2.4±0.3	6.3±0.7	5.3±0.6 (87.2±10.5%)	0.2±0.02 (3.8±0.4%)	0.3±0.1 (4.9±0.8%)	0.2±0.03 (3.9±0.5%)	0.01±0.000 (0.2±0.04%)	-1.2±0.2 (18.7±2.5%)	-4.6±0.5 (69.5±7.8%)	-0.2±0.03 (2.7±0.5%)	-0.6±0.1 (9.1±1.5%)
TC*	2.3±0.2	7.7±0.8	6.1±0.7 (80.5±8.9%)	1.1±0.1 (14.2±1.2%)	0.3±0.1 (4.0±0.7%)	0.1±0.01 (1.2±0.1%)	0.0001±0.0001 (0.04±0.01%)	-1.1±0.1 (13.8±1.3%)	-4.0±0.5 (50.6±6.4%)	-0.6±0.1 (7.9±1.0%)	-2.2±0.2 (27.7±2.7%)
QA**	2.7±0.1	7.6±0.2	6.7±0.2 (85.2±2.2%)	0.3±0.01 (3.9±0.1%)	0.3±0.01 (4.3±0.2%)	0.5±0.01 (6.5±0.1%)	0.007±0.0003 (0.1±0.0%)	-1.3±0.03 (16.7±0.4%)	-5.3±0.1 (68.6±1.7%)	-0.3±0.01 (4.0±0.2%)	-0.8±0.02 (10.7±0.3%)
TC**	2.0±0.1	4.7±0.1	3.1±0.1 (65.1±1.9%)	1.4±0.03 (29.3±0.6%)	0.2±0.01 (4.6±0.2%)	0.2±0.001 (3.5±0.2%)	0.0005±0.00002 (0.0±0.0%)	-0.9±0.03 (20.1±0.6%)	-1.6±0.1 (34.1±1.3%)	-0.7±0.02 (14.9±0.4%)	-1.4±0.03 (30.9±0.7%)

*****pattern 1

**pattern 2

Table 5.6 OH reactivity of VOC groups in pattern 1 and pattern 2 at both sites.

OH reactivity of VOC group (s^{-1})*	Alkanes**	Alkenes**	Aromatics**	OVOCs**	TVOCs
Pattern 1					
QA	3.9±1.3	4.7±1.1	2.2±0.7	2.7±0.8	13.6±3.5
TC	2.4±0.9	2.9±0.6	1.0±0.4	2.3±0.6	8.6±2.3
Pattern 2					
QA	1.2±0.1	3.5±0.2	1.8±0.2	1.5±0.1	7.9±0.4
TC	0.5±0.1	1.9±0.2	0.6±0.1	1.1±0.2	4.1±0.4

*OH reactivity of VOC group=$\sum(k_i * [VOC]_i)$, where k_i represents the rate constant of OH with individual VOC species, $[VOC]_i$ means the concentration of individual VOC species in each VOC group.

**Alkanes, alkenes, aromatics, OVOCs include 18 C_2-C_{10} alkane hydrocarbons, 16 C_2-C_7 alkene and alkyne hydrocarbons, 10 C_6-C_9 aromatic hydrocarbons and 4 C_1-C_3 OVOCs, respectively (Table 5.2).

5.5 Impact of VOC species on O_3 formation pathways

As the 10 VOCs most responsible for O_3 formation were determined at both sites in the two patterns (Section 5.3.3), it is worthwhile to comprehensively investigate their impacts on O_3 formation pathways. As described above, VOCs contributed to O_3 formation mainly through the reactions with OH to generate RO_2 radicals and the cycling processes (*i.e.*, RO_2+NO) to produce HO_2 radicals. Therefore, the pathways of VOCs to O_3 formation were summarized into two reactions, *i.e.*, RO_2+NO and HO_2+NO. In this study, the impacts of the selected VOCs in pattern 2 were explored as an example.

5.5.1 RO_2+NO pathway

Figure 5.7 shows the simulated contributions of top 10 VOC species to O_3 formation pathways in pattern 2 at QA and TC. The simulated contribution of each VOC was estimated from the difference between a base case (with all required observed data as inputs into the PBM-MCM model) and a constrained case (with all required observed data exclusive of the selected one VOC as inputs). Besides, the contributions of the top 10 VOC species to the variations of radicals and NO_x at QA and TC are listed in Table 5.7.

At QA, xylenes (16.3%) were the largest contributor to RO_2+NO, followed by trimethylbenzene (15.0%), isoprene (13.7%) and formaldehyde (10.4%) (Figure 5.7 (a)). In total, the 10 major VOCs contributed 65.3% of the pathway of RO_2+NO. In comparison, at TC isoprene made the highest contribution (27.1%) to RO_2+NO, while the second and third contributors were xylenes (18.1%) and formaldehyde (13.3%), respectively (Figure 5.76(b)). The top 10 VOCs at TC accounted for 67.8% of the pathway of RO_2+NO. In general, the contributions of most VOC species to RO_2+NO at QA were higher ($p < 0.05$) than the corresponding species at TC (Table 5.7), which was partially due to the fact that the concentrations of most VOCs at QA were much higher than those at TC though NO was lower ($p < 0.05$) at QA (Table 5.2 and Table 5.1).

The positive contribution of each VOC to RO_2+NO at both sites could be explained by the variations of radicals and NO. In Table 5.7, it was found that all RO_2 and HO_2 increased at both sites, while all NO decreased at QA and most NO decreased at TC, and all (most) OH increased at TC (QA). Using isoprene at QA as an example (Row 3 in Table 5.7), isoprene reacted with OH to generate RO_2 (R1 below, where M is an energy-absorbing molecule, *e.g.* N_2 or O_2), resulting in the 5.5% reduction of OH and 16.6% increase of RO_2. Further reaction of RO_2 with NO created 11.3% elevation of HO_2. Because RO_2 and HO_2 both consumed NO to produce O_3 (R2 and R3), NO had 0.44% decrease. The significant increase of RO_2 and minor reduction of NO led to a positive dedication of isoprene to RO_2+NO pathway (13.7%). It is noted that though OH was largely consumed through the reactions with VOCs (R1) and CO (R4), the reactions of HO_2+NO also reproduced OH at the same time (R3). Therefore, the variations of OH affected by each VOC species, which could be either positive or negative, were strongly influenced by the variations of all formation and loss pathways of OH.

$$OH+VOCs+O_2+M \rightarrow RO_2+H_2O+M \quad \text{(R1)}$$

$$RO_2+NO+O_2 \rightarrow HO_2+R'CHO \quad \text{(R2)}$$

$$HO_2+NO \rightarrow NO_2+OH \quad \text{(R3)}$$

$$OH+CO+O_2+M \rightarrow HO_2+CO_2+M \quad (R4)$$

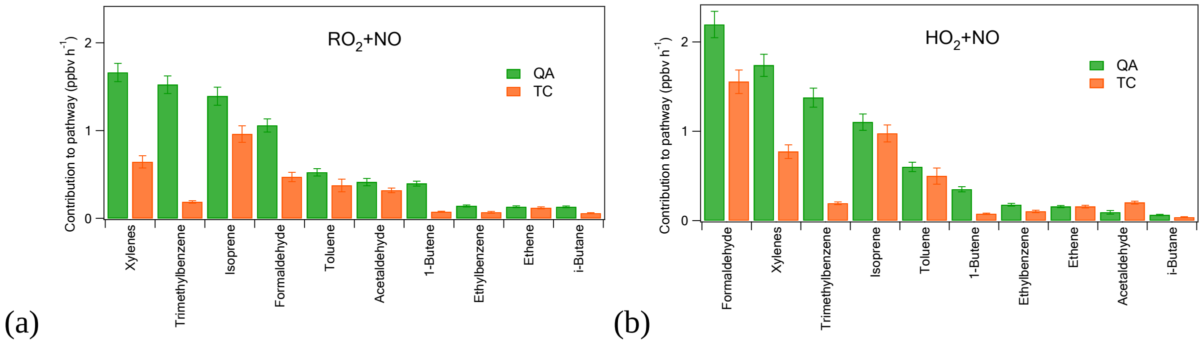

Figure 5.7 Simulated contributions of top 10 VOC species to O_3 formation pathways (a) RO_2+NO and (b) HO_2+NO in pattern 2 at QA and TC. Error bars represent 95% C.I. of the average.

Table 5.7 Variations of radicals (*i.e.*, OH, HO_2 and RO_2), NO and NO_2, and O_3 production rates (k_1[HO_2][NO] and ∑k_2[RO_2][NO]) caused by the addition of a selected VOC species in Figure 5.7 in pattern 2 at QA and TC (unit: ppbv for NO and NO_2; molecules cm^{-3} for concentration of radicals; molecules cm^{-3} s^{-1} for reaction rate; percentage in bracket).

Rank	VOC	△NO	△NO_2	△OH	△HO_2	△RO_2	△∑k1(HO_2)(NO)	△∑k1(RO_2)(NO)
QA								
1	Xylenes	-0.07 (-0.96%)	-0.007 (-0.08%)	2.1 (4.0%)	3.3 (10.6%)	3.9 (13.7%)	1.2 (13.9%)	1.2 (16.3%)
2	Trimethylbenzene	-0.05 (-0.79%)	-0.008 (-0.10%)	2.0 (3.9%)	2.8 (8.8%)	3.6 (12.4%)	1.0 (11.0%)	1.1 (15.0%)
3	Isoprene	-0.03 (-0.44%)	0.004 (0.05%)	-2.9 (-5.5%)	3.6 (11.3%)	4.8 (16.6%)	0.8 (8.8%)	1.0 (13.7%)
4	Formaldehyde	-0.07 (-1.01%)	-0.013 (-0.16%)	5.6 (10.8%)	4.6 (14.7%)	2.2 (7.6%)	1.5 (17.6%)	0.7 (10.4%)
5	Toluene	-0.02 (-0.30%)	0.001 (0.01%)	0.2 (0.4%)	1.2 (3.8%)	1.3 (4.7%)	0.4 (4.8%)	0.4 (5.1%)
6	Acetaldehyde	-0.007 (-0.1%)	-0.0003 (-0.003%)	-1.1 (-2.2%)	0.2 (0.7%)	0.8 (2.7%)	0.1 (0.7%)	0.3 (4.1%)
7	1-Butene	-0.01 (-0.2%)	-0.020 (-0.25%)	0.3 (0.6%)	0.8 (2.6%)	0.9 (3.2%)	0.2 (2.8%)	0.3 (3.9%)
8	Ethylbenzene	-0.01 (-0.14%)	-0.004 (-0.04%)	0.1 (0.1%)	0.3 (1.0%)	0.3 (1.1%)	0.1 (1.4%)	0.1 (1.4%)
9	Ethene	-0.005 (-0.07%)	0.001 (0.02%)	-0.1 (-0.1%)	0.3 (0.9%)	0.3 (0.9%)	0.1 (1.3%)	0.1 (1.3%)
10	i-Butane	-0.005 (-0.07%)	0.002 (0.02%)	-0.1 (-0.3%)	0.1 (0.3%)	0.3 (1.1%)	0.04 (0.5%)	0.1 (1.3%)
TC								
1	Isoprene	-0.02 (-0.1%)	0.006 (0.03%)	0.9 (2.5%)	0.6 (18.9%)	0.6 (29.5%)	0.7 (15.3%)	0.7 (27.1%)
2	Xylenes	-0.03 (-0.1%)	-0.004 (-0.02%)	1.6 (4.4%)	0.4 (13.8%)	0.4 (19.4%)	0.5 (12.1%)	0.5 (18.1%)
3	Formaldehyde	-0.05 (-0.2%)	-0.04 (-0.2%)	4.6 (12.5%)	0.8 (24.0%)	0.3 (14.7%)	1.1 (24.4%)	0.3 (13.3%)
4	Toluene	-0.01 (-0.1%)	-0.001 (-0.01%)	0.6 (1.7%)	0.4 (11.3%)	0.3 (15.2%)	0.3 (7.8%)	0.3 (10.6%)
5	Acetaldehyde	-0.006 (-0.02%)	0.005 (0.02%)	0.1 (0.3%)	0.1 (3.1%)	0.1 (6.9%)	0.1 (3.2%)	0.2 (9.0%)
6	Trimethylbenzene	-0.003 (-0.01%)	0.004 (0.02%)	0.5 (1.3%)	0.1 (3.0%)	0.1 (4.6%)	0.1 (3.0%)	0.1 (5.3%)
7	Ethene	0.002 (0.01%)	0.009 (0.04%)	0.1 (0.2%)	0.1 (2.2%)	0.1 (2.8%)	0.1 (2.4%)	0.1 (3.4%)
8	1-Butene	0.003 (0.01%)	0.005 (0.02%)	0.1 (0.4%)	0.04 (1.1%)	0.03 (1.8%)	0.1 (1.2%)	0.1 (2.1%)
9	Ethylbenzene	0.003 (0.01%)	0.003 (0.02%)	0.1 (0.4%)	0.1 (1.9%)	0.05 (2.3%)	0.1 (1.6%)	0.05 (1.9%)
10	i-Butane	0.0005 (0.002%)	0.005 (0.02%)	0.001 (0.003%)	0.02 (0.5%)	0.03 (1.6%)	0.03 (0.6%)	0.04 (1.6%)

Note: The variations are calculated using the equation (Equation. 5.1): $\Delta X = [X]_B - [X]_C$; where ΔX represents the variations of radicals (*i.e.*, OH, HO_2 and RO_2) and NO_x, and O_3 production rates (*i.e.*, $k_1[HO_2][NO]$ and $\sum k_2[RO_2][NO]$). $[X]_B$ and $[X]_C$ represent the daytime averaged concentrations of radicals and NO_x, and reaction rate of O_3 production in the base case and constrained case, respectively.

5.5.2 HO_2+NO pathway

At both sites, formaldehyde (QA: 17.6%; TC: 24.4%) made the largest contribution to HO_2+NO because formaldehyde directly produces HO_2 by its photolysis (R5) and the reaction with OH (R6) (Table 5.7). At QA, xylenes (13.9%), trimethylbenzenes (11.0%) and isoprene (8.8%) were the 2nd to 4th contributors to the HO_2+NO pathway, respectively, while they were isoprene (15.3%), xylenes (12.1%) and toluene (7.8%) at TC. In total, the 10 VOCs accounted for 58.3% and 55.3% of HO_2+NO pathway at QA and TC, respectively. Again, using isoprene at QA as an example (Row 3 in Table 5.7), HO_2 increased 11.3% and NO only decreased 0.44%, leading to a positive contribution to HO_2+NO (8.8%). Overall, the contributions of individual VOCs to HO_2+NO pathway at QA were greater than those at TC, in line with the findings on the contributions of VOCs to RO_2+NO pathways (Section 5.5.1).

$$HCHO+O_2+h\nu\ (\lambda<320nm) \rightarrow HO_2+CO \qquad \text{(R5)}$$

$$HCHO+OH \rightarrow HO_2+H_2O+CO \qquad \text{(R6)}$$

5.6 Summary

A photochemical box model was applied to understand the O_3 formation mechanisms and radical chemistry in the two patterns of 16 O_3 episode days captured on the west and east banks of the PRE in autumn 2016. In pattern 1, severe O_3 pollution was found on both banks. The downwind east bank (TC) suffered from worse O_3 pollution than the upwind west bank (QA) due to the accumulation of O_3 precursors and favorable meteorological conditions, resulting in large oxidative capacity and strong photochemical reactions over the PRE. In pattern 2, the maximum hourly O_3 values exceeded 100 ppbv on the west bank, while no O_3 episode days were found on the east bank, implying much stronger oxidative capacity on the west bank, likely related to the higher VOC levels and lower NO_x emissions. The O_3 formation was limited by VOCs on the east bank in both patterns because of high local emissions of NO_x, while it was co-controlled by VOCs and NO_x on some days and limited by VOCs on the other days on the west bank in both patterns. Isoprene, formaldehyde, xylenes and trimethylbenzenes were the main contributors to the O_3 formation at QA, while isoprene, formaldehyde, xylenes and toluene should be more focused on when controlling local O_3 formation at TC. In pattern 1, elevated O_3 production rate, OH cycling rate and OH radical concentration were found on both banks, confirming the intense photochemical reactions over the PRE. In pattern 2, the higher OH radical concentration and cycling rate and O_3 production rate simulated on the west bank verified the stronger photochemistry over there. These findings help to understand O_3 photochemistry in estuaries.

Chapter 6 Intercomparison of ozone formation and radical chemistry in the past decade at a suburban site in Hong Kong

6.1 Introduction

Ground-level ozone (O_3) is one of the most representative air pollutants in photochemical smog, produced through photochemical reactions between volatile organic compounds (VOCs) and nitrogen oxides (NO_x) in the presence of sunlight (NRC, 1992; Jacob et al., 1999; Guo et al., 2017). It is well documented that O_3 is harmful to human health (Bell et al., 2004), crops (Wang et al., 2005) and natural ecosystems (Ashmore, 2005). Throughout the last 30 years, extensive efforts have been made by the local and federal governments to alleviate the tropospheric O_3 pollution around the world (NRC, 1992; NARSTO, 2000; Wang T. et al., 2017; Wang et al., 2018a). Effectiveness of the control measures has gradually shown in some countries/regions, such as Switzerland, Germany, Ireland and eastern North America (Lefohn et al., 2010; Cui et al., 2011; Derwent et al., 2013; Parrish et al., 2014; Lin et al., 2017). In contrast, the O_3 levels in many places are still increasing or not decreasing at the expected rates, particularly in East Asia (Ding et al., 2008; Xu X. et al., 2008; Parrish et al., 2014; Xue et al., 2014b; Wang Y. et al., 2017).

Hong Kong, as one of the densely populated metropolises in East Asia, has been suffering from severe photochemical smog in the past decades, though the locally-emitted NO_x and total VOCs (TVOCs) were significantly reduced (Xue et al., 2014b; Ou et al., 2015; Lyu et al., 2016a; Wang Y, et al., 2017). On one hand, this indicates the non-linear relationship between O_3 and its precursors. On the other hand, in addition to local O_3 formation, the observed O_3 in Hong Kong is also influenced by the regional transport due to the proximity of the highly industrialized Pearl River Delta (PRD) region. Earlier studies revealed that the local O_3 production is typically limited by VOCs in urban and some suburban areas in Hong Kong (Zhang et al., 2007; Ling et al., 2014; Wang H.et al., 2017). Namely, cutting VOCs emissions will reduce O_3 production, while the reduction of NO_x may cause an O_3 increment (Cheng et al., 2010, 2013; Guo et al., 2011; Wang Y. et al., 2017). Previous studies also documented that photochemical O_3 formation is dependent upon the ratios between TVOCs and NO_x (Sillman, 1999; Guo et al., 2013a; Ling et al., 2013), reactivity of VOC species (Zhang et al., 2007; Liu et al., 2008a; Cheng et al., 2010) and the composition of NO_x (*i.e.* relative abundances of NO_2 and NO) (Richter et al., 2005; Xu X. et al., 2008; Wang H. et al., 2018). Moreover, located in the subtropical region, Hong Kong has relatively high temperature and strong solar radiation, which are favorable for local O_3 formation. For regional transport, studies (Wang et al., 2001b; Ding et al., 2004; Wang Y. et al., 2017) indicated that O_3 was generally built up in Hong Kong under the northerly winds, whereas it was often cleaned up by the sea breeze from South China Sea (SCS) and by the southwest monsoon in warm seasons. The contribution of regional transport to O_3 in Hong Kong even reached 70% under the dominance of tropical cyclone (Huang et al., 2005), a typical synoptic condition conducive to severe O_3 pollution in the Northern Hemisphere (So and Wang, 2003; Huang et al., 2005; Lam et al., 2005). To improve the air quality in Hong Kong, a series of control measures aiming at restriction of VOC emissions have been implemented by the Hong Kong government since 2007, which effectively reduced the concentrations of some VOCs, such as propane and *i-/n*-butanes emitted from taxis and public light buses fuelled by liquefied petroleum gas (LPG) (Lyu et al., 2016b), the aromatics mainly attributable to solvent usage, and the alkenes in association with diesel exhaust (Lyu et al., 2017a). As a result, Xue et al. (2014b) and Wang Y. et al. (2017) found that the locally produced O_3 decreased. However, the regional and super-regional transport of O_3 and its precursors from PRD and eastern China to Hong Kong had offset the decrease of the local O_3 production, resulting in an overall increase of the observed O_3 in Hong Kong from 2005 to 2013. Overall, the previous studies have greatly deepened the understandings of O_3 pollution in Hong Kong, and details about the studies can be referred to in Table 6.1.

Despite many previous studies (Xue et al., 2014b, 2016; Ou et al., 2015; Lyu et al., 2016a; Wang Y. et al., 2017; Wang H. et al., 2018), the inter-annual variations of the O_3 formation regimes and radical chemistry have yet been fully understood in Hong Kong. Additionally, the online measurement data used in previous long-term O_3 study might hamper the exact understanding of the local O_3 formation mechanisms, due to the unavailability of many reactive

VOCs, such as formaldehyde. Besides, the trends of the local production and regional transport of O_3 were only updated to 2013 in previous studies (Xue et al., 2014b; Wang Y.et al., 2017). In fact, many measures were taken to reduce the emission of air pollutants in recent years in Hong Kong and PRD. For examples, nearly 75% of the old catalytic converters on LPG-fuelled vehicles were renewed from September 2013 to May 2014. A program to eliminate the pre-Euro IV diesel vehicles or to upgrade their emission standards to Euro IV was initiated in March 2014 and completed in 2019 at its third phase. In PRD, the second stage of the clean air controlling program was implemented in 2013 - 2015 (DGEPD, 2013). In 2014, the Guangdong provincial government has launched an Action Plan for Air Pollution Prevention and Control (MEE PRC, 2014), putting the emphases on the emission control of traffics, coal-fired power plants and industrial sources. Investigations on the post-2013 variations of the local O_3 production in Hong Kong and the regional impacts provide a good opportunity for us to evaluate the effectiveness of these local and regional measures.

The objectives of this study were to re-examine the O_3 trend in the pre-2013 and trace the O_3 evolution in the post-2013 in Hong Kong, and to explore the underlying mechanisms for the variations of O_3 formation and radical chemistry. With the aid of a photochemical box model, the locally-produced and regionally-transported O_3, as well as their variation trends, were determined. Under the assumption that the local O_3 production in these years was changed due to a series of control measures in Hong Kong, the actual effectiveness of these control measures was also evaluated. China is suffering from severe O_3 pollution, almost second to none over the world. While O_3 began to decrease in most areas of North America and Europe, China's O_3 pollution was even aggravated in recent years. A series of air pollution control strategies have been implemented in China, though most of them were not specifically designed for O_3 abatement. Investigations on O_3 trends and the potential causes in Hong Kong would provide a good example of assessing the evolution of O_3 pollution and the effects of artificial interventions in China. In addition, the changes in the regional contribution to O_3 in Hong Kong determined in this study would shed light upon the variations of O_3 in China, particularly in

South China. It is expected that this study would have some inspiration to the O_3 pollution control in other cities and regions in China.

Table 6.1 Summary of the representative studies regarding O_3 pollution in Hong Kong.

Reference	Site	Measurement period	Nature of monitoring	Target	Main conclusions
Cheng et al, 2010	Wanqingsha (WQS), Guangdong and Tung Chung (TC), Hong Kong	Oct-Dec 2007	Suburban	O_3	O_3 formation was limited by VOCs at both sites. Carbonyls played important roles in photochemistry.
Cheng et al, 2013	TC, HK	Sep 2007 and Sep 2008	Suburban	O_3, VOCs	Major sources of VOCs in HK included consumer products, paint and printing solvent, road transport, and industrial, commercial, domestic and off-road transport.
Ding et al, 2004	PRD	Sep 2001	Large area	O_3	O_3 pollution events in PRD were close associated with sea-land breezes and tropical cyclones.
Guo et al, 2011	WQS and TC	Oct-Dec 2007	Suburban	VOCs	Solvent use, vehicular emissions, biomass burning, LPG usage and gasoline evaporation dominated the sources of VOCs in PRD.
Guo et al, 2013a	Tsuen Wan (TW) and Tai Mao Shan (TMS), HK	Sep-Nov 2010	TW: Urban TMS: Mountainous	O_3	Less NO titration, vertical transport, valley breeze and regional transport caused higher O_3 at the mountainous site.
Huang et al, 2005	HK	1999-2003	Large area	O_3	Tropical cyclones, continental anticyclones and troughs were conducive to O_3 pollution events in Hong Kong.
Lam et al, 2005	TC, HK	Aug 1999	Suburban	O_3, VOCs	Local thermal circulation under calm synoptic conditions trapped air pollutants, resulting in O_3 enhancements in HK.
Ling et al, 2013	TC, HK	Sep-Nov 2010	Suburban	O_3	High O_3 in HK was a combined effect of both local formation and regional transport
Ling et al, 2014	TW and TMS, HK	Sep-Nov 2010	TW: Urban TMS: Mountainous	O_3	Different O_3 production and destruction pathways at two sites. More aged air masses at the mountainous site favored O_3 formation.

Lyu et al, 2016b	Multiple, HK	Sep 2013 and Sep 2014	Urban Suburban Rural	VOCs	VOCs emitted from LPG-fueled vehicles significantly decreased at urban roadside sites. O_3 formation was limited by VOCs regardless of locations, while VOCs and NO_x co-limited O_3 formation in rural areas.
Lyu et al, 2016c	Mong Kok (MK), HK	Jun 2011-May 2014	Roadside	O_3, VOCs	Replacing catalytic converters in LPG-fueled vehicles led to substantial reductions of VOCs and NO_x emissions.
Lyu et al, 2017a	TC, HK	2005-2013	Suburban	VOCs	VOCs emitted from solvent usage and diesel exhaust decreased in Hong Kong from 2005 to 2013.
Ou et al, 2015	TC, HK	2005-2013	Suburban	VOCs	Vehicular exhaust, gasoline evaporation and LPG usage, consumer product and printing, architectural paints, and biogenic emissions were identified as the sources of VOCs in the study area.
So and Wang, 2003	Multiple, HK	Jun 1999-May 2000	Urban Suburban Rural	O_3	Air quality in rural areas was frequently influenced by regional air masses, while was predominantly affected by local emissions in urban areas.
Wang Y.et al, 2017	TC, HK	2005-2014	Suburban	O_3	Locally produced autumn O_3 decreased in Hong Kong, which was reversed by regionally-transported O_3 between 2005 and 2013.
Wang H.et al, 2018	Wan Shan Island (WSI), GD	Aug-Nov 2013	Rural	O_3	O_3 formation switched from the NO_x-limited regime on low O_3 days to VOC-limited regime on high O_3 days over South China Sea.
Xu X. et al, 2008	Linan, Zhejiang	Aug 1991-Jul 2006	Rural	O_3	Monthly highest 5% of O_3 increased from 1991 to 2006, with enhanced variability, likely due to the increased NO_x emissions.
Xue et al, 2014b	TC, HK	Sep-Nov of 2002-2013	Suburban	O_3	Increase of regionally-transported O_3 offset the decrease of locally-produced O_3 and resulted in the increase of observed O_3 in the autumn in HK during 2002-2013.
Zhang et al, 2007	Multiple, HK	Oct-Dec 2002	Urban Suburban Rural	O_3	50-100% of O_3 enhancement during O_3 episodes in HK was explained by local photochemical formation, following the oxidation of anthropogenic VOCs.

6.2 Observation overview

Figure 6.1 shows the hourly mixing ratios of O_3 observed at TC in the autumns of 2007-2017 with the data on VOC sampling days being highlighted in red. It was found that the autumn O_3 increased significantly from 2007 to 2013 (p<0.01), with a rate of 0.34±0.002 ppbv yr^{-1}. This was consistent with Wang Y. et al. (2017) who reported an overall increase rate of autumn O_3 of 0.67±0.07 ppbv yr^{-1} at the same site for the period of 2005-2013. On one hand, the discrepancy in O_3 increasing rates might be due to the different statistics used to draw the rates, *i.e.* hourly values in this study and monthly averages in Wang Y. et al. (2017). On the other hand, the autumn O_3 increased substantially from 23.9±0.97 ppbv in 2005 to 30.2±0.97 ppbv in 2007, much quicker than the increase between 2007 and 2013. Exclusion of the period of 2005-2007 might be another reason of the less O_3 enhancement calculated here. In contrast to the increased autumn O_3 during 2007-2013, the autumn O_3 decreased obviously from 2013 to 2017 (p<0.01), at a rate of -2.27 ± 0.003 ppbv yr^{-1}, indicating a fundamental alleviation of O_3 pollution in Hong Kong in the latest 5 years. Overall, a statistically significant decreasing trend (rate = -0.44±0.001 ppbv yr^{-1}) was observed for the autumn O_3 at TC from 2007 to 2017 (p < 0.05). The average O_3 on VOC sampling days in the three sampling campaigns also followed the same pattern, which increased from 32.8±2.6 ppbv in 2007 to 36.9±2.3 ppbv in 2013, while decreased to 24.4±1.9 ppbv in 2016. Further, the number of O_3 episode days in the autumns of the three VOC sampling years was investigated (see Figure 6.2) and found to be 15 (16.5% of the autumn days, same below) and 16 (17.6%) O_3 episode days in 2007 and 2013, respectively. However, there was only 5 (5.5%) O_3 episode days in the autumn of 2016. Similarly, the O_3 episode days accounted for 12.5%, 26.3% and 5.6% of the 2007, 2013 and 2016 sampling campaigns, respectively. Therefore, the increase of O_3 from 2007 to 2013 and the decrease in the following years could be represented by O_3 observed in the three sampling periods.

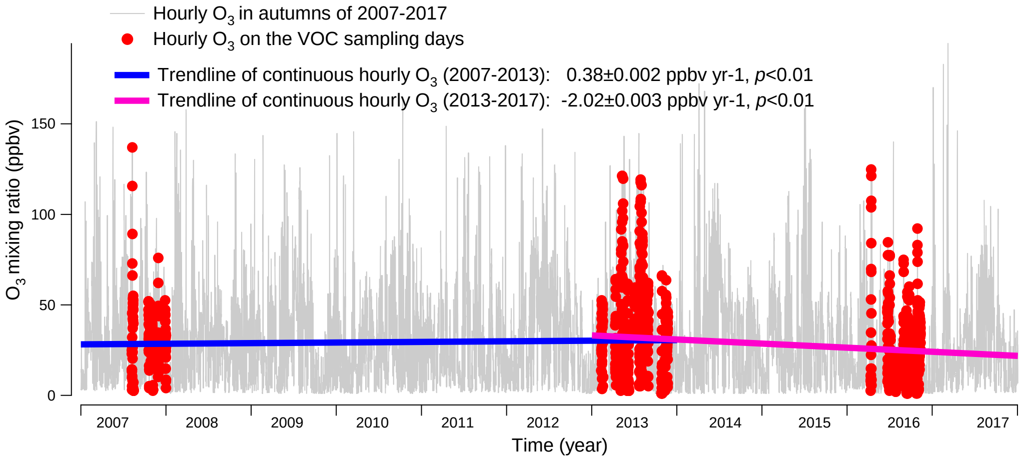

Figure 6.1 Long-term trends of the observed O_3 at TC from 2007 to 2017. Hourly O_3 values on the VOC sampling days in the autumns of 2007, 2013 and 2016 are marked in red. The hourly variation rates of O_3 are converted to yearly rates in periods of 2007 – 2013 and 2013 – 2017.

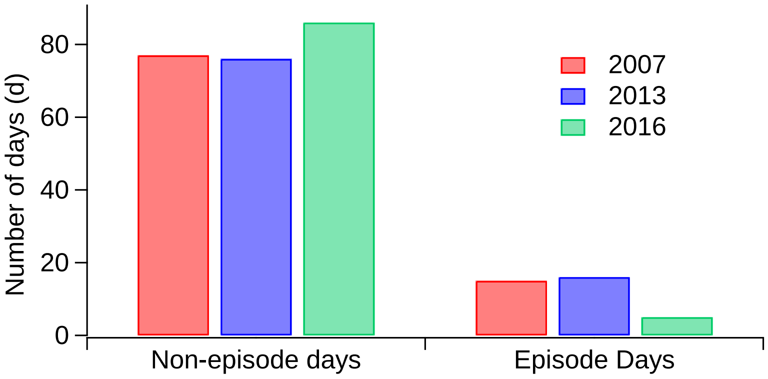

Figure 6.2 Number of O_3 episode days and non-O_3 episode days in the autumns of 2007, 2013 and 2016.

Table 6.2, Table 6.3 and Table 6.4 present the observed O_3, CO, NO, NO_2, SO_2 and TVOCs, 48 VOC/OVOC species as well as the meteorological conditions averaged on the VOC sampling days in 2007, 2013 and 2016, respectively. From 2007 to 2013, the TVOCs decreased by nearly a half, which was expected to result in the reduction of O_3 in view of the VOC-limited regime of O_3 formation at TC (Cheng et al., 2010; Wang Y. et al., 2017). However, the increases of CO and the notable decrease of NO in 2013 could enhance the O_3 production. The higher O_3 in 2013 indicated that this effect overrode the reduction of TVOCs in influencing the O_3 production. In particular, the decrease of NO meant the reduced NO titration to O_3, which has been recognized as a primary reason of O_3 increase in VOC-limited regime (Chou et al., 2006; Wang H. et al., 2018). From 2013 to 2016, the decrease of O_3 was accompanied by the reductions of TVOCs and NO_2, though CO remained increasing at the same time. NO_2, as a direct source of O_3 through photolysis, plays important role in modulating the O_3 variation. Though the causes of NO_2 reduction are unknown to us, it might be one of the critical factors contributing to the decline of O_3 in Hong Kong in recent years. On the contrary, the increase of CO was also confirmed by the continuous monitoring data at TC, with a rate of 33.9±0.7 ppbv yr^{-1} between 2013 and 2016. In fact, the consistent increasing trend ($p < 0.05$) was also observed at the roadside sites in Hong Kong (not shown here). While the causes of CO increase in Hong Kong may be complicated, the increased vehicle emission is a plausible explanation. Studies (Johnson, 2008; Yao et al., 2008) revealed that while the new engine technologies performed well in reducing NO_x emission, they might lead to the increased emission of CO, with the application of lower air-to-fuel ratio and engine temperature.

In addition, studies have confirmed that continental anticyclones and tropical cyclones are conducive to severe O_3 pollution in Hong Kong, because these synoptic systems are often accompanied with northerly winds, high temperature, strong solar radiation, and relatively high pressure in Hong Kong (Ding et al., 2004; Huang et al., 2005; Jiang et al., 2015). Table 6.5 summarizes number of O_3 episode days with tropical cyclone, continental anticyclone and low pressure trough in the autumns of 2007, 2013 and 2016. In autumn 2007, 8, 8 and 1 O_3 episode day(s) were found to be related to the tropical cyclone, continental anticyclone and low-pressure trough, respectively, with 2 O_3 episode days under the combined influence of tropical cyclone and continental anticyclone. There were also 11 and 5 O_3 episode days in association with tropical cyclone and continental anticyclone in autumn 2013, respectively (Wang H. et al., 2018). However, 4 out of the 5 episode days found in autumn 2016 were associated with tropical cyclone, with the other one related to low-pressure trough. Therefore, the lower O_3 and less O_3 episode days in 2016 were also benefited from the meteorological conditions.

Table 6.2 Mixing ratios of the measured trace gases and TVOCs averaged on the selective 45 VOC sampling days in 2007, 2013 and 2016.

	2007		2013		2016	
Unit: ppbv	Mean ± 95% C.I.	Max.	Mean ± 95% C.I.	Max.	Mean ± 95% C.I.	Max.
O_3	32.8±2.6	137.0	36.9±2.2	121.2	24.4±1.9	124.9
CO	456.3±19.8	847.0	585.0±11.9	1047.9	691.8±9.5	1074.7
NO	17.2±3.2	124.7	10.9±1.3	98.6	11.3±1.4	94.6
NO_2	27.7±2.1	69.6	31.5±1.4	80.8	22.0±1.1	103.2
SO_2	6.9±0.4	21.8	7.0±0.2	18.0	3.0±0.1	10.7
TVOCs	49.7±4.4	111.1	25.1±1.4	68.0	21.1±1.4	71.9

Table 6.3 Descriptive statistics of VOC mixing ratios measured in 2007, 2013 and 2016. The 95% C.I. and Max. denote the 95% confidence interval and of the mixing ratios of VOC species, respectively (Unit: pptv).

VOC species	2007			2013			2016		
	Mean	95%CI	Max.	Mean	95%CI	Max.	Mean	95%CI	Max.
Ethane	1587.6	37.3	1994.6	1918.9	140.1	5700.4	1729.1	85.3	3951.2
Ethene	1388.7	53.5	2284.7	1074.9	94.3	4529.8	886.8	79.1	4335.5
Ethyne	1939.3	105.3	3855.4	1563.4	94.8	3339	1399.2	83.1	4254.7
Propane	2826.2	94.1	3889.6	1619.1	110.4	5826.3	2308.4	224.2	13269.8
Propene	325.2	34	1036.7	296.1	20.3	1052.3	192.3	13.8	773.6
i-Butane	790.9	40.7	1269.3	1556.4	115.5	5778.5	901.5	67.5	3229.9
n-Butane	1562.4	124.3	3360.3	1402.6	95.8	5353.7	1403.8	116.3	5001.2
1-/i-Butene	275.1	71.2	2945.2	240.7	70.6	5944.6	98	9.4	715.8
trans-2-Butene	22.5	6	213.4	31.2	6.7	387.1	12.1	2.9	184.1
cis-2-Butene	24.4	6	201.9	25.2	5	275.2	9.3	2.8	178.5
3-methyl-1-Butene	12	2.4	76.6	35.6	16	332	8.7	5.5	207
2-methyl-1-Butene	16.4	3.3	89	47.4	25.3	1074	17.4	11.4	765.6
cis-2-Pentene	28.6	5.1	130.4	34.5	7.9	273.9	5.5	3.4	130.1
2-methyl-2-Butene	4.6	1	25.8	37.4	14.6	558	10.2	3.6	139.3
Butyne	41	6.3	171.2	40.5	12.1	406.7	18.5	2.8	142.2
i-Pentane	1809.6	339.6	7793.6	827.5	63.3	4646.9	466.3	33.2	1681.2

n-Pentane	351.9	63.7	2271.2	50.1	8.6	416.2	265.1	25.1	1104
1-Pentene	20.4	5.7	244.3	50.1	8.6	416.2	15.6	2.9	182.5
trans-2-Pentene	15.3	4.1	182	23.6	7.7	302.1	9.8	4.9	189.6
2-Methylpentane	268.8	68.7	2253	257.1	29.6	1643.9	195.5	27.1	1171.6
n-Hexane	1785.2	547.3	17974.4	930.6	147.7	9829	163.4	23.8	1426.7
n-Heptane	113.8	39.3	1196.3	100.2	12.8	877.3	65.9	5.8	290.7
n-Octane	42.4	9.6	245.2	47.5	8.9	739.3	34	3.9	188
2,2-Dimethylbutane	18.7	2.2	64.8	52.7	8.7	719.6	20.2	2	91.9
2,3-Dimethylbutane	31.2	17.1	822.5	68.8	7.1	389.3	46.3	7.3	311.9
3-Methylpentane	1911.5	423	10292	172	20.5	1260.3	131.8	18.9	1025.8
Cyclohexane	66.1	29.1	905.4	84.1	8.7	601.5	68.1	8	414.4
2-Methylhexane	49	16.4	557	85.7	9.7	429.6	205.8	19.2	492.8
3-Methylhexane	172.8	53.5	1651.2	171.5	19.4	1171.5	43.7	5.4	271.3
n-Nonane	29.1	6.4	226.8	47.6	8.1	621.6	39.9	7.3	477.2
n-Decane	457.3	138.9	3680.5	72.2	15.7	1198.3	34	3.9	188
Isoprene	270.6	53	868.5	417	44.4	1561	409.1	52.5	3122
α-Pinene	261.8	191.5	6810	29.9	4.4	321.5	21.1	2.9	218
β-Pinene	30.3	10.1	306.4	53.8	7.3	314.5	9.9	0.7	32
Benzene	567	99.7	3761.2	493.1	33.2	2308	257.3	14.5	658.2
Toluene	2878.9	845.3	26556.8	1445.3	149.2	6494.2	1169.5	229.5	13376
Ethylbenzene	358.8	63.2	1597.7	389.1	52.3	4274	193.6	20.7	1350.2
m/p/o-Xylene	579.2	112.1	2563.2	723.1	143.8	12250	451.1	42.1	2492
1,3,5/1,2,4/1,2,3 -Trimethylbenzene	285.8	72.7	2791.9	245	45.1	2982.3	67.9	10.7	782.5
i-Propylbenzene	7.4	1.2	38	16.5	1.8	111.1	7.5	0.7	63
n-Propylbenzene	16.4	2.6	68.9	34.3	4.3	305.2	12.4	2	188.6
3-Ethyltoluene	34.6	7.2	212.4	74	10.6	653	24.7	2.9	171.4
4-Ethyltoluene	18.1	3.4	114.4	45.4	6.1	429.8	16.6	2.4	220.2
2-Ethyltoluene	23.2	4.3	143	40.4	6.7	476.3	14	2.1	186.1
Formaldehyde	8608.3	1298	30244.3	2729	146.5	6403.5	2673.3	283.1	13633
Acetaldehyde	9853.8	1732.6	46380	1395.9	81.1	3694.8	779.4	92.1	3126
Acetone	12786.4	2712.9	75590	5156.2	421.3	22921.5	4995.6	460.6	13370.9
Propionaldehyde	--		--	325	38.2	1593.2	1547.9	547.2	3071.6

Table 6.4 Comparison of meteorological conditions in the autumns of 2007, 2013 and 2016 (HKO, 2017).

	2007		2013		2016	
	Mean ± 95%C.I.	Max.	Mean ± 95%C.I.	Max.	Mean ± 95%C.I.	Max.
Temperature (℃)	23.5±0.4	30.0	25.2±0.3	33.9	25.0±0.3	32.7
Relative humidity (%)	64.4±1.4	80.0	58.6±1.3	83.1	77.1±0.7	94.5
Solar radiation (W m^{-2})	190.3±37.7	788.9	159.2±21.3	869.1	119.8±18.2	829.3
Pressure (hPa)	1016.9±0.4	1024.3	1015.0±0.3	1023.1	1012.3±0.3	1020.2
Wind speed at the sampling site (m s^{-1})	2.3±0.2	5.3	1.0±0.1	3.2	0.9±0.1	4.3
Wind speed at HKIA* (m s^{-1})	4.7±0.3	10.8	4.8±0.4	11.7	4.5±0.3	12.4

*HKIA: Hong Kong International Airport.

Table 6.5 Number of O_3 episode days identified under the tropical cyclone, continental anticyclone and low pressure trough in the autumns of 2007, 2013 and 2016.

Year	Total No. of Episode	Tropical cyclone	Continental anti-cyclone	Low Pressure trough
2007	15*	8 (4 typhoons)	8	1
2013	16	11 (5 typhoons)	5	0
2016	5	4 (3 typhoons)	0	1

*Two O_3 episode days were under the combined influence of tropical cyclone and continental anticyclone.

6.3 Model simulation of O_3

6.3.1 Model validation

Figure 6.3 compares the simulated O_3 in scenario A and the observed O_3 on the VOC sampling days. Overall, both the magnitudes and the temporal patterns of the observed O_3 were reasonably reproduced, though the mean of the simulated O_3 (33.8±1.9 ppbv) was slightly lower than the observed average (37.1±2.0 ppbv). To quantitatively evaluate the model performance, the index of agreement (IOA) was used to examine the goodness of fit between simulated and observed O_3. Within the range of 0-1, higher IOA represents better agreement between the simulated and observed values (Willmott, 1982). In this study, the overall IOA for the three sampling periods was 0.74, within the range of IOA (0.67-0.89) accepted by the previous studies (Wang N. et al., 2015; Lyu et al., 2015, 2016a, 2016c; Wang Y. et al., 2017, 2018). Good correlations (R^2=0.61) were also shown between the simulated and observed hourly O_3. Bearing in mind the deficiencies of the box model in describing the atmospheric dynamics, it was believed that the modelling results were acceptable, but special attention and explanation to the discrepancies between the simulated and observed O_3 was needed.

It was found that the discrepancies were most likely caused by the transport processes, *i.e.*, vertical and horizontal transport, which were not fully represented in the PBM-MCM model (George et al., 2013; Lakey et al., 2015; Wang Y. et al., 2017). For example, the simulated O_3 (maximum: 122.6 ppbv) was much higher than the observed O_3 (maximum: 44.3 ppbv) on November 16, 2007, when the strong southeast winds (wind direction: 90°-180°) with the highest wind speed of 5.3 m s^{-1} prevailed in Hong Kong. The south sector winds from SCS might dilute the locally produced O_3 and the O_3 precursors/intermediates (such as the radicals) which were not constrained by the observations. The same circumstances were also observed on October 27, November 17, 2007 and September 11-12, November 20, 2013, with southeast winds dominated (74.4%) during the daytime (Figure 6.3). For those days with the simulated O_3 lower than the observed O_3, *i.e.* October 3, 22-25, 2013 and November 6, 2016, 69.3% of the winds during the daytime came from the north (wind directions: 0-90° and 270°-360°), which might transport the air masses laden with O_3 and/or O_3 precursors/intermediates not constrained to the observations from inland PRD to the sampling site. The observed O_3 mixing ratios are plotted against the wind fields in Figure 6.4 It is obvious that O_3 were higher under the north winds, while lower in the south wind sectors, confirming the effects of dilution and regional transport of the south and north winds on O_3 pollution in Hong Kong, respectively.

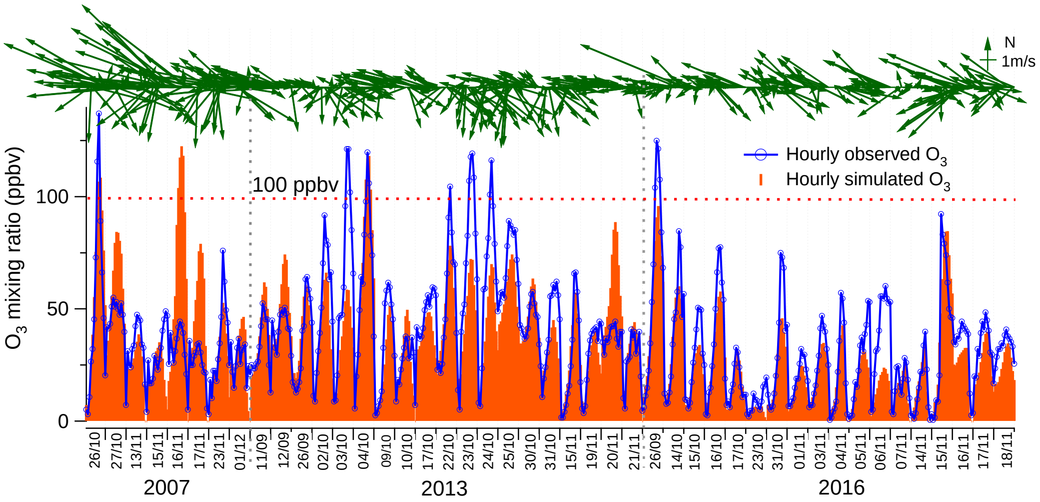

Figure 6.3 Hourly mixing ratio of the simulated and observed O_3 at TC during the VOC sampling periods in 2007, 2013 and 2016. The arrows represent the hourly wind sectors monitored at the sampling site.

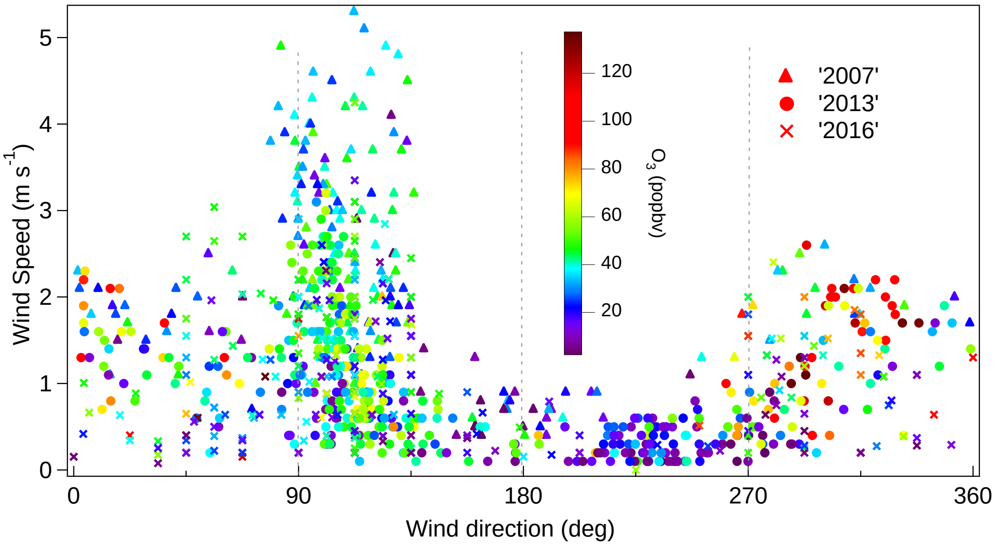

Figure 6.4 Relationship between the hourly observed O_3 and the wind fields at TC in the three sampling campaigns.

6.3.2 Inter-annual variations of the locally produced and regional transported O_3

As discussed in Section 3.3.3.1, the simulated O_3 in scenario A could be regarded as the locally produced O_3. Therefore, the differences between the observed O_3 and O_3 simulated in scenario A were treated as the regionally transported O_3 (Wang Y. et al., 2017). It is noteworthy that some negative values were generated with this method, corresponding to the dilution of the south winds to the locally produced O_3 as elaborated in Section 6.3.1. Figure 6.5 shows the hourly mixing ratios of the observed, local and regional O_3 at TC in daytime hours (07:00-19:00 LT) of the three sampling campaigns. Overall, the observed O_3 was mainly (88.7±2.5%) contributed by the local photochemical production, with regional transport only accounting for 11.3±2.5% of the observed daily maximum O_3. However, regional transport was responsible for as high as 58.0±5.4% of the observed daily maximum O_3 in Hong Kong on the O_3 episode days when northerly winds prevailed, indicating the heavy O_3 burden superimposed by regional air masses from PRD. From 2007 to 2013, the simulated locally-produced O_3 remained statistically unchanged (p>0.1), in contrast to the increase of observed O_3 and regional O_3 at rates of 1.78±0.05 ppbv yr^{-1} ($p < 0.05$) and 1.77±0.04 ppbv yr^{-1} ($p < 0.05$), respectively, the same trends as those reported by Wang Y. et al. (2017) for the autumn O_3 during 2005-2013. However, the decease of the locally produced O_3 in the same period as that simulated by Wang Y. et al. (2017) was not seen here according to the simulated O_3 in the 2007 and 2013 sampling campaigns. This discrepancy was likely caused by the limited samples in this study, no OVOCs considered in Wang Y. et al. (2017) and/or the inexactly same study periods between the two studies. Instead, it was found that the locally produced O_3 showed a significant decline at a rate of -5.52±0.05 ppbv yr^{-1} during 2013-2016 ($p < 0.05$), when the regionally transported O_3 did not change ($p = 0.32$), resulting in a downward trend (-5.31±0.07) of the observed O_3. As such, the increase of the observed O_3 from 2007 to 2013 was reversed by the decrease between 2013 and 2016, leading to an overall decreasing trend of the observed O_3 during 2007-2016 (rate = -0.57±0.03 ppbv yr^{-1}, $p < 0.05$).

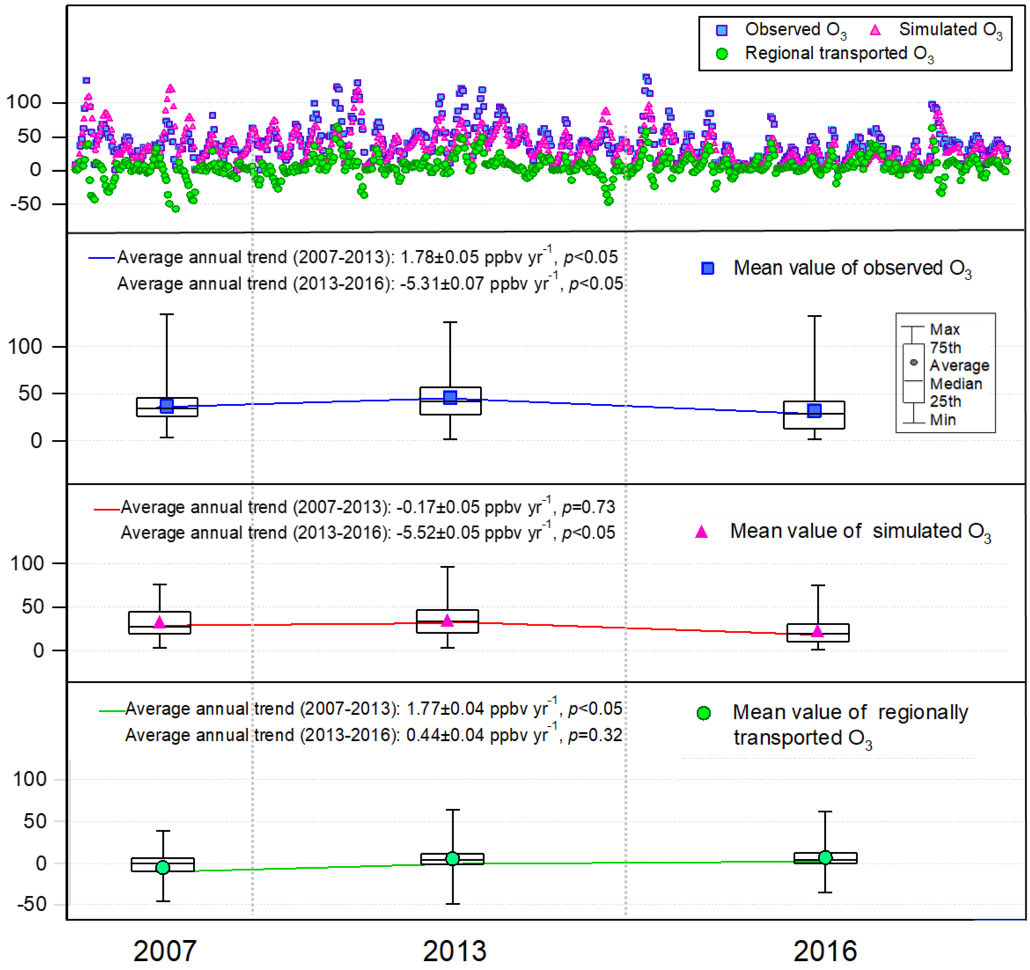

Figure 6.5 Hourly values (first panel) and the throughout-campaign statistical results (second to fourth panels) of the observed, simulated (locally-produced) and regional O_3 mixing ratios in daytime hours (07:00 – 19:00 LT) in the three sampling campaigns.

The significant alleviation of O_3 pollution in Hong Kong from 2013 to 2016 might be related to the measures taken to control the emissions of O_3 precursors in Hong Kong and in mainland China. The effectiveness of the actions launched by the Hong Kong government in O_3 abatement was fully demonstrated in previous studies (Xue et al., 2014b; Lyu et al., 2017a; Wang Y. et al., 2017), and would be further evaluated in this study (Section 6.5). Besides, the emission controls in mainland China might contribute to the decrease of O_3 or at least lessened the regional O_3 burden in this period. For example, the China's NO_x emissions for the first time showed a decreasing trend from 2013, benefited from the implementation of the China's Clean Air Action Plan (Zheng et al., 2018). Furthermore, the monthly average O_3 observed at the 12 air quality monitoring stations across the inland PRD were investigated, including three regional monitoring stations, *i.e.* Tianhu, Wanqingsha and Jinguowan, and nine urban monitoring stations, *i.e.* Xiapu, Jinjuzui, Donghu, Tangjia, Liyuan, Huijingcheng, Zimaling, Luhu and Chengzhong (https://www.epd.gov.hk/epd/sc_chi/resources_pub/publications/m_report.html). As shown in Figure 6.6, O_3 at these stations remained relatively stable ($p = 0.68$) during 2006-2013, which however showed a contrastively decreasing trend at a rate of -1.27±0.25 ppbv yr^{-1} from 2013 to 2016. This corroborated the modelling results that the regional contribution to O_3 in Hong Kong ceased increasing or even began to decrease since 2013. While the substantial decrease of NO_x was a plausible reason for the alleviated regional O_3 pollution, meteorological variations might also play roles in modulating O_3 variations in these years (Li K. et al., 2019). However, analyses on the causes are out of the scope of this study. In addition to the reduced local formation and regional transport of O_3, the more favorable meteorological conditions in 2016 might be another reason of the O_3 decrease, as discussed in Section 6.2.

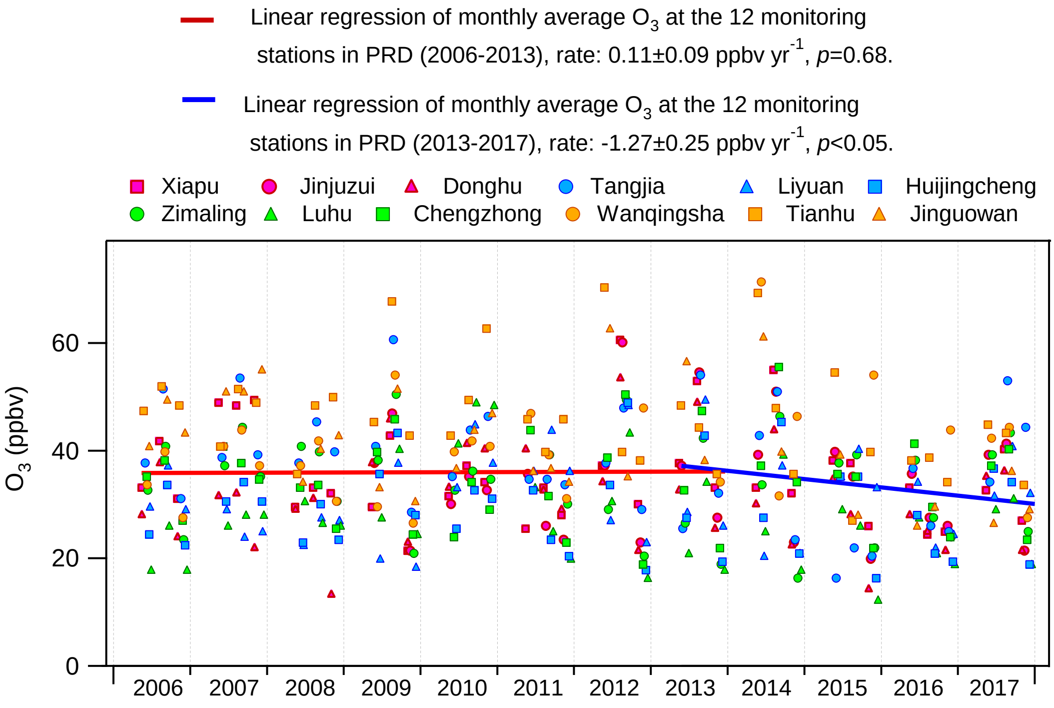

Figure 6.6 Trends of the observed monthly average O_3 at the 12 air quality monitoring stations in inland PRD.

6.4 Local production and destruction pathways of O_3 and OH radical

6.4.1 In-situ net O_3 production

Figure 6.7 shows the average diurnal profiles of the simulated O_3 production and destruction pathways during the three sampling campaigns. Also shown are the average diurnal cycles of the simulated O_3. The shift of the peaks between the net O_3 production rate and the simulated O_3 was due to the accumulation of the newly generated O_3 over time in the model, which was also true in the real situations. The reactions between NO_2 and O_3, leading to the formation of NO_3 and N_2O_5, in addition to dry deposition and aloft exchange, were the main depletions of the simulated O_3 in the late afternoon. Consistent with previous studies (Kanaya et al., 2009; Liu et al., 2012; Xue et al., 2014b), these pathways were not included in the calculation of the net O_3 production rate, because this study mainly focused on the photochemical processes in the hours when O_3 was accumulated. It was found that the reaction between HO_2 with NO dominated the O_3 production rates in all the cases, with an average rate of 3.7±0.7 ppbv h^{-1} (56.5±1.1%, percentage of the total O_3 production rate, same below), 2.5±0.3 ppbv h^{-1} (64.3±0.8%) and 1.4±0.2 ppbv h^{-1} (67.7±0.7%) in the 2007, 2013 and 2016 sampling campaigns, respectively. In addition, the sum of the reaction rates between RO_2 radicals and NO contributed 3.0±0.6 ppbv h^{-1} (43.5±1.1%), 1.5±0.2 ppbv h^{-1} (35.7±0.8%) and 0.7±0.1 ppbv h^{-1} (32.3±0.7%) to the O_3 production rate in 2007, 2013 and 2016, respectively.

The formation of HNO_3 though the reaction between OH and NO_2 served as the main scavenger pathway of O_3, as NO_2 would be photolyzed and produce O_3 otherwise. On average, O_3 was consumed in this way at a rate of -1.3±0.2 ppbv h^{-1} (80.7±3.3%, percentage of the total O_3 destruction rate, same below), -1.0±0.1 ppbv h^{-1} (79.3±1.8%) and -0.6±0.07 ppbv h^{-1} (81.6±2.0%) in 2007, 2013 and 2016, respectively. The photolysis of O_3 was the second contributor to O_3 destruction, with an average contribution of -0.11±0.01 ppbv h^{-1} (8.5±0.5%) for the three sampling periods. Besides, the ozonolysis of unsaturated VOCs and the reactions between O_3 and radicals (OH and HO_2) were responsible for 3.5±0.3% and 1.7±0.2% of the total destruction rate of the locally produced O_3, respectively.

Overall, the net local O_3 production rate decreased from 5.2±1.1 ppbv h^{-1} in 2007, to 2.7±0.4 ppbv h^{-1} in 2013, till 1.4±0.3 ppbv h^{-1} in 2016, corresponding to the decline of the locally produced O_3 from 2007 to 2016 (Section 6.3.2).

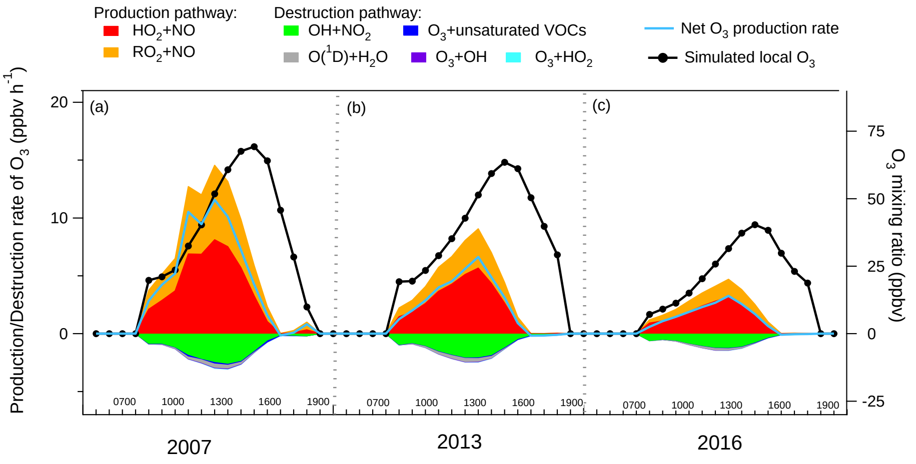

Figure 6.7 Average diurnal profiles of the local O_3 production and destruction rates in the sampling campaigns of (a) 2007, (b) 2013 and (c) 2016.

6.4.2 Cycling of OH radical

As one of the most important radicals in the atmosphere, OH initiates the oxidation of VOCs, leading to O_3 formation. Figure 6.8 presents the average diurnal profiles of the simulated OH and the formation and loss pathways dominating the recycling of OH during the three sampling periods, which roughly follow the typical pattern of the intensities of photochemical reactions, *i.e.* higher at noon and lower at the beginning and end of the day. On average, the simulated OH concentration was comparable (p = 0.4) between the 2007 sampling campaign ($(1.6\pm0.3)\times10^6$ molecules cm^{-3}) and the 2013 sampling campaign ($(1.5\pm0.2)\times10^6$ molecules cm^{-3}), but it decreased ($p < 0.05$) to $(1.0\pm0.2)\times10^6$ molecules cm^{-3} in the 2016 sampling campaign.

As expected, the formation and loss rates of OH were basically balanced in all the cases. OH was mainly formed from the reaction of HO_2+NO, which accounted for 69.8±1.1% of the total OH production rate over the three sampling campaigns. The photolysis of HONO ranked the second in supplying OH with the contribution of 22.0±1.4%. As stated in Section 3.3.2.1, the average diurnal cycle of HONO measured at TC in 2011 was adopted in the simulations. To assess the uncertainties, the HONO concentrations were also calculated according to the measured HONO/NO_x ratios and the NO_x concentrations at TC in the three sampling campaigns (Figure 6.9). To evaluate the uncertainties of adopting the HONO concentrations in 2011 in the model, the average diurnal cycles of HONO in the 2007, 2013 and 2016 sampling campaigns were calculated (Figure 6.5), according to the diurnal patterns of HONO/NO_x ratios determined at the same site (Xu et al., 2015). It was found that by adopting the values in 2011, the HONO concentrations were underestimated by 14.9% and 11.6% in 2007 and 2013, respectively, but were overestimated by 10.4% 2016. Further, the sensitivity tests indicated that the maximum underestimation (overestimation) of the total OH production rate was 2.3±2.3% (21.6±5.2%) in 2007, 5.8±1.3% (3.4±1.0%) in 2013 and 5.7±1.3% (3.4±0.9%) in 2016. It should be noted that the maximum overestimation of the total OH production rate in 2007 (21.6±5.2%) occurred at 07:00 LT when the OH recycling was weak. During 08:00 – 19:00 LT, both the underestimation and overestimation of the simulated total OH production rates were less than 3%. Therefore, it was concluded that the simulated OH formation and loss rates were not largely biased by adopting the measured HONO at TC in 2011 in all the simulations. Besides, the HONO concentrations calculated from the HONO/NO_x ratios and NO_x concentrations also had certain uncertainties. Thus, the calculated HONO concentrations were not used to constrain the model. In fact, the consistent input of the diurnal cycle of HONO concentrations in the three sampling campaigns enabled us to dig into the changes of O_3 and radical photochemistry induced by the other factors, such as VOCs, NO_x and meteorological conditions.

The formation of OH from HONO photolysis was most efficient in the early morning, which was explained by the morning peak of HONO concentration, due to the nocturnal heterogeneous formation and the vehicle emissions in morning rush hours. Apart from the two dominating pathways, O_3 photolysis (6.3±0.2%), ozonolysis of unsaturated VOCs (1.5±0.2%) and H_2O_2 photolysis (0.2±0.01%) also made some contributions to the formation of OH, with the highest rates at noon or in the afternoon when the productions of O_3 and H_2O_2 were the most intensive. To sum up, the total formation rates of OH from the primary sources (photolysis of HONO, O_3 and H_2O_2, and ozonolysis of VOCs) were lower than the recycling rates of OH

(HO_2+NO) throughout the day at TC, consistent with the results in Xue et al. (2016) simulated at the same site. The dominant role of HO_2+NO in OH formation at TC (average contribution of 69.8±1.1%) might be related to the abundant NO. This pathway was simulated to only account for 42.7±0.2% of the total OH formation rate at an island more than 40 km away from Hong Kong with very low NO concentrations, *i.e.* maximum of 0.56 ppbv (Wang Y. et al., 2018).

OH was mainly depleted by the reactions with VOCs (32.3±1.2%), NO_2 (31.9±0.9%), CO (19.3±0.6%) and NO (16.5±1.1%). The reaction rates of OH+NO (formation rates of HONO) got the highest values in the morning, roughly in line with the diurnal pattern of the HONO photolysis rates, which however were not completely balanced due to the constraint of HONO to observations in the model. The average net photolysis rates of HONO (differences between the HONO photolysis and formation rates) were $0.68\pm0.21\times10^6$, $0.70\pm0.12\times10^6$ and $0.87\pm0.12\times10^6$ molecules cm^{-3} s^{-1} in the 2007, 2013 and 2016 sampling campaign, respectively. The losses of OH through the other pathways all exhibited the highest efficiencies at noon or in the early afternoon. It should be noted that the reaction between OH and NO_2 was the sink of OH and was also a termination reaction in the photochemical system. In comparison, the termination reaction rates were lower than the OH formation rates from the primary sources (photolysis of HONO, O_3 and H_2O_2, and ozonolysis of VOCs) in the morning (7:00 – 10:00 LT), which were reversed in the following hours of the day due to the increases in OH concentrations.

Consistent with the variations of the local O_3 production, both the local formation and loss rates of OH decreased from 2007 to 2016 ($p < 0.05$), with much more obvious reductions in the later phase (2013-2016). On one hand, the continuous reduction of VOCs resulted in lower HO_2 and RO_2 concentrations (Figure 6.10), hence the lower production rate of OH through the reaction of HO_2+NO. At the same time, the destruction rates of OH also decreased due to the reductions of OH and the O_3 precursors, except for CO (Figure 6.8 and Table 6.2). The decreases of the OH production and destruction rates indicated that the propagation of the reaction cycles, namely the recycling of OH, became slower from 2007 to 2016. This also explained why the locally produced O_3 decreased in these ten years, since O_3 is formed with the consumption and recycling of OH radical.

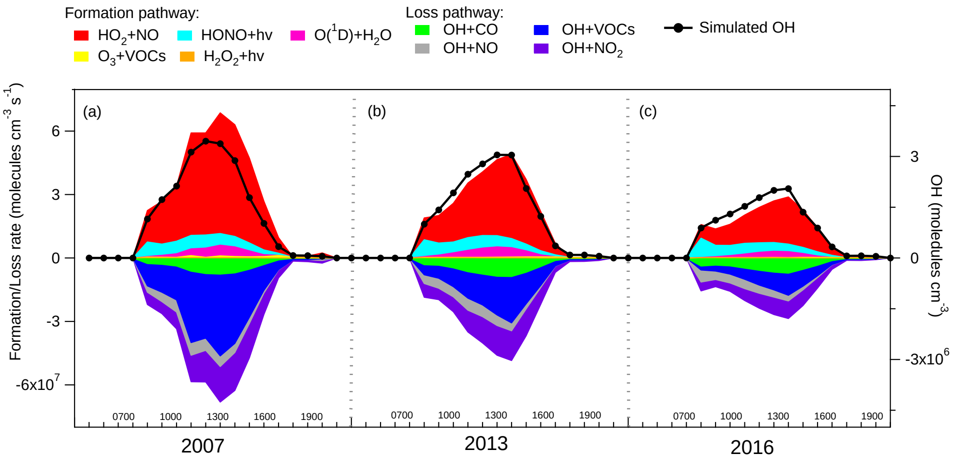

Figure 6.8 Average diurnal cycles of the OH formation and loss rates during the sampling periods in (a) 2007, (b) 2013 and (c) 2016.

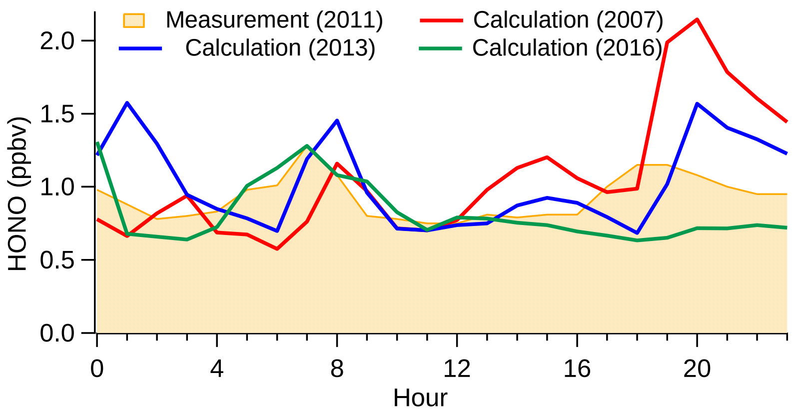

Figure 6.9 Diurnal cycles of HONO mixing ratios measured at TC in the autumn of 2011 and those calculated from the measured HONO/NO_x ratios and NO_x mixing ratios at the same site in the three sampling campaigns.

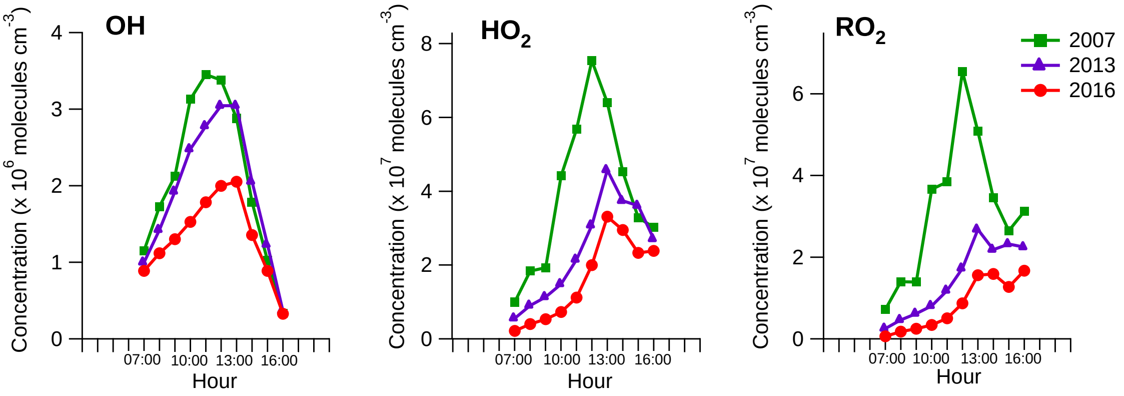

Figure 6.10 Average diurnal profiles of the simulated OH, HO_2 and RO_2 concentrations on VOC sampling days in 2007, 2013 and 2016. The rebounding of HO_2 and RO_2 concentrations in the late afternoon in 2007 and 2016 were caused by the substantial increases in the concentrations of some VOCs or OVOCs in several samples.

6.5 Source contributions to the production of O_3 and radicals

6.5.1 Source apportionment

To resolve the sources of O_3 precursors, 27 species, including CO, NO, NO_2, 12 alkanes, 4 alkenes and 8 aromatics, were applied to PMF for source apportionment. These species were either of high abundances or typical tracers of VOC sources in Hong Kong. Source apportionment was conducted for a total of 414 samples covering the three sampling periods, so that the uncertainty of the source apportionment results could be reduced, compared to separate source apportionments for each of the three sampling periods. Figure 6.11 shows the average profiles of the six sources resolved by PMF. The modelling errors were estimated with the bootstrap method integrated in PMF (Brown et al., 2015).

Factor 1 was assigned as the combination of LPG usage and gasoline evaporation, in view of the high loadings of C_2-C_5 hydrocarbons. Specifically, propane and *i*-/*n*-butanes are the main components of LPG in Hong Kong, and gasoline evaporation generally contains large quantities of *i*-/*n*-pentanes, in particularly *i*-pentane (Guo et al., 2013a; Lyu et al., 2017a). Factor 2 was characterized by moderate to high percentages of *i*-/*n*-pentanes and TEX (toluene, ethylbenzene and xylenes). These species are commonly seen in gasoline exhausts. Therefore, this factor was defined as gasoline exhausts. Both the third and fourth factors indicated solvent-related emissions. While Factor 3 likely represented household solvent usage, due to the dominance of hexane and hexane isomer (3-methylpentane) (Ling and Guo, 2014; Ou et al., 2015), Factor 4 was more related to emissions from coatings and paints, in view of the dominance of the aromatics (Ling and Guo, 2014). Factor 5 was distinguished by the high concentrations of ethane, ethene, ethyne and benzene, together with the relatively heavy (C_7-C_{10}) alkanes, which are typical species in diesel exhausts (Schauer et al., 1999; Kashdan et al., 2008; Sahoo et al., 2011). Therefore, this factor was designated as diesel exhausts. The last factor denoted for biogenic emissions (BVOCs), due to the exclusive dominance of isoprene (Guenther, 2006).

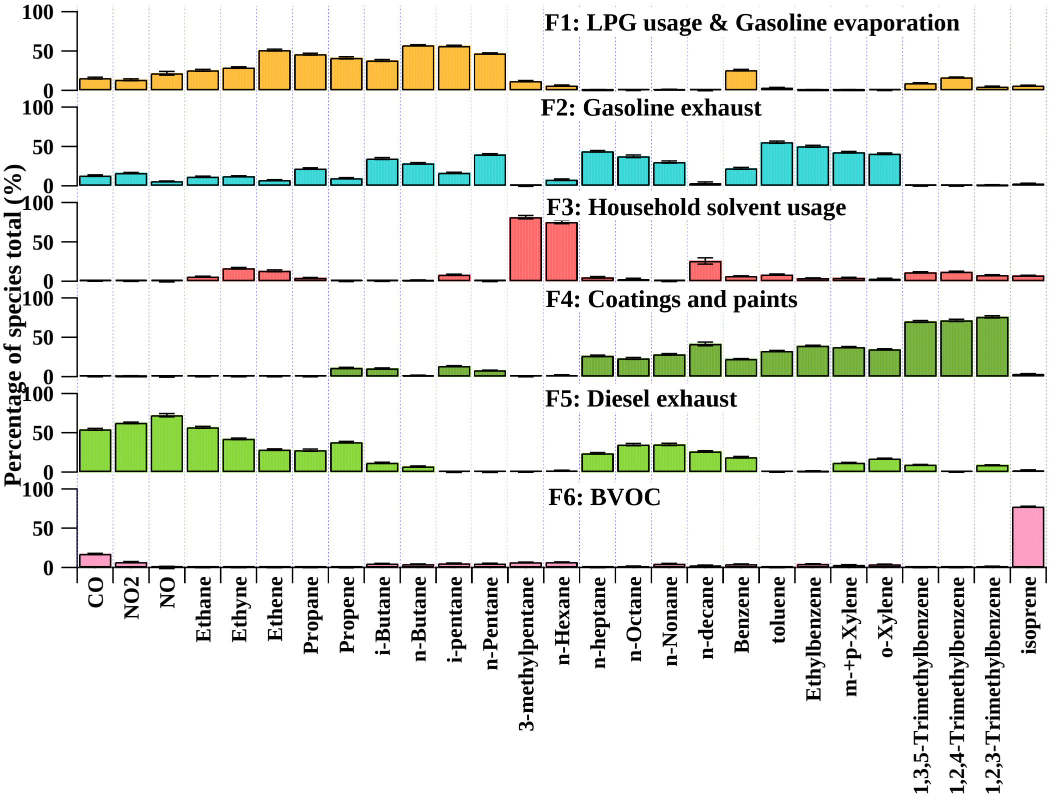

Figure 6.11 Average profiles of the O_3 precursors sources at TC in the three sampling campaigns. The uncertainties were estimated with the bootstrap method in PMF.

Figure 6.12 presents the total mixing ratio of VOCs emitted from each individual source extracted from PMF during the three sampling periods in Hong Kong. The VOC emissions from LPG usage and gasoline evaporation decreased significantly ($p < 0.05$) at a rate of -2.61±0.03 ppbv yr^{-1} from 2007 to 2016. However, the VOCs in association with gasoline exhausts experienced an increase (rate = 1.32±0.02 ppbv yr^{-1}, $p < 0.05$) in these years, indicating that the reduction of VOC emissions from LPG usage and gasoline evaporation was not attributable to the change in emissions of gasoline-fuelled vehicles. Insight into the mixing ratios of propane and *i*-/*n*-butanes (LPG tracers) in this source revealed a significant decline from 3.51±0.52 ppbv in the 2007 sampling campaign to 1.27±0.11 ppbv in the 2016 sampling campaign. Therefore, the reduction of VOC emissions from LPG usage was most likely the reason of the decrease of VOCs allocated to the source of LPG usage and gasoline evaporation. In fact, it was confirmed by previous studies (Lyu et al., 2016b; Yao et al., 2019) that the replacement of catalytic converters on LPG-fuelled vehicles during September 2013-May 2014 effectively reduced the VOC emissions from LPG-fuelled vehicles in Hong Kong. In addition, the variations in LPG usage in inland PRD, where LPG was extensively used as vehicular and domestic fuels (Liu et al., 2008b), might also contribute to the emission reduction of VOCs, in view of the decrease of LPG tracers in this source from 2007 (3.51±0.52 ppbv) to 2013 (2.04±0.27 ppbv), when no control was performed against LPG fuelled vehicle emissions in Hong Kong. The VOCs emitted from solvent usage (including the household solvent, coatings and paints) also decreased significantly ($p < 0.05$) from 2007 to 2016, likely benefiting from the actions taken to restrict the VOC contents in solvent products starting from 2007 (phase I) and 2010 (phase II) in Hong Kong (Lyu et al., 2017a). VOCs attributable to diesel exhausts decreased ($p < 0.05$) from the 2007 (2.6±0.3 ppbv) to 2013 sampling campaign (2.0±0.2 ppbv), which however were unchanged between 2013 and 2016 (2.2±0.2 ppbv). In fact, a subsidy program has been implemented in Hong Kong since 2007 to progressively eliminate the pre-Euro IV diesel vehicles or to upgrade their emission standards to Euro IV (HKEPD, 2017b), and the effectiveness of this program in VOC reductions till 2013 was confirmed by Lyu et al. (2017a) with the online measurement data at the same site. However, while the phase III of this program (2014-2019) is still ongoing, the VOCs emitted from diesel vehicles remained stable between the 2013 and 2016 sampling campaigns. This undesirable result might be due to the fact that the actions were mainly targeted at the pre-Euro, Euro I and Euro II diesel vehicles before 2013, whereas the phase III of the program initiated in 2014 focused on the Euro III vehicles (HKEPD, 2017b, 2018). Since the former were vehicles with higher emissions, it is not unreasonable that reduction of VOCs was more discernible between 2007 and 2013. Further, the effectiveness of the phase III program might be somewhat offset by the wearing-out of the pre-existing vehicles and the increase of diesel vehicle populations (Competition Commission, 2017). Further evaluation with more data in a longer period is recommended. At last, the increase of BVOCs from 2007 to 2013 but comparable levels between 2013 and 2016 seemed to be related to the lower ($p < 0.05$) temperature in the 2007 sampling campaign (Figure 6.13 and Table 6.4). Besides, the more frequent (62.8%) southeast winds from SCS with higher wind speeds (2.3±0.2 m s^{-1}) might also diluted BVOCs emitted from the terrestrial plants in the 2007 sampling campaign.

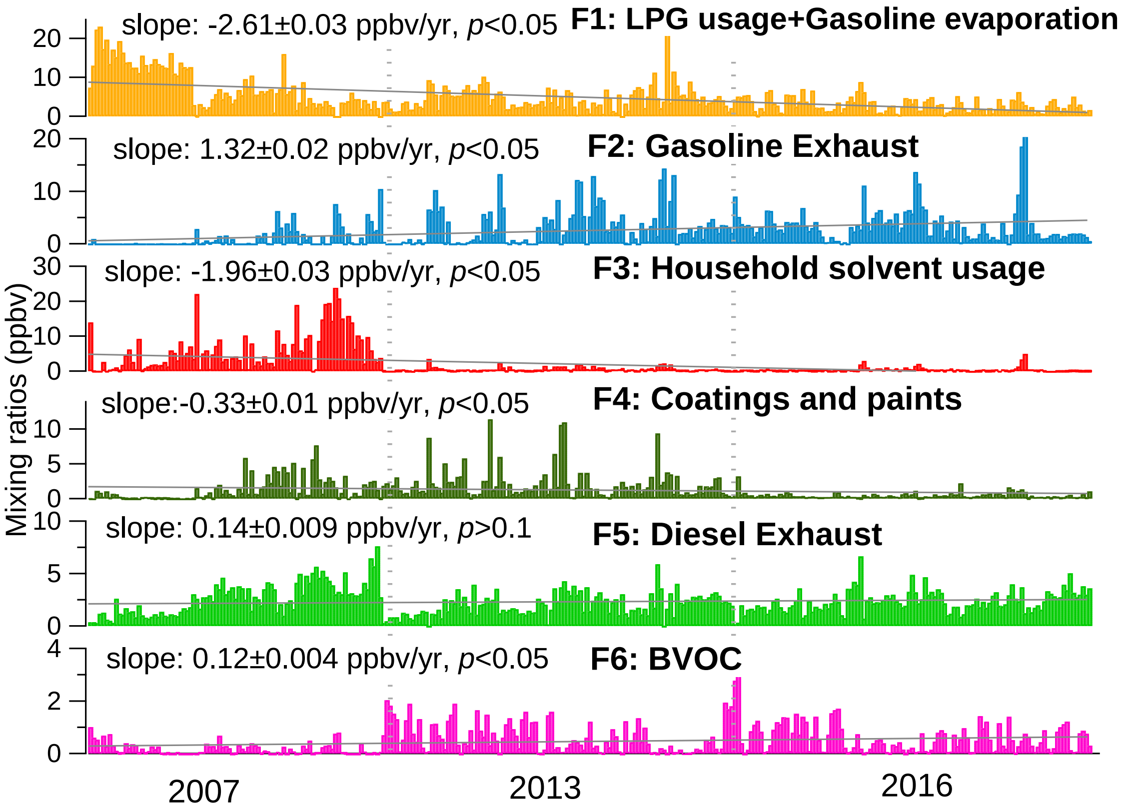

Figure 6.12 Total mixing ratio of VOCs emitted from each individual source extracted from PMF in the 2007, 2013 and 2016 sampling campaigns. The solid lines represent the linear regressions of the VOC mixing ratios against the sequence number of the samples, with the slope being converted to yearly rates.

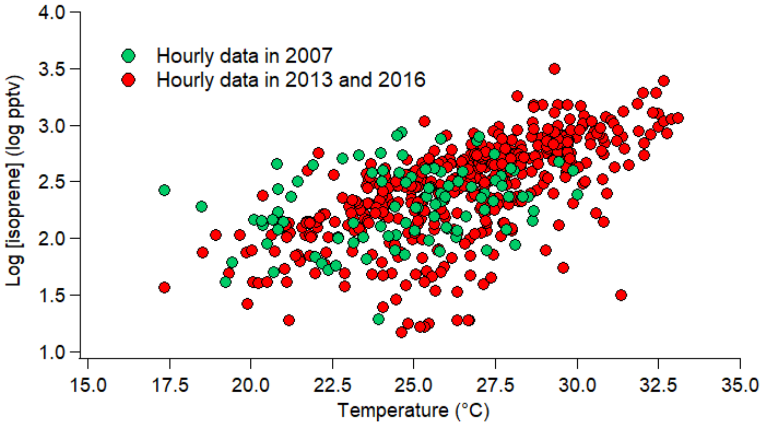

Figure 6.13 Relationship between the common logarithm of isoprene mixing ratios and temperature.

6.5.2 Source contributions to O_3 production

Figure 6.14 presents the contributions of VOCs emitted from individual sources to the production and destruction rates of O_3, as well as the simulated contributions to the O_3 mixing ratios. NO_x was not included in these analyses, because of its relatively high uncertainties in source apportionment results due to the short lifetimes. Consistent with the O_3 production and destruction in the whole air, the pathway of HO_2+NO dominated over the reactions between RO_2 and NO in O_3 production for all the individual sources. The destruction of O_3 was mainly driven by NO_2 reacting with OH. For the net O_3 production rate, VOCs attributable to the coatings and paints made the largest contribution (0.38±0.05 ppbv h^{-1}), followed by gasoline exhausts (0.22±0.03 ppbv h^{-1}), LPG and gasoline evaporation (0.21±0.03 ppbv h^{-1}), BVOCs (0.19±0.03 ppbv h^{-1}), household solvent usage (0.15±0.04 ppbv h^{-1}) and diesel exhausts (0.13±0.01ppbv h^{-1}). Despite some peak shifts for the reasons illustrated in Section 6.4.1, the O_3 mixing ratios elevated by the individual sources followed the same pattern as the net O_3 production rates, with the highest O_3 enhancement (1.92±0.21 ppbv) by the source of coatings and paints and the lowest increase by household solvent usage (0.86±0.06 ppbv) and diesel exhausts (0.83±0.06 ppbv). The contributions of source-specific VOCs to O_3 production, particularly the importance of solvent usage in O_3 formation in Hong Kong, were generally in line with previous studies (Ling and Guo, 2014; Ou et al., 2015). This was expected according to the reactivity of major VOCs in each source. For example, the TEX in the source of coatings and paints (Figure 6.11) have been identified to be of high O_3 formation potentials (Lau et al., 2010; Ling et al., 2011, 2013). However, the PBM-MCM model simulations enabled us to quantitatively evaluate the contributions of VOC sources to O_3 production rates.

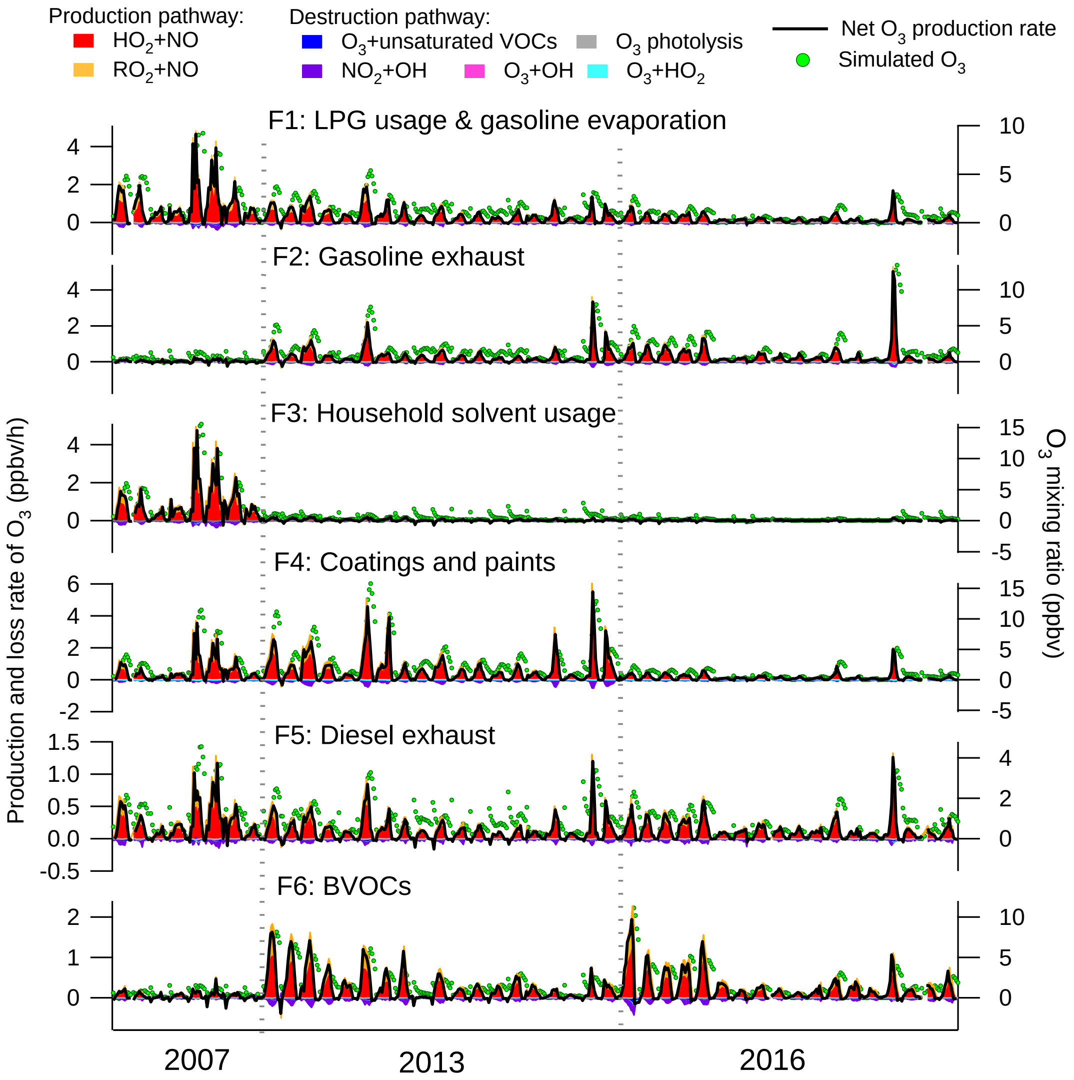

Figure 6.14 Contributions of VOCs in individual sources to the production and destruction rates of O_3 and to the O_3 mixing ratios in the three sampling campaigns.

From a historical perspective, it was found that the contribution of LPG usage and gasoline evaporation to O_3 production significantly decreased ($p < 0.05$) from 2007 to 2016 sampling campaign (2007: 0.51±0.11 ppbv h^{-1}; 2013: 0.20±0.03 ppbv h^{-1}; 2016: 0.10±0.02 ppbv h^{-1}), which coincided with the variations of VOCs emitted from LPG-fuelled vehicles as discussed above. Gasoline exhaust contributed much less ($p < 0.05$) to the net O_3 production rate in 2007 (0.02±0.01ppbv h^{-1}), than those in 2013 (0.26±0.05ppbv h^{-1}) and 2016 (0.27±0.07ppbv h^{-1}), in line with the variations of VOCs emitted from this source. The reductions of VOC emissions from solvents also resulted in the consistent decrease of the net O_3 production rate from

1.22±0.17 ppbv h^{-1} in the 2007 to 0.14±0.05 ppbv h^{-1} in the 2016 sampling campaign. The O_3 production rates contributed by VOCs in diesel exhausts were reduced from 2007 (0.21±0.05 ppbv h^{-1}) to 2013 (0.11±0.02 ppbv h^{-1}) and remained unchanged thereafter (2016: 0.11±0.02 ppbv/h). The O_3 production rate traceable to BVOCs showed a significant increase from 2007 (0.04±0.02 ppbv h^{-1}) to 2016 (0.22±0.04 ppbv h^{-1}), since the mixing ratios of BVOCs significantly increased ($p < 0.05$) in these years. It is noteworthy that the changes in meteorological conditions in these three sampling campaigns might also partially account for the variations in the source contributions to O_3 production. For example, the 2013 sampling campaign was characterized by the relatively higher temperature and lowest relative humidity among the three sampling periods, which favored O_3 formation in 2013 (Table 6.4). Besides, due to limited samples in this study, further assessments with more data in longer periods are recommended to be carried out in future study.

6.6 Summary

Photochemical pollution with high and increasing concentrations of O_3 has been an important environmental issue in South China. With the observation data of O_3 and its precursors at a suburban site in Hong Kong, downwind of South China, this study analyzed the inter-annual variations of O_3 and its photochemistry, as well as the contributions of VOC sources to the local O_3 production rates in 2007, 2013 and 2016. To my knowledge, this is the first time that a substantial alleviation of O_3 pollution in this region was identified between 2013 and 2016, in contrast to the repeatedly confirmed O_3 increase before 2013. In addition to the changes in meteorological conditions among the three sampling campaigns, the termination of the rise in regionally transported O_3 and the decrease of the local O_3 production rate contributed to the decline of O_3 in the later period. The emission reductions (particularly for NO_x) in mainland China starting from 2013, the year when the China’s Clean Air Action Plan was launched, might more or less play a role in ceasing the increase of regional O_3. In Hong Kong, the replacement of catalytic converters and the constraints of VOC contents in solvent products led to the reductions of VOC emissions from LPG-fuelled vehicles and solvent usage, respectively. As a result, the local O_3 production rate and the recycling rate of OH radical decreased substantially from 2013 to 2016. Though the variations in meteorological conditions and the limited sample size might somewhat introduce uncertainties to the conclusions drawn from the present study, it is plausible that the local and regional interventions were effective on the control of O_3 pollution in Hong Kong. Nevertheless, studies with more data in longer periods should be conducted, not only in Hong Kong but also in mainland China where O_3 is still increasing in most of the territories.

Chapter 7 Conclusions and suggestions for future study

7.1 Conclusions

This study focused on photochemical O_3 formation mechanism and radical chemistry in five Chinese megacities and PRE area through intensive field measurements and diverse model simulations. Specifically, this study investigated the spatial variations of O_3 photochemistry in urban areas of five major megacities in China; the photochemical O_3 formation mechanisms and radical chemistry in the PRE; and the inter-annual variations of O_3 formation mechanisms and radical chemistry in Hong Kong. The main findings are listed below.

1) Through the concurrent field measurements in five Chinese megacities in summer 2018, the spatial variations and photochemical formation mechanisms of O_3 pollution were evaluated. Compared to cities in eastern and southwestern China (*i.e.* Shanghai and Chengdu), cities in northwestern, northern and central China (*i.e.* Lanzhou, Beijing and Wuhan) had severer O_3 pollution, which was indicated by the higher net O_3 production rate and stronger atmospheric oxidative capacity.
2) After investigating the O_3-precursor relationship in the five megacities, it was found that O_3 formation in urban area of Lanzhou was controlled by both VOCs and NO_x, indicating cutting the two precursors would effectively reduce O_3 production, while it was mainly controlled by VOCs in the urban areas of the other four megacities. In these cities, the reduction of NO_x might increase O_3 production. In each megacity, the main VOC groups that led to O_3 formation were different, and more attention should be paid when formulating O_3 control strategies.
3) Study on the contribution of VOC sources to O_3 formation in five megacities revealed that diesel exhaust and solvent usage in Beijing contributed the most, while the industrial emissions in Lanzhou contributed to O_3 formation as much as diesel exhaust and solvent usage. Furthermore, O_3 formation in Shanghai, Wuhan and Chengdu was completely determined by VOCs from solvent usage.
4) Based on the simultaneous sampling campaigns at two banks of PRE in autumn 2016, it was found that the photochemical formation mechanisms of O_3 pollution varied on

different high O_3 days, which could be categorized into two patterns. In pattern 1, the O_3 pollution at both banks of PRE was severe, with large net O_3 production rates, high OH concentrations, and accelerated cycling rates of radicals over PRE area. However, in pattern 2, high O_3 events only occurred on the west bank of PRE, with much larger net O_3 production rate, higher OH concentration and stronger cycling rate of radicals than the east bank.

5) The O_3-precursor relationship on the two sides of PRE in both patterns were investigated. It was found that O_3 formation was always limited by VOCs at the east bank due to the large local NO_x emissions no matter which pattern it was. However, O_3 formation was controlled by both VOCs and NO_x at the west bank in pattern 1, but it was VOC-limited in pattern 2. Despite the differences in O_3 formation regimes in PRE in the two patterns, the top four VOC species that modulated O_3 formation at each bank of PRE were the same regardless of the patterns, which would help policy makers formulate appropriate measures at each sampling site.
6) During the period of 2007-2013, the locally produced O_3 in Hong Kong remained unchanged ($p = 0.73$) but the observed O_3 greatly increased ($p < 0.05$) driven by the rise ($p < 0.05$) in regionally transported O_3. However, although the regionally transported O_3 did not change ($p = 0.32$) from 2013 to 2016, both the locally produced and observed O_3 decreased significantly ($p < 0.05$) during this period.
7) The inter-annual O_3 study in Hong Kong revealed that both local net O_3 production rate and cycling rate of OH radical remarkably decreased ($p < 0.05$) from 2007 to 2016, which was mainly attributed to the air pollution control measures taken in Hong Kong during the last decade. Source apportionment results confirmed that the decrease of VOCs emitted from LPG usage and gasoline evaporation (decreasing rate: -2.61 ± 0.03 ppbv year^{-1}, $p < 0.05$) resulted in a reduction of local net O_3 production rate (~0.41 ppbv h^{-1}, $p < 0.05$) from 2007 to 2016. Meanwhile, the lowered VOCs emitted from solvent usage (decreasing rate: -2.29 ± 0.03 ppbv year^{-1}, $p < 0.05$) led to a lower contribution to local net O_3 production rate (~1.08 ppbv h^{-1}, $p < 0.05$) during this period.

7.2 Suggestions for future study

Although this study filled some knowledge gaps in the field of O_3 photochemistry in Chinese megacities and the PRE, many problems still need to be solved. To better understand the photochemical O_3 formation mechanisms in China, the following suggestions are proposed based on the findings of my study:

1) In view of the very short sampling period of this study in August 2018, it is strongly suggested to conduct a long-term study in different seasons in the five megacities. In addition, O_3 pollution in more major Chinese cities is worth investigating. The differences in O_3 formation mechanisms and radical chemistry between different land-use functional areas also need attention.
2) The regional impact of VOCs on O_3 formation in Chinese megacities deserves further exploration. Chemical Transport Models (CTMs) are better tools for studying physical dynamics on a regional scale. However, the chemical mechanisms in the CTMs are lumped-based, which lacks speciated photochemistry of VOCs that leads to O_3 formation. Combination of the explicit Master Chemical Mechanism (MCM) with the CTMs can better understand the impacts of VOC species on O_3 photochemistry.
3) Although this study presented the long-term trends of O_3 formation mechanisms and radical chemistry in Hong Kong, the field measurements were not conducted in consecutive periods. Therefore, it is suggested to conduct continuous field measurements of O_3 precursors, especially VOCs, to obtain more comprehensive data for a longer period. It is worth exploring the trend of O_3 pollution in Hong Kong after 2016, so the control measures implemented in the PRD region can be evaluated in recent years.
4) In this study, only the contribution of four OVOC species to O_3 formation was studied. Furthermore, when investigating their impacts on O_3 photochemistry, the primary and secondary OVOCs were not separated. Hence, it is suggested to conduct more comprehensive field measurements for more OVOC species in major cities and the PRE in China. In addition, the feedback of secondary OVOCs on net O_3 production should be explored in future study.

5) Considering the importance of HONO in O_3 formation, it is suggested to conduct HONO measurements in the five megacities, so that the photochemical O_3 formation mechanisms in each city can be more fully understood through PBM-MCM.

References

Alicke, B., Platt, U. and Stutz, J., 2002. Impact of nitrous acid photolysis on the total hydroxyl radical budget during the Limitation of Oxidant Production/Pianura Padana Produzione di Ozono study in Milan. Journal of Geophysical Research: Atmospheres, 107(D22).

An, J., Wang, J., Zhang, Y. and Zhu, B., 2017. Source apportionment of volatile organic compounds in an urban environment at the Yangtze River Delta, China. Archives of environmental contamination and toxicology, 72(3), 335-348.

Ashmore, M.R., 2005. Assessing the future global impacts of ozone on vegetation. Plant Cell and Environment, 28 (8), 949–964.

Atkinson, R., 2000. Atmospheric chemistry of VOCs and NOx. Atmospheric Environment, 34(12-14), 2063-2101.

Bannan, T.J., Booth, A.M., Bacak, A., Muller, J.B., Leather, K.E., Le Breton, M., Jones, B., Young, D., Coe, H., Allan, J. and Visser, S., 2015. The first UK measurements of nitryl chloride using a chemical ionization mass spectrometer in central London in the summer of 2012, and an investigation of the role of Cl atom oxidation. Journal of Geophysical Research: Atmospheres, 120(11), 5638-5657.

Barletta, B., Meinardi, S., Simpson, I.J., Zou, S., Rowland, F.S. and Blake, D.R., 2008. Ambient mixing ratios of nonmethane hydrocarbons (NMHCs) in two major urban centers of the Pearl River Delta (PRD) region: Guangzhou and Dongguan. Atmospheric Environment, 42(18), 4393-4408.

Bell, M.L., McDermott, A., Zeger, S.L., Samet, J.M. and Dominici, F., 2004. Ozone and short-term mortality in 95 US urban communities, 1987-2000. Journal of the American Medical Association, 292(19), 2372-2378.

Bell, M.L., Goldberg, R., Hogrefe, C., Kinney, P.L., Knowlton, K., Lynn, B., Rosenthal, J., Rosenzweig, C. and Patz, J.A., 2007. Climate change, ambient ozone, and health in 50 US cities. Climatic Change, 82(1-2), 61-76.

Bloss, C., Wagner, V., Jenkin, M., Volkamer, R., Bloss, W., Lee, J., Heard, D., Wirtz, K., Martin-Reviejo, M. and Rea, G. 2005. Development of a detailed chemical mechanism (MCMv3.1) for the atmospheric oxidation of aromatic hydrocarbons. Atmospheric Chemistry and Physics, European Geosciences Union, 5 (3), 641-664.

Brown, S. G., Frankel, A., and Hafner, H. R., 2007. Source apportionment of VOCs in the Los Angeles area using positive matrix factorization, Atmospheric Environment, 41, 227-237.

Brown, S.S. and Stutz, J., 2012. Nighttime radical observations and chemistry. Chemical Society Reviews, 41(19), 6405-6447.

Brown, S. G., Eberly, S., Paatero, P., and Norris, G. A., 2015. Methods for estimating uncertainty in PMF solutions, Science of the Total Environment, 518, 626-635.

Cai, C., Geng, F., Tie, X., Yu, Q. and An, J., 2010. Characteristics and source apportionment of VOCs measured in Shanghai, China. Atmospheric Environment, 44(38), 5005-5014.

Cardelino, C.A. and Chameides, W.L., 1995. An observation-based model for analyzing ozone precursor relationships in the urban atmosphere. Journal of the Air and Waste Management Association, 45(3), 161-180.

Carter, W.P., 1994. Development of ozone reactivity scales for volatile organic compounds. Air Waste, 44 (7), 881-899.

Carter, W.P. 2000a. Implementation of the SAPRC-99 chemical mechanism into the Models-3 framework. Report to the United States Environmental Protection Agency, 29 January 2000.

Carter, W.P. 2000b. Documentation of the SAPRC-99 chemical mechanism for VOC reactivity assessment. Contract, 92, 95-308.

Carter, W.P. 2010. Development of the SAPRC-07 chemical mechanism. Atmospheric Environment, 44, 5324-5335.

Chameides, W.L. and Walker, J.C., 1973. A photochemical theory of tropospheric ozone. Journal of Geophysical Research,78(36): 8751–8760.

Chameides, W.L. and Walker, J.C., 1976. A time-dependent photochemical model for ozone near the ground. Journal of Geophysical Research, 81(3), 413-420.

Chameides, W.L., Fehsenfeld, F., Rodgers, M.O., Cardelino, C., Martinez, J., Parrish, D., Lonneman, W., Lawson, D.R., Rasmussen, R.A., Zimmerman, P. and Greenberg, J., 1992. Ozone precursor relationships in the ambient atmosphere. Journal of Geophysical Research: Atmospheres, 97(D5), 6037-6055.

Chameides, W.L., Yu, H., Liu, S.C., Bergin, M., Zhou, X., Mearns, L., Wang, G., Kiang, C.S., Saylor, R.D., Luo, C. and Huang, Y., 1999. Case study of the effects of atmospheric aerosols and regional haze on agriculture: an opportunity to enhance crop yields in China through emission controls? Proceedings of the National Academy of Sciences, 96(24), 13626-13633.

Chan, L.Y., Chan, C.Y. and Qin, Y., 1998a. Surface ozone pattern in Hong Kong. Journal of Applied Meteorology, 37(10), 1153-1165.

Chan, L.Y., Liu, H.Y., Lam, K.S., Wang, T., Oltmans, S.J. and Harris, J.M., 1998b. Analysis of the seasonal behavior of tropospheric ozone at Hong Kong. Atmospheric Environment, 32(2), 159-168.

Chang, K.L., Petropavlovskikh, I., Cooper, O.R., Schultz, M.G., Wang, T., Helmig, D. and Lewis, A., 2017. Regional trend analysis of surface ozone observations from monitoring networks in eastern North America, Europe and East Asia. Elementa: Science of the Anthropocene, 5: 50.

Cheng, H., Guo, H., Wang, X., Saunders, S.M., Lam, S.H.M., Jiang, F., Wang, T., Ding, A., Lee, S. and Ho, K.F., 2010. On the relationship between ozone and its precursors in the Pearl River Delta: application of an observation-based model (OBM). Environmental Science and Pollution Research, 17(3), 547-560.

Cheng, H. R., Saunders, S. M., Guo, H., Louie, P. K. K., and Jiang, F., 2013. Photochemical trajectory modeling of ozone concentrations in Hong Kong, Environmental Pollution180, 101-110.

Cheng, N., Li, Y., Zhang, D., Chen, T., Sun, F., Chen, C. and Meng, F., 2016. Characteristics of ground ozone concentration over Beijing from 2004 to 2015: Trends, transport, and effects of reductions. Atmospheric Chemistry and Physics Discussion, doi:10.5194/acp-2016-508.

Chin, M., Jacob, D.J., Munger, J.W., Parrish, D.D. and Doddridge, B.G., 1994. Relationship of ozone and carbon monoxide over North America. Journal of Geophysical Research: Atmospheres, 99(D7), 14565-14573.

China Council for International Cooperation on Environment and Development (CCICED), 2019. Targets and Paths for environmental quality improvement by 2035. http://www.cciced.net/zcyj/yjbg/zcyjbg/2019/201908/P020190830109949890545.pdf (last access: 9 November 2020).

Chinese Meteorological Administration (CMA), 2019. China Climate Bulletin of 2018. http://zwgk.cma.gov.cn/zfxxgk/gknr/qxbg/201903/t20190319_1709281.html (last access: 17 December 2020).

Chou, C.C.K., Liu, S.C., Lin, C.Y., Shiu, C.J. and Chang, K.H., 2006. The trend of surface ozone in Taipei, Taiwan, and its causes: Implications for ozone control strategies. Atmospheric Environment, 40(21), 3898-3908.

Chou, C.C.K., Tsai, C.Y., Shiu, C.J., Liu, S.C. and Zhu, T., 2009. Measurement of NOy during campaign of air quality research in Beijing 2006 (CAREBeijing-2006): Implications for the ozone production efficiency of NOx. Journal of Geophysical Research: Atmospheres, 114(D2).

Coates, J., Mar, K.A., Ojha, N. and Butler, T.M., 2016. The influence of temperature on ozone production under varying NOx conditions–a modelling study. Atmospheric Chemistry and Physics,16(18), 11601-11615.

Colman, J. J., Swanson, A. L., Meinardi, S., Sive, B. C., Blake, D. R., and Rowland, F. S., 2001. Description of the analysis of a wide range of volatile organic compounds in whole air samples collected during PEM-Tropics A and B, Anal. Chem., 73, 3723-3731.

Competition Commission, 2017. Report on Study into Hong Kong’s Auto-fuel Market, available at:

https://www.compcomm.hk/en/media/press/files/Full_Report_Auto_fuel_Market_Study_Report_Eng.pdf (last access: 25 October 2018).

Cooper, O.R., Parrish, D.D., Stohl, A., Trainer, M., Nédélec, P., Thouret, V., Cammas, J.P., Oltmans, S.J., Johnson, B.J., Tarasick, D. and Leblanc, T., 2010. Increasing springtime ozone mixing ratios in the free troposphere over western North America. Nature, 463(7279), 344-348.

Crutzen, P.J. 1973. A discussion of the chemistry of some minor constituents in the stratosphere and troposphere. Pure and Applied Geophysics, 106, 1385-1399.

Crutzen PJ. 1974. Photochemical reactions initiated by and influencing ozone in the unpolluted troposphere. Tellus, 26: 47–57.

Crutzen, P. J., 1995. Overview of tropospheric chemistry: Developments during the past quarter century and a look ahead. Faraday Discussions, 100, 1-21.

Cui, J., Pandey Deolal, S., Sprenger, M., Henne, S., Staehelin, J., Steinbacher, M., and Nédélec, P., 2011. Free tropospheric ozone changes over Europe as observed at Jungfraujoch (1990–2008): An analysis based on backward trajectories, Journal of Geophysical Research: Atmospheres, 116, D10304.

Deng, Y., Li, J., Li, Y., Wu, R. and Xie, S., 2019. Characteristics of volatile organic compounds, NO2, and effects on ozone formation at a site with high ozone level in Chengdu. Journal of Environmental Sciences, 75, 334-345.

Derwent, R.G., Manning, A.J., Simmonds, P.G., Spain, T.G. and O'Doherty, S., 2013. Analysis and interpretation of 25 years of ozone observations at the Mace Head Atmospheric Research Station on the Atlantic Ocean coast of Ireland from 1987 to 2012. Atmospheric Environment, 80, 361-368.

Ding, A., Wang, T., Zhao, M., Wang, T. and Li, Z., 2004. Simulation of sea-land breezes and a discussion of their implications on the transport of air pollution during a multi-day ozone episode in the Pearl River Delta of China. Atmospheric Environment, 38(39), 6737-6750.

Ding, A.J., Wang, T., Thouret, V., Cammas, J.P. and Nédélec, P., 2008. Tropospheric ozone climatology over Beijing: analysis of aircraft data from the MOZAIC program. Atmospheric Chemistry and Physics, 8(1), 1-13.

Ding, A.J., Fu, C.B., Yang, X.Q., Sun, J.N., Zheng, L.F., Xie, Y.N., Herrmann, E., Nie, W., Petäjä, T., Kerminen, V.M. and Kulmala, M., 2013. Ozone and fine particle in the western Yangtze River Delta: an overview of 1 yr data at the SORPES station. Atmospheric Chemistry and Physics, 13(11), 5813-5830.

Dodge, M.C., 2000. Chemical oxidant mechanisms for air quality modeling: critical review. Atmospheric Environment, 34(12-14), 2103-2130.

Dongguan Environment Protection Department (DGEPD), 2013. Clean air action plan in Pearl River Delta region, Phase II (2013-2015), available at:

http://dgepb.dg.gov.cn/publicfiles///business/htmlfiles/dgepb/cmsmedia/document/doc172679.pdf (last access: 22 December 2020).

Duan, J., Tan, J., Yang, L., Wu, S. and Hao, J., 2008. Concentration, sources and ozone formation potential of volatile organic compounds (VOCs) during ozone episode in Beijing. Atmospheric Research, 88(1), 25-35.

Duncan, B.N., Lamsal, L.N., Thompson, A.M., Yoshida, Y., Lu, Z., Streets, D.G., Hurwitz, M.M. and Pickering, K.E., 2016. A space-based, high-resolution view of notable changes in urban NOx pollution around the world (2005–2014). Journal of Geophysical Research: Atmospheres, 121(2), 976-996.

Elshorbany, Y.F., Kurtenbach, R., Weisen, P., Lissi, E., Rubio, R., Villena, G., Gramsch, E., Rickard, A.R., Pilling, M.J. and Kleffmann, J., 2009a. Oxidation capacity of the city air of Santiago, Chile. Atmospheric Chemistry and Physics, 9(6), 2257–2273.

Elshorbany, Y.F., Kleffmann, J., Kurtenbach, R., Rubio, M., Lissi, E., Villena, G., Gramsch, E., Rickard, A., Pilling, M. and Wiesen, P. 2009b. Summertime photochemical ozone formation in Santiago, Chile. Atmospheric Environment, 43, 6398-6407.

Emmerson, K.M., Carslaw, N., Carpenter, L.J., Heard, D.E., Lee, J.D. and Pilling, M.J., 2005. Urban atmospheric chemistry during the PUMA campaign 1: Comparison of modelled OH and HO2 concentrations with measurements. Journal of Atmospheric Chemistry, 52(2), 143-164.

Emmerson, K.M., Carslaw, N., Carslaw, D.C., Lee, J.D., Mcfiggans, G., Bloss, W.J., Gravestock, T., Heard, D.E., Hopkins, J., Ingham, T. and Pilling, M.J., 2007. Free radical modelling studies during the UK TORCH Campaign in Summer 2003. Atmospheric Chemistry and Physics, European Geosciences Union, 7 (1), 167-181.

Feister U, Warmbt WG. 1987. Long-term measurements of surface ozone in the German Democratic Republic. J. Atmospheric Chemistry, 5: 1–21.

Fishman, J. and Crutzen, P.J., 1978. The origin of ozone in the troposphere. Nature, 274(5674), 855-858.

Fu, Y., Liao, H. and Yang, Y., 2019. Interannual and decadal changes in tropospheric ozone in China and the associated chemistry-climate interactions: A review. Advances in Atmospheric Sciences, 36(9), 975-993.

Gao, M., Gao, J., Zhu, B., Kumar, R., Lu, X., Song, S., Zhang, Y., Jia, B., Wang, P., Beig, G., Hu, J., Ying, Q., Zhang, H., Sherman, P. and McElroy, M., 2020. Ozone pollution over China and India: seasonality and sources. Atmospheric Chemistry and Physics, 20, 4399-4414.

Gao, W., Tie, X., Xu, J., Huang, R., Mao, X., Zhou, G. and Chang, L. 2017. Long-term trend of O3 in a mega City (Shanghai), China: Characteristics, causes, and interactions with precursors. Sci Total Environ, 603-604, 425-433.

Gaudel, A., Cooper, O.R., Ancellet, G., Barret, B., Boynard, A., Burrows, J.P., Clerbaux, C., Coheur, P.F., Cuesta, J., Cuevas, E. and Doniki, S., 2018. Tropospheric Ozone Assessment Report: Present-day distribution and trends of tropospheric ozone relevant to climate and global atmospheric chemistry model evaluation. Elementa: Science of the Anthropocene, 6, 39, 1-58.

Geng, F., Tie, X., Xu, J., Zhou, G., Peng, L., Gao, W., Tang, X. and Zhao, C., 2008. Characterizations of ozone, NOx, and VOCs measured in Shanghai, China. Atmospheric Environment, 42(29), 6873-6883.

Geng, F.H., Zhang, Q., Tie, X.X., Huang, M.Y., Ma, X.C., Deng, Z.Z., Yu, Q., Quan, J.N., Zhao, C.S., 2009. Aircraft measurements of O3, NOx, CO, VOCs, and SO2 in the Yangtze River Delta region. Atmospheric Environment, 43, 584–593.

George, I. J., Matthews, P. S. J., Whalley, L. K., Brooks, B., Goddard, A., Baeza-Romero, M. T., and Heard, D. E., 2013. Measurements of uptake coefficients for heterogeneous loss of HO_2 onto submicron inorganic salt aerosols, Phys. Chem. Chem. Phys., 15, 12829-12845.

Gery, M., Whitten, G., Killus, J. and Dodge, M.C. 1988. Development and testing of the CBM-IV for urban and regional modeling. U.S. Environmental Protection Agency, Atmospheric Sciences Research Laboratory, 1 January 1988, EPA/600/S3-88/012.

Goliff, W.S., Stockwell, W.R. and Lawson, C.V. 2013. The regional atmospheric chemistry mechanism, version 2. Atmospheric Environment, 68, 174-185.

Grell, G. A., Peckham, S. E., Schmitz, R., McKeen, S. A., Frost, G., Skamarock, W. C., and Eder, B., 2005. Fully coupled "online" chemistry within the WRF model. Atmospheric Environment, 39, 6957-6975.

Guenther, A., Karl, T., Harley, P., Wiedinmyer, C., Palmer, P.I. and Geron, C., 2006. Estimates of global terrestrial isoprene emissions using MEGAN (model of emissions of gases and aerosols from nature). Atmospheric Chemistry and Physics, 6, 11, 3181-3210.

Guerreiro, C.B., Foltescu, V. and De Leeuw, F., 2014. Air quality status and trends in Europe. Atmospheric Environment, 98, 376-384.

Guo, H., T. Wang and P. K. K. Louie, 2004. Source apportionment of ambient non-methane hydrocarbons in Hong Kong: Application of a principal component analysis/absolute principal component scores (PCA/APCS) receptor model. Environmental Pollution, 129, 489-498.

Guo, H., T. Wang, D. R. Blake, I. J. Simpson, Y. H. Kwok and Y. S. Li, 2006. Regional and local contributions to ambient non-methane volatile organic compounds at a polluted rural/coastal site in Pearl River Delta, China. Atmospheric Environment, 40, 2345-2359.

Guo, H., K. L. So, I. J. Simpson, B. Barletta, S. Meinardi and D. R. Blake, 2007. C1–C8 volatile organic compounds in the atmosphere of Hong Kong: Overview of atmospheric processing and source apportionment. Atmospheric Environment, 41, 1456-1472.

Guo, H., Jiang, F., Cheng, H.R., Simpson, I.J., Wang, X.M., Ding, A.J., Wang, T.J., Saunders, S.M., Wang, T., Lam, S.H.M. and Blake, D.R., 2009. Concurrent observations of air pollutants at two sites in the Pearl River Delta and the implication of regional transport. Atmospheric Chemistry and Physics, 9(19), 7343-7360.

Guo, H., H. R. Cheng, Z. H. Ling, P. K. Louie and G. A. Ayoko, 2011. Which emission sources are responsible for the volatile organic compounds in the atmosphere of Pearl River Delta? Journal of Hazardous Materials, 188, 116-24.

Guo, H., Ling, Z. H., Cheung, K., Jiang, F., Wang, D. W., Simpson, I. J., Barletta, B., Meinardi, S., Wang, T. J., Wang, X. M., Saunders, S. M., and Blake, D. R., 2013a. Characterization of photochemical pollution at different elevations in mountainous areas in Hong Kong, Atmospheric Chemistry and Physics, 13, 3881-3898.

Guo, H., Ling, Z. H., Cheung, K., Wang, D. W., Simpson, I. J., and Blake, D. R., 2013b. Acetone in the atmosphere of Hong Kong: Abundance, sources and photochemical precursors, Atmospheric Environment, 65, 80-88.

Guo, H., Ling, Z.H., Cheng, H.R., Simpson, I.J., Lyu, X.P., Wang, X.M., Shao, M., Lu, H.X., Ayoko, G., Zhang, Y.L. and Saunders, S.M., 2017. Tropospheric volatile organic compounds in China. Science of the Total Environment, 574, 1021-1043.

Haagen-Smit, A.J., 1952. Chemistry and physiology of Los Angeles smog. Industrial and Engineering Chemistry, 44(6), 1342-1346.

Han, M., Lu, X., Zhao, C., Ran, L. and Han, S., 2015. Characterization and source apportionment of volatile organic compounds in urban and suburban Tianjin, China. Advances in Atmospheric Sciences, 32(3), 439-444.

Han, S., Yao, Q., Tie, X., Zhang, Y., Zhang, M., Li, P. and Cai, Z. 2020. Analysis of surface and vertical measurements of O3 and its chemical production in the NCP region, China. Atmospheric Environment, 241, 117759.

Hao, J., Wu, Y., Fu, L., He, D. and He, K., 2001. Source contributions to ambient concentrations of CO and NOx in the urban area of Beijing. Journal of Environmental Science and Health, Part A, 36(2), 215-228.

Ho, K.F., Lee, S.C., Guo, H. and Tsai, W.Y., 2004. Seasonal and diurnal variations of volatile organic compounds (VOCs) in the atmosphere of Hong Kong. Science of the Total Environment, 322(1-3), 155-166.

Ho, K.F., Lee, S.C., Ho, W.K., Blake, D.R., Cheng, Y., Li, Y.S., Ho, S.S.H., Kung, K., Louise, P.K.K. and Park, D., 2009. Vehicular emission of volatile organic compounds (VOCs) from a tunnel study in Hong Kong. Atmospheric Chemistry and Physics, 9 (19), 7491-7504.

Hong Kong Environmental Protection Department (HKEPD), 2017a. Air quality in Hong Kong 2016. https://www.aqhi.gov.hk/mobile/api_history/english/report/files/AQR2016e_final.pdf (last access: 22 December 2020).

Hong Kong Environmental Protection Department (HKEPD), 2017b. Cleaning the Air at Street Level, available at: http://www.epd.gov.hk/epd/english/environmentinhk/air/prob_solutions /strategies_apc.html (last access: 25 October 2018).

Hong Kong Environmental Protection Department (HKEPD), 2018. Phasing Out Pre-Euro IV Diesel Commercial Vehicles, available at: https://www.epd.gov.hk/epd/english /environmentinhk/air/prob_solutions/Phasing_out_diesel_comm_veh.html (last access: 25 October 2018).

Hong Kong Observatory (HKO), 2017. Real-time Data Display from ENVF Atmospheric and Environmental Database, available at: http://envf.ust.hk/dataview/hko_wc/current/ (last access: 25 October 2018).

Hong Kong Observatory (HKO), 2021. Climate in Hong Kong, available at: https://www.hko.gov.hk/en/cis/climahk.htm (last access: 1 April 2021).

Huang, J.P., Fung, J.C., Lau, A.K. and Qin, Y., 2005. Numerical simulation and process analysis of typhoon-related ozone episodes in Hong Kong. Journal of Geophysical Research: Atmospheres, 110(D05301).

Huang, Y., Ling, Z.H., Lee, S.C., Ho, S.S.H., Cao, J.J., Blake, D.R., Cheng, Y., Lai, S.C., Ho, K.F., Gao, Y. and Cui, L., 2015. Characterization of volatile organic compounds at a roadside environment in Hong Kong: an investigation of influences after air pollution control strategies. Atmospheric Environment, 122, 809-818.

Hui, L., Liu, X., Tan, Q., Feng, M., An, J., Qu, Y., Zhang, Y. and Jiang, M., 2018. Characteristics, source apportionment and contribution of VOCs to ozone formation in Wuhan, Central China. Atmospheric Environment, 192, 55-71.

IPCC (Intergovernmental Panel on Climate Change). 2013. Working Group I contribution to the IPCC Fifth Assess-ment Report “Climate Change 2013: The Physical Science Basis”, Final Draft Underlying Scientific-Technical Assessment. https://www.ipcc.ch/site/assets/uploads/2018/03/WG1AR5_SummaryVolume_FINAL.pdf (last access: 15 December 2020).

Jacob, D. J. 1999. Introduction to atmospheric chemistry. Princeton university press, Princeton, New Jersey

Jenkin, M. E., Saunders, S. M., and Pilling, M. J., 1997 The tropospheric degradation of volatile organic compounds: a protocol for mechanism development, Atmospheric Environment, 31, 81-104.

Jenkin, M. E., Saunders, S. M., Wagner, V., and Pilling, M. J., 2003. Protocol for the development of the Master Chemical Mechanism, MCM v3 (Part B): tropospheric degradation of aromatic volatile organic compounds, Atmospheric Chemistry and Physics, 3, 181-193.

Jenkin, M., Wyche, K., Evans, C., Carr, T., Monks, P., Alfarra, M., Barley, M., McFiggans, G., Young, J. and Rickard, A. 2012. Development and chamber evaluation of the MCM v3.

2 degradation schemes for β-caryophyllene. Atmospheric Chemistry and Physics, 12, 5275-5308.

Jenkin, M., Young, J. and Rickard, A. 2015. The MCM v3. 3.1 degradation scheme for isoprene. Atmospheric Chemistry and Physics, 15, 11433.

Jia, C., Mao, X., Huang, T., Liang, X., Wang, Y., Shen, Y., Jiang, W., Wang, H., Bai, Z., Ma, M., Yu, Z., Ma, J. and Gao, H., 2016. Non-methane hydrocarbons (NMHCs) and their contribution to ozone formation potential in a petrochemical industrialized city, Northwest China. Atmospheric Research, 169, 225-236.

Jiang, F., Guo, H., Wang, T.J., Cheng, H.R., Wang, X.M., Simpson, I.J., Ding, A.J., Saunders, S.M., Lam, S.H.M. and Blake, D.R., 2010. An ozone episode in the Pearl River Delta: Field observation and model simulation. Journal of Geophysical Research: Atmospheres, 115(D22).

Jiang, Y.C., Zhao, T.L., Liu, J., Xu, X.D., Tan, C.H., Cheng, X.H., Bi, X.Y., Gan, J.B., You, J.F. and Zhao, S.Z., 2015. Why does surface ozone peak before a typhoon landing in southeast China? Atmospheric Chemistry and Physics Discussions, 15(18).

Jin, X. and Holloway, T., 2015. Spatial and temporal variability of ozone sensitivity over China observed from the Ozone Monitoring Instrument. Journal of Geophysical Research: Atmospheres, 120(14), 7229-7246.

Johnson, B.T., 2008. Diesel engine emissions and their control, Platinum Metals Review, 52, 23-37.

Jones, M.D., 2014. Catalytic transformation of ethanol into 1, 3-butadiene. Chemistry Central Journal, 8(1), 1-5.

Jorquera, H. and Rappenglück, B., 2004. Receptor modeling of ambient VOC at Santiago, Chile. Atmospheric Environment, 38(25), 4243-4263.

Kanaya, Y., Cao, R., Akimoto, H., Fukuda, M., Komazaki, Y., Yokouchi, Y., Koike, M., Tanimoto, H., Takegawa, N. and Kondo, Y., 2007. Urban photochemistry in central Tokyo: 1. Observed and modeled OH and HO2 radical concentrations during the winter and summer of 2004. Journal of Geophysical Research: Atmospheres, 112(D21).

Kanaya, Y., Pochanart, P., Liu, Y., Li, J., Tanimoto, H., Kato, S., Suthawaree, J., Inomata, S., Taketani, F., Okuzawa, K. and Kawamura, K., 2009. Rates and regimes of photochemical ozone production over Central East China in June 2006: a box model analysis using comprehensive measurements of ozone precursors. Atmospheric Chemistry and Physics,9(20), 7711-7723.

Kashdan, J.T., 2008. Tracer LIF Visualisation Studies of Piston-Top Fuel Films in a Wall-Guided, Low-NO_x Diesel Engine, SAE Tech. Paper, 2008-01-2474.

Killus, J. and Whitten, G. 1982. A new carbon-bond mechanism for air quality modeling. Report. US Environ. Prot. Agency, DC. EPA-600/3-82-041.

Knighton, W.B., Herndon, S.C., Wood, E.C., Fortner, E.C., Onasch, T.B., Wormhoudt, J., Kolb, C.E., Lee, B.H., Zavala, M., Molina, L. and Jones, M., 2012. Detecting fugitive emissions of 1, 3-butadiene and styrene from a petrochemical facility: An application of a mobile laboratory and a modified proton transfer reaction mass spectrometer. Industrial and Engineering Chemistry Research, 51(39), 12706-12711.

Kryza, M., Werner, M., Dudek, J. and Dore, A.J., 2020. The effect of emission inventory on modelling of seasonal exposure metrics of particulate matter and ozone with the WRF-Chem model for Poland. Sustainability, 12(13), p.5414.

Lai, C.H., Chang, C.C., Wang, C.H., Shao, M., Zhang, Y. and Wang, J.L., 2009. Emissions of liquefied petroleum gas (LPG) from motor vehicles. Atmospheric Environment, 43(7), 1456-1463.

Lakey, P. S. J., George, I. J., Whalley, L. K., Baeza-Romero, M. T., and Heard, D. E., 2015. Measurements of the HO_2 uptake coefficients onto single component organic aerosols, Environmental Science and Technology., 49, 4878-4885.

Lam, K. S., Wang, T. J., Wu, C. L., and Li, Y. S., 2005. Study on an ozone episode in hot season in Hong Kong and transboundary air pollution over Pearl River Delta region of China, Atmospheric Environment, 39, 1967-1977.

Lam, S.H.M., Saunders, S.M., Guo, H., Ling, Z.H., Jiang, F., Wang, X.M. and Wang, T.J., 2013. Modelling VOC source impacts on high ozone episode days observed at a mountain summit in Hong Kong under the influence of mountain-valley breezes. Atmospheric Environment, 81, 166-176.

Lau, A. K. H., Yuan, Z., Yu, J. Z., and Louie, P. K., 2010. Source apportionment of ambient volatile organic compounds in Hong Kong, Science of the Total Environment, 408, 4138-4149.

Lee, E., Chan, C. K., and Paatero, P., 1999. Application of positive matrix factorization in source apportionment of particulate pollutants in Hong Kong, Atmospheric Environment, 33, 3201-3212.

Lefohn, A. S., Shadwick, D. and Oltmans, S. J., 2010. Characterizing changes in surface ozone levels in metropolitan and rural areas in the United States for 1980–2008 and 1994–2008, Atmospheric Environment, 44, 5199-5210.

Lefohn, A.S., Shadwick, D. and Oltmans, S.J., 2008. Characterizing long-term changes in surface ozone levels in the United States (1980–2005). Atmospheric Environment, 42(35), 8252-8262. Liu, S.C., McFarland, M., Kley, D., Zafiriou, O. and Huebert, B.1., 1983. Tropospheric NOx and O3 budgets in the equatorial Pacific. Journal of Geophysical Research: Oceans, 88(C2), 1360-1368.

Lelieveld, J., Van Aardenne, J., Fischer, H., De Reus, M., Williams, J. and Winkler, P., 2004. Increasing ozone over the Atlantic Ocean. Science, 304(5676), 1483-1487.

Levy, H. 1971. Normal Atmosphere: Large Radical and Formaldehyde Concentrations Predicted. Science. Science, 173, 3992, 141-143.

Li, J., Zhai, C., Yu, J., Liu, R., Li, Y., Zeng, L. and Xie, S., 2018. Spatiotemporal variations of ambient volatile organic compounds and their sources in Chongqing, a mountainous megacity in China. Science of the Total Environment, 627, 1442-1452.

Li, K., Jacob, D. J., Liao, H., Shen, L., Zhang, Q. and Bates, K. H., 2019. Anthropogenic drivers of 2013-2017 trends in summer surface ozone in China. Proceedings of the National Academy of Sciences, 116(2), pp.422-427.

Li, L., Chen, C.H., Huang, C., Huang, H.Y., Zhang, G.F., Wang, Y.J., Wang, H.L., Lou, S.R., Qiao, L.P., Zhou, M. and Chen, M.H., 2012. Process analysis of regional ozone formation over the Yangtze River Delta, China using the Community Multi-scale Air Quality modeling system. Atmospheric Chemistry and Physics, 12, 10971–10987,

Li, M., Zhang, Q., Zheng, B., Tong, D., Yu, L., Liu, F., Hong, C., Kang, S., Liu, Y., Zhang, Y. and Yu, B., 2019. Persistent growth of anthropogenic non-methane volatile organic compound (NMVOC) emissions in China during 1990–2017: Drivers, speciation and ozone formation potential. Atmospheric Chemistry and Physics, 19(13), 8897-8913.

Li, Z., Xue, L., Yang, X., Zha, Q., Tham, Y. J., Yan, C., Louie, P. K. K., Luk, C. W. Y., Wang, T. and Wang, W., 2018. Oxidizing capacity of the rural atmosphere in Hong Kong, Southern China. Science of the Total Environment, 612, 1114-1122.

Lin, M., Horowitz, L.W., Payton, R., Fiore, A.M. and Tonnesen, G., 2017. US surface ozone trends and extremes from 1980 to 2014: quantifying the roles of rising Asian emissions, domestic controls, wildfires, and climate. Atmospheric Chemistry and Physics, 17(4), 2943-2970.

Ling, Z.H. and Guo, H., 2014. Contribution of VOC sources to photochemical ozone formation and its control policy implication in Hong Kong. Environmental Science and Policy, 38, 180-191.

Ling, Z. H., Guo, H., Cheng, H. R., and Yu, Y. F., 2011. Sources of ambient volatile organic compounds and their contributions to photochemical ozone formation at a site in the Pearl River Delta, southern China, Environmental Pollution, 159, 2310-2319.

Ling, Z. H., Guo, H., Zheng, J. Y., Louie, P. K. K., Cheng, H. R., Jiang, F., Cheung, K., Wong, L. C., and Feng, X. Q., 2013. Establishing a conceptual model for photochemical ozone pollution in subtropical Hong Kong, Atmospheric Environment, 76, 208–220.

Ling, Z.H., Guo, H., Lam, S.H.M., Saunders, S.M. and Wang, T., 2014. Atmospheric photochemical reactivity and ozone production at two sites in Hong Kong: Application of a master chemical mechanism–photochemical box model. Journal of Geophysical Research: Atmospheres, 119(17), 10567-10582.

Ling, Z., Guo, H., Simpson, I.J., Saunders, S.M., Lam, S.H.M., Lyu, X. and Blake, D.R. 2016a. New insight into the spatiotemporal variability and source apportionments of C1-C4 alkyl nitrates in Hong Kong. Atmospheric Chemistry and Physics, 16, 8141-8156.

Ling, Z., Guo, H., Chen, G., Lam, S. H. M., and Fan, S., 2016b. Formaldehyde and acetaldehyde at different elevations in mountainous areas in Hong Kong, Aerosol and Air Quality Research16, 1868-1878.

Liu, F., Beirle, S., Zhang, Q., Zheng, B., Tong, D. and He, K., 2017. NOx emission trends over Chinese cities estimated from OMI observations during 2005 to 2015. Atmospheric Chemistry and Physics, 17(15), 9261-9275.

Liu, H., Zhang, M. And Han, X., 2020. A review of surface ozone source apportionment in China. Atmospheric and Oceanic Science Letters, 13:5, 470-484.

Liu, S.C., McFarland, M., Kley, D., Zafiriou, O. and Huebert, B. 1983. Tropospheric NOx and O3 budgets in the equatorial Pacific. Journal of Geophysical Research, 88(C2), 1360-1368.

Liu, S.C., Trainer, M., Fehsenfeld, F.C., Parrish, D.D., Williams, E.J., Fahey, D.W., Hübler, G. and Murphy, P.C., 1987. Ozone production in the rural troposphere and the implications for regional and global ozone distributions. Journal of Geophysical Research: Atmospheres, 92(D4), 4191-4207.

Liu, X., Lyu, X., Wang, Y., Jiang, F. and Guo, H., 2019. Intercomparison of O3 formation and radical chemistry in the past decade at a suburban site in Hong Kong. Atmospheric Chemistry and Physics. 19, 7, 5127-5145.

Liu, X.H., Zhang, Y., Xing, J., Zhang, Q., Wang, K., Streets, D.G., Jang, C., Wang, W.-X. and Hao, J.-M. 2010. Understanding of regional air pollution over China using CMAQ, part II. Process analysis and sensitivity of ozone and particulate matter to precursor emissions. Atmospheric Environment, 44, 3719-3727.

Liu, X., Wang, N., Lyu, X., Zeren, Y., Jiang, F., Wang, X., Zou, S., Ling, Z. and Guo, H., 2020. Photochemistry of ozone pollution in autumn in Pearl River Estuary, South China. Science of The Total Environment, 754, 141812.

Liu, Y., Shao, M., Chang, C. C., Wang, J. L. and Chen, G. 2008a. Volatile Organic Compound (VOC) measurements in the Pearl River Delta (PRD) region, China. Atmospheric Chemistry and Physics,8, 1531-1545.

Liu, Y., Shao, M., Lu, S., Chang, C.C., Wang, J.L. and Fu, L., 2008b. Source apportionment of ambient volatile organic compounds in the Pearl River Delta, China: Part II. Atmospheric Environment, 42(25), 6261-6274.

Liu, Y., M. Shao, L. Fu, S. Lu, L. Zeng and D. Tang, 2008c. Source profiles of volatile organic compounds (VOCs) measured in China: Part I. Atmospheric Environment, 42, 6247-6260.

Liu, Y.F., Song, M., Liu, X., Zhang, Y., Hui, L., Kong, L., Zhang, Y., Zhang, C., Qu, Y., An, J. and Ma, D., 2020. Characterization and sources of volatile organic compounds (VOCs) and their related changes during ozone pollution days in 2016 in Beijing, China. Environmental Pollution, 257, 113599.

Liu, Y.H., Wang, H., Jing, S., Gao, Y., Peng, Y., Lou, S., Cheng, T., Tao, S., Li, L., Li, Y., Huang, D., Wang, Q. and An, J., 2019. Characteristics and sources of volatile organic compounds (VOCs) in Shanghai during summer: Implications of regional transport. Atmospheric Environment, 215, 116902.

Liu, Y.M. and Wang, T., 2020a. Worsening urban ozone pollution in China from 2013 to 2017–Part 1: The complex and varying roles of meteorology. Atmospheric Chemistry and Physics, 20(11), 6305-6321.

Liu, Y.M. and Wang, T., 2020b. Worsening urban ozone pollution in China from 2013 to 2017–Part 2: The effects of emission changes and implications for multi-pollutant control. Atmospheric Chemistry and Physics, 20(11), 6323-6337.

Liu, Z., Wang, Y., Gu, D., Zhao, C., Huey, L. G., Stickel, R., Liao, J., Shao, M., Zhu, T., Zeng, L., Amoroso, A., Costabile, F., Chang, C. C. and Liu, S. C., 2012. Summertime photochemistry during CAREBeijing-2007: RO_x budgets and O3 formation. Atmospheric Chemistry and Physics, 12, 7737-7752.

Louie, P.K., Ho, J.W., Tsang, R.C., Blake, D.R., Lau, A.K., Yu, J.Z., Yuan, Z., Wang, X., Shao, M. and Zhong, L., 2013. VOCs and OVOCs distribution and control policy implications in Pearl River Delta region, China. Atmospheric Environment, 76, 125-135.

Lu, H., Lyu, X., Cheng, H., Ling, Z. and Guo, H., 2019. Overview on the spatial-temporal characteristics of the ozone formation regime in China. Environ Sci Process Impacts, 21, 916-929.

Lu, K., Zhang, Y., Su, H., Shao, M., Zeng, L., Zhong, L., Xiang, Y., Chang, C., Chou, C.C. and Wahner, A., 2010. Regional ozone pollution and key controlling factors of photochemical ozone production in Pearl River Delta during summertime. Science China Chemistry, 53(3), 651-663.

Lu, K., Rohrer, F., Holland, F., Fuchs, H., Bohn, B., Brauers, T., Chang, C.C., Häseler, R., Hu, M., Kita, K. and Kondo, Y., 2012. Observation and modelling of OH and HO2 concentrations in the Pearl River Delta 2006: a missing OH source in a VOC rich atmosphere. Atmospheric Chemistry and Physics, 12(3), 1541-1569.

Lu, K.D., Hofzumahaus, A., Holland, F., Bohn, B., Brauers, T., Fuchs, H., Hu, M., Häseler, R., Kita, K., Kondo, Y. and Li, X., 2013. Missing OH source in a suburban environment near Beijing: observed and modelled OH and HO2 concentrations in summer 2006. Atmospheric Chemistry and Physics,13(2), 1057-1080.

Lu, Q., Zheng, J., Ye, S., Shen, X., Yuan, Z. and Yin, S., 2013. Emission trends and source characteristics of SO2, NOx, PM10 and VOCs in the Pearl River Delta region from 2000 to 2009. Atmospheric Environment, 76, 11-20.

Lu, X., Chen, N., Wang, Y., Cao, W., Zhu, B., Yao, T., Fung, J.C. and Lau, A.K., 2017. Radical budget and ozone chemistry during autumn in the atmosphere of an urban site in central China. Journal of Geophysical Research: Atmospheres, 122(6), 3672-3685.

Lu, X., Zhang, L., Liu, X., Gao, M., Zhao, Y. and Shao, J., 2018. Lower tropospheric ozone over India and its linkage to the South Asian monsoon. Atmospheric Chemistry and Physics, 18(5), 3101-3118.

Lu, X., Zhang, L., Chen, Y.F., Zhou, M., Zheng, B., Li, K., Liu, Y.M., Lin, J.T., Fu, T.M. and Zhang, Q., 2019. Exploring 2016-2017 surface ozone pollution over China: source contributions and meteorological influences. Atmospheric Chemistry and Physics.

Lu, X., Zhang, L., Wang, X., Gao, M., Li, K., Zhang, Y., Yue, X. and Zhang, Y., 2020a. Rapid Increases in Warm-Season Surface Ozone and Resulting Health Impact in China Since 2013. Environmental Science and Technology Letters, 7, 240-247.

Lu, X., Zhang, S., Xing, J., Wang, Y., Chen, W., Ding, D., Wu, Y., Wang, S., Duan, L. and Hao, J., 2020b. Progress of air pollution control in China and its challenges and opportunities in the ecological civilization era. Engineering, 6, 12, 1423-1431.

Lv, Z., Liu, H., Ying, Q., Fu, M., Meng, Z., Wang, Y., Wei, W., Gong, H. and He, K., 2018. Impacts of shipping emissions on PM2.5 pollution in China. Atmospheric Chemistry and Physics, 18, 15811–15824.

Lyu, X. P., Ling, Z. H., Guo, H., Saunders, S. M., Lam, S. H. M., Wang, N., Wang, Y., Liu, M., and Wang, T., 2015. Re-examination of C_1-C_5 alkyl nitrates in Hong Kong using an observation-based model, Atmospheric Environment, 120, 28-37.

Lyu, X. P., Chen, N., Guo, H., Zhang, W. H., Wang, N., Wang, Y. and Liu, M., 2016a. Ambient volatile organic compounds and their effect on ozone production in Wuhan, central China. Sci Total Environ, 541, 200-209.

Lyu, X.P., Liu, M., Guo, H., Ling, Z.H., Wang, Y., Louie, P.K.K. and Luk, C.W.Y., 2016b. Spatiotemporal variation of ozone precursors and ozone formation in Hong Kong: Grid field measurement and modelling study. Science of The Total Environment, 569, 1341-1349.

Lyu, X. P., Guo, H., Simpson, I. J., Meinardi, S., Louie, P. K. K., Ling, Z. H., Wang, Y., Liu, M., Luk, C. W. Y., Wang, N., and Blake, D. R., 2016c. Effectiveness of replacing catalytic converters in LPG-fuelled vehicles in Hong Kong, Atmospheric Chemistry and Physics, 16, 6609-6626.

Lyu, X.P., Zeng, L.W., Guo, H., Simpson, I.J., Ling, Z.H., Wang, Y., Murray, F., Louie, P.K.K., Saunders, S.M., Lam, S.H.M. and Blake, D.R., 2017a. Evaluation of the effectiveness of air pollution control measures in Hong Kong. Environmental pollution, 220, 87-94.

Lyu, X.P., Guo, H., Wang, N., Simpson, I.J., Cheng, H., Zeng, L., Saunders, S.M., Lam, S.H.M., Meinardi, S. and Blake, D.R., 2017b. Modeling C1–C4 alkyl nitrate photochemistry and their impacts on O3 production in urban and suburban environments of Hong Kong. Journal of Geophysical Research: Atmospheres, 122(19), 10539-10556.

Lyu, X. P., Guo, H., Cheng, H. R. and Wang, D. W., 2018. New particle formation and growth at a suburban site and a background site in Hong Kong. Chemosphere, 193, 664-674.

Lyu, X.P., Wang, N., Guo, H., Xue, L.K., Jiang, F., Zeren, Y.Z., Cheng, H.R., Cai, Z., Han, L.H. and Zhou, Y., 2019. Causes of a continuous summertime O3 pollution event in Jinan, a central city in the North China Plain. Atmospheric Chemistry and Physics. 19, 5, 3025-3042.

Lyu, X., Guo, H., Wang, Y., Zhang, F., Nie, K., Dang, J., Liang, Z., Dong, S., Zeren, Y., Zhou, B. and Gao, W., 2020. Hazardous volatile organic compounds in ambient air of China. Chemosphere, 246, 125731.

Ma, X., Tan, Z., Lu, K., Yang, X., Liu, Y., Li, S., Li, X., Chen, S., Novelli, A., Cho, C. and Zeng, L., 2019. Winter photochemistry in Beijing: Observation and model simulation of OH and HO2 radicals at an urban site. Science of The Total Environment, 685, 85-95.

Ma, Z.Q., Wang, Y.S., Zhang, X.L. and Xu, J., 2011. Comparison of ozone between Beijing and downstream area. Environmental Science (Chinese), 32(4), 924-929.

Madronich, S. and Flocke, S., 1999. The role of solar radiation in atmospheric chemistry, Environmental Photochemistry, 1-26.

Marenco A, Gouget H, Nédélec P, Pagés J-P. 1994. Evidence of a long-term increase in tropospheric ozone from Pic du Midi series: consequences: positive radiative forcing. Journal of Geophysical Research, 99, 16,617–16,632.

Martinez, M., Harder, H., Kovacs, T.A., Simpas, J.B., Bassis, J., Lesher, R., Brune, W.H., Frost, G.J., Williams, E.J., Stroud, C.A. and Jobson, B.T., 2003. OH and HO2 concentrations, sources, and loss rates during the Southern Oxidants Study in Nashville, Tennessee, summer 1999. Journal of Geophysical Research: Atmospheres, 108(D19).

Michoud, V., Kukui, A., Camredon, M., Colomb, A., Borbon, A., Miet, K., Aumont, B., Beekmann, M., Durand-Jolibois, R. and Perrier, S. 2012. Radical budget analysis in a suburban European site during the MEGAPOLI summer field campaign. Atmospheric Chemistry and Physics, 12 (24), 11951-11974.

Mills, G., Pleijel, H., Malley, C.S., Sinha, B., Cooper, O.R., Schultz, M.G., Neufeld, H.S., Simpson, D., Sharps, K., Feng, Z.Z., Gerosa, G., Harmens, H., Kobayashi, K., Saxena, P., Paoletti, E., Sinha, V. and Xu, X.B., 2018. Tropospheric Ozone Assessment Report: Present-day tropospheric ozone distribution and trends relevant to vegetation. Elementa-Science of the Anthropocene, 6, 47.

Ministry of Ecology and Environment of the People’s Republic of China (MEE PRC), 2014. Action plan for preventing and controlling air pollution in Guangdong Province, China, available at: http://www.mee.gov.cn/xxgk/hjyw/201403/t20140303_268619.shtml (last access: 25 October 2018).

Ministry of Ecology and Environment of the People’s Republic of China (MEE PRC), 2018. The State Council issued a notice on the issuance of a three-year Action Plan for Winning the Battle against Blue Skies. http://www.gov.cn/zhengce/content/2018-07/03/content_5303158.htm (last access: 9 November 2020).

Ministry of Ecology and Environment of the People's Republic of China (MEE PRC), 2019. MEE releases Report on Air Quality Improvement in China (2013-2018) https://www.mee.gov.cn/xxgk2018/xxgk/xxgk15/201906/t20190606_705778.html (last access: 9 November 2020).

Mo, Z., Shao, M., Wang, W., Liu, Y., Wang, M. and Lu, S., 2018. Evaluation of biogenic isoprene emissions and their contribution to ozone formation by ground-based measurements in Beijing, China. Science of The Total Environment, 627, 1485-1494.

Monks, P.S., Archibald, A.T., Colette, A., Cooper, O., Coyle,M., Derwent, R., et al., 2015. Tropospheric ozone and its precursors from the urban to the global scale from air quality to short-lived climate forcer. Atmospheric Chemistry and Physics, 15, 8889–8973.

Moradzadeh, M., Ashrafi, K. and Shafiepour-Motlagh, M., 2019. The Evaluation of Tropospheric Ozone Formation in the Downwind of the South Pars Industrial Zone. Pollution, 5(2), 361-375.

NARSTO, 2000. An Assessment of tropospheric ozone pollution: A North American perspective, NARSTO synthesis team, available at: http://cdiac.ess-dive.lbl.gov/programs/NARSTO/ozone_assessment.html (last access: 14 May 2020).

National Research Council (NRC), 1992. Rethinking the ozone problem in urban and regional air pollution. National Academies Press.

Ning G., Yim S.H.L., Yang Y., Gu Y., Dong G., 2020. Modulations of synoptic and climatic changes on ozone pollution and its health risks in mountain-basin areas. Atmospheric Environment, 240, 117808.

Norris, G., Wade, K., and Foley, C., 2008. EPA Positive Matrix Factorization (PMF) 3.0 Fundamentals and User Guide, US Environmental Protection Agency, Office of Research and Development, Washington, EPA 600/R-08/108.

Oltmans, S.J. and Komhyr, W.D., 1976. Surface ozone in Antarctica. Journal of Geophysical Research,81: 5359–5364.

Oltmans, S.J. and Komhyr, W.D., 1986. Surface ozone distributions and variations from 1973–1984: Measurements at the NOAA Geophysical Monitoring for Climatic Change Baseline Observatories. Journal of Geophysical Research: Atmospheres, 91(D4), 5229-5236.

Oltmans, S.J., Johnson, B.J., Harris, J.M., Thompson, A.M., Liu, H.Y., Chan, C.Y., Vömel, H., Fujimoto, T., Brackett, V.G., Chang, W.L. and Chen, J.P., 2004. Tropospheric ozone over the North Pacific from ozonesonde observations. Journal of Geophysical Research: Atmospheres, 109(D15).

Oltmans, S.J., Lefohn, A.S., Shadwick, D., Harris, J.M., Scheel, H.E., Galbally, I., Tarasick, D.W., Johnson, B.J., Brunke, E.G., Claude, H. and Zeng, G., 2013. Recent tropospheric ozone changes–A pattern dominated by slow or no growth. Atmospheric Environment, 67, 331-351.

Osthoff, H.D., Roberts, J.M., Ravishankara, A.R., Williams, E.J., Lerner, B.M., Sommariva, R., Bates, T.S., Coffman, D., Quinn, P.K., Dibb, J.E. and Stark, H., 2008. High levels of nitryl chloride in the polluted subtropical marine boundary layer. Nature Geoscience, 1(5), 324-328.

Ou, J.M., Guo, H., Zheng, J.Y., Cheung, K., Louie, P.K.K., Ling, Z.H., and Wang, D.W., 2015. Concentrations and sources of non-methane hydrocarbons (NMHCs) from 2005 to 2013 in Hong Kong: A multi-year real-time data analysis. Atmospheric Environment, 103, 196-206.

Ou, J., Yuan, Z., Zheng, J., Huang, Z., Shao, M., Li, Z., Huang, X., Guo, H. and Louie, P.K., 2016. Ambient ozone control in a photochemically active region: short-term despiking or long-term attainment? Environmental Science and Technology, 50(11), 5720-5728.

Paatero, P., 1997. Least squares formulation of robust non-negative factor analysis. Chemometrics and intelligent laboratory systems, 37(1), 23-35.

Paatero, P., 2000a. User's Guide for Positive Matrix Factorization Programs PMF2 and PMF3, Part 1: Tutorial, Prepared by University of Helsinki, Finland. US Environmental Protection Agency, 2000.

Paatero, P., 2000b. User's Guide for Positive Matrix Factorization Programs PMF2 and PMF3, Part 2: Reference, Prepared by University of Helsinki, Finland. US Environmental Protection Agency, 2000.

Parrish DD, Law KS, Staehelin J, Derwent R, Cooper OR, et al. 2012. Long-term changes in lower tropospheric baseline ozone concentrations at northern mid-latitudes. Atmospheric Chemistry and Physics 12: 11485–11504.

Parrish, D. D., Lamarque, J. F., Naik, V., Horowitz, L., Shindell, D. T., Staehelin, J., Derwent, R., Cooper, O. R., Tanimoto, H., Volz-Thomas, A., and Gilge, S., 2014. Long-term changes in lower tropospheric baseline ozone concentrations: Comparing chemistry-climate models and observations at northern midlatitudes., Journal of Geophysical Research: Atmospheres, 119, 5719-5736.

Polissar, A. V., Hopke, P. K., Paatero, P., Malm, W. C., and Sisler, J. F., 1998. Atmospheric aerosol over Alaska: 2. Elemental composition and sources, Journal of Geophysical Research: Atmospheres, 103 (D15).

Ran, L., Zhao, C., Geng, F., Tie, X., Tang, X., Peng, L., Zhou, G., Yu, Q., Xu, J. and Guenther, A., 2009. Ozone photochemical production in urban Shanghai, China: Analysis based on ground level observations. Journal of Geophysical Research: Atmospheres, 114(D15).

Ran, L., Zhao, C. S., Xu, W. Y., Han, M., Lu, X. Q., Han, S. Q., Lin, W. L., Xu, X. B., Gao, W., Yu, Q., Geng, F. H., Ma, N., Deng, Z. Z. And Chen, J., 2012. Ozone production in summer in the megacities of Tianjin and Shanghai, China: a comparative study. Atmospheric Chemistry and Physics, 12, 7531-7542.

Reff, A., Eberly, S. I., and Bhave, P. V., 2007. Receptor modeling of ambient particulate matter data using positive matrix factorization: review of existing methods, Journal of the Air and Waste Management Association, 57, 146-154.

Ren, X., Harder, H., Martinez, M., Lesher, R.L., Oliger, A., Shirley, T., Adams, J., Simpas, J.B. and Brune, W.H., 2003. HOx concentrations and OH reactivity observations in New York City during PMTACS-NY2001. Atmospheric Environment, 37(26), 3627-3637.

Richter, A., Burrows, J.P. Nub, H., Granier, C., and Niemeier, U., 2005. Increase in tropospheric nitrogen dioxide over China observed from space, Nature, 437, 129.

Riedel, T.P., Wolfe, G.M., Danas, K.T., Gilman, J.B., Kuster, W.C., Bon, D.M., Vlasenko, A., Li, S.M., Williams, E.J., Lerner, B.M. and Veres, P.R., 2014. An MCM modeling study of nitryl chloride (ClNO 2) impacts on oxidation, ozone production and nitrogen oxide partitioning in polluted continental outflow. Atmospheric Chemistry and Physics, 14(8), 3789-3800.

Sahoo, D., Petersen, B. and Miles, P., 2011. Measurement of equivalence ratio in a light-duty low temperature combustion diesel engine by planar laser induced fluorescence of a fuel tracer. SAE International Journal of Engines, 4(2), 2312-2325.

Saunders, S.M., Jenkin, M.E., Derwent, R. and Pilling, M. 2003. Protocol for the development of the Master Chemical Mechanism, MCM v3 (Part A): tropospheric degradation of non-aromatic volatile organic compounds. Atmospheric Chemistry and Physics, 2003, 3 (1), 161-180.

Simon, H., Reff, A., Wells, B., Xing, J. and Frank, N., 2015. Ozone trends across the United States over a period of decreasing NOx and VOC emissions. Environmental Science and Technology, 49(1), 186-195.

Saunders, S.M., Jenkin, M.E., Derwent, R.G., Pilling, M.J., 2003. Protocol for the development of the Master Chemical Mechanism, MCM v3 (Part A): Tropospheric degradation of non-aromatic volatile organic compounds. Atmospheric Chemistry and Physics, 3, 161-180.

Schauer, J.J., Kleeman, M.J., Cass, G.R. and Simoneit, B.R., 1999. Measurement of emissions from air pollution sources. 2. C1 through C30 organic compounds from medium duty diesel trucks. Environmental Science and Technology, 33(10), 1578-1587.

Seigneur, C. and Moran, M., 2004. Chemical Transport Models, in Particulate Matter Science for Policy Makers, Cambridge University Press, 283-323.

Seinfeld, J.H. and Pandis, S.N., 2016. Atmospheric Chemistry and Physics: from air pollution to climate change. John Wiley and Sons.

Shao, M., Zhang, Y., Zeng, L., Tang, X., Zhang, J., Zhong, L. and Wang, B., 2009a. Ground-level ozone in the Pearl River Delta and the roles of VOC and NOx in its production. Journal of Environmental Management, 90(1), 512-518.

Shao, M., Lu, S., Liu, Y., Xie, X., Chang, C., Huang, S. and Chen, Z., 2009b. Volatile organic compounds measured in summer in Beijing and their role in ground-level ozone formation. Journal of Geophysical Research: Atmospheres, 114(D2).

Shao, P., An, J., Xin, J., Wu, F., Wang, J., Ji, D. and Wang, Y., 2016. Source apportionment of VOCs and the contribution to photochemical ozone formation during summer in the typical industrial area in the Yangtze River Delta, China. Atmospheric Research, 176, 64-74.

Sheehy, P.M., Volkamer, R., Molina, L.T. and Molina, M.J., 2010. Oxidative capacity of the Mexico City atmosphere -Part 2: A ROx radical cycling perspective.

Shi, C., Wang, S., Liu, R., Zhou, R., Li, D., Wang, W., Li, Z., Cheng, T. and Zhou, B., 2015. A study of aerosol optical properties during ozone pollution episodes in 2013 over Shanghai, China. Atmospheric Research, 153, 235-249.

Sillman, S., 1995. The use of NOy, H2O2, and HNO3 as indicators for ozone-NOx-hydrocarbon sensitivity in urban locations. Journal of Geophysical Research: Atmospheres, 100(D7), 14175-14.

Sillman, S., 1999. The relation between ozone, NOx and hydrocarbons in urban and polluted rural environments. Atmospheric Environment, 33(12), 1821-1845.

Simon, H., Reff, A., Wells, B., Xing, J. and Frank, N., 2015. Ozone trends across the United States over a period of decreasing NOx and VOC emissions. Environmental Science and Technology, 49(1), 186-195.

Simpson, I. J., Blake, N. J., Barletta, B., Diskin, G. S., Fuelberg, H. E., Gorham, K., Huey, L. G., Meinardi, S., Rowland, F. S., Vay, S. A., Weinheimer, A. J., Yang, M., and Blake, D. R., 2010. Characterization of trace gases measured over Alberta oil sands mining operations: 76 speciated C_2-C_{10} volatile organic compounds (VOCs), CO_2, CH_4, CO, NO, NO_2, NO_y, O_3 and SO_2, Atmospheric Chemistry and Physics, 10, 11931−11954.

Slater, E.J., Whalley, L.K., Woodward-Massey, R., Ye, C., Lee, J.D., Squires, F., Hopkins, J.R., Dunmore, R.E., Shaw, M., Hamilton, J.F. and Lewis, A.C., 2020. Elevated levels of OH observed in haze events during wintertime in central Beijing. Atmospheric Chemistry and Physics Discussions, 20, 14847–14871.

So, K. L. and Wang, T., 2003. On the local and regional influence on ground-level ozone concentrations in Hong Kong, Environmental Pollution, 123, 307-317.

Solomon, P., Cowling, E., Hidy, G. and Furiness, C., 2000. Comparison of scientific findings from major ozone field studies in North America and Europe. Atmospheric Environment, 34, 1885-1920.

Song, C., Liu, B., Dai, Q., Li, H. and Mao, H., 2019. Temperature dependence and source apportionment of volatile organic compounds (VOCs) at an urban site on the north China plain. Atmospheric Environment, 207, 167-181.

Song, Y., Shao, M., Liu, Y., Lu, S., Kuster, W., Goldan, P. and Xie, S., 2007. Source apportionment of ambient volatile organic compounds in Beijing. Environmental Science and Technology, 41(12), 4348-4353.

Song, M., Tan, Q., Feng, M., Qu, Y., Liu, X., An, J. and Zhang, Y., 2018. Source Apportionment and Secondary Transformation of Atmospheric Nonmethane Hydrocarbons in Chengdu, Southwest China. Journal of Geophysical Research: Atmospheres, 123, 9741-9763.

Staehelin J, Thudium J, Buehler R, Volz-Thomas A, Graber W. 1994. Trends in surface ozone concentrations at Arosa (Switzerland). Atmospheric Environment, 28: 75–87.

Stockwell, W.R., Middleton, P., Chang, J.S. and Tang, X. 1990. The second generation regional acid deposition model chemical mechanism for regional air quality modeling. Journal of Geophysical Research: Atmospheres, 95, 16343-16367.

Stockwell, W.R., Kirchner, F., Kuhn, M. and Seefeld, S. 1997. A new mechanism for regional atmospheric chemistry modeling. Journal of Geophysical Research: Atmospheres, 102, 25847-25879.

Stone, D., Whalley, L.K. and Heard, D.E., 2012. Tropospheric OH and HO2 radicals: Field measurements and model comparisons. Chemical Society Reviews, 41(19), 6348-6404.

Su, R., Lu, K., Yu, J., Tan, Z., Jiang, M., Li, J., Xie, S., Wu, Y., Zeng, L., Zhai, C. and Zhang, Y., 2017. Exploration of the formation mechanism and source attribution of ambient ozone in Chongqing with an observation-based model. Science China Earth Sciences, 61, 23-32.

Tan, J.H., Guo, S.J., Ma, Y.L., Yang, F.M., He, K.B., Yu, Y.C., Wang, J.W., Shi, Z.B. and Chen, G.C., 2012. Non-methane hydrocarbons and their ozone formation potentials in Foshan, China. Aerosol and Air Quality Research, 12(3), 387-398.

Tan, Z., Fuchs, H., Lu, K., Hofzumahaus, A., Bohn, B., Broch, S., Dong, H., Gomm, S., Häseler, R., He, L., Holland, F., Li, X., Liu, Y., Lu, S., Rohrer, F., Shao, M., Wang, B., Wang, M., Wu, Y., Zeng, L., Zhang, Y., Wahner, A. and Zhang, Y., 2017. Radical chemistry at a rural site (Wangdu) in the North China Plain: observation and model calculations of OH, HO_2 and RO_2 radicals. Atmospheric Chemistry and Physics, 17, 663-690.

Tan, Z., Lu, K., Jiang, M., Su, R., Dong, H., Zeng, L., Xie, S., Tan, Q. and Zhang, Y., 2018a. Exploring ozone pollution in Chengdu, southwestern China: A case study from radical chemistry to O_3-VOC-NO_x sensitivity. Sci Total Environ, 636, 775-786.

Tan, Z., Lu, K., Dong, H., Hu, M., Li, X., Liu, Y., Lu, S., Shao, M., Su, R., Wang, H. and Wu, Y., 2018b. Explicit diagnosis of the local ozone production rate and the ozone-NOx-VOC sensitivities. Science bulletin, 63(16), 1067-1076.

Tan, Z., Lu, K., Hofzumahaus, A., Fuchs, H., Bohn, B., Holland, F., Liu, Y., Rohrer, F., Shao, M., Sun, K. and Wu, Y., 2019. Experimental budgets of OH, HO2, and RO2 radicals and implications for ozone formation in the Pearl River Delta in China 2014. Atmospheric Chemistry and Physics, 19(10).

Tang, J.H., Chan, L.Y., Chan, C.Y., Li, Y.S., Chang, C.C., Liu, S.C., Wu, D. and Li, Y.D., 2007. Characteristics and diurnal variations of NMHCs at urban, suburban, and rural sites in the Pearl River Delta and a remote site in South China. Atmospheric Environment, 41(38), 8620-8632.

Tang, W., Zhao, C., Geng, F., Peng, L., Zhou, G., Gao, W., Xu, J. and Tie, X., 2008. Study of ozone “weekend effect” in Shanghai. Science in China Series D: Earth Sciences, 51(9), 1354-1360.

Tang, X., Wang, Z., Zhu, J., Gbaguidi, A.E., Wu, Q., Li, J. and Zhu, T., 2010. Sensitivity of ozone to precursor emissions in urban Beijing with a Monte Carlo scheme. Atmospheric Environment, 44(31), 3833-3842.

Tarasick, D.W., Galbally, I.E., Cooper, O.R., Schultz, M., Ancellet, G., Leblanc, T., Wallington, T.J., Ziemke, J.R., Xiong, L., Steinbacher, M. and Staehelin, J., 2019. Tropospheric Ozone Assessment Report: Tropospheric ozone from 1877 to 2016, observed levels, trends and uncertainties. 7, 39, 1-72.

Tessum, C.W., Hill, J.D. and Marshall, J.D., 2015. Twelve-month, 12km resolution North American WRF-Chem v3. 4 air quality simulation: performance evaluation. Geoscientific Model Development, 8(4).

Thompson, D.W., Solomon, S., Kushner, P.J., England, M.H., Grise, K.M. and Karoly, D.J., 2011. Signatures of the Antarctic ozone hole in Southern Hemisphere surface climate change. Nature Geoscience, 4(11), 741-749.

Tie, X., Geng, F., Peng, L., Gao, W. and Zhao, C., 2009. Measurement and modeling of O3 variability in Shanghai, China: Application of the WRF-Chem model. Atmospheric Environment, 43(28), 4289-4302.

Turner, M.C., Jerrett, M., Pope III, C.A., Krewski, D., Gapstur, S.M., Diver, W.R., Beckerman, B.S., Marshall, J.D., Su, J., Crouse, D.L. and Burnett, R.T., 2016. Long-term ozone exposure and mortality in a large prospective study. American Journal of Respiratory and Critical Care Medicine, 193(10), 1134-1142.

United States Environmental Protection Agency (US EPA), 2017. Positive Matrix Factorization Model for environmental data analyses, available at https://www.epa.gov/air-research/positive-matrix-factorization-model-environmental-data-analyses (last access: 25 October 2018).

Volkamer, R., Sheehy, P.M., Molina, L.T. and Molina, M.J., 2010. Oxidative capacity of the Mexico City atmosphere -Part 1: A radical source perspective. Atmospheric Chemistry and Physics, 10,14, 6969-6991.

Wang, B., Shao, M., Lu, S. H., Yuan, B., Zhao, Y., Wang, M., Zhang, S. Q. and Wu, D., 2010. Variation of ambient non-methane hydrocarbons in Beijing city in summer 2008. Atmospheric Chemistry and Physics, 10, 5911-5923.

Wang, G., Cheng, S., Wei, W., Zhou, Y., Yao, S. and Zhang, H., 2016. Characteristics and source apportionment of VOCs in the suburban area of Beijing, China. Atmospheric Pollution Research, 7(4), 711-724.

Wang, G., Jia, S., Li, R., Ma, S., Chen, X., Li, L., Shi, G. and Niu, X., 2020. Seasonal variation characteristics of hydroxyl radical pollution and its potential formation mechanism during the daytime in Lanzhou. Journal of Environmental Sciences. 95, 58-64.

Wang, H., Lyu, X.P., Guo, H., Wang, Y., Zou, S.C., Ling, Z.H., Wang, X.M., Jiang, F., Zeren, Y.Z., Pan, W.Z. and Huang, X.B., 2018. Ozone pollution around a coastal region of South China Sea: interaction between marine and continental air. Atmospheric Chemistry and Physics, 18, 4277-4295.

Wang, H.L., Chen, C.H., Wang, Q., Huang, C., Su, L.Y., Huang, H.Y., Lou, S.R., Zhou, M., Li, L., Qiao, L.P. and Wang, Y.H., 2013. Chemical loss of volatile organic compounds and its impact on the source analysis through a two-year continuous measurement. Atmospheric Environment, 80, 488-498.

Wang, H.L., Yan, R., Xu, T., Wang, Y., Wang, Q., Zhang, T., An, J., Huang, C., Gao, Y., Gao, Y. and Li, X., 2020. Observation constrained aromatic emissions in Shanghai, China. Journal of Geophysical Research: Atmospheres, 125, e2019JD031815.

Wang, H.X., Kiang, C.S., Tang, X.Y., Zhou, X.J., and Chameides, W.L., 2005. Surface ozone: A likely threat to crops in Yangtze delta of China, Atmospheric Environment, 39, 3843–3850.

Wang, M., Chen, W., Zhang, L., Qin, W., Zhang, Y., Zhang, X., Z. and Xie, X., 2020. Ozone pollution characteristics and sensitivity analysis using an observation-based model in Nanjing, Yangtze River Delta Region of China. Journal of Environmental Sciences, 93, 13-22.

Wang M.Y., Yim S.H.L., Wong D.C., Ho K.F., 2019a. Source contributions of surface ozone in China using an adjoint sensitivity analysis. Science of the Total Environment, 662, 385-392.

Wang M.Y., Yim S.H.L., Dong G.H., Ho K.F., Wong D.C., 2019b. Mapping ozone source-receptor relationship and apportioning the health impact in the Pearl River Delta region using adjoint sensitivity analysis. Atmospheric Environment, 222, 117026.

Wang, N., Guo, H., Jiang, F., Ling, Z.H. and Wang, T., 2015. Simulation of ozone formation at different elevations in mountainous area of Hong Kong using WRF-CMAQ model. Science of the total environment, 505, 939-951.

Wang, N., Lyu, X.P., Deng, X.J., Guo, H., Deng, T., Li, Y., Yin, C.Q., Li, F. and Wang, S.Q., 2016. Assessment of regional air quality resulting from emission control in the Pearl River Delta region, southern China. Science of the total environment, 573, 1554-1565.

Wang, N., Lyu, X.P., Deng, X.J., Huang, X., Jiang, F. and Ding, A.J., 2019. Aggravating O_3 pollution due to NO_x emission control in eastern China. Science of the Total Environment, 677, 732-744.

Wang, S.W., Zhang, Q., Streets, D.G., He, K.B., Martin, R.V., Lamsal, L.N., Chen, D., Lei, Y. and Lu, Z., 2012. Growth in NOx emissions from power plants in China: bottom-up estimates and satellite observations. Atmospheric Chemistry and Physics, 12, 4429–4447.

Wang, T., Lam, K.S., Lee, A.S., Pang, S.W. and Tsui, W.S., 1998. Meteorological and chemical characteristics of the photochemical ozone episodes observed at Cape D'Aguilar in Hong Kong. Journal of applied Meteorology, 37(10), 1167-1178.

Wang, T., Cheung, V.T., Lam, K.S., Kok, G.L. and Harris, J.M., 2001a. The characteristics of ozone and related compounds in the boundary layer of the South China coast: temporal and vertical variations during autumn season. Atmospheric Environment, 35(15), 2735-2746.

Wang, T., Wu, Y.Y., Cheung, T.F. and Lam, K.S., 2001b. A study of surface ozone and the relation to complex wind flow in Hong Kong. Atmospheric Environment, 35(18), 3203-3215.

Wang, T., Wei, X.L., Ding, A.J., Poon, S.C., Lam, K.S., Li, Y.S., Chan, L.Y. and Anson, M., 2009. Increasing surface ozone concentrations in the background atmosphere of Southern China, 1994-2007. Atmospheric Chemistry and Physics, 9, 6217–6227.

Wang, T., Tham, Y.J., Xue, L., Li, Q., Zha, Q., Wang, Z., Poon, S.C., Dubé, W.P., Blake, D.R., Louie, P.K. and Luk, C.W., 2016. Observations of nitryl chloride and modeling its source and effect on ozone in the planetary boundary layer of southern China. Journal of Geophysical Research: Atmospheres, 121(5), 2476-2489.

Wang, T., Xue, L., Brimblecombe, P., Lam, Y.F., Li, L. and Zhang, L., 2017. Ozone pollution in China: A review of concentrations, meteorological influences, chemical precursors, and effects. Science of the Total Environment, 575, 1582-1596.

Wang, W, Cheng, T., Gu, X., Chen, H., Guo, H., Wang, Y., Bao, F., Shi, S., Xu, B., Zuo, X. and Meng, C., 2017. Assessing spatial and temporal patterns of observed ground-level ozone in China. Scientific reports, 7(1), 1-12.

Wang, X., Zhang, Y., Hu, Y., Zhou, W., Lu, K., Zhong, L., Zeng, L., Shao, M., Hu, M. and Russell, A.G., 2010. Process analysis and sensitivity study of regional ozone formation over the Pearl River Delta, China, during the PRIDE-PRD2004 campaign using the Community Multiscale Air Quality modeling system. Atmospheric Chemistry and Physics, 10, 4423–4437.

Wang, Y., Wang, H., Guo, H., Lyu, X.P., Cheng, H.R., Ling, Z.H., Louie, P.K., Simpson, I.J., Meinardi, S. and Blake, D.R., 2017. Long-term O_3-precursor relationships in Hong Kong: field observation and model simulation. Atmospheric Chemistry and Physics, 17, 10919-10935.

Wang, Y., Guo, H., Zou, S., Lyu, X., Ling, Z., Cheng, H. and Zeren, Y., 2018. Surface O_3 photochemistry over the South China Sea: Application of a near-explicit chemical mechanism box model. Environmental Pollution, 234, 155-166.

Wang, Y., Guo, H., Lyu, X., Zhang, L., Zeren, Y., Zou, S. and Ling, Z., 2019. Photochemical evolution of continental air masses and their influence on ozone formation over the South China Sea. Science of the Total Environment, 673, 424-434.

Wang, Z.S., Li, Y., Chen, T., Zhang, D., Sun, F., Wei, Q., Dong, X., Sun, R., Huan, N. and Pan, L., 2015. Ground-level ozone in urban Beijing over a 1-year period: Temporal variations and relationship to atmospheric oxidation. Atmospheric Research, 164, 110-117.

Wexler H, Moreland WB, Weyant WS. 1960. A preliminary report on ozone observations at Little America, Antarctica. Monthly Weather Review, 88, 43–54.

Whitten, G. and Hogo, H. 1980a. Modelling of simulated photochemical smog with kinetic mechanisms. Volume 1 (Final Report). United States Environmental Protection Agency, EPA-600/3-80-028a.

Whitten, G. and Hogo, H. 1980b. Modelling of simulated photochemical smog with kinetic mechanisms. Volume 2 (Final Report). United States Environmental Protection Agency, EPA-600/3-80-028b.

William A, M. and Michael W, H. 1999. Compendium Method TO-15, Determination of Volatile Organic Compounds (VOCs) in Air Collected in Specially-Prepared Canisters and Analyzed by Gas Chromatography. Mass Spectrometry. United States Environmental Protection Agency, Cincinnati, OH, 1.

Willmott, C. J., 1982. Some comments on the evaluation of model performance., Bulletin of the American Meteorological Society, 63(11), 1309-1313.

Wood, E.C., Herndon, S.C., Onasch, T.B., Kroll, J.H., Canagaratna, M.R., Kolb, C.E., Worsnop, D.R., Neuman, J.A., Seila, R., Zavala, M. and Knighton, W.B., 2009. A case study of ozone production, nitrogen oxides, and the radical budget in Mexico City. Atmospheric Chemistry and Physics, 9(7).

Woody, M.C., West, J.J., Jathar, S.H., Robinson, A.L. and Arunachalam, S. 2015. Estimates of non-traditional secondary organic aerosols from aircraft SVOC and IVOC emissions using CMAQ. Atmospheric Chemistry and Physics, 15, 6929-6942.

Wu, F., Yu, Y., Sun, J., Zhang, J., Wang, J., Tang, G. and Wang, Y., 2016. Characteristics, source apportionment and reactivity of ambient volatile organic compounds at Dinghu Mountain in Guangdong Province, China. Science of the Total Environment, 548, 347-359.

Wu, R., Li, J., Hao, Y., Li, Y., Zeng, L. and Xie, S., 2016. Evolution process and sources of ambient volatile organic compounds during a severe haze event in Beijing, China. Science of the Total Environment, 560, 62-72.

Wu, R. and Xie, S., 2017. Spatial distribution of ozone formation in China derived from emissions of speciated volatile organic compounds. Environmental Science and Technology 51, 2574–2583.

Wu, W., Xue, W., Lei, Y. and Wang, J., 2018. Sensitivity analysis of ozone in Beijing-Tianjin-Hebei (BTH) and its surrounding area using OMI satellite remote sensing data. China Environmental Science, 38(4), 1201-1208.

Xie, X., Shao, M., Liu, Y., Lu, S., Chang, C.C. and Chen, Z.M., 2008. Estimate of initial isoprene contribution to ozone formation potential in Beijing, China. Atmospheric Environment, 42(24), 6000-6010.

Xing, J., Wang, J., Mathur, R., Wang, S., Sarwar, G., Pleim, J., Hogrefe, C., Zhang, Y., Jiang, J., Wong, D.C. and Hao, J., 2017. Impacts of aerosol direct effects on tropospheric ozone through changes in atmospheric dynamics and photolysis rates. Atmospheric Chemistry and Physics, 17(16), p.9869.

Xu, J., Zhang, Y., Fu, J.S., Zheng, S. and Wang, W., 2008. Process analysis of typical summertime ozone episodes over the Beijing area. Science of the Total Environment, 399(1-3), 147-157.

Xu, J., Zhang, X., Xu, X., Zhao, X., Meng, W. and Pu, W., 2011. Measurement of surface ozone and its precursors in urban and rural sites in Beijing. Procedia Earth and Planetary Science, 2, 255-261.

Xu, S.C., Li, Y.W., Miao, Y.M., Gao, C., He, Z.X., Shen, W.X., Long, R.Y., Chen, H., Zhao, B. and Wang, S.X., 2019. Regional differences in nonlinear impacts of economic growth, export and FDI on air pollutants in China based on provincial panel data. Journal of Cleaner Production, 228, 455-466.

Xu, X., Lin, W., Wang, T., Yan, P., Wang, J., Meng, Z., and Wang, Y., 2008. Long-term trend of surface ozone at a regional background station in eastern China 1991-2006: enhanced variability, Atmospheric Chemistry and Physics, 8, 2595-2607.

Xu, Z., Wang, T., Wu, J., Xue, L., Chan, J., Zha, Q., Zhou, S., Louie, P.K. and Luk, C.W., 2015. Nitrous acid (HONO) in a polluted subtropical atmosphere: Seasonal variability, direct vehicle emissions and heterogeneous production at ground surface. Atmospheric Environment, 106, 100-109.

Xu, Z., Huang, X., Nie, W., Chi, X., Xu, Z., Zheng, L., Sun, P. and Ding, A., 2017. Influence of synoptic condition and holiday effects on VOCs and ozone production in the Yangtze River Delta region, China. Atmospheric Environment, 168, 112-124.

Xue, L. K., Wang, T., Gao, J., Ding, A. J., Zhou, X. H., Blake, D. R., Wang, X. F., Saunders, S. M., Fan, S. J., Zuo, H. C., Zhang, Q. Z. and Wang, W. X., 2014a. Ground-level ozone in four Chinese cities: precursors, regional transport and heterogeneous processes. Atmospheric Chemistry and Physics, 14, 13175-13188.

Xue, L. K., Wang, T., Louie, P. K., Luk, C. W., Blake, D. R., and Xu, Z., 2014b. Increasing external effects negate local efforts to control ozone air pollution: a case study of Hong

Kong and implications for other Chinese cities, Environmental Science and Technology., 48, 10769-10775.

Xue, L.K., Saunders, S.M., Wang, T., Gao, R., Wang, X.F., Zhang, Q.Z. and Wang, W.X., 2015. Development of a chlorine chemistry module for the Master Chemical Mechanism. Geoscientific model development. 8, 10, 3151-3162.

Xue, L., Gu, R., Wang, T., Wang, X., Saunders, S., Blake, D., Louie, P.K., Luk, C.W., Simpson, I., Xu, Z. and Wang, Z., 2016. Oxidative capacity and radical chemistry in the polluted atmosphere of Hong Kong and Pearl River Delta region: analysis of a severe photochemical smog episode. Atmospheric Chemistry and Physics, 16, 9891–9903.

Xue, L., Ding, A., Cooper, O., Huang, X., Wang, W., Zhou, D., Wu, Z., McClure-Begley, A., Petropavlovskikh, I., Andreae, M.O. and Fu, C., 2020. ENSO and Southeast Asian biomass burning modulate subtropical trans-Pacific ozone transport. National Science Review, 0, 1–8.

Yang, G., Liu, Y. and Li, X., 2020. Spatiotemporal distribution of ground-level ozone in china at a city level. Scientific Reports, 10(1), 1-12.

Yang, X., Xue, L., Wang, T., Wang, X., Gao, J., Lee, S., Blake, D. R., Chai, F. And Wang, W., 2018. Observations and Explicit Modelling of Summertime Carbonyl Formation in Beijing: Identification of Key Precursor Species and Their Impact on Atmospheric Oxidation Chemistry. Journal of Geophysical Research: Atmospheres, 123, 1426-1440.

Yang, Y., Liu, X., Zheng, J., Tan, Q., Feng, M., Qu, Y., An, J. and Cheng, N., 2019. Characteristics of one-year observation of VOCs, NOx, and O3 at an urban site in Wuhan, China. Journal of Environmental Sciences, 79, 297-310.

Yao, C., Cheung, C. S., Cheng, C., Wang, Y., Chan, T. L., and Lee, S. C., 2008. Effect of diesel/methanol compound combustion on diesel engine combustion and emissions, Energy Convers. Manag., 49, 1696-1704.

Yao, D., Lyu, X., Murray, F., Morawska, L., Yu, W., Wang, J., and Guo, H., 2019. Continuous effectiveness of replacing catalytic converters on liquified petroleum gas-fueled vehicles in Hong Kong., Science of the Total Environment, 648, 830-838.

Yarwood, G., Rao, Sunja 2005. Updates to the Carbon Bond Chemical Mechanism: CB05. (Final report). United States Environmental Protection Agency, EPA-RT-04-00675.

Yim S.H.L., Wang M.Y., Gu Y., Yang Y., Dong G.H., Li Q., 2019. Effect of Urbanization on Ozone and Resultant Health Effects in the Pearl River Delta Region of China. Journal of Geophysical Research: Atmospheres, 124, 11568-11579.

Yuan, B., Shao, M., Lu, S. and Wang, B., 2010. Source profiles of volatile organic compounds associated with solvent use in Beijing, China. Atmospheric Environment, 44(15), 1919-1926.

Yuan, Z., Lau, A.K.H., Shao, M., Louie, P.K., Liu, S.C. and Zhu, T., 2009. Source analysis of volatile organic compounds by positive matrix factorization in urban and rural environments in Beijing. Journal of Geophysical Research: Atmospheres, 114(D2).

Zeng, L., Lyu, X., Guo, H., Zou, S. and Ling, Z., 2018. Photochemical formation of C1–C5 alkyl nitrates in suburban Hong Kong and over the South China Sea. Environmental Science and Technology, 52(10), 5581-5589.

Zeng, P., Lyu, X. P., Guo, H., Cheng, H. R., Jiang, F., Pan, W. Z., Wang, Z. W., Liang, S. W. and Hu, Y. Q., 2018. Causes of ozone pollution in summer in Wuhan, Central China. Environmental Pollution, 241, 852-861.

Zeng, P., Lyu, X., Guo, H., Cheng, H., Wang, Z., Liu, X. and Zhang, W., 2019. Spatial variation of sources and photochemistry of formaldehyde in Wuhan, Central China. Atmospheric Environment, 214, 116826.

Zeren, Y., Guo, H., Lyu, X., Jiang, F., Wang, Y., Liu, X., Zeng, L., Li, M. and Li, L., 2019. An ozone "pool" in South China: Investigations on atmospheric dynamics and photochemical processes over the Pearl River Estuary. Journal of Geophysical Research: Atmospheres, 124(22), 12340-12355.

Zha, Q., 2015. Measurement of nitrous acid (HONO) and the implications to photochemical pollution, MPhil dissertation, The Hong Kong Polytechnic University.

Zhang, J., Wang, T., Chameides, W.L., Cardelino, C., Kwok, J., Blake, D.R., Ding, A. and So, K.L., 2007. Ozone production and hydrocarbon reactivity in Hong Kong, Southern China. Atmospheric Chemistry and Physics, 7 (2), 557-573.

Zhang, J., Sun, Y., Wu, F., Sun, J. and Wang, Y., 2014. The characteristics, seasonal variation and source apportionment of VOCs at Gongga Mountain, China. Atmospheric Environment, 88, 297-305.

Zhang, Q., Yuan, B., Shao, M., Wang, X., Lu, S., Lu, K., Wang, M., Chen, L., Chang, C.C. and Liu, S.C., 2014. Variations of ground-level O3 and its precursors in Beijing in summertime between 2005 and 2011. Atmospheric Chemistry and Physics, 14(12), 6089-6101.

Zhang, Y., Su, H., Zhong, L.J., Cheng, Y.F., Zeng, L.M., Wang, X.S., Xiang, Y.R., Wang, J.L., Gao, D.F., Shao, M. and Fan, S.J., 2008. Regional ozone pollution and observation-based approach for analyzing ozone–precursor relationship during the PRIDE-PRD2004 campaign. Atmospheric Environment, 42(25), 6203-6218.

Zhang, Y.L., Wang, X., Blake, D.R., Li, L., Zhang, Z., Wang, S., Guo, H., Lee, S.C., Gao, B., Chan, L., and Wu, D., 2012. Aromatic hydrocarbons as ozone precursors before and after outbreak of the 2008 financial crisis in the Pearl River Delta region, south China., Journal of Geophysical Research: Atmospheres, 117, D15306.

Zhang, Y.Q., Cooper, O.R., Gaudel, A., Thompson, A.M., Nédélec, P., Ogino, S.Y. and West, J.J., 2016. Tropospheric ozone change from 1980 to 2010 dominated by equatorward redistribution of emissions. Nature Geoscience, 9(12), 875-879.

Zhao, B., Wang, S.X., Liu, H., Xu, J.Y., Fu, K., Klimont, Z., Hao, J.M., He, K.B., Cofala, J. and Amann, M., 2013. NOx emissions in China: historical trends and future perspectives. Atmospheric Chemistry and Physics, 13(19), 9869-9897.

Zhao, Y., Chen, L., Li, K., Han, L., Zhang, X., Wu, X., Gao, X., Azzi, M. and Cen, K., 2020. Atmospheric ozone chemistry and control strategies in Hangzhou, China: Application of a 0-D box model. Atmospheric Research, 105109.

Zheng, B., Tong, D., Li, M., Liu, F., Hong, C., Geng, G., Li, H., Li, X., Peng, L., Qi, J. and Yan, L., 2018. Trends in China's anthropogenic emissions since 2010 as the consequence of clean air actions. Atmospheric Chemistry and Physics, 18(19), 14095-14111.

Zheng, J., Zhang, L., Che, W., Zheng, Z. and Yin, S., 2009a. A highly resolved temporal and spatial air pollutant emission inventory for the Pearl River Delta region, China and its uncertainty assessment. Atmospheric Environment, 43, 5112-5122.

Zheng, J., Shao, M., Che, W., Zhang, L., Zhong, L., Zhang, Y. and Streets, D., 2009b. Speciated VOC emission inventory and spatial patterns of ozone formation potential in the Pearl River Delta, China. Environmental Science and Technology, 43(22), 8580-8586.

Zheng, J., Zheng, Z., Yu, Y. and Zhong, L., 2010a. Temporal, spatial characteristics and uncertainty of biogenic VOC emissions in the Pearl River Delta region, China. Atmospheric Environment, 44(16), 1960-1969.

Zheng, J., Zhong, L., Wang, T., Louie, P.K. and Li, Z., 2010b. Ground-level ozone in the Pearl River Delta region: Analysis of data from a recently established regional air quality monitoring network. Atmospheric Environment, 44(6), 814-823.

Zhu, C., Zhang, N. and Shi, Y., 2017. Consideration on Features of Ozone Pollution and Countermeasure. Huan Jing Bao Hu, 16, 64-66.

Zhu, J., Wang, S., Wang, H., Jing, S., Lou, S., Saiz-Lopez, A. And Zhou, B., 2020. Observationally constrained modelling of atmospheric oxidation capacity and photochemical reactivity in Shanghai, China. Atmospheric Chemistry and Physics, 20, 1217-1232.

Zhu, J.X., Cheng, H.R., Peng, J., Zeng, P., Wang, Z., Lyu, X.P. and Guo, H., 2020. O3 photochemistry on O3 episode days and non-O3 episode days in Wuhan, Central China. Atmospheric Environment, 223, 117236.

Zhu, Y., Yang, L., Chen, J., Wang, X., Xue, L., Sui, X., Wen, L., Xu, C., Yao, L., Zhang, J. and Shao, M., 2016. Characteristics of ambient volatile organic compounds and the influence of biomass burning at a rural site in Northern China during summer 2013. Atmospheric Environment, 124, 156-165.

Zong, R., Yang, X., Wen, L., Xu, C., Zhu, Y., Chen, T., Yao, L., Wang, L., Zhang, J., Yang, L. and Wang, X., 2018a. Strong ozone production at a rural site in the North China Plain: Mixed effects of urban plumes and biogenic emissions. Journal of Environmental Sciences, 71, 261-270.

Zong, R., Xue, L., Wang, T. and Wang, W. 2018b. Inter-comparison of the Regional Atmospheric Chemistry Mechanism (RACM2) and Master Chemical Mechanism (MCM) on the simulation of acetaldehyde. Atmospheric Environment, 186, 144-149.

Zou, Y., Deng, X.J., Zhu, D., Gong, D.C., Wang, H., Li, F., Tan, H.B., Deng, T., Mai, B.R., Liu, X.T. and Wang, B.G., 2015. Characteristics of 1 year of observational data of VOCs, NOx and O3 at a suburban site in Guangzhou, China. Atmospheric Chemistry and Physics, 15(12), 6625-6636.